STUDIES OF OVERLAYER VIBRATIONAL STRUCTURE AND IDENTIFICATION OF ADSORBED REACTION INTERMEDIATES VIA ELECTRON ENERGY LOSS SPECTROSCOPY

Thesis by

Alan Brad Anton

In Partial Fulfillment of the Requirements

for the Degree of

Doctor of Philosophy

California Institute of Technology

Pasadena, California

1986

(Submitted July 12, 1985)

This Thesis is dedicated to the
memory of my father.

Table of Contents

Page

Acknowledgments

The influence of a few people has had profound effects on my success as a student and my development as a scientist, and to them I am eternally grateful. Mrs. Kernosky sparked my interest with her clever demonstrations of the laws of physics in elementary school, Jim Blunkowski made chemistry fascinating in high school, Henry McGee was the exemplary educator in college, Neil Avery demonstrated the enthusiasm for learning which I hope to maintain, and my research advisor, Henry Weinberg, taught me how to make accurate and important scientific contributions.

The task of preparing this Thesis and obtaining my PhD, though long and arduous, was made bearable (and frequently delightful!) by my interactions with the friends I've been lucky to find on this adventure. Many thanks and good luck to Jane and John, the Sierra Madre gang, Barry and Karen, Kathy, Rick and Darnelle, Strawberry, Roxy, Jim, the basketball team, the football team, the softball team, and many others. Special thanks to Kelly and the Morrow family. Also, thanks to Buck, Gordon, Lori and David, Genine, and others from the past who stayed in touch.

I am particularly indebted to Henry Weinberg. His support not only as a research advisor, but also as colleague and friend, has prepared me well for a fruitful and rewarding future.

Finally, I thank my parents, without whom this and countless other adventures could not have been possible.

Abstract

Electron energy loss vibrational spectroscopy (EELS) and thermal desorption mass spectrometry (TDMS) have been used to investigate the chemisorption of several molecules on the hexagonally close-packed Ru(001) surface. The adsorption of N_2, O_2, and N_2 with O_2 and CO was investigated to characterize the chemical state of adsorbed molecules, including their interactions with the substrate and with their adsorbed neighbors, through effects manifest in their vibrational spectra. The adsorption of $(CH_3)_2CO$ and H_2CO and their subsequent thermal decomposition was investigated to identify the structures of reactive and nonreactive adsorbed intermediates, to identify the products of surface reactions and their structures, to identify surface reaction mechanisms, and to correlate reactivity with the structure of adsorbed intermediates.

N_2 binds to the Ru(001) surface at on-top sites with its molecular axis perpendicular to the surface. In contrast to results reported for the isoelectronic molecule CO on the same surface, however, ν(NN) decreases with increasing surface coverage, a result which is explained in terms of increasing population of the $1\pi_g$ antibonding orbital of N_2 with increasing surface coverage.

The vibrational spectra of ordered p(2x2) and p(1x2) overlayers of oxygen adatoms on Ru(001) were studied via comparison of experimental EEL spectra to vibrational spectra calculated with a Green's function lattice dynamical technique. The results identify features due to coupling of the overlayers to substrate phonons and illustrate a unique effect of adsorption site symmetry which distinguishes the vibrational spectra of the two overlayers.

EELS and TDMS results used in conjunction to determine the effects of interactions between contrasting adsorbates in mixed adlayers of N_2 with oxygen and N_2 with CO on Ru(001). Preadsorbed oxygen produces a strong chemical effect on subsequently adsorbed N_2, stabilizing σ-donation while destabilizing $1\pi_g$-backdonation in the N_2-surface bond. Preadsorbed N_2 increases the ability of the Ru surface atoms to backdonate electron density into the 2π orbital of subsequently adsorbed CO, producing values of ν(CO) which are lower than are observed under any circumstances for the adsorption of CO on the clean Ru(001) surface.

Adsorption of $(CH_3)_2CO$ on the clean Ru(001) surface produces η^2-bonded molecular acetone which decomposes to CO, carbon and hydrogen upon heating the surface. If the surface is instead precovered with a p(2x2) oxygen overlayer, a significant fraction of the subsequently adsorbed acetone exists in an η^1-bonded configuration which, like η^1 acetone observed on the clean Pt(111) surface, desorbs molecularly upon heating. These results demonstrate in a quantifiable way how the reactivity of the Ru(001) surface can be modified by the presence of a coadsorbed species, and that the change in reactivity can be correlated with the selectivity of the surface toward reactive (η^2) and nonreactive (η^1) intermediate bonding configurations.

Adsorption of the chemically similar molecule H_2CO on Ru(001) produces many effects analogous to those observed for $(CH_3)_2CO$ adsorption: η^2 bonding is observed on the clean surface and η^1 bonding is observed when the surface is precovered with a p(2x2) oxygen overlayer. The H_2CO is more reactive than $(CH_3)_2CO$, however, decomposing at low coverages and low temperature on the clean surface to give hydrogen and CO before any molecular adsorption is observed. At coverages intermediate between total decomposition and near monolayer saturation, where the η^2–H_2CO species is observed, partial decomposition to yield an η^2-HCO species is observed. The results have important implications for the mechanistic understanding of CO hydrogenation reactions catalyzed under heterogeneous conditions.

Chapter I.

Introduction

Eventual progress in technological fields dominated by reactive processes at metal surfaces, such as the effective design of metal devices to be operated in corrosive environments or the optimization of yield and selectivity in commercial catalytic processes, demands a fundamental understanding of the physical and chemical effects which control these reactive gas-surface interactions. Recent history has witnessed a huge effort aimed at gaining this fundamental understanding through the experimental (and associated theoretical) techniques of modern surface science, where model studies of the pertinent gas-surface interactions are conducted on well-characterized single crystal metal surfaces under ultrahigh vacuum conditions. This careful control of surface geometry and reactant concentration, coupled with judicious application of appropriate spectroscopic techniques, allows separation and individual scrutiny of many of the reactant-surface-product interactions which accompany the surface reactions. A series of investigations of adsorption and reaction on a single crystal ruthenium surface, employing surface science techniques such as thermal desorption mass spectrometry (TDMS) and high-resolution electron energy loss spectroscopy (EELS) to understand some of these interactions, is presented in this Thesis.

First, to provide a framework within which the goals of the investigations to be described in this Thesis can be addressed clearly, consider the following step-by-step description of the representative reactant-surface-product interactions which accompany a surface reaction **(1-3)**:

1. The gas phase reactant molecules, with their internal degrees of freedom in equilibrium at the temperature T_g of the gas phase, approach the surface and are "trapped" by their interaction with the attractive surface potential, transferring momentum to the surface and becoming localized at adsorption sites.

2. Equilibrium of the internal degrees of freedom of the reactants with those of the surface at temperature T_s leads to dissociation or structural rearrangement of the reactants to form the precursors to the surface reaction products.

3. Transfer of energy from the surface heat bath, characterized by its spectrum of allowed quantum states **(4,5)** and its temperature T_s, to the adsorbed intermediates produces the transition state species, a fraction of which in turn proceeds to the surface reaction products **(6)**.

4. Energy liberated by formation of products from the transition state species is temporarily trapped in excited states of the reaction products. Transfer of some of this energy to the surface occurs, leading either to equilibration of the products on the suface at T_s or to desorption with some of the excess energy of reaction appearing as excitation of the internal modes of the product molecules and some as residual excitation of the surface reaction zone **(7,8)**.

The surface reaction rates and the selectivity toward specific products which could potentially be formed are sensitive to the physical properties of the reactant-surface system just described. For example, energy placed selectivity in the electronic, vibrational rotational or translational **(3,9)** degrees of freedom of the arriving reactant molecules may act in concert with the effect of the surface to increase reaction rates or selectivity toward desired products. Similarly, variation of the surface geometry **(10)** or the adsorption potential [by addition of coadsorbed species, for example **(11)**] can affect the ability of the surface to selectively bind reactants into the intermediate configurations which most readily lead to the desired reaction products. Also, the excitation spectrum of the surface reaction zone, including particularly its electronic and vibrational degrees of freedom **(5)**, affects the rates of energy exchange to and from the adsorbed reactants, and therefore dominates the kinetics of the surface reactions in most cases **(1,2,12,13)**.

Via studies of the chemisorption of a number of small molecules on the hexagonally close-packed (001) surface of ruthenium **(14)**, the work presented in this Thesis focuses on two important aspects of these reactant-surface-product interactions, both of which are particularly well suited to the application of a vibrational spectroscopic technique. Included in Chapters II, III and IV are measurements of the vibrational structure of adsorbed overlayers of atomic and diatomic species, the details of which are interpreted in terms of current models that describe the effects of chemical **(15)**, electrodynamic **(16)** and mechanical **(17)** interactions between adsorbates on the vibrational spectra of such overlayers. In addition to elucidating the structure and chemical state of the adsorbates, the results obtained provide valuable tests of the applicability of the popular models and their ability to accurately describe the vibrational structure of surface layers. Chapters V through VIII, making use of spectra-structure correlations first developed for gas phase vibrational spectroscopy **(18,19)**, apply surface vibrational spectroscopy to the structural identification of adsorbed reaction intermediates and products, seeking to identify surface reaction mechanisms and to delimit the structures of the transition states which lead to the observed products. In addition to EEL vibrational spectroscopy, all the above mentioned investigations also make use of thermal desorption measurements to quantify surface coverages and binding energies, characterizing further the adsorbed state of the surface species investigated.

To facilitate the reader's understanding of the results obtained and the significance of the conclusions drawn, a brief review of the important experimental techniques employed, with emphasis on the information available from the results they provide, is presented below.

In a TDMS experiment, after exposure to the gas of interest at low temperature to form a chemisorbed overlayer, the crystal is heated linearly with time ($T = T_0 + \beta t$, where T is the sample temperature, β is the heating rate in K/s, and t is time), and the partial pressures of desorbing surface reaction products are measured with a quadrupole mass spectrometer as a function either of time or the sample temperature. A mass balance for the desorption reaction yields **(20)**:

$$-\frac{d\sigma_i}{dt} = \frac{V}{AkT_g}\left[\frac{dp_i}{dt} + \frac{S_i p_i}{V}\right] \qquad (1)$$

where σ_i is the surface coverage of species i, p_i is its partial pressure, S_i is the vacuum chamber pumping speed for species i, V is the chamber volume, A is the adsorbent surface area, and T_g is the temperature of the gas phase. For low values of β and high values of S_i, both conditions which prevail typically in ultrahigh vacuum experiments, the term proportional to p_i on the right-hand side of Eq. (1) is very large with respect to the term proportional to dp_i/dt, and the desorption rate is conveniently proportional to the partial pressure of species i as measured with the mass spectrometer, i.e.

$$-\frac{d\sigma_i}{dt} = \left(\frac{S_i}{AkT_g}\right)p_i\,. \qquad (2)$$

From this it can be easily seen that the time integral of the total pressure signal (or equivalently, the area under a trace of mass spectrometer signal versus time or temperature, since $dT = \beta dt$) is proportional to the initial surface coverage of species i, as shown below:

$$\sigma_o = \int_0^{t'}\left(-\frac{d\sigma_i}{dt}\right)dt = \left(\frac{S_i}{AkT_g}\right)\int_0^{t'} p_i dt = \left(\frac{S_i}{AkT_g}\right)\int_0^{T'}\left(\frac{p_i}{\beta}\right)dT\,. \qquad (3)$$

If a kinetic model for the desorption reaction is assumed, for example

$$-\frac{d\sigma_i}{dt} = k_i\sigma_i^n = \nu_i\sigma_i^n\exp(-E_i/kT)\ , \qquad (4)$$

where n is the desorption reaction order species i, k_i is the rate coefficient, ν_i is the preexponential factor, and E_i the activation energy of the desorption reaction, a lineshape analysis of the TDMS traces can be performed to extract kinetic parameters. In the absence of a true activation barrier to desorption other than the breaking of chemisorption bonds, the E_i's so obtained correspond to thermodynamic binding energies for th adsorbed species. Such lineshape analyses rarely provide enough information to allow discrimination among several possible models for the desorption kinetics **(21)**, so the absolute thermodynamic values obtained by this method are suspect. However, they do provide useful comparisons of the effects of surface coverage, interactions with coadsorbed species, etc. on binding energies, and therefore are invaluable in identifying the chemical state of adsorbed species.

For the EELS experiments which are presented in this Thesis, a low energy (less than 10 eV) beam of electrons is generated by a thermionic emitter, passed through a dispersive electrostatic energy selector to attain monochromaticity sufficient for the rigors of vibrational spectroscopy, and focused on the surface of the crystal sample. Although most of the incident beam (100 pA total current) is collected by the sample as current, some electrons (roughly 10%) scatter from the surface, and a fraction of those (roughly 1%) lose discrete amounts of energy to excite surface vibrations. The scattered beam is subsequently collected, counted, and energy analyzed by a second dispersive electrostatic selector to give an intensity versus energy loss spectrum. The geometry of the scattering arrangement is important in distinguishing between various operable scattering mechanisms which describe the inelastic encounters of the electrons with the surface vibrations **(22)**.

Long-range "dipolar" scattering is the dominant inelastic channel observed in EELS measurements. In this mechanism, the electrons approaching the surface interact with the time dependent electric field which results from the oscillation of separated charges in the adsorbed species. The dielectric properties of metals at infrared frequencies insure that the resulting field has components only perpendicular to the surface, thus only adsorbate vibrations with components of motion perpendicular to the surface conducting plane can produce this type of inelastic scattering. Cast in the jargon of group theory, only those vibrations which belong to the totally symmetric representation of the adsorbate-surface complex point group can couple to the incident electron to give dipolar scattering. Also, the absence of oscillating field components parallel to the surface insures that the transfer of momentum from the incident electron to the surface vibration includes only a perpendicular component, i.e. momentum parallel to the surface is conserved through the scattering event. The important result of these considerations is that electrons which scatter by this mechanism, arriving with an incident kinetic energy of E_0 and losing energy $\hbar\omega_0$ to excite a surface vibration, emerge from the surface in a direction which deviates from that of the specularly reflected elastic beam by only a small angle $\Delta\theta_s$, which is given by **(22)**

$$\Delta\theta_s = \frac{\hbar\omega_0}{2E_0}. \tag{5}$$

For typical experimental parameters, i.e. $E_0 = 5$ eV and $\hbar\omega_0 = 200$ mV (1600 cm^{-1}), $\Delta\theta_s < 1.5°$, and, when this is compared to a typical electron analyzer acceptance angle of 2-3°, it can be seen that electrons which scatter by this mechanism can be readily collected by centering the electron analyzer on the elastically scattered specular beam.

Inelastic scattering also occurs via interaction of the incident electrons with the short-range repulsive potentials of the adsorbate atoms **(22)**, and, since dielectric screening plays no role in this mechanism, no restrictions on the polarization of vibrational motion or on electron-adsorbate momentum transfer apply. Two important results follow: all normal vibrational modes of the adsorbate complex can in principle produce inelastic scattering by this "impact" mechanism; and those electrons scattered by this mechanism emerge diffusely from the surface, thus rotation of the electron analyzer away from the sharply defined specular beam to a point where the inelastic contribution due to dipolar scattering is suppressed allows observation of the inelastic spectrum due almost exclusively to impact scattering. A theoretical analysis of this scattering mechanism shows that the strength of coupling to a particular mode is proportional to the square of the product of momentum transfer, $\Delta\bar{k}$, and vibrational amplitude, $\bar{u}$ **(22)**, i.e.

$$I \propto (\Delta\bar{k}\cdot\bar{u})^2 . \tag{6}$$

Using the zero point vibrational amplitude to express $|\bar{u}|$ for a particular mode in terms of ω, its frequency and M, its reduced mass,

$$|\bar{u}|^2 = \frac{\hbar}{2M\omega} \tag{7}$$

and assuming $|\Delta\bar{k}|^2$ is proportional to the incident beam energy E_0 through

$$|\Delta\bar{k}|^2 = \frac{2mE_0}{\hbar^2} \tag{8}$$

where m is the electron mass, gives the following result for I:

$$I \propto \frac{mE_0}{\hbar\omega M} . \tag{9}$$

A more thorough analysis, including all pertinent constants **(22)** shows that for beam energies less than 10 eV, as were used for all experiments described in this

Thesis, scattering by this mechanism is detectable only for vibrational modes dominated by hydrogen (or deuterium) motion. Detection of impact scattering for modes dominated by motion of heavier atoms such as carbon, nitrogen and oxygen requires beam energies in excess of 50 eV. The presence of two separable scattering mechanisms, one of which is selectively sensitive to hydrogenic vibrational modes, proves to be a powerful asset in the assignment of features and deduction of adsorbate structures from EEL vibrational spectra.

Also, occasional use is made in this thesis of data collected by low energy electron diffraction (LEED) **(23)**, Auger electron spectroscopy (AES) **(24)**, and contact potential difference ($\Delta\varphi$) **(25)** measurements. The reader is directed to the appropriate references for information on the implementation of these experimental techniques and discussion of the information their results provide.

With this framework of experimental techniques established, it remains then to introduce the specific subjects of each chapter and to describe more thoroughly the theoretical background within which the results are interpreted.

Chapter II presents an investigation of the chemisorption of N_2 on Ru(001) with emphasis on correlating changes in the vibrational spectrum of adsorbed N_2 with changes in its local environment as the order and total surface coverage of the adsorbate layer is varied. Since N_2 is isoelectronic with CO and its surface bonding interaction is qualitatively similar **(26)**, use is made of previously developed theoretical explanations of coverage dependent vibrational frequency shifts first observed in investigations of CO adsorption. One explanation ascribes increases of ν(CO) with increasing surface coverage to chemical interactions, where at high coverage increased competition among CO molecules for metal d electrons occurs, leading to decreased average population of the π^*_{CO}

antibonding orbital and concomitant increase in the C-O force constant **(15)**. It has since been recognized, however, that interaction of the oscillating dipolar electric field of an adsorbed molecule with those of its neighbors also occurs, a purely physical effect which also increases ν(CO) with coverage **(16)**. Isotopic mixing experiments, using mixtures of $C^{12}O$ and $C^{13}O$ to separate the chemical and physical interactions, show their effects to be nearly additive **(16)**. Contrary to the increase of ν(CO) with coverage observed on the Ru(001) surface **(27)**, ν(NN) decreases sharply with increasing surface coverage. This result is reconciled with subtle differences in the N_2-surface bond which cause the occupation of the $1\pi_g$ antibonding orbital of N_2 to instead increase with surface coverage, causing the resultant decrease in ν(NN) to exceed the superimposed increase due to dipolar coupling.

In Chapter III, both the p(2x2) and p(1x2) ordered overlayers which dissociated adsorbed oxygen forms on Ru(001) are analyzed via comparison of experimental EEL spectra to those calculated via lattice dynamical techniques. The calculations use a Green's function method to generate exact solutions for both the frequencies and relative intensities of vibrational modes for a harmonic mechanical model of the adsorbate layer and the semi-infinite substrate **(17)**. In addition to verifying that certain features observed in the experimental spectra are due to coupling of the overlayer to motion of the surface Ru atoms, the calculation also verifies that the dipolar EEL spectrum is sensitive to the overall symmetry of the oxygen adsorption site, explaining important differences in the vibrational spectra of the two overlayers.

Chapter IV builds on the results of both Chapters II and III by investigating the coadsorption of N_2 with CO and oxygen. Interactions between the contrasting adsorbates lead to some interesting effects, manifest in both the EELS and TDMS results. Adsorption of N_2 on the Ru(001) surface precovered with a p(2x2) overlayer of oxygen forms a new binding state with a heat of adsorption 1-2 kcal/mole greater than the highest value observed on the clean Ru(001) surface. Addition of the electronegative oxygen adatoms stabilizes the σ donor portion of the N_2-surface bond, but decreases the amount of $1\pi_g$ backdonation, as is evidenced in the anomalously high value of ν(NN) observed. Adsorption of CO onto a saturated N_2 adsorbed layer yields values for ν(CO) lower than can be observed under any circumstances on the clean surface. The preadsorbed N_2 increases the Lewis basicity of the Ru surface atoms, increasing their ability to backdonate electron density into the 2π orbital of subsequently adsorbed CO.

Chapters V and VI concern the adsorption of acetone on clean and p(2x2) oxygen precovered Ru(001) surfaces and compare the results to those obtained for adsorption of acetone on the geometrically identical, but chemically different, Pt(111) surface. On clean Pt(111), an η^1 bonding configuration is observed which adsorbs reversibly. On clean Ru(001), however, an η^2 form is instead observed which decomposes to CO, carbon, and hydrogen upon heating of the surface. Preadsorption of oxygen causes the Ru(001) suface to behave more like the electronegative Pt(111) surface, and a significant fraction of the adsorbed acetone exists in an η^1 configuration which desorbs reversibly. The results demonstrate in a quantifiable way how the reactivity of a surface can be modified by the presence of a coadsorbed species, and that the change in reactivity can be correlated directly with a change in the selectivity of the surface toward reactive (η^2) and nonreactive (η^1) bonding configurations.

Chapter VII investigates the interaction of formaldehyde with the Ru(001) surface, and, due to its structural similarity to acetone, provides an interesting comparison with the results of Chapters V and VI. Formaldehyde is more reactive than acetone due to differences in its electronic structure and decomposes to hydrogen and CO at low coverages and low temperature. As the surface becomes poisoned to further decomposition by the filling of adsorption sites which bind the decomposition products, however, the EEL spectra reveal first an η^2-formyl species at intermediate coverage and finally an η^2-formaldehyde species at monolayer coverage. These results have important implications for heterogeneously catalyzed CO hydrogenation reactions, which presumably proceed through coordinated formyl and formaldehyde intermediates **(28)**.

Finally, Chapter VIII provides a more thorough summary of the results of Chapter VII and includes results for the adsorption of formaldehyde on the Ru(001) suface precovered with a p(2x2) oxygen overlayer. Again, the oxygen stabilizes the η^1-formaldehyde configuration analogous to the results obtained for acetone adsorption on the same surface. Also, a detailed analysis of the decomposition reaction mechanism for adsorbed formaldehyde on both surfaces is presented.

References

1. U. Landman, ed., *Aspects of the Kinetics and Dynamics of Surface Reactions*, AIP Conf. Proc., Vol. 61, 1980.
2. J. Tully, Ann. Rev. Phys. Chem. **31**, 319 (1980).
3. J. W. Gadzuk and S. Holloway, Chem. Phys. Letters **114**, 314 (1985).
4. J. W. Gadzuk and H. Metiu in *Vibrations at Surfaces*, R. Caudano, J.-M. Gilles and A. A. Lucas, eds., Plenum, New York, 1982, p. 519-540.
5. M. Sunjic′ in *Dynamics of Gas-Surface Interaction*, G. Benedek and U. Valbusa, eds., Springer-Verlag, Berlin, 1982, p. 154-185.
6. S. Gladsstone, K. J. Laidler and H. Eyring, *The Theory of Rate Processes*, McGraw-Hill, New York, 1941.
7. G. Comsa, ibid. 5, p. 117-127.
8. J. A. Barker and D. J. Auerbach, Surface Sci. Reports **4**, 1 (1985).
9. R. B. Bernstein, *Chemical Dynamics via Molecular Beam and Laser Techniques*. Oxford, New York, 1982, Chapters 2 and 7.
10. W. H. Weinberg in *Survey of Progress in Chemistry*, Academic Press, New York, 1983, p. 1-59; P. D. Szuromi, J. R. Engstrom and W. H. Weinberg, J. Chem. Phys. **80**, 508 (1984).
11. F. M. Hoffmann and R. A. de Paola, Phys. Rev. Letters **52**, 1697 (1984); Chapters VI, VII and IX of this Thesis.
12. S. A. Adelman and J. D. Doll, Acc. Chem. Res. **10**, 378 (1977); J. Tully, Acc. Chem. Res. **14**, 188 (1981).
13. B. Kasemo, ibid, **4**, 501.

14. The distance between adjacent Ru atoms in the (001) surface plane is 2.70 Å, giving a surface atom density of 1.58×10^{15} Ru atoms/cm^2. For a discussion of the electronic properties of the clean Ru(001) surface, see P. J. Feibelman, Phys. Rev. B **26**, 5347 (1982). The vibrational properties of the Ru(001) surface can be obtained by using the experimental bulk phonon data for Ru given in R. R. Rao and J. V. S. S. N. Murthy, Z. Naturforsch **34a**, 724 (1979) to scale the calculated surface phonon dispersion curves given in R. E. Allen, G. P. Allredge and F. W. De Wette, Phys. Rev. B **6**, 632 (1972).

15. G. Blyholder, J. Phys. Chem. **68**, 2772 (1964).

16. B. N. J. Persson and R. Ryberg, Phys. Rev. B **24**, 6954 (1981).

17. H. Ibach and D. L. Mills, *Electron Energy Loss Spectroscopy and Surface Vibrations*, Academic Press, 1982, Chapters 4 and 5.

18. G. Herberg, *Infrared Raman Spectra of Polyatomic Molecules*, Van Nostrand, New York, 1945.

19. N. B. Colthup, L. H. Daly and S. E. Wiberley, *Introduction to Infrared and Raman Spectroscopy*, Academic Press, 1975.

20. D. A. King, Surface Sci. **47**, 384 (1975).

21. J. M. Soler and N. Garcia, Surface Sci. **124**, 563 (1983).

22. Ibid. **17**, Chapters 1 and 3.

23. P. M. Marcus and F. Jona, Appl. Surface Sci. **11/12**, 20 (1982).

24. R. Weissmann and K. Müller, Surface Sci. Reports **105**, 251 (1981).

25. G. Ertl and J. Küppers, *Low Energy Electrons and Surface Chemistry*,

26. K. Horn, J. DiNardo, W. Eberhardt, H.-J. Freund and E. W. Plummer, Surface Sci. **118**, 465 (1982).

27. G. E. Thomas and W. H. Weinberg, J. Chem. Phys. **70**, 954 (1979).

28. B. D. Dombek, Advan. Catal. **32**, 325 (1983).

Chapter II.

The Chemisorption of Nitrogen on the (001) Surface of Ruthenium

Journal of Electron Spectroscopy and Related Phenomena, 29 (1983) 181—186
Elsevier Scientific Publishing Company, Amsterdam — Printed in The Netherlands

THE CHEMISORPTION OF NITROGEN ON THE (001) SURFACE OF RUTHENIUM*

A.B. ANTON,[1] N.R. AVERY,[2] B.H. TOBY[1] and W.H. WEINBERG[1]

[1]Division of Chemistry and Chemical Engineering, California Institute of Technology, Pasadena, CA 91125 USA

[2]Division of Materials Science, CSIRO, University of Melbourne, Parkville, Australia 3052

ABSTRACT

High resolution electron energy loss spectroscopy (EELS), thermal desorption mass spectrometry (TDMS) and low energy electron diffraction (LEED) have been used to investigate the molecular chemisorption of N_2 on Ru(001) at 75 K and 95 K. Adsorption at 95 K produces a single chemisorbed state, and, at saturation, a $(\sqrt{3}\times\sqrt{3})R30^\circ$ LEED pattern is observed. Adsorption at 75 K produces an additional chemisorbed state of lower binding energy, and the probability of adsorption increases by a factor of two from its zero coverage value when the second chemisorbed state begins to populate. EEL spectra recorded for all coverages at 75 K show only two dipolar modes — $\nu(Ru\text{-}N_2)$ at 280-300 cm^{-1} and ν(N-N) at 2200-2250 cm^{-1} — indicating adsorption at on-top sites with the axis of the molecular standing perpendicular to the surface. The intensities of these loss features increase and ν(N-N) decreases with increasing surface coverage of both chemisorbed states.

INTRODUCTION

For years CO has served as the prototype for molecular chemisorption studies on well characterized surfaces (ref.1). Although the surface chemical bond in N_2 adsorption is fundamentally different from that of CO due to subtle differences in the electronic structure of the two molecules (ref.2), N_2 is isoelectronic with CO, making the investigation of N_2 adsorption and its comparison to CO a logical next step in understanding the surface chemical bond and interactions among chemisorbed molecules. With this goal in mind, the present investigation concerns the chemisorption of N_2 on the Ru(001) surface.

EXPERIMENTAL

The experiments described here were performed in two separate UHV systems, one equipped for LEED and Auger electron spectroscopy (AES) (ref.3), and the other for TDMS and EELS (ref.4). Ru(001) samples for both systems were prepared and cleaned by standard techniques (ref.5). Sample cooling allowed adsorption at 95 K in the LEED system and 75 K in the EELS system.

---

*Supported by the National Science Foundation under Grant No. CHE82-06487.

RESULTS AND DISCUSSION

Adsorption of N_2 at 95 K

Exposure of the Ru(001) surface to N_2 at 95 K gives a single, first order, TDMS feature, the binding energy of which shifts from 31.4 kJ/mole at low coverage to 29.4 kJ/mole at saturation (via the method of Redhead, ref.6). Saturation coverage at this temperature also produces a strong $(\sqrt{3}\times\sqrt{3})R30^\circ$ LEED pattern (ref.7). Coverage estimates for these conditions, obtained by comparison of TDMS spectra to those obtained for desorption of a known coverage of CO, yield θ(sat. at 95 K)=0.35±0.10, implying formation of a complete $(\sqrt{3}\times\sqrt{3})R30^\circ/\theta=0.33$ overlayer.

EEL spectra recorded for adsorption at 95 K show only two dipolar modes — $\nu(\text{Ru-N}_2)$, appearing *initially at 280 cm^{-1} and shifting upward with increasing* coverage to 301 cm^{-1} at saturation; and ν(N-N), appearing initially at 2252 cm^{-1} and shifting downward to 2212 cm^{-1} at saturation. These frequencies are plotted as a function of exposure in Fig. 1.

The absence of bending modes in the EEL spectra indicates that the chemisorbed N_2 *molecules have their axes perpendicular to the surface plane*, and the frequency of ν(N-N) indicates that they are coordinated to single Ru atoms. The latter conclusion is substantiated by data for linear Ru-N_2 complexes which show $\nu(\text{N-N})>2000$ cm^{-1} (ref.8).

As is the case for CO, the bonding of N_2 to a metal center is primarily via *σ donation from the valence orbitals of* N_2 to the metal (ref.2). The valence orbitals in N_2, $2\sigma_u$ and $3\sigma_g$, are shared equally between the two nitrogen atoms, and, although they mix upon interaction with a metal center to form two new σ orbitals with some lone pair character, the resulting donor bond is weak compared to that of CO, which bonds through its 5σ lone pair orbital, localized strongly on the carbon atom. Back-donation from the $d\pi$ levels of the metal to the $1\pi_g$ *anti-bonding level* of N_2 weakens the N-N bond, and changes in the amount of $d\pi$ back-donation with surface coverage can cause ν(N-N) to vary with coverage.

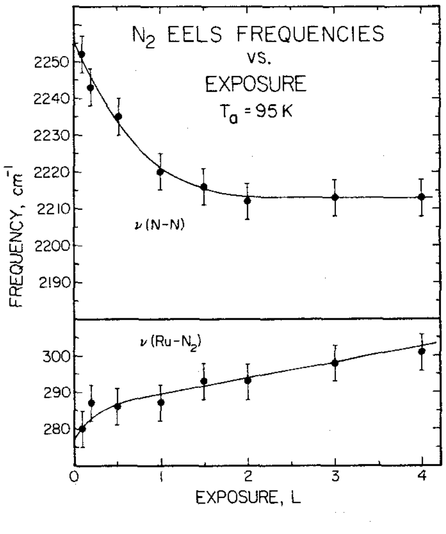

Fig. 1. EELS frequencies as a function of exposure for adsorption at 95 K.

Well-established theory (ref.9) which describes the interaction of an incident electron with an array of dipoles on a metal surface shows that the same properties of an adlayer which produce dipolar scattering also produce dipolar coupling in the adlayer, and this coupling interaction causes vibrational frequencies to increase monatonically with coverage. The intensity of the ν(N-N) mode seen in EELS is comparable to that seen for ν(C-O) at the same coverage (ref.10), indicating that N_2 is strongly polarized upon adsorption and has an induced dipolar moment approximately equal to that of CO. It follows that a 30-40 cm^{-1} upward shift of ν(N-N) from zero coverage to completion of a $(\sqrt{3}x\sqrt{3})$ R30^{o}/θ=0.33 overlayer occurs due to dipolar coupling (ref.10), as has been shown for CO on Ru(001) (refs.9,11). Then the data in Fig. 1 indicate that ν(N-N) shifts downward by 70-80 cm^{-1} due to coverage dependent changes in the N-N bond.

Although negative frequency shifts with increasing surface coverage have been reported for CO adsorption on Cu(111) (ref.12) and on polycrystalline Au (ref.13) and for N_2 adsorption on Ni(110)(ref.14), the change in ν(C-O) and ν(N-N) observed in these investigations was less than $\sim$10 cm^{-1} and no detailed explanations of the change in the C-O or N-N bond with coverage were offered. A plausible explanation describes the decrease in ν(N-N) with increasing coverage as being due to formation of a $1\pi_g$ band with increasing coverage, broadening the $1\pi_g$ level and changing its population due to overlap with the fermi level of the substrate (ref.15).

If the energy of the $1\pi_g$ level for an isolated N_2 molecule chemisorbed on Ru(001) is above the fermi level of the metal, the $1\pi_g$ level is unpopulated and does not affect ν(N-N). Increasing the density of N_2 admolecules on the surface, however, could cause the $1\pi_g$ orbitals of adjacent molecules to overlap, forming a band and broadening the $1\pi_g$ level due to dispersion. Band formation at low coverage (θ<0.33) is not unreasonable — the spatial extent of the $1\pi_g$ orbitals would be greater than the Van der Waals' diameter of N_2 ($\sim$5 Å), allowing significant overlap at the $\sqrt{3}$ intermolecular spacing of 4.6 Å. Island formation at low coverage, as is seen for CO adsorption on Ru(001) (ref.11), would enhance the effect. If the $1\pi_g$ level broadens sufficiently in energy to cross the fermi level, increasing population of this band would cause the N-N bond to weaken and decrease ν(N-N) for the adlayer. Broadening on the order of 1 eV due to dispersion is quite reasonable and has been reported for the 1π level of CO adsorbed on Ni(110) (ref.2).

Adsorption of N_2 at 75 K

Initial exposure of N_2 at 75 K produces the high temperature state seen for adsorption at 95 K. For exposures of 1.0 L or greater (θ/θ_{max}>0.4), however, a second feature appears with an initial binding energy of 24.4 kJ/mole, shifting to 21.3 kJ/mole at saturation. The probability of adsorption, S(θ), doubles from its initial value of 0.4±0.2 when the low temperature state begins to populate, then gradually decreases as the surface coverage approaches saturation (ref.7). TDMS spectra recorded after a 2.0 L exposure of $^{15}N_2$ at 100 K, then a 2.0 L exposure of $^{14}N_2$ at 75 K (or vice versa), show only partial mixing of the two isotopes upon desorption, verifying the existence of two distinct binding states on the surface and ruling out the possibility of a compression structure at high coverage, as is seen for CO on Ru(001) (ref.3). Coverage estimates for saturation at 75 K yield θ=0.58±0.17 and indicate that the surface density (N_2/Ru surface atoms) in the low temperature state is approximately twice that in the high temperature state.

Although TDMS results show two distinct binding states, EELS results for adsorption at 75 K, illustrated in Fig. 2, again show only two modes, ν(Ru-N_2) and ν(N-N). Figure 3 shows the coverage dependence of the frequencies of these two modes. As was shown in Fig. 1 for adsorption at 95 K, ν(N-N) shifts downward with increasing coverage, a total shift of 49 cm^{-1} from 2247 cm^{-1} to 2198 cm^{-1} in this case, and ν(Ru-N_2) shifts upward from 278 cm^{-1} to 291 cm^{-1}.

The addition of the second chemisorbed state, present only for adsorption at 75 K, contributes no new features to the specular EEL spectrum, causes no new features to appear in off-specular measurements, causes no abrupt changes in surface reflectivity, and causes no noticeable increase in the linewidth of either EELS band. Also, the intensities of both EELS bands, shown in Fig. 4, grow monotonically with total surface coverage of both chemisorbed states, exceeding the intensities of ν(Ru-N_2) and ν(N-N) seen for saturation at 95 K by 20% and 50%, respectively (ref.10). Although it has been shown that intensities of EELS bands are not absolute indicators of surface coverage (ref.9), the monatonic increase in the intensity of both modes with surface coverage and the absence of new features in the EEL spectra attributable to the other species does suggest that EELS is probing both chemisorbed states, i.e. the vibrational

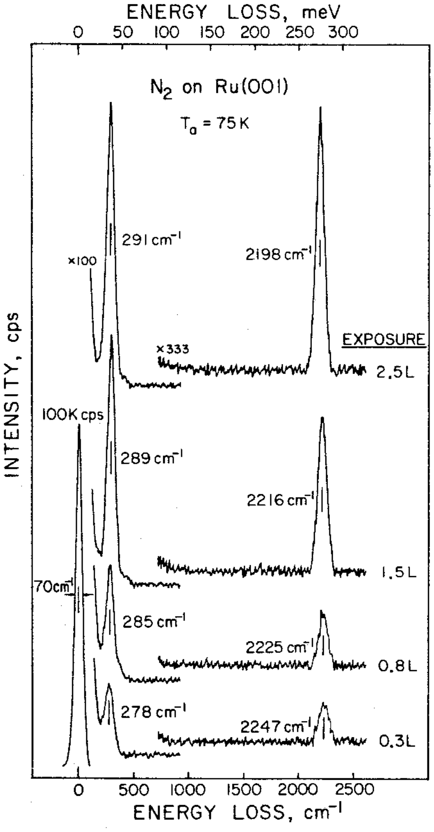

Fig. 2. Representative EEL spectra for adsorption at 75 K.

spectra of the two states are identical within instrumental resolution. By these arguments, N_2 molecules in the low temperature state are also bonded with their molecular axes perpendicular to the surface, but, as was shown by TDMS coverage comparisons for adsorption at 95 K and 75 K, they are bonded in areas "crowded" with N_2 molecules, as surface density in the low temperature state is approximately twice that of the high temperature $\sqrt{3}$ state.

CONCLUSIONS

The conclusions of this work can be summarized as follows:

1. Adsorption of N_2 on Ru(001) at 95 K produces an ordered $(\sqrt{3}\times\sqrt{3})R30^{\circ}/\theta=0.33$ overlayer with the N_2 molecules at on-top sites, standing perpendicular to the surface plane. The binding energy of N_2 in this state is 31.4 kJ/mole at low coverage, shifting to 29.4 kJ/mole at saturation.

2. Adsorption at 75 K produces a second, distinct chemisorbed state, appearing for relative coverages (θ/θ_{max}) greater than 0.4 with an initial binding energy of 24.4 kJ/mole and shifting to 21.3 kJ/mole at saturation. This state is indistinguishable from the $\sqrt{3}$ state in EELS and is therefore also attributed to molecules standing upright on the surface.

3. Changes in the N-N bond with coverage, due presumably to changes in the relative amount of $1\pi_g$ backbonding, cause ν(N-N) to decrease with increasing coverage for adsorption at both 75 K and 95 K.

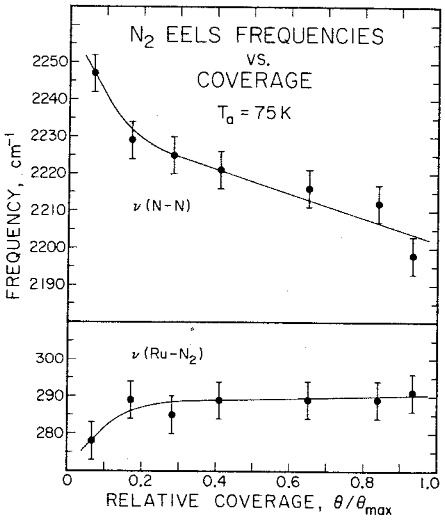

Fig. 3. EELS frequencies as a function of coverage for adsorption at 75 K.

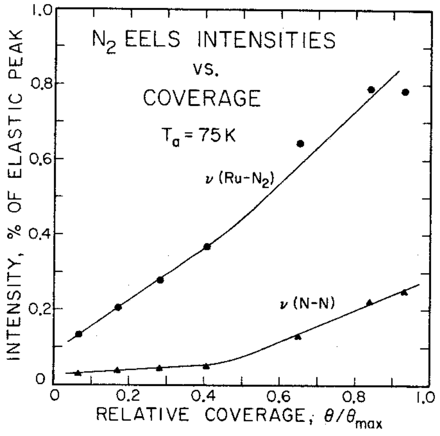

Fig. 4. EELS intensities as a function of coverage for adsorption at 75 K.

ACKNOWLEDGMENTS

We wish to acknowledge the assistance of Ted Madey in the collection and interpretation of data at the beginning of this project

REFERENCES

1 See, for example, *Vibrational Spectroscopy of Adsorbates*, R.F. Willis, ed., (Springer-Verlag, Berlin, 1980).
2 K. Horn, J. DiNardo, W. Eberhardt, H.-J. Freund and E.W. Plummer, Surface Sci. 118 (1982) 465.
3 E.D. Williams and W.H. Weinberg, Surface Sci. 82 (1979) 93.
4 G.E. Thomas and W.H. Weinberg, Rev. Sci. Instr. 50 (1979) 497.
5 G.E. Thomas and W.H. Weinberg, J. Chem. Phys. 69 (1978) 3611; 70 (1979) 954.
6 P.A. Redhead, Vacuum 12 (1979) 203.
7 P. Feulner and D. Menzel, Phys. Rev. B 25 (1982) 4295.
8 B. Folkesson, Acta. Chem. Scand. 26 (1972) 4008.
9 B.N.J. Persson and R. Ryberg, Phys. Rev. B 24 (1981) 6954, and references therein.
10 A.B. Anton, N.R. Avery, B.H. Toby and W.H. Weinberg, in preparation.
11 H. Pfnür, D. Menzel, F.M. Hoffmann, A. Ortega and A.M. Bradshaw, Surface. Sci. 93 (1980) 431.
12 P. Hollins and J. Pritchard, Surface Sci. 89 (1979) 486.
13 M.L. Kottke, R.G. Greenler and H.G. Tompkins, Surface Sci. 32 (1972) 231.
14 M Grunze, R.K. Driscoll, G.N. Burland, J.C.L. Cornish and J. Pritchard, Surface Sci. 89 (1979) 381.
15 A.M. Bradshaw, private communication.

Chapter III.

Electron-Energy-Loss Spectroscopy of Ordered Oxygen Overlayers on Ru(001)

Electron-Energy-Loss Spectroscopy of Ordered Oxygen Overlayers on Ru(001)

Talat S. Rahman[a]
Department of Physics, University of California, Irvine, California 92717
and
A. B. Anton, N. R. Avery,[b] and W. H. Weinberg
Division of Chemistry and Chemical Engineering, California Institute of Technology, Pasadena, California 91125

(Received 27 December 1982)

High-resolution electron-energy-loss measurements and relevant theoretical calculations for the vibrational structure of ordered oxygen overlayers on the Ru(001) surface are presented. The vibrational spectrum of the $p(2\times 2)$ overlayer shows a single dipolar-active mode above the substrate phonon band. Because of a reduction in symmetry of the threefold adsorption site, however, the vibrational spectrum of the $p(1\times 2)$ overlayer is fundamentally different, showing two dipolar-active modes above the substrate phonon band.

PACS numbers: 68.30.+z, 63.20.Dj, 68.20.+t, 79.20.Kz

Well before spectroscopic methods were developed for their observation, the existence of vibrations localized at clean metal surfaces had been predicted and described in lattice-dynamical calculations.[1] Recently, significant improvements in the resolution and spectral range of electron-energy-loss (EEL) measurements has rendered feasible the observation of *substrate* vibrational modes in dipolar scattering from ordered adsorbate overlayers on single-crystal metal surfaces.[2] The adlayer provides a dipolar coupling[3] of the incident electrons to the surface resonance modes, and the activity (or absence) of these modes in EEL spectra has been shown to delimit the overlayer periodicity and adsorption site. For example, detailed structural information concerning the adsites of oxygen overlayers on Ni(100)[4] and Ni(111)[5] surfaces has been obtained via a comparison of calculated and experimental EEL spectra.

Here we present the results of an experimental and theoretical study of oxygen overlayers on the Ru(001) surface. Oxygen forms two ordered overlayers on Ru(001)—a $p(2\times 2)$ structure at a fractional surface coverage of $\theta = 0.25$ and three independent domains of $p(1\times 2)$ overlayers rotated 120° with respect to one another at $\theta = 0.50$,[6,7] both of which give "(2×2)" LEED patterns and similar calculated I-V beam profiles.[8] The EEL spectra of these structures show dipolar loss features at frequencies *below* the maximum substrate phonon frequency similar to surface resonance modes discussed previously,[2,4,5] and indicative of the twofold periodicity of both overlayers. Furthermore, we show for the first time that the dipolar activity of modes *above* the maximum bulk phonon frequency of the metal depends on the symmetry of the *combined* overlayer plus substrate structure and in this case serves to distinguish unambiguously the $p(2\times 2)$ and $p(1\times 2)$ overlayers in EELS measurements.

The $p(2\times 2)$ overlayer and its two-dimensional Brillouin zone are illustrated in Fig. 1(a). The oxygen threefold absorption site,[5,8,9] including all neighbors in the surface and adsorbate layers, has three reflection planes perpendicular to the surface and hence has a point group symmetry that is C_{3v}. Because of the large difference in mass of the adsorbate oxygen atoms and the substrate Ru atoms, vibrational modes associated with motion of the adsorbate atoms have their displacements strongly localized in the adsorbate

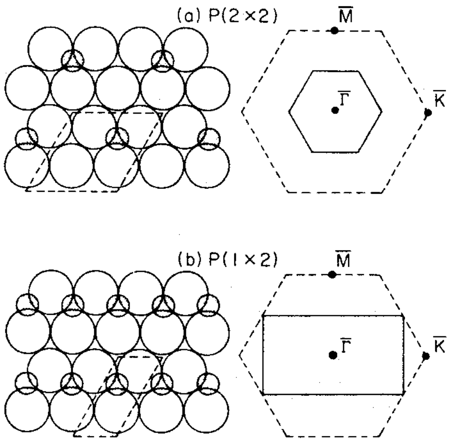

FIG. 1. Overlayers and unit cells (left) and two-dimensional Brillouin zones (right) for (a) the $p(2\times 2)$ structure and for (b) a single domain of the $p(1\times 2)$ structure that oxygen forms on Ru(001). The dashed lines represent the substrate Brillouin zone and the solid lines represent the overlayer Brillouin zones.

layer at frequencies above the substrate phonon band. The substrate is therefore effectively "rigid" with respect to the adsorbate vibrations, and the three normal modes of the oxygen atom are the following: two degenerate modes of E symmetry, polarized strictly parallel to the surface plane and dipolar inactive[3]; and a single dipolar-active A_1 mode, henceforth referred to as $\nu_\perp$(Ru-O), polarized strictly perpendicular to the surface. Because of its twofold periodicity, the reciprocal-lattice vectors of the $p(2\times 2)$ overlayer fold the $\bar{M}$ point of the substrate Brillouin zone into the $\bar{\Gamma}$ point. Thus, substrate modes at $\bar{M}$ should appear in the EEL spectrum if they couple to vertical motion of atoms in the threefold sites.[2,5]

In contrast, the threefold absorption site of the $p(1\times 2)$ overlayer, a single domain of which is illustrated in Fig. 1(b), has only a single reflection plane perpendicular to the close-packed rows. Its symmetry is therefore lowered from C_{3v} to C_s, and the three normal modes of the oxygen atom are the following: a single, dipolar-inactive mode of A'' symmetry, polarized perpendicular to the reflection plane and parallel to the surface; and *two dipolar-active modes* of A' symmetry, polarized in the reflection plane. One of these, henceforth referred to as $\nu_\parallel$(Ru-O), involves motion of the oxygen atoms perpendicular to the close-packed rows and nearly (but not strictly) parallel to the surface, and the other is the perpendicular mode, $\nu_\perp$(Ru-O). The reciprocal-lattice vectors of the $p(1\times 2)$ overlayer, shown in Fig. 1(b), fold the $\bar{M}$ point of the substrate Brillouin zone into the $\bar{\Gamma}$ point.[10]

To understand fully and interpret the data to be presented here, we have performed lattice-dynamical calculations to describe the vibrational structure of both the $p(2\times 2)$ and the $p(1\times 2)$ overlayers. In these calculations, the atoms interact only with their nearest neighbors through central forces. The details of the method used to calculate the inelastic scattering cross section for dipolar-enhanced modes have been presented previously,[5] and additional details specific to the $p(2\times 2)$ and $p(1\times 2)$ overlayers discussed here will be presented in a subsequent publication.[10]

We have calculated scattering amplitudes for the two overlayer structures with the oxygen atom at both threefold sites, i.e., the site over a second-layer Ru atom ("hcp" site) and the site over a second-layer vacancy ("fcc" site).[5] Oxygen-ruthenium bond lengths were estimated from a consideration of the covalent radii of O (0.73 Å) and Ru (1.3 Å)[9] and adjusted, together with the Ru-O force constant, to give optimum agreement between theoretical and experimental results. The Ru-Ru force constant was obtained from a one-parameter fit to the maximum bulk phonon frequency of Ru, 310 cm^{-1}.[11]

It should be noted that the adsorption site (hcp versus fcc) only affects the calculated vibrational spectra below 310 cm^{-1}, where vertical motion of the oxygen adlayer couples differently to the various substrate modes for the two sites.[5,10] Calculated spectra for the two sites are nearly identical, differing significantly only in the relative intensities of modes below 310 cm^{-1}. Since these modes are near the limit of the experimental spectral range, no unambiguous conclusion concerning a preferred adsite for the oxygen can be drawn from the experimental data, and only the calculations for hcp sites are shown in the figures and discussed in the text.

The EEL spectrometer used for the measurements reported here and the vacuum system in which it is contained have been described previously.[12] The Ru(001) sample was prepared and cleaned by standard techniques.[6,7,13] EEL spectra were recorded in the specular direction (± 1°) with an incident beam energy of 4 eV, an elastically scattered count rate of $10^5\ \text{s}^{-1}$, and a resolution of 70 cm^{-1} full width at half maximum.

The experimental and calculated EEL spectra of the $p(2\times 2)$ oxygen overlayer are shown in Figs. 2(a) and 2(b), respectively. For the calculation, the Ru-O bond length was chosen to be 2.05 Å giving a distance between the oxygen overlayer and the first substrate plane of $R_\perp = 1.3$ Å. Variation of $R_\perp$ between 1.2 and 1.6 Å did not affect the calculated spectrum significantly. The single feature above the substrate phonon band at 535 cm^{-1} in both spectra is the $\nu_\perp$(Ru-O) mode of oxygen in the threefold site.[13] The two narrow features in the calculated spectrum at 135 cm^{-1} and 260 cm^{-1} are surface resonance modes of the type discussed previously[4,5] and result, respectively, from the S_1 and S_2 surface phonons[14] at the $\bar{M}$ point of the surface Brillouin zone. The S_1 mode is indiscernible in the experimental spectrum, and S_2 appears as a shoulder near 250 cm^{-1}.

The experimental and calculated EEL spectrum of the $p(1\times 2)$ overlayer are shown in Figs. 3(a) and 3(b), respectively. For the calculation, optimal agreement with the experimental data was obtained with a Ru-O bond length of 2.26 Å ($R_\perp = 1.6$ Å). Since measurements of the work-func-

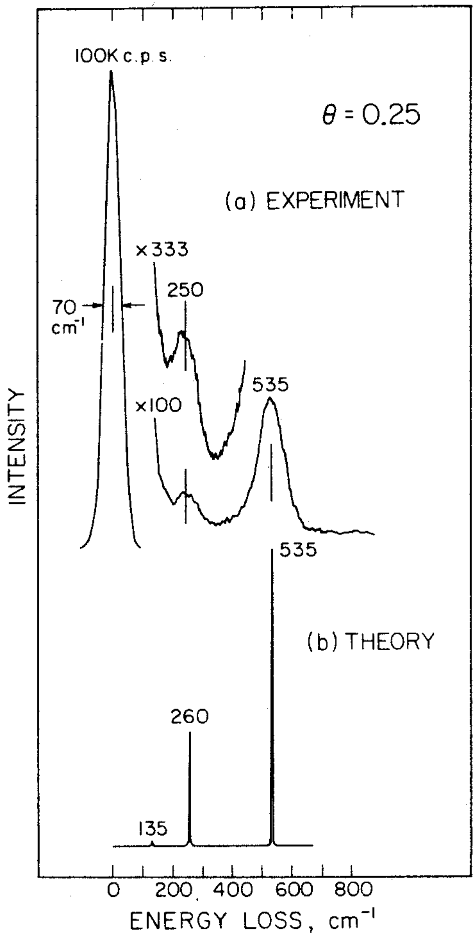

FIG. 2. (a) Experimental and (b) theoretical EEL spectra for the $p(2\times2)$ oxygen overlayer.

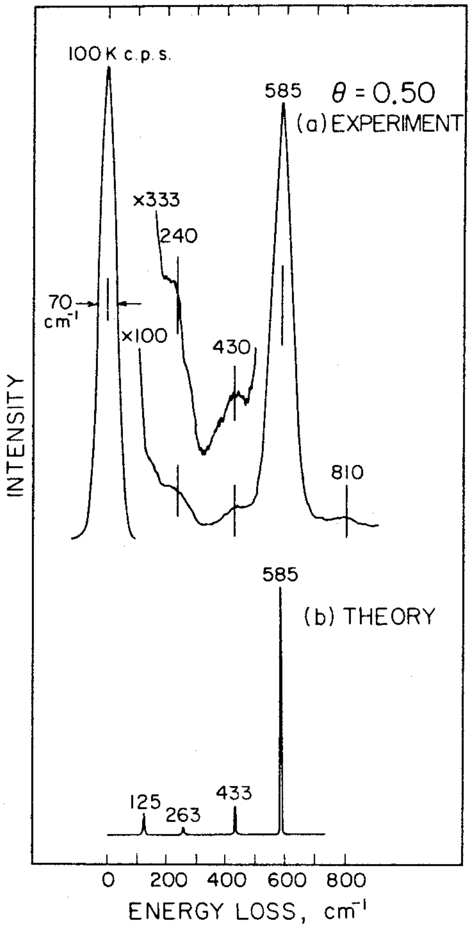

FIG. 3. (a) Experimental and (b) theoretical EEL spectra for the $p(1\times2)$ oxygen overlayer.

tion change upon adsorption indicate that the average static dipole moment per adsorbed atom is approximately 3 times as great for the $p(1\times2)$ as for the $p(2\times2)$ overlayer,[6] the use of different bond lengths in the calculations for the two overlayers is justifiable.

In addition to the $\nu_\perp$(Ru-O) mode at 585 cm^{-1}, the calculated spectrum shows a second feature above the substrate phonon band at 433 cm^{-1}. This is the $\nu_\parallel$(Ru-O) mode of A' symmetry in the $p(1\times2)$ overlayer, and results from motion of the oxygen atoms nearly parallel to the surface and perpendicular to the close-packed rows of the $p(1\times2)$ structure. A reduction of the adsorption-site symmetry from C_{3v} in the $p(2\times2)$ overlayer to C_s in the $p(1\times2)$ overlayer adds a new dipolar mode to the EEL spectrum. The vibrations of the oxygen atoms perpendicular and parallel to the surface are no longer decoupled, and the displacements of the substrate atoms no longer have triangular symmetry, but instead become vertical and horizontal "shear" motions. The corresponding dipolar-enhanced modes appear in the experimental spectrum at 585 and 430 cm^{-1}. The calculated spectrum also shows features at 125 and 263 cm^{-1}, again due to the surface phonons S_1 and S_2 at $\bar{M}$, respectively.[14] Although no feature near 125 cm^{-1} is discernible in the experimental spectrum, the S_2 mode appears near 240 cm^{-1}, and the weak feature at 810 cm^{-1} is due to the combination loss of S_2 and $\nu_\perp$(Ru-O).

Finally, it should be noted that the intensity of the 430 cm^{-1} mode depends more strongly on the *order* of the surface layer than on the coverage. In spectra recorded after annealing to 350 K to ensure surface order, the intensity of this mode increases with coverage from undetectable in the $p(2\times2)$, $\theta = 0.25$ spectrum, to the reproducible intensity shown in the $p(1\times2)$, $\theta = 0.50$ spectrum. In keeping with the symmetry arguments presented above, this increase in intensity occurs as oxygen adatoms fill the sites between those of the

$p(2\times 2)$ overlayer. Addition of each adatom above $\theta = 0.25$ creates (on the average) two sites with broken symmetry and dipolar-active modes near 430 cm^{-1}.

In EEL spectra for *disordered* layers of oxygen adsorbed at 100 K, however, the 430 cm^{-1} mode appears for all coverages, but with intensity varying widely from spectrum to spectrum. Upon adsorption at 100 K, the oxygen adatoms are "frozen" into threefold sites at random, forming a disordered overlayer with some fraction occupying adjacent sites. In fact, the dipolar spectrum of *two atoms* on the surface, were it observable, would look very much like the $p(1\times 2)$ spectrum if the two atoms happened to occupy adjacent sites, where interactions could lead to site-symmetry breaking. For coverages of disordered oxygen below $\theta = 0.25$, annealing to 350 K causes the mode at 430 cm^{-1} to vanish, as the overlayer orders into a configuration consistent with the $p(2\times 2)$ structure.

To summarize, we have shown, via comparison of experimental to theoretical EEL spectra of $p(2\times 2)$ and $p(1\times 2)$ overlayers of oxygen on Ru(001), that the dipolar activity of the normal modes of a high-symmetry (threefold, C_{3v}) adsorption site can be modified by the presence of near neighbors in the adlayer which reduce the site symmetry (to C_s in this case).

We are grateful to Professor D. L. Mills for many helpful discussions. This work was supported by the National Science Foundation through Grant No. CHE82-06487 and by the U. S. Department of Energy under Contract No. DEAT0379-ER-10432.

(a)Permanent address: Department of Physics, Kansas State University, Manhattan, Kans. 66506.

(b)Permanent address: Division of Materials Science, Commonwealth Scientific and Industrial Research Organization, Catalysis and Surface Science Laboratory, University of Melbourne, Parkville 3052, Victoria, Australia.

[1] See R. F. Wallis, Prog. Surf. Sci. 4, 233 (1973), and references therein.

[2] H. Ibach and D. Bruckmann, Phys. Rev. Lett. 44, 36 (1980); S. Andersson and M. Persson, Phys. Rev. B 24, 3659 (1981); S. Lehwald and H. Ibach, *Vibrations at Surfaces*, edited by R. Caudano, J. M. Gilles, and A. A. Lucas (Plenum, New York, 1982), p. 137.

[3] E. Evans and D. L. Mills, Phys. Rev. B 5, 4126 (1972).

[4] T. S. Rahman, J. E. Black, and D. L. Mills, Phys. Rev. Lett. 46, 1469 (1981), and Phys. Rev. B 25, 883 (1981).

[5] T. S. Rahman, J. E. Black, and D. L. Mills, Phys. Rev. B 27, 4059 (1983).

[6] T. E. Madey, H. A. Engelhardt, and D. Menzel, Surf. Sci. 48, 304 (1975).

[7] S. L. Parrott, G. Praline, B. E. Koel, J. M. White, and T. N. Taylor, J. Chem. Phys. 71, 3352 (1979).

[8] C.-M. Chan and W. H. Weinberg, J. Chem. Phys. 71, 2788 (1979).

[9] M. Van Hove, in *The Nature of the Surface Chemical Bond*, edited by T. N. Rhodin and G. Ertl (North-Holland, Amsterdam, 1979), Chap. 4.

[10] T. S. Rahman, to be published.

[11] R. R. Rao and J. V. S. S. N. Murthy, Z. Naturforsch. 34a, 724 (1979).

[12] G. E. Thomas and W. H. Weinberg, Rev. Sci. Instrum. 50, 497 (1979).

[13] G. E. Thomas and W. H. Weinberg, J. Chem. Phys. 69, 3611 (1978), and 70, 954 (1979).

[14] R. E. Allen, G. P. Allredge, and F. W. de Wette, Phys. Rev. B 6, 632 (1972).

Chapter IV.

The Coadsorption of Nitrogen with Carbon Monoxide and Oxygen on the Ru(001) Surface: Local Chemical Interactions in Mixed Overlayers

The Coadsorption of Nitrogen with Carbon Monoxide and Oxygen on the Ru(001) Surface: Local Chemical Interactions in Mixed Overlayers

by

A. B. Anton, N. R. Avery,[a] T. E. Madey[b] and W. H. Weinberg
Division of Chemistry and Chemical Engineering
California Institute of Technology
Pasadena, CA 91125

Submitted to *Surface Science*

July 1985

---

[b] Current address: Division of Materials Science, C.S.I.R.O., Catalysis and Surface Science Laboratory, University of Melbourne, Parkville 3052, Victoria, Australia.

[b] Current address: Surface Chemistry Section, Institute for Materials Research, National Bureau of Standards, Washington, D.C. 20234.

Abstract

High resolution electron energy loss spectroscopy and thermal desorption mass spectrometry have been employed to investigate the chemisorption of N_2 on both disordered and ordered overlayers of atomic oxygen, as well as the chemisorption of CO on overlayers of N_2. Pertinent results obtained for the adsorption of N_2 on the clean Ru(001) surface are also presented for comparison. *Disordered* oxygen poisons a fraction of the surface to the subsequent adsorption of N_2, leaving the remainder of the surface to adsorb N_2 into binding sites indistinguishable from those observed for the adsorption of N_2 on the clean Ru(001) surface. The amount of the surface that is poisoned to the adsorption of N_2 is approximately twice the fractional surface coverage of disordered oxygen. The p(2x2) overlayer of *ordered* oxygen adatoms, which is formed at a fractional surface coverage of 0.25 monolayer, stabilizes the chemisorption of N_2 into a new binding state with a heat of adsorption that is approximately 1.5 kcal/mole greater than that observed for the adsorption of N_2 on the clean surface. Coverage measurements indicate that this state results from the stoichiometric addition of one N_2 molecule to each unit cell of the p(2x2) overlayer. EELS results suggest that this N_2 binding state results from stabilization of the dominant σ donor contribution to the Ru-N_2 bond due to the presence of the electronegative oxygen adatoms of the p(2x2) overlayer. Measurements for the adsorption of CO on saturated overlayers of N_2 show that N_2 is displaced from the surface by increasing coverages of subsequently adsorbed CO. For low coverages of CO in the presence of N_2 , the value of ν(CO) observed is lower than that observed under any conditions for the adsorption of CO alone on the Ru(001) surface. The N_2 admolecules enhance the ability of the surface Ru atoms to backdonate electron density into the 2π orbital of coadsorbed CO under these conditions. At coverages of CO in excess of 0.10 monolayer, the

results are consistent with segregation of N_2 and CO admolecules into different local regions of the surface.

I. Introduction

For years CO has served as the prototypical reagent for molecular chemisorption studies on single crystalline metal surfaces. Theoretical calculations of the electronic structure of chemisorbed CO **(1-3)** have provided both a thorough understanding of the nature of the metal-CO bond and detailed interpretations of the results of photoemission experiments. Investigations of the chemisorption of CO on metals employing vibrational spectroscopy have made use of the σ donation and π^* backdonation interpretation of metal-CO bonding provided by these calculations to correlate CO stretching frequencies [ν(CO)] both with the adsorption site geometry (e.g. on-top, twofold bridge, etc.) **(4)** and with coverage dependent changes in the metal-CO bond **(3,5)**. Furthermore, chemisorbed overlayers of CO have served as model systems for theoretical investigations which treat adsorbed molecules as oscillating point dipoles to describe inelastic scattering cross sections and coverage dependent frequency shifts **(4,6)**.

Since N_2 is isoelectronic with and structurally similar to CO, the investigation of the chemisorption of N_2 and a comparison to CO is the logical next step in understanding surface chemical bonding and interactions among adsorbed molecules. Recognizing this, several investigations have undertaken both theoretical **(7-10)** and experimental **(11-13)** investigations to compare the bonding of N_2 and CO to metals, and from these studies a clear picture of the differences between metal-N_2 and metal-CO bonding has evolved **(14)**. Briefly, bonding of both CO and N_2 to a metal surface occurs via a combination of σ electron donation from CO or N_2 to the metal and backdonation from the metal d band to the antibonding π^* orbitals of CO or N_2. For CO the σ donor bond results from the interaction of the 5σ "lone pair" orbital of CO, localized on the carbon atom, with the valence band of the metal surface. For N_2, however, the σ valence orbitals, $2\sigma_u$ and $3\sigma_g$, are shared equally between the two nitrogen atoms in the free molecule, and although they mix upon interaction with a metal surface to form two new σ orbitals with some lone pair character, the resulting donor bond is weak compared to that of CO. Backdonation from the d band of the metal to the 2π antibonding level of CO weakens the C≡O bond and lowers ν(CO) from its gas phase value upon adsorption. Analogous arguments apply to the $1\pi_g$ antibonding orbital of N_2, and changes in the amount of backdonation with surface coverage can cause ν(CO) and ν(NN) to vary with coverage. Furthermore, ν(CO) and ν(NN) can be affected by the presence of coadsorbed species which either suppress **(15)** or enhance **(16)** backdonation.

This paper presents the results of an experimental investigation which applies high resolution electron energy loss vibrational spectroscopy (EELS) and thermal desorption mass spectrometry (TDMS) to the identification of the structure and bonding properties of the adsorbed species present in mixed overlayers of atomic oxygen and N_2 and of CO and N_2 on the Ru(001) surface. The aim of this investigation is to understand quantitatively the appropriateness of the bonding scheme outlined above. Oxygen coadsorption was chosen to investigate the effects of an increase in the Lewis acidity of the surface metal atoms on the bonding of N_2 to the surface and to compare the results to those of previous investigations of oxygen and CO coadsorption on Ru(001) **(17,18)**, and CO coadsorption was chosen to investigate intermolecular interactions (including those mediated by the ruthenium substrate) between adsorbed CO and N_2 molecules, with particular emphasis on the effects manifest in the vibrational spectra of each species. For completeness and comparison, results obtained for the adsorption of N_2 on the clean Ru(001) surface **(19)** are also presented and discussed.

II. Experimental Procedures

The measurements described here were performed in a stainless steel, ion pumped ultrahigh vacuum system with a base pressure below 1 x 10^{-10} Torr. Its description, including details pertinent to the EELS and TDMS experiments, is presented in Ref. 20, and the preparation of the Ru(001) sample is documented in Ref. 17.

The crystal was exposed to the gases by backfilling the entire vacuum chamber through leak valves. The CO, O_2 and $^{14}N_2$ gases were Matheson Research Purity (99.9% minimum), and the $^{15}N_2$ was obtained from Prochem (99 atom % ^{15}N). Exposures are measured in units of Langmuirs (1 L ≡ 1 Langmuir ≡ 10^{-6} Torr-s) with a Bayard-Alpert ionization gauge, uncorrected for relative ionization cross sections.

Adsorption temperatures of 75 K were reached by pumping on the cooling reservoir of the crystal manipulator with a mechanical vacuum pump while feeding liquid N_2 at atmospheric pressure to the reservoir through a restriction orifice. This allowed continuous operation of the reservoir at a total pressure near 160 Torr, where the boiling temperature of N_2 is near 65 K. Crystal temperatures were measured with a calibrated W-26%Re/W-5%Re thermocouple which was spot welded to the rear face of the single crystal sample.

The crystal was cleaned by repeated thermal cycling between 400 and 1100 K in 5 x 10^{-8} Torr of O_2 to oxidize surface impurities, followed by annealing to 1750 K to remove all chemisorbed oxygen. Occasional Ar^+ bombardment was also used to clean the surface. Surface cleanliness was monitored via EELS and thermal desorption spectra, and the surface was judged clean when the EEL spectrum was featureless, and the peak positions and intensities in thermal desorption spectra for various coverages of CO were reproduced.

The EEL spectra were collected at 70 to 80 cm^{-1} resolution (full-width at half-maximum) in the specular direction with an electron count rate of 1 to 3 x 10^5 c.p.s. in the elastically scattered beam. Band positions in the EEL spectra are accurate to an estimated ±5 cm^{-1}. The beam was incident on the crystal at 60° from the surface normal, and the kinetic energy of the electron beam at the surface varied between 4 and 5 eV.

Thermal desorption measurements were conducted in a line-of-sight configuration with a UTI 100C quadrupole mass spectrometer, oriented approximately 40° from the sample normal and controlled by a DEC PDP 11/10 computer. This system allowed multiplexing for simultaneous collection of thermal desorption spectra at several m/e ratios and provided routines for accurate determinations of TDMS peak areas for surface coverage measurements. Surface coverages for the N_2 thermal desorption spectra were obtained by comparison of the integrated areas of the desorption traces to those obtained for desorption from a saturated monolayer of CO on the Ru(001) surface, where θ = adsorbed CO molecules per ruthenium surface atom = 49/75 **(21)**. Coverages obtained by this method are reproducible and precise to ±5%, but a potential systematic error resulting from the calibration against the desorption of CO makes their accuracy uncertain by an estimated ±15%. The surface coverages obtained for the thermal desorption spectra of N_2 by this method, however, do show excellent agreement (approximately 10% discrepancy) with those reported in Ref. 22, where coverages for N_2 on Ru(001) were calibrated against the desorption of N_2 from a well-developed $(\sqrt{3} \times \sqrt{3})R30°$ ordered overlayer, the fractional surface coverage of which is 0.33. Oxygen coverages were obtained by first identifying the O_2 exposures necessary to form the p(2x2) [θ = 0.25] and the p(1x2) [θ = 0.50] ordered overlayers of atomic oxygen on Ru(001) **(23)**, and then using these benchmark exposures to scale the exposure versus surface coverage data given for the adsorption of O_2 on Ru(001) in Ref. 24. The surface coverages of atomic oxygen obtained by this method are accurate to an estimated ±15%.

III. Results and Discussion

A. The Adsorption of Nitrogen on the Clean Ru(001) Surface

Exposure of the clean Ru(001) surface to N_2 at 95 K produces a single first-order TDMS feature, the peak temperature of which shifts from 128 K at low coverage to 119 K at saturation coverage. The binding energy of this state, estimated for first-order desorption kinetics via the method of Redhead **(25)**, is approximately 7.2 kcal/mole. The saturation coverage for N_2 adsorption at 95 K, estimated via comparison to desorption of known coverages of CO, is $\theta = 0.35$, and the observation of a sharp $(\sqrt{3} \times \sqrt{3})R30^\circ$ low energy electron diffraction (LEED) pattern under these conditions **(22)** implies formation of an ordered $\theta = 0.33$ overlayer.

The EEL spectra recorded for adsorption at 95 K show two dipolar-enhanced modes. The frustrated translation of the N_2 molecules perpendicular to the surface, $\nu(Ru{-}N_2)$, appears initially at 280 cm^{-1} and shifts with increasing coverage to 298 cm^{-1} at saturation, and the nitrogen-nitrogen stretching vibration, $\nu(NN)$, appears initially at 2252 cm^{-1} and shifts to 2212 cm^{-1} at saturation. By analogy to the vibrational spectra of linear Ru-N_2 inorganic compounds, which show $\nu(NN)$ between 2085 and 2125 cm^{-1} **(26)**, these results suggest strongly that the N_2 molecules are coordinated to the surface at on-top sites, and the absence of bending modes in the spectra indicates that their interatomic axes are perpendicular to the surface.

Well-established theory which describes the interaction of electrons with arrays of adsorbed dipoles **(4,6)** shows that the same physical properties of an adsorbed overlayer which cause inelastic scattering of electrons via the dipolar mechanism also produce vibrational coupling among the molecules of the adsorbed overlayer. This dipolar coupling causes vibrational frequencies to increase monotonically with increasing surface coverage. An estimate of the contribution of this effect to the coverage dependence of ν(NN) can be made by using the following information:

1. The intensity of the ν(NN) feature for a saturation coverage of N_2 at 95 K, where a $(\sqrt{3} \times \sqrt{3})R30^\circ$ [$\theta = 0.33$] overlayer is formed, is approximately a third of that observed for the same overlayer of CO on the Ru(001) surface (at the same incident electron kinetic energy). For the latter, accurate values of the vibrational polarizability, α_v, the electronic polarizability, α_e, and the dipole lattice sum, Σ, have been obtained **(6)**.
2. Since the corresponding bond lengths for adsorbed N_2 and CO are equal to within approximately 0.2 Å **(8,10)**, the dipole lattice sums for $(\sqrt{3} \times \sqrt{3})R30^\circ$ overlayers of N_2 and CO can be assumed to be equal, i.e. $\Sigma = 0.17$ Å^{-3}.
3. Applications of this theory to other adsorption systems has shown that although α_v may differ significantly from its gas phase value for an adsorbed molecule, α_e is nearly unchanged upon chemisorption **(4,27)**. Consequently, the gas phase value of α_e, 2.4 Å^3 **(28)**, can be used to a good approximation in this analysis.

Employing these approximations and the results obtained for the analysis of CO on Ru(001), a value of $\alpha_v = 0.09$ Å^3 can be calculated with an estimated accuracy of ±20% for adsorbed N_2 on Ru(001). Note that this result follows from the use of the cross section for dipolar inelastic scattering from the ν(NN) vibration at a single coverage. Inserting the frequency for ν(NN) observed for low coverages of N_2 on the Ru(001) surface, $\omega_o = 2252$ cm^{-1}, the calculated value of $\alpha_v = 0.09$ Å^3, and the assumed values of $\alpha_e = 2.4$ Å^3 and $\Sigma = 0.17$ Å^{-3} into the expression derived for the frequency shift due to dipolar coupling upon going from a surface coverage of zero to the $(\sqrt{3} \times \sqrt{3})R30^\circ$ overlayer,

$$\left(\frac{\omega}{\omega_o}\right)^2 = 1 + \frac{\alpha_v\Sigma}{1 + \alpha_e\Sigma},$$

gives $\omega = 2264\ \mathrm{cm}^{-1}$ at $\theta = 0.33$ for N_2 on Ru(001), an increase of approximately 12 cm^{-1}. Variation of α_e by ±50% from its gas phase value of 2.4 $Å^3$ only changes this result by ±1 cm^{-1}. Since the experimental results for N_2 show a net decrease of 40 cm^{-1} when going from $\theta = 0$ to $\theta = 0.33$, and the previous analysis shows an increase of 12 cm^{-1} occurs due to dipolar coupling, it follows that a decrease of approximately 52 cm^{-1} in $\nu(NN)$ occurs due to coverage dependent chemical changes in the N≡N bond.

Although negative frequency shifts with increasing surface coverage have been reported for the $\nu(CO)$ mode of CO adsorbed on Cu(111) **(29)** and on polycrystalline Au **(30)** and for the $\nu(NN)$ mode of N_2 adsorbed on Ni(110) **(31)**, the decrease in $\nu(CO)$ or $\nu(NN)$ observed in these investigations was less than 10 cm^{-1}, and no detailed explanations for the change in the C≡O or N≡N bond with increasing surface coverage were offered. One plausible explanation for this effect attributes the decrease in $\nu(NN)$ with increasing coverage to formation of a $1\pi_g$ *band* with increasing surface coverage, broadening the energy of this π^* antibonding level and causing its population to vary due to coverage dependent changes in its overlap with the d band below the Fermi level of the metal substrate. This mechanism was first offered to explain the results of infrared reflection absorption spectroscopy (IRAS) measurements of the vibrational structure of mixed overlayers of ^{12}CO and ^{13}CO on Cu(110), where chemical interactions among adsorbed CO molecules were identified which produce a downward shift of $\nu(CO)$ with increasing surface coverage, more than compensating for the upward shift attributable to dipolar coupling **(32)**.

The arguments presented in Ref. 32 for CO on Cu(110) can be readily cast in terms appropriate to the phenomena observed for the adsorption of N_2 on Ru(001). If the energy of the $1\pi_g$ orbital of an isolated, chemisorbed N_2 molecule on the Ru(001) surface lies above the Fermi level, the $1\pi_g$ orbital is unpopulated and does not affect ν(NN). Increasing the density of N_2 admolecules on the surface, however, could cause the $1\pi_g$ orbitals of neighboring molecules to overlap and interact, and at sufficiently high coverages a band with significant energy dispersion would result. Band formation even at coverages of N_2 below $\Theta = 0.33$ is not unreasonable since the spatial extent of the $1\pi_g$ orbital of N_2 is greater than its van der Waals diameter (approximately 5 Å), allowing significant overlap at the $\sqrt{3}$ intermolecular spacing of 4.7 Å. Island formation at low coverage, as is observed for CO on Ru(001) **(33)**, would enhance this effect. If the $1\pi_g$ band broadens sufficiently with increasing coverage to cross the Fermi level, increasing the population of this band by increasing the coverage would cause the N≡N bond to weaken and ν(NN) to decrease. For example, inverse photoemission measurements for CO on Ni(111) show that the width of the 2π level increases by approximately 3 eV upon going from zero coverage to a fractional surface coverage of 0.33 **(34)**.

Two important points concerning this hypothesis should be noted. First, the ability of this mechanism to accurately describe the decrease of ν(NN) with increasing surface coverage depends on the energy of the $1\pi_g$ orbital of an isolated N_2 admolecule lying above the Fermi level. If the energy of this orbital were to lie just below the Fermi level, band formation would cause its population to *decrease* and cause ν(NN) to *increase* with increasing surface coverage. This situation may prevail for the 2π level of CO when adsorbed on most transition metal surfaces, where shifts to higher frequency for ν(CO) are observed which exceed those attributable to dipolar coupling **(5)**. Second, this mechanism does not take into account a possible perturbation of the electronic structure of the metal substrate by the adsorbed overlayer. For noble metals such as copper, the d bands lie several eV below the Fermi level, and the density of d states at the Fermi level is nearly zero for the clean surface **(35,36)**. Consequently, a mechanism such as that just proposed, which attributes the changing population of the π^* antibonding orbitals of the adsorbate molecules to interactions localized in the adsorbate overlayer, is reasonable, since their interaction with the metallic states should be weak. Indeed, angle resolved photoemission measurements for the c(2x2) ordered overlayer which CO forms on Cu(100) at a fractional surface coverage of 0.5 show the 2π band of CO crossing the Fermi level at the Brillouin zone edge **(36)**, supporting this model. For other transition metals such as ruthenium, however, the d band density of states at the Fermi level is large, and mixing of these metallic states with the π^* antibonding orbitals of the adsorbate molecules would lead to more complex coverage dependent bonding effects. This point will be considered in more detail in conjunction with results obtained for the coadsorption of N_2 and CO on the Ru(001) surface, presented later in this paper.

Results of thermal desorption measurements for the adsorption of N_2 on the clean Ru(001) surface at 75 K are shown in Fig. 1. Initial exposure produces the state near 125 K, as was described for adsorption at 95 K. For exposures of 1.0 L or greater ($\theta > 0.22$), however, a second feature appears near 105 K, with an initial binding energy of approximately 6.0 kcal/mole, shifting to 90 K and 5.2 kcal/mole for a saturation exposure of 2.5 L or more. The saturation coverage for N_2 observed under these conditions is approximately 0.50 monolayer. LEED shows the development of a weak, diffuse $(\sqrt{3} \times \sqrt{3})R30^\circ$ pattern and indicates the presence of substantial disorder (i.e. only small domains of the $\sqrt{3}$

structure) in the overlayer under these adsorption conditions **(22)**. The probability of adsorption approximately doubles from its initial value of 0.4 ± 0.2 when the low temperature state begins to populate **(22,37)**. As shown in Fig. 2, thermal desorption spectra recorded after a 2.0 L exposure of the Ru(001) surface to $^{15}N_2$ at 100 K to populate partially the high temperature state, followed by a 2.0 L exposure of the surface to $^{14}N_2$ at 75 K (or vice versa), show incomplete mixing of the two isotopes upon desorption, ruling out the possibility of simple two-dimensional compression of the adlayer at high coverage.

Figure 3 illustrates the effects of the adsorption temperature on the relative populations of the two binding states. The thermal desorption spectrum recorded after a saturation exposure of the Ru(001) surface to N_2 at 75 K (Fig. 3, *top*, $\theta = 0.50$) shows decreased population of the high temperature state relative to the spectrum obtained for a saturation exposure at 95 K (Fig. 3, *middle*, $\theta = 0.35$), indicating nonequilibrium adsorption at 75 K with population of the low temperature state occurring at the expense of population in the high temperature state. From the decrease in the intensity of high temperature state upon going from adsorption at 95 to 75 K, it can be concluded that the surface *density* (N_2 molecules/Ru surface atom) in the low temperature state is twice to three times that of the high temperature state, where each N_2 admolecule is associated with three ruthenium surface atoms ($\theta \cong 0.33$). As shown in the spectrum at the bottom of Fig. 3 ($\theta = 0.46$), the high temperature state, when saturated, poisons the surface almost completely to subsequent adsorption into the low temperature state.

Although the thermal desorption results show two apparent binding states for N_2 on Ru(001) at 75 K, EEL spectra recorded for adsorption at 75 K, illustrated in Fig. 4, show only two modes, $\nu(Ru{-}N_2)$ and $\nu(NN)$, as were observed for adsorption at 95 K. Furthermore, the coverage dependence of the frequencies of these modes (cf. Fig. 5) is similar to that observed for adsorption at 95 K, i.e. ν(NN) shifts downward from 2247 to 2198 cm^{-1} at saturation, and ν(Ru–N$_2$) shifts upward from 278 to 291 cm^{-1} (cf. 2252 to 2212 cm^{-1} and 280 to 298 cm^{-1} for adsorption at 95 K). Finally, the intensities of these bands increase monotonically with increasing surface coverage of both apparent binding states, as may be seen in Fig. 6, exceeding the intensities of ν(Ru–N$_2$) and ν(NN) that are observed for saturation coverage at 95 K by 20% and 50%, respectively.

The addition of the second apparent binding state for N$_2$, present only for adsorption at 75 K, contributes no extra vibrational features to the specular EEL spectrum, causes no extra features to appear in off-specular EELS measurements, causes no abrupt changes in the electron reflectivity of the ruthenium surface, and causes no detectable increase in the linewidth of either EELS band. This, coupled with the monotonic increase in the intensities of both EELS bands with increasing surface coverage of both binding states, indicates that the EELS results are probing the vibrational structure of both chemisorbed states, i.e. the vibrational spectra of the two states are identical within the resolution of the EELS measurements (70 to 80 cm^{-1}). By these arguments, it can be concluded that the N$_2$ molecules in the low temperature state are also bonded to the ruthenium surface atoms at on-top sites with their molecular axes perpendicular to the surface plane. However, as was illustrated by the thermal desorption results of Fig. 3 which showed that the surface density in the low temperature state is twice to three times that of the high temperature state, the N$_2$ molecules in the low temperature state are bonded in areas locally "crowded" with N$_2$ admolecules. These molecules desorb at a lower temperature due to repulsive lateral interactions with their near neighbors in the adlayer.

All of these experimental results, including those obtained by TDMS, EELS and LEED **(22)**, can be described by the following adsorption scenario. Upon adsorption at 95 K, the N_2 molecules have sufficient mobility to find the most favorable adsorption sites, and attractive next-nearest neighbor lateral interactions at the $(\sqrt{3} \times \sqrt{3})R30°$ intermolecular distance on the Ru(001) surface (4.66 Å) lead to the formation of large domains of the $(\sqrt{3} \times \sqrt{3})R30°$ overlayer. Upon adsorption at 75 K, however, the decrease in thermal energy causes the mobility of the N_2 admolecules to be limited, and smaller domains of the $(\sqrt{3} \times \sqrt{3})R30°$ structure form until the fractional surface coverage approaches 0.2. Subsequent adsorption of N_2 not only contributes to the development of the high temperature state associated with the $(\sqrt{3} \times \sqrt{3})R30°$ structure, but also deposits N_2 molecules at antiphase domain boundaries between and interstices within these $\sqrt{3}$ domains where the resulting intermolecular spacing is less than the $\sqrt{3}$ distance, resulting in crowding. Each molecule that is adsorbed in such a surface site has its binding energy lowered relative to those in an ordered $(\sqrt{3} \times \sqrt{3})R30°$ structure due to repulsive interactions with the N_2 molecules in nearest neighbor adsorption sites, and its near neighbors have their binding energies similarly lowered by its presence. The last molecules to adsorb on the surface before the saturation coverage is reached are most likely to find these less favorable adsorption sites and are therefore most likely to desorb in the low temperature peak associated with repulsive lateral interactions. Some fraction of the molecules adsorbed in the $(\sqrt{3} \times \sqrt{3})R30°$ superstructure at low surface coverage before crowding occurs also desorb in the low temperature peak due to repulsive interactions with the N_2 molecules added at high coverage. As molecules desorb from the crowded areas of the surface, they leave adjacent molecules in the $(\sqrt{3} \times \sqrt{3})R30°$ structure, free of repulsive lateral interactions, to desorb in the high temperature state. Furthermore, some molecules which are adsorbed in crowded sites at high surface coverage will be relieved of repulsive lateral interactions during desorption and will desorb in the high temperature state. This explains the *partial* mixing of $^{14}N_2$ and $^{15}N_2$ upon desorption in the spectra of Fig. 2. All aspects of this adsorption scenario, including the coverage dependence of the probability of adsorption, are quantitatively duplicated in a recent Monte Carlo simulation of both the adsorption and desorption kinetics for N_2 on Ru(001) **(37)**. The results of these calculations indicate that the binding energy for N_2 on Ru(001) in the limit of zero coverage is 6.4 kcal/mole, that attractive next-nearest neighbor lateral interactions of 0.45 kcal/mole exist at the $(\sqrt{3} \times \sqrt{3})R30°$ intermolecular spacing of 4.66 Å, and that repulsive lateral interactions of 0.25 kcal/mole exist at the Ru-Ru (near-neighbor) distance of 2.70 Å.

B. The Adsorption of Nitrogen on Ru(001) Surfaces Precovered with both Disordered and Ordered Overlayers of Oxygen Adatoms

Exposure of the clean Ru(001) surface to O_2 at 100 K results in the formation of disordered overlayers of atomic oxygen, the properties of which have been characterized in previous investigations employing EELS **(23)**, LEED, TDMS, and contact potential difference ($\Delta\varphi$) measurements **(24)**. The oxygen adatoms occupy threefold hollow sites on the surface, and the saturation coverage of atomic oxygen is approximately 0.5 monolayer.

Thermal desorption spectra of N_2 recorded after varying exposures of the Ru(001) surface to O_2 at 100 K, followed by exposure to N_2 at 75 K *(not shown)*, indicate that the primary effect of disordered oxygen is to poison a fraction of the surface to subsequent N_2 adsorption, leaving the remainder of the surface to bind N_2 into states indistinguishable from those observed on the clean surface. The peak shapes and relative intensities evidenced in these spectra are very similar to those observed for the adsorption of N_2 on the clean Ru(001) surface (cf. Fig. 1), but the intensities of both features are attenuated proportionally to the precoverage of disordered atomic oxygen. Comparison of the decrease in the amount of N_2 adsorption to the coverage of atomic oxygen indicates that the fractional surface area excluded from adsorption of N_2 by oxygen is twice the fractional surface coverage of disordered atomic oxygen.

For fractional surface coverages of disordered atomic oxygen below 0.25, annealing the surface to temperatures in excess of 300 K causes the oxygen adatoms to order into a configuration consistent with a p(2x2) structure, which reaches full development at $\theta = 0.25$ **(23,24)**. The contact potential difference between this p(2x2) structure and the clean Ru(001) surface is $\Delta\varphi = 0.20$ eV **(24)**, and, ignoring depolarization effects and utilizing a Ru=O bond distance of 2.05 Å **(23)**, this $\Delta\varphi$ can be shown **(38)** to be equivalent to the transfer of approximately 0.02 electron from the ruthenium surface to each oxygen adatom of the p(2x2) overlayer, representing a quantifiable increase in the Lewis acidity of the ruthenium surface atoms. For fractional surface coverages of ordered atomic oxygen between 0.25 and 0.50, the oxygen adatoms fill the threefold sites between those of the p(2x2) overlayer **(23)**, producing three independent domains of a p(1x2) overlayer rotated 120° with respect to one another. Saturation of the ordered atomic oxygen is reached when the fractional surface coverage is 0.50, consistent with the p(1x2) domains. The contact potential difference between the fully developed p(1x2) structure and the clean Ru(001) surface is $\Delta\varphi = 1.06$ eV **(24)**, and, utilizing a Ru=O bond length of 2.26 Å **(23)**, this $\Delta\varphi$ is equivalent to the transfer of approximately 0.05 electron from the surface to each oxygen adatom of the p(1x2) overlayer. Inclusion of depolarization effects in this calculation, which would be expected to be more important for the higher fractional surface coverage of the p(1x2) overlayer than for the p(2x2) overlayer, would increase slightly the amount of electron transfer resulting from the measured value of $\Delta\varphi$.

Thermal desorption spectra of N_2 recorded after preparation of ordered overlayers of atomic oxygen with varying fractional surface coverages, followed by exposure to 1.5 L of N_2 at 75 K, are shown in Fig. 7. The top spectrum shows desorption of N_2 after an equal exposure of the clean surface to N_2 for comparison. As the surface coverage of ordered oxygen is increased from zero to 0.25, the desorption states of N_2 associated with the clean surface at 94 and 117 K attenuate, and a new feature appears at 140 K. For fractional surface coverages of ordered oxygen adatoms between 0.25 and 0.50, the clean surface states are nearly extinguished, and the state at 140 K is attenuated. For a saturation coverage of ordered oxygen of 0.50 monolayer, almost no adsorption of N_2 is detected. The weak desorption rate maximum near 90 K for coverages of ordered oxygen in excess of 0.25 monolayer is associated either with imperfections in the crystal surface, with imperfections in the order of the atomic oxygen overlayers, or with desorption from the crystal edges or support leads, and is clearly not associated with the well-ordered portions of the crystal face from which the majority of the desorption signal for N_2 originates. This conclusion has been verified via EELS, which shows no signal attributable to adsorbed N_2 after exposure of the Ru(001) surface, precovered with the fully developed p(1x2) overlayer of atomic oxygen, to N_2 at 75 K, conditions under which only the (weak) 90 K feature at is observed in TDMS.

The fact that the occupation of the state at 140 K peaks at a fractional surface coverage of ordered oxygen adatoms of 0.25, where the surface is populated by a well-developed p(2x2) overlayer, and that its occupation decreases for higher coverages of oxygen, where parts of the surface are populated by the p(1x2) overlayer, indicates that the formation of this desorption state of N_2 is intimately related to the presence of the p(2x2) overlayer of oxygen.

Shown in Fig. 8 are thermal desorption spectra recorded after increasing exposures of the Ru(001) surface, upon which a p(2x2) ordered overlayer of oxygen adatoms is present, to N_2 at 75 K. The N_2 state which is stabilized by the presence of the oxygen adatoms of the p(2x2) overlayer first appears at 149 K [the corresponding binding energy is 8.7 kcal/mole **(25)**] and shifts to 141 K (8.3 kcal/mole) with increasing coverage. The saturation coverage of N_2 attainable under these conditions depends critically on the fractional surface coverage of oxygen present on the surface prior to the exposure to N_2. Values between 0.21 and 0.26 for the fractional surface coverage of N_2 were observed, and these results, compared with the ideal fractional surface coverage of the p(2x2) overlayer of oxygen of 0.25, indicate that one N_2 molecule is adsorbed for each unit cell of the p(2x2) overlayer. If this is true, and all adsorption sites for N_2 in the presence of the p(2x2) overlayer of oxygen are equivalent, long-range p(2x2) order for the mixed adlayer should be evident via LEED. Unfortunately, LEED data to afford a conclusion on this hypothesis could not be obtained. The EELS results described below, however, do substantiate this conclusion.

A comparison of the vibrational structure of N_2 adsorbed on both disordered and ordered overlayers of oxygen is provided in Fig. 9. The EEL spectrum recorded after exposure of the clean Ru(001) surface to 0.8 L of O_2 at 100 K *(upper left panel)*, an exposure sufficient to produce a quarter-monolayer of disordered oxygen adatoms, shows the ν(RuO) mode at 558 cm^{-1} and a shoulder at 427 cm^{-1} which results from the disorder present in the oxygen overlayer under these conditions **(23)**. Subsequent exposure of the surface to 2.0 L of N_2 at 75 K gives a surface coverage of N_2 of 0.16 monolayer and produces the EEL spectrum shown in the upper right panel of Fig. 9. The vibrations attributable to adsorbed N_2 appear at 268 and 2232 cm^{-1}, differing by only 20 and 8 cm^{-1} from their expected values for the same coverage of N_2 on the clean surface

(288 and 2224 cm^{-1}, respectively, cf. Fig. 5). Moreover, the ratio of the intensity of $\nu(\mathrm{R{-}N_2})$ to that of $\nu(\mathrm{NN})$ is approximately 3:1, as was observed on the clean surface. This suggests that the N_2 molecules adsorbed in the presence of disordered atomic oxygen on Ru(001) are bonded in sites very similar to those available on the clean surface and agrees with the results of the TDMS measurements described earlier.

Also noteworthy in the EEL spectrum for postadsorption of N_2 on the disordered quarter-monolayer of atomic oxygen is the strong attenuation of the $\nu(\mathrm{RuO})$ feature in the presence of N_2 relative to the spectrum for oxygen alone on the surface. In dipolar inelastic electron scattering, the ratio of the intensity of a loss feature to the intensity of the elastically scattered beam, I/I_o, depends on the vibrational polarizability of the vibration considered, α_v, and the electronic polarizability and dipole sum, α_e and Σ, of the surrounding atoms or molecules through the relationship **(4,6)**

$$\frac{I}{I_o} \propto \frac{\alpha_v}{(1 + \alpha_e \Sigma)^2} .$$

For atomically adsorbed species such as oxygen, α_e is small, and $\alpha_e \Sigma$ can be assumed to be much less than unity. For atomic oxygen in the presence of coadsorbed N_2, however, the values of α_e and Σ of the surrounding N_2 admolecules must be included in this expression for the intensity of the $\nu(\mathrm{RuO})$ vibration through the formalism described in Ref. 6. Since Σ varies with the inverse third power of the distances to the dipoles surrounding the vibrating atom or molecule being probed **(4,6)**, however, this quantity is strongly structure sensitive, precluding a rigorous analysis and unambiguous justification of this proposed mechanism. It is sufficient to realize that the rather large polarizability of N_2, i.e. $\alpha_e = 2.4$ Å^3, would cause substantial dielectic screening of the intensity of the ν(RuO) vibration when N_2 molecules and oxygen adatoms are adsorbed in close proximity to one another, as would be expected for at least a fraction of the surface under these disordered adsorption conditions.

The EEL spectrum in the lower left panel of Fig. 9 shows the effects of annealing the surface with the disordered quarter-monolayer of atomic oxygen present to 400 K. The ν(RuO) feature sharpens and shifts to 527 cm^{-1}, the shoulder at 427 cm^{-1} disappears, and a weak mode due to coupling of the p(2x2) overlayer to a surface phonon appears at 243 cm^{-1} **(23)**. Subsequent exposure to 2 L of N_2 at 75 K gives a fractional surface coverage of N_2 of 0.21 and produces the EEL spectrum shown in the lower right panel of Fig. 9. Note that the ratio of the intensity of $\nu(R{-}N_2)$ to that of ν(NN) is now approximately 6:1. Furthermore, $\nu(R{-}N_2)$ appears at 249 cm^{-1}, 30 cm^{-1} lower than the lowest value observed for adsorption on the clean surface, and ν(NN) appears at 2263 cm^{-1}, approximately 15 cm^{-1} higher than the highest value observed on the clean surface and 43 cm^{-1} higher than observed for the same fractional coverage of N_2 on the clean surface (cf. Fig. 5). Thus the vibrational spectrum of the state produced by the interaction of the p(2x2) oxygen overlayer with adsorbed N_2 is significantly different from that of the N_2 which exists on the clean Ru(001) surface or in the presence of disordered oxygen.

In contrast to the results for the adsorption of N_2 on the Ru(001) surface on which there is disordered oxygen, the intensity of the ν(RuO) mode for the ordered p(2x2) overlayer remains unchanged upon the subsequent adsorption of N_2 (cf. the lower left and lower right panels of Fig. 9). This suggests that under these conditions the N_2 molecules are bonded at distances sufficiently separated from the oxygen adatoms of the p(2x2) overlayer to decrease drastically their ability to affect the intensity of the ν(RuO) vibration, giving clear evidence for the structural sensitivity of the dielectric screening mechanism described earlier.

As was stated earlier, the addition of the electronegative oxygen adatoms withdraws charge from the ruthenium surface atoms, increasing their Lewis acidity. This increases the ability of the Ru surface atoms to accept lone pair electrons from adsorbates and inhibits their ability to backdonate electrons to otherwise unoccupied adsorbate levels. The dramatic effect of the p(2x2) oxygen overlayer on the chemistry of the Ru(001) surface has been demonstrated in previous investigations of the chemisorption of acetone **(39)** and formaldehyde **(40)**. Both of these molecules are π acids like N_2 and CO, and both have occupied lone pair orbitals for σ donor bonding and unoccupied antibonding orbitals of π^* symmetry for backdonor bonding to metal surfaces. Whereas the σ donor and π^* backdonor contributions to the bonds which N_2 and CO form with metal surfaces can be measured only in terms of binding energies and intramolecular stretching frequencies, the balance between the strengths of the σ donor and π^*-backdonor interactions for acetone and formaldehyde with metal surfaces is evidenced by the configurations in which they bond. For both acetone and formaldehyde, adsorption on the clean Ru(001) surface produces η^2 configurations indicative of strong π^*-backdonor bonding. On the Ru(001) surface, modified by the presence of the p(2x2) oxygen overlayer, however, σ donor bonding in an η^1 configuration is stabilized with respect to π^*-backdonor bonding for both acetone and formaldehyde.

Qualitatively similar results are evidenced in these results for the adsorption of N_2. The appearance of ν(NN) at 2263 cm^{-1} (higher than is observed under any conditions for the adsorption of N_2 on the clean surface) for N_2 adsorbed on the Ru(001) surface on which a p(2x2) oxygen precovered surface indicates that the oxygen decreases the $1\pi_g$ backdonation contribution to the Ru-N_2 bond. Even with decreased backdonation, however, the binding energy of the N_2 molecules to the ruthenium surface increases from approximately 7.2 to 8.5 kcal/mole. This suggests that for N_2 on the clean Ru(001) surface, $1\pi_g$ backdonation contributes little to the Ru-N_2 bond strength. It is the increased strength of the dominant σ donation contribution to the bonding which is evidenced in the TDMS results for the p(2x2) oxygen precovered surface.

An interesting comparison of these results to those of a previous investigation of oxygen and CO coadsorption on the Ru(001) surface **(17)** can be drawn. The effects of preadsorbed, ordered oxygen on the EEL spectrum of subsequently adsorbed CO are similar to those reported here, ν(CO) increased to 2032 cm^{-1} from 1980 cm^{-1} on the clean surface, indicating decreased 2π backdonor bonding in the presence of oxygen. The thermal desorption, however, results indicated a *decrease* of the Ru-CO binding energy from 28 kcal/mole on the clean surface to 22 kcal/mole in the presence of ordered oxygen. Moreover, in agreement with the results reported here, the results of a more recent investigation have shown that this effect for CO on Ru(001) depends critically on the oxygen overlayer being ordered prior to exposure of the surface to CO **(18)**. This result suggests that the 2π backdonor contribution to the Ru-CO bond contributes significantly to the binding energy of CO on the Ru(001) surface, much more so than $1\pi_g$ backdonor bonding for N_2.

With this understanding of the electronic effects of adsorbed oxygen on the bonding of coadsorbed N_2 established, it remains to identify from the EELS data the binding sites occupied by N_2 in the presence of the p(2x2) oxygen overlayer. In the EEL spectrum in the lower right panel of Fig. 9, the absence of vibrational features attributable to more than one form of chemisorbed N_2 existing in conjunction with the p(2x2) overlayer of oxygen, coupled with the near 1:1 stoichiometry of the fractional surface coverages of both atomic oxygen and N_2 for a saturation exposure of this surface to N_2, indicate that all of the N_2

admolecules occupy equivalent adsorption sites on the surface with one site available in each unit cell of the p(2x2) oxygen overlayer. The absence of strong bending modes for N_2 in this spectrum indicates that only high symmetry sites with the axis of the N_2 molecule oriented perpendicularly to the surface need be considered. The four sites available in the presence of the p(2x2) oxygen overlayer which meet these criteria are illustrated in Fig. 10. In this figure, the dark circles represent the oxygen adatoms of the p(2x2) overlayer, the open circles represent the ruthenium surface atoms, the dashed circles represent the additional oxygen adatoms added to form the p(1x2) overlayer, and the cross-hatched circles, labeled A-D, represent possible adsorption sites for N_2. Sites A and C are threefold bridging sites, site C is an on-top site, and site D is a twofold bridging site. Sites A and B have C_{3v} symmetry, and therefore show only two dipolar active modes for N_2 — $\nu(R{-}N_2)$ and $\nu(NN)$. For sites B and D, direct lateral interactions among the N_2 admolecule and its nearest neighbor oxygen adatoms in the p(2x2) overlayer would reduce the adsorption site symmetries from C_{3v} to C_s for B and from C_{2v} to C_s for D **(23)**. This would cause two additional vibrations to be dipolar active for both of these sites — a frustrated rotation and a frustrated translation. These modes are expected to be weak and would be located in the region of the EEL spectrum where the strong modes due to $\nu(R{-}N_2)$ and $\nu(RuO)$ are observed. Since they would likely be unresolved from these strong features even if they were present in the EEL spectrum of N_2 on the p(2x2) oxygen overlayer, their absence in Fig. 9 cannot be taken as firm evidence to rule out adsorption sites such as B or D for N_2.

By analogy to results obtained for the vibrational spectra of CO adsorbed in sites of various symmetries on metal surfaces **(4)**, the high frequency of $\nu(NN)$, 2263 cm^{-1}, is suggestive of coordination at on-top sites (site C of Fig. 10) where less backdonation generally occurs in the case of twofold or threefold bridging sites. This conclusion is also supported by the results of structural investigations of the coordination of N_2 to organometallic complexes in solution **(41)**, where no precedent for twofold or threefold bridging configurations analogous to those of sites A, B or D of Fig. 10 have been obtained. Another result to be considered is the fact that no adsorption of N_2 occurs in the presence of the p(1x2) overlayer which oxygen forms at a fractional surface coverage of 0.5. This can be taken as evidence in support of sites A or C of Fig. 10, where addition of the p(1x2) overlayer puts oxygen adatoms within the van der Waals radius (approximately 2.5 Å) of N_2, providing a steric barrier to adsorption in these sites.

Based on a consideration of the aforementioned arguments, it seems reasonable to conclude that the on-top site (C) in Fig. 10 is preferred for N_2 on Ru(001) in the presence of the p(2x2) oxygen overlayer. Although adsorption at the on-top site (C) of Fig. 10 seems extremely probable, the arguments leading to this conclusion are somewhat circumstantial. This coadsorption system, as well as the complementary system of CO and oxygen on the Ru(001) surfaces, would be an excellent candidate for investigation by other structure sensitive experimental techniques such as LEED **(43)** or surface extended X-ray absorption fine structure (SEXAFS) **(44)**, since unequivocal identification of the bonding configurations for N_2 and CO in the presence of ordered oxygen would contribute important information toward our understanding of their bonding interactions with metal surfaces.

C. The Adsorption of Carbon Monoxide on the Ru(001) Surface Precovered with Overlayers of Nitrogen

Thermal desorption spectra recorded after exposure of the clean Ru(001) surface to 2.25 L of N_2 at 75 K, an exposure sufficient to produce a fractional surface coverage of 0.44, followed by increasing exposures to CO at 75 K, are shown in Fig. 11. For fractional surface coverages of CO below approximately 0.35, the adsorbed N_2 in both apparent binding states which are present on the clean surface is readily displaced by CO, as would be expected based on a comparison of their binding energies to the Ru(001) surface [approximately 7 kcal/mole for N_2 and 28 kcal/mole for CO **(17)**]. The probability of adsorption for CO on the Ru(001) surface precovered with N_2 is constant within experimental uncertainty up to this coverage and is only decreased by approximately 5% from the value obtained for the adsorption of CO on the clean Ru(001) surface at this temperature, suggesting a similar precursor mechanism controls the rate of CO adsorption on both surfaces **(13)**. For coverages of CO equal to or greater than approximately 0.22 monolayer, the attenuation of the high temperature state exceeds that of the low temperature state. For coverages approaching 0.5 monolayer of CO, desorption of the remaining N_2 occurs only in the low temperature peak near 90 K. It is interesting to note that as CO is added to and N_2 displaced from the Ru(001) surfaces in the measurements of Fig. 11, the *total* fractional surface coverage of both species remains nearly constant at a value between 0.44 and 0.54. This indicates that the effective surface area occupied by each added CO molecule is nearly equal to that of the N_2 molecule which it displaces.

These observations, considered in conjunction with the results of previous investigations which have described the behavior of adsorbed CO on the clean Ru(001) surface **(21,33,45)**, allow a reasonable mechanism for the desorption of

N_2 in the presence of coadsorbed CO to be developed which explains the effects evident in Fig. 11. On the clean Ru(001) surface, attractive lateral interactions on the order of 0.75 kcal/mole at the $\sqrt{3}$ intermolecular spacing of 4.66 Å **(45)** lead to the formation of islands of the $(\sqrt{3} \times \sqrt{3})R30°$ structure at coverages of CO below 0.33 monolayer. As the coverage of CO is increased past 0.33 monolayer, repulsive lateral interactions produce uniform two-dimensional compression of the CO overlayer, causing the CO admolecules to lose registry with the on-top adsorption sites which are occupied at low coverage. Commensurate hexagonal overlayers which result from this compression are observed at fractional surface coverages of 7/12 $[(2\sqrt{3} \times 2\sqrt{3})R30°]$ and 49/75 $[(5\sqrt{3} \times 5\sqrt{3})R30°]$ **(21)**. On the basis of a kinetic model for the rate of CO desorption from the clean Ru(001) surface, the pairwise repulsion which leads to compression of the CO overlayer for fractional surface coverages in excess of 0.33 has been estimated to be approximately 3 kcal/mole **(45)**. The results of the EELS measurements, to be discussed below, suggest that as CO is added to the Ru(001) surface precovered with a saturated overlayer of N_2, segregation of the CO admolecules into islands begins as the coverage of CO exceeds 0.10 monolayer. Since the total surface coverage of N_2 and CO remains nearly constant at approximately 0.5 monolayer as CO is added, the islands of CO are compressed to a surface *density* greater than that of the optimal $(\sqrt{3} \times \sqrt{3})R30°$ overlayer by the presence of the coadsorbed N_2. The magnitude of the repulsive lateral interactions among CO admolecules at surface densities above that of the $(\sqrt{3} \times \sqrt{3})R30°$ structure, i.e. 3 kcal/mole, is greater than the difference in the binding energies of the two apparent states observed for the adsorption of N_2 on the clean Ru(001) surface. Thus, for fractional surface coverages of CO in excess of 0.10 monolayer in the presence of coadsorbed N_2, the repulsive lateral interactions among CO admolecules in islands force the remaining N_2 admolecules into the "crowded" sites which produce the low temperature binding state for high coverages of N_2 alone on the Ru(001) surface. As the desorption of N_2 proceeds, expansion of the islands of CO forces more N_2 molecules into the crowded binding sites. This explains the more rapid attenuation of the high temperature state than the low temperature state of N_2 for coverages of CO equal to or greater than 0.22 in the spectra of Fig. 11 and the lack of significant desorption from the high temperature state of N_2 for coverages of CO in excess of 0.33 monolayer.

The results of an experiment designed to test this hypothesis are shown in Fig. 12. The spectrum at the top of Fig. 12 shows desorption of N_2 from a partially filled $(\sqrt{3} \times \sqrt{3})R30^\circ$ overlayer, formed by exposing the clean Ru(001) surface to 2.25 L of N_2 at 100 K. The resulting surface coverage is 0.22 monolayer, and the low temperature "binding state" for N_2 is left unpopulated. For the spectrum at the bottom of Fig. 12, an identically prepared overlayer of N_2 was exposed to 1.0 L of CO at 75 K, producing a coverage of CO of 0.39 monolayer and reducing the coverage of N_2 to 0.11 monolayer. The resulting desorption spectrum for N_2 is nearly identical to that shown in Fig. 11 for a 1.0 L exposure of CO and demonstrates clearly the shift of N_2 admolecules from the high energy to the low energy binding sites upon the adsorption of CO.

EEL spectra recorded after exposure of the clean Ru(001) surface to 4 L of N_2 at 85 K, an exposure sufficient to produce a fractional surface coverage of 0.40 monolayer, followed by the indicated exposures to CO, are shown in Fig. 13. Several important features of these spectra should be noted. First, the anomalously low value of ν(CO) observed in the bottom spectrum, 1958 cm^{-1}, is evidence for strong interactions, either direct or mediated by the ruthenium substrate, between CO and N_2 admolecules at low coverages of CO. Furthermore, for all coverages of CO, the values of $\nu(Ru{-}N_2)$ ranged between 283 and 295

cm^{-1}, and the values of ν(NN) ranged between 2197 and 2216 cm^{-1}. These values are typical of high coverages of N_2 on the clean surface (cf. Fig. 5) and suggest that the N_2 molecules are segregated from the CO molecules as the CO surface coverage is increased. Finally, the feature at 247 cm^{-1} in the spectrum at the top of Fig. 13 is not attributable to adsorbed N_2, but instead results from a surface phonon which couples to the hexagonal compression structure that CO forms on the clean Ru(001) surface for coverages near 0.5 monolayer. Thermal desorption measurements confirm that approximately 0.02 monolayer of N_2 is present on the surface for this spectrum, but the features due to adsorbed N_2 are too weak for this coverage of N_2 to be resolved from the strong modes due to adsorbed CO.

Figure 14 shows the frequency of ν(CO) as a function of the coverage of CO for experiments performed under conditions identical to those represented by the EEL spectra of Fig. 13. For comparison is the frequency of ν(CO) as a function of the coverage of CO for adsorption on the clean Ru(001) surface. The lines drawn through the data points of this figure are merely a visual guide. Several important effects are evident in these data. First, ν(CO) at low coverage on the N_2 precovered surface is 34 cm^{-1} lower than the lowest value of ν(CO) observed on the clean surface. In addition, ν(CO) increases sharply from this low value until a coverage of CO of approximately 0.10 monolayer is reached, indicating that changes which strongly affect the vibrational structure of the mixed overlayer are occurring in this coverage range. Finally, the curve for CO adsorption on the N_2 precovered surface crosses the curve for CO adsorption on the clean surface at a coverage of CO near 0.3 monolayer. As will be described below, all of these results are consistent with CO island formation at intermediate coverages which causes CO and N_2 to be segregated in different local areas of the surface.

The first evidence which supports this conclusion is the nearly constant value of ν(NN) that is observed as the CO coverage is varied. In the limit of infinite dilution of N_2 in an overlayer of CO (i.e. a single N_2 molecule as an interstitial impurity in an overlayer of CO), the effect of dipolar interactions with the surrounding CO admolecules on ν(NN) results from the solution of

$$\left[\frac{\omega}{\omega_o}\right]^2 = 1 + \frac{\alpha_v \Sigma}{1 + \alpha_e \Sigma},$$

where ω_o is the zero coverage value of ν(NN), but α_v, α_e and Σ are appropriate to the CO overlayer **(6)**. Consequently, N_2 molecules that are surrounded by CO molecules have ν(NN) blue shifted by dipolar interactions with the CO molecules, just as a CO molecule would in the same environment. For a single N_2 molecule in a $(\sqrt{3} \times \sqrt{3})R30°$ overlayer of CO, ν(NN) would increase from its zero coverage value of 2247 cm^{-1} to 2283 cm^{-1} in the absence of other interactions which affect ν(NN). The only other interaction which would contribute to changes in ν(NN) is competition for electron density to be donated into the 2π antibonding orbital of the CO admolecules and the $1\pi_g$ antibonding orbital of the N_2 admolecules. As was discussed earlier and demonstrated with the results for the coadsorption of N_2 with oxygen, N_2 is a weaker π acid than CO. Thus N_2 should lose $1\pi_g$ electron density in the presence of CO, further increasing ν(NN). The low values of ν(NN) observed in the presence of coadsorbed CO are only consistent with N_2 molecules adsorbed in areas of the surface free of CO, where their behavior mimics that observed for the adsorption of N_2 on the clean Ru(001) surface.

The value of ν(CO) observed for a low coverage of CO in the presence of N_2, 1958 cm^{-1}, has important consequences for understanding the bonding of N_2 to the clean Ru(001) surface. Results of an IRAS investigation of the chemisorption of CO on Ru(001) **(46)**, as well as the EELS data for the adsorption of CO on the clean surface presented here in Fig. 14, demonstrate clearly that ν(CO) in the limit of zero coverage on Ru(001) is approximately 1990 cm^{-1}. Employing the analysis presented above, the value of ν(CO) expected for a single CO admolecule surrounded by N_2 molecules is approximately 2002 cm^{-1}. Thus, the low value of ν(CO) observed in the presence of a sea of N_2 is clearly the result of changes in the Ru-CO bond produced by the adsorption of N_2. From this effect, manifest in the vibrational spectrum of a small concentration of CO coadsorbed with N_2, it can be inferred that the decrease of ν(NN) with increasing surface coverage of N_2 on the clean surface cannot be attributed simply to the formation of a $1\pi_g$ band with increasing surface coverage, the increasing dispersion of which increases its population and causes ν(NN) to decrease **(32)**. If $1\pi_g$ band formation were the dominant mechanism, the 2π antibonding orbital of the CO added to the surface on which a high coverage of N_2 is present would not participate in the $1\pi_g$ band, but would rather compete with N_2 for the electron density available at the surface for backdonation. The value of ν(CO) observed in this circumstance would reflect this competition for electron density and would be expected to be similar to that observed for CO adsorption on the clean Ru(001) surface, modified only by the presence of dipolar interactions with the N_2 admolecules which surround the adsorbed CO. Instead, the low value of ν(CO) observed under these circumstances indicates that the ruthenium surface atoms have their Lewis basicity, as measured by their ability to backdonate electrons into the $1\pi_g$ orbital of adsorbed N_2 or the 2π orbital of adsorbed CO, increased by the presence of N_2 on the surface. *This proves that a mechanism for the decrease of* ν(NN) *with increasing surface coverage of* N_2 *on the Ru(001) surface which considers only* $1\pi_g$ *band formation in the adsorbate overlayer is inadequate.*

The strong shift of ν(CO) with increasing coverage in the CO coverage range between zero and 0.10 monolayer is indicative of interactions among CO admolecules in addition to those which existed among CO and N_2 admolecules in the limit of zero coverage of CO. Two mechanisms contribute additively, both of which must be attributed to the segregation of CO admolecules into islands as the coverage of CO increases. One mechanism is the increased dipolar coupling of CO which exists with near neighbor CO admolecules than exists with near neighbor N_2 admolecules due to the high value of the vibrational polarizability of CO [$\alpha_v = 0.28$ Å^3 **(6)**] relative to that of N_2 ($\alpha_v = 0.09$ Å^3). The increase of 30 cm^{-1} in the value of ν(CO) in this coverage range (cf. Fig. 14) is within the limits of the total coverage dependent increase of ν(CO) observed for the adsorption of CO on the clean Ru(001) surface, suggesting that this frequency shift could be attributed solely to dipolar coupling effects. Furthermore, compression by the presence of N_2 of the CO islands formed, as was evidenced in the TDMS data of Fig. 11, would decrease the distance between CO near neighbors in the mixed overlayer, causing a more rapid shift of ν(CO) with increasing coverage via dipolar coupling than is observed for the adsorption of CO on the clean Ru(001) surface. For example, calculation of ν(CO) as a function of the number of near neighbors of CO at a distance of 3.8 Å, as is appropriate for the hexagonal compression structure which CO forms at a coverage near 0.5 monolayer on the clean Ru(001) surface, shows that only six near neighbors are required to produce a shift of 28 cm^{-1} in the resulting value of ν(CO). Segregation of CO admolecules into islands would reduce the local effect of coadsorbed N_2 on the backdonor properties of the ruthenium atoms to which the CO molecules bind, also producing an upward shift of ν(CO) as the occupation of the 2π orbitals for CO is decreased. The net shift of ν(CO) probably represents the additive result of these two effects. If island formation did not occur, but rather a homogeneous mixed overlayer of N_2 and CO existed at all coverages of CO, these effects would be distributed over a broader range of CO coverages, and a more uniform increase of ν(CO) with coverage would result.

Finally, the increase of ν(CO), evident in Fig. 14 for coverages above 0.3 monolayer in the presence of coadsorbed N_2, above that observed for the same coverage of CO on the clean Ru(001) surface gives a further indication of the compression of adsorbed CO by the N_2 in this coverage range. Notice in the data of Fig. 14 that ν(CO), for a coverage of CO of approximately 0.4 monolayer in the presence of N_2, matches that observed for CO alone on the surface at a coverage near 0.5 monolayer, indicating that the CO admolecules under both of these circumstances are in the same adsorption environment, i.e. the local suface ***density*** (CO molecules per ruthenium surface atom) is the same in both cases. This corresponds well with the TDMS results of Fig. 11, where it was demonstrated that the total surface coverage, and therefore the local surface density of each species, remains nearly constant as the CO coverage is increased and N_2 molecules are displaced from the coadsorbed overlayer.

IV. Summary

The principal results of this work may be summarized as follows:

1. Due to a local perturbation of the electronic structure of the Ru(001) surface, the p(2x2) ordered overlayer of oxygen adatoms increases the σ donor contribution and decreases the $1\pi_g$ backdonor contribution to the bond which N_2 forms with Ru(001). The net increase in the binding energy of N_2 to the Ru(001) surface is approximately 1.5 kcal/mole. These results are in contrast to those obtained for the coadsorption of CO with oxygen, where a net decrease in the binding energy was observed in the presence of oxygen, illustrating important differences in the bonding of N_2 and CO to the Ru(001)

surface.

2. The results of measurements for the adsorption of CO on the Ru(001) surface precovered with a saturated monolayer of N_2 are consistent with segregation of the two species into different local regions of the surface for CO coverages above 0.10 monolayer. An anomalously low value of ν(CO) is observed for low coverages of CO surrounded by N_2 on the surface, giving clear evidence of a modification of the electronic properties of the Ru(001) surface by chemisorbed N_2. The N_2 admolecules increase the ability of the ruthenium surface atoms to backdonate electron density to the π^* antibonding orbitals of π acid molecules like CO, and this effect also explains the coverage dependent decrease of ν(NN) observed for the adsorption of N_2 on the clean Ru(001) surface.

3. The details of the interaction of a single adsorbed species with a clean metal surface, in this case N_2 with Ru(001), can be clarified by carefully designed experiments which feature coadsorption with other species, the adsorption characteristics of which are well understood. In this case, a clearer picture of the bonding of N_2 to the Ru(001) surface has emerged through experiments with coadsorbed oxygen and CO.

Acknowledgment

This research was supported by the National Science Foundation under Grant No. CHE82-06487.

References

1. K. Hermann and P. S. Bagus, Phys. Rev. B. **16**, 4195 (1977).
2. A. Rosen, P. Grundevik and T. Morovic, Surface Sci. **95**, 477 (1980).
3. J. Paul and A. Rosen, Phys. Rev. B **26**, 4073 (1982).
4. H. Ibach and D. L. Mills, *Electron Energy Loss Spectroscopy and Surface Vibrations*, Academic Press, New York, 1982.
5. B. E. Nieuwenhuys, Surface Sci. **105**, 505 (1981).
6. B. N. J. Persson and R. Ryberg, Phys. Rev. B **24**, 6954 (1981).
7. K. Hermann, P. S. Bagus, C. R. Brundle and D. Menzel, Phys. Rev. B. **24**, 7025 (1981).
8. A. Schichl, D. Menzel and N. Rösch, Chem. Phys. Letters **65**, 225 (1982).
9. A. Schichl, D. Menzel and N. Rösch, Chem. Phys. Letters **105**, 285 (1984).
10. C. W. Bauschlicher, Chem. Phys. Letters **115**, 387 (1985).
11. C. R. Brundle, P. S. Bagus, D. Menzel and K. Hermann, Phys. Rev. B. **24**, 7041 (1981).
12. J. Stöhr and R. Jaeger, Phys. Rev. B. **26**, 4111 (1982).
13. D. Menzel, H. Pfnür and P. Feulner, Surface Sci. **126**, 374 (1983).
14. K. Horn, J. DiNardo, W. Eberhardt, H.-J. Freund and E. W. Plummer, Surface Sci. **118**, 465 (1982).
15. J. L. Gland, R. J. Madix, R. W. McCabe and C. DeMaggio, Surface Sci. **143**, 46 (1984).
16. F. M. Hoffmann and R. A. de Paola, Phys. Rev. Letters **52**, 1697 (1984).

17. G. E. Thomas and W. H. Weinberg, J. Chem. Phys. **70**, 954 (1979).

18. H.-I. Lee, G. Praline and J. M. White, Surface Sci. **91**, 581 (1980).

19. A. B. Anton, N. R. Avery, B. H. Toby and W. H. Weinberg, J. Elec. Spectros. **29**, 181 (1983).

20. G. E. Thomas and W. H. Weinberg, Rev. Sci. Instrum. **50**, 497 (1979).

21. E. D. Williams and W. H. Weinberg, Surface Sci. **82**, 93 (1979).

22. P. Feulner and D. Menzel, Phys. Rev. B. **25**, 4295 (1982).

23. T. S. Rahman, A. B. Anton, N. R. Avery and W. H. Weinberg, Phys. Rev. Letters **51**, 1979 (1983).

24. T. E. Madey, H. A. Engelhardt and D. Menzel, Surface Sci. **48**, 304 (1975).

25. P. A. Redhead, Vacuum **12**, 203 (1962).

26. B. Folkesson, Acta Chem. Scand. **26**, 4008 (1972).

27. B. N. J. Persson and A. Liebsch, Surface Sci. **110**, 356 (1981).

28. K. L. Wolf, H. Briegleb and H. A. Stuart, Z. Phys. Chem. B **6**, 429 (1929).

29. P. Hollins and J. Pritchard, Surface Sci. **89**, 486 (1979).

30. M. L. Kottke, R. G. Greenler and H. G. Tompkins, Surface Sci. **32**, 231 (1972).

31. M. Grunze, R. K. Driscoll, G. N. Burland, J. C. L. Cornish and J. Pritchard, Surface Sci. **89**, 381 (1979).

32. D. P. Woodruff, B. E. Hayden, K. Prince and A. M. Bradshaw, Surface Sci. **123**, 397 (1982).

33. E. D. Williams, W. H. Weinberg and A. C. Sobrero, J. Chem. Phys. **76**, 1150 (1982).

34. T. Fauster and F. J. Himpsel, Phys. Rev. B **27**, 1390 (1983).

35. D. Westphal and A. Goldmann, Surface Sci. **126**, 253 (1983).

36. C. F. McConville, C. Somerton and D. P. Woodruff, Surface Sci. **139**, 75 (1984).

37. E. S. Hood, B. H. Toby and W. H. Weinberg (to be published).

38. J. Topping, Proc. Roy. Soc. London A **114**, 67 (1927).

39. N. R. Avery, W. H. Weinberg, A. B. Anton and B. H. Toby, Phys. Rev. Letters **51**, 6829 (1983); A. B. Anton, N. R. Avery, W. H. Weinberg and B. H. Toby, J. Am. Chem. Soc., submitted.

40. A. B. Anton, J. E. Parmeter and W. H. Weinberg, J. Am. Chem. Soc., submitted.

41. J. Chatt and G. J. Leigh, Chem. Soc. Rev. **1**, 121 (1972).

42. H. Ibach and D. Bruchmann, Phys. Rev. Letters **44**, 36 (1980).

43. P. M. Marcus and F. Jona, Appl. Surface Sci. **11/12**, 20 (1982).

44. A. Bianconi, Appl. Surface Sci. **6**, 392 (1980).

45. H. Pfnür, P. Feulner, H. A. Engelhardt and D. Menzel, Chem. Phys. Letters **59**, 481 (1978).

46. H. Pfnür, D. Menzel, F. M. Hoffmann, A. Orgeta and A. M. Bradshaw, Surface Sci. **93**, 431 (1980).

Figure Captions

Figure 1. Thermal desorption spectra of N_2 (m = 14 amu) recorded after the indicated exposures of the clean Ru(001) surface to N_2 at 75 K. The fractional surface coverages of N_2 for each exposure are also listed. The heating rate, β, for these measurements is 6 K/s.

Figure 2. Thermal desorption spectra of $^{15}N_2$ (m = 14 amu) and $^{14}N_2$ (m = 15 amu) collected simultaneously after exposures of the clean Ru(001) surface first to 2 L $^{15}N_2$ at 100 K, and then to 2 L $^{14}N_2$ at 75 K.

Figure 3. Thermal desorption spectra for N_2 following the indicated exposures of the clean Ru(001) surface to N_2 at the indicated temperatures, illustrating the effects of the adsorption temperature on the relative populations of the two binding states for N_2.

Figure 4. EEL spectra recorded following the indicated exposures of the Ru(001) surface to N_2 at 75 K.

Figure 5. Frequencies of the vibrations of adsorbed N_2 as a function of relative surface coverage for adsorption on the Ru(001) surface at 75 K. The saturation coverage of N_2 under these adsorption conditions, θ_{max}, is approximately 0.5 monolayer.

Figure 6. Intensities of the EELS bands of adsorbed N_2 as a function of relative surface coverage for adsorption on the Ru(001) surface at 75 K.

Figure 7. Thermal desorption spectra of N_2 (m = 14 amu) recorded after exposure of the Ru(001) surface, precovered with the indicated fractional surface coverages of ordered oxygen adatoms, to N_2 at

75 K.

Figure 8. Thermal desorption spectra of N_2 recorded after the indicated exposures of N_2 at 75 K to the Ru(001) surface on which a p(2x2) overlayer of oxygen adatoms is present.

Figure 9. EEL spectra comparing the vibrational structure of a disordered quarter-monolayer of oxygen adatoms *(upper left panel)*, followed by exposure to 2 L N_2 at 75 K *(upper right panel)*, to that of a p(2x2) ordered quarter-monolayer of oxygen adatoms *(lower left panel)*, followed by exposure to 2 L N_2 at 75 K *(lower right panel)*.

Figure 10. Schematic illustration of possible binding sites for N_2 in the presence of both the p(2x2) and p(1x2) oxygen overlayers on the Ru(001) surface. The significance of the various symbols is discussed in the text.

Figure 11. Thermal desorption spectra of N_2 recorded after the indicated exposures of CO at 75 K to the Ru(001) surface, preexposed to 2.25 L of N_2 at 75 K.

Figure 12. Thermal desorption spectra of N_2 illustrating both the displacement and the shift to sites of lowered binding energy of adsorbed N_2 by subsequently adsorbed CO. Spectrum (1), for exposure of the clean Ru(001) surface to 2.25 L N_2 at 100 K, shows the occupation of the state associated with the $(\sqrt{3} \times \sqrt{3})R30°$ overlayer of N_2. Spectrum (2) shows the desorption of N_2 from an overlayer prepared via the same procedure as for (1), and then exposed to 1.0 L CO at 75 K.

Figure 13. EEL spectra recorded after exposure of the clean Ru(001) surface to 4 L N_2 at 85 K, followed by the indicated exposures to CO at 85

K.

Figure 14. The frequency of ν(CO) as a function of the fractional surface coverage of CO for adsorption on both the clean and N_2 precovered Ru(001) surfaces.

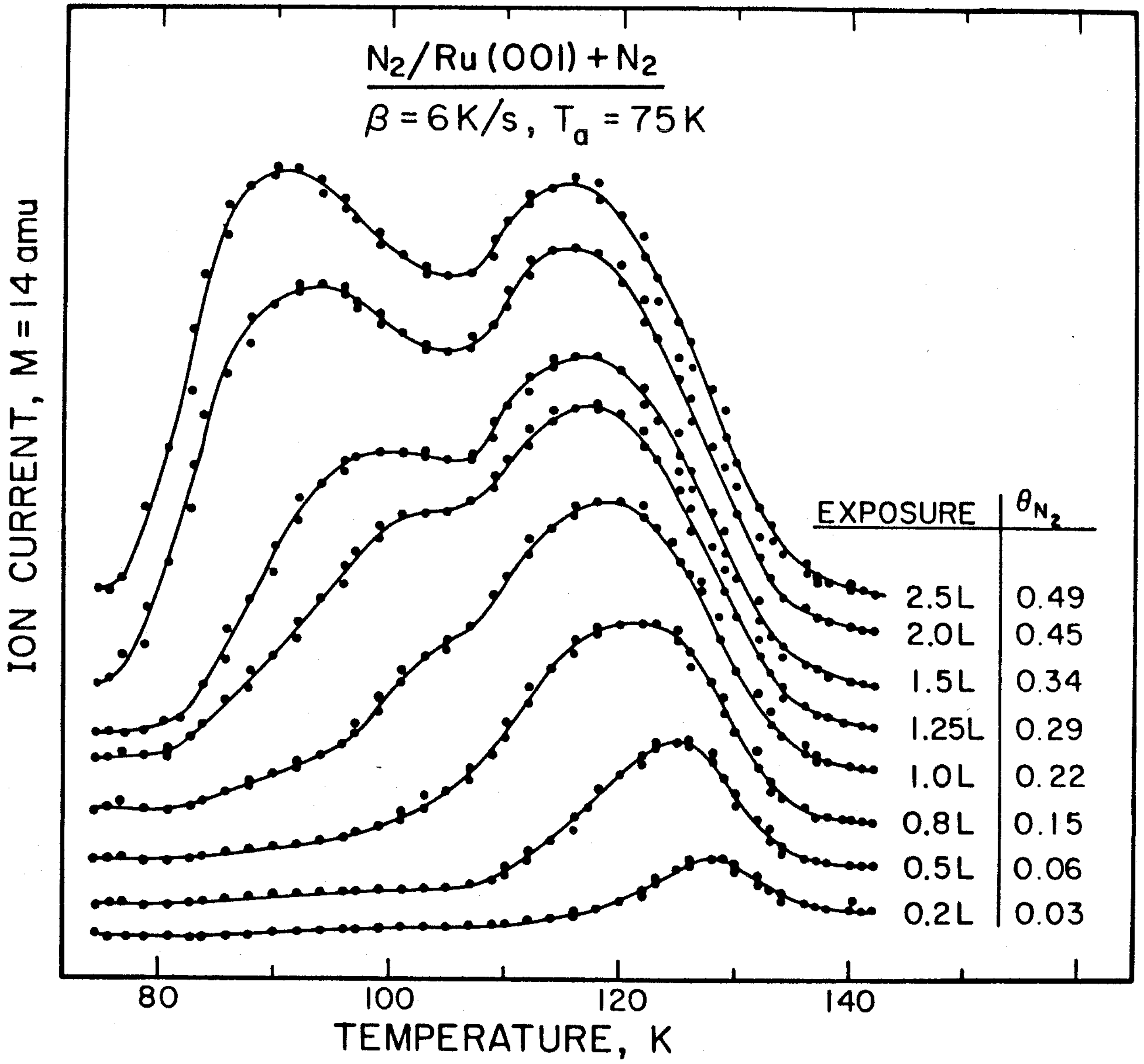
$N_2/Ru(001) + N_2$
$\beta = 6 K/s, T_a = 75 K$
ION CURRENT, M = 14 amu
TEMPERATURE, K
80
100
120
140
EXPOSURE
θ_{N_2}
2.5L 0.49
2.0L 0.45
1.5L 0.34
1.25L 0.29
1.0L 0.22
0.8L 0.15
0.5L 0.06
0.2L 0.03

Figure 1

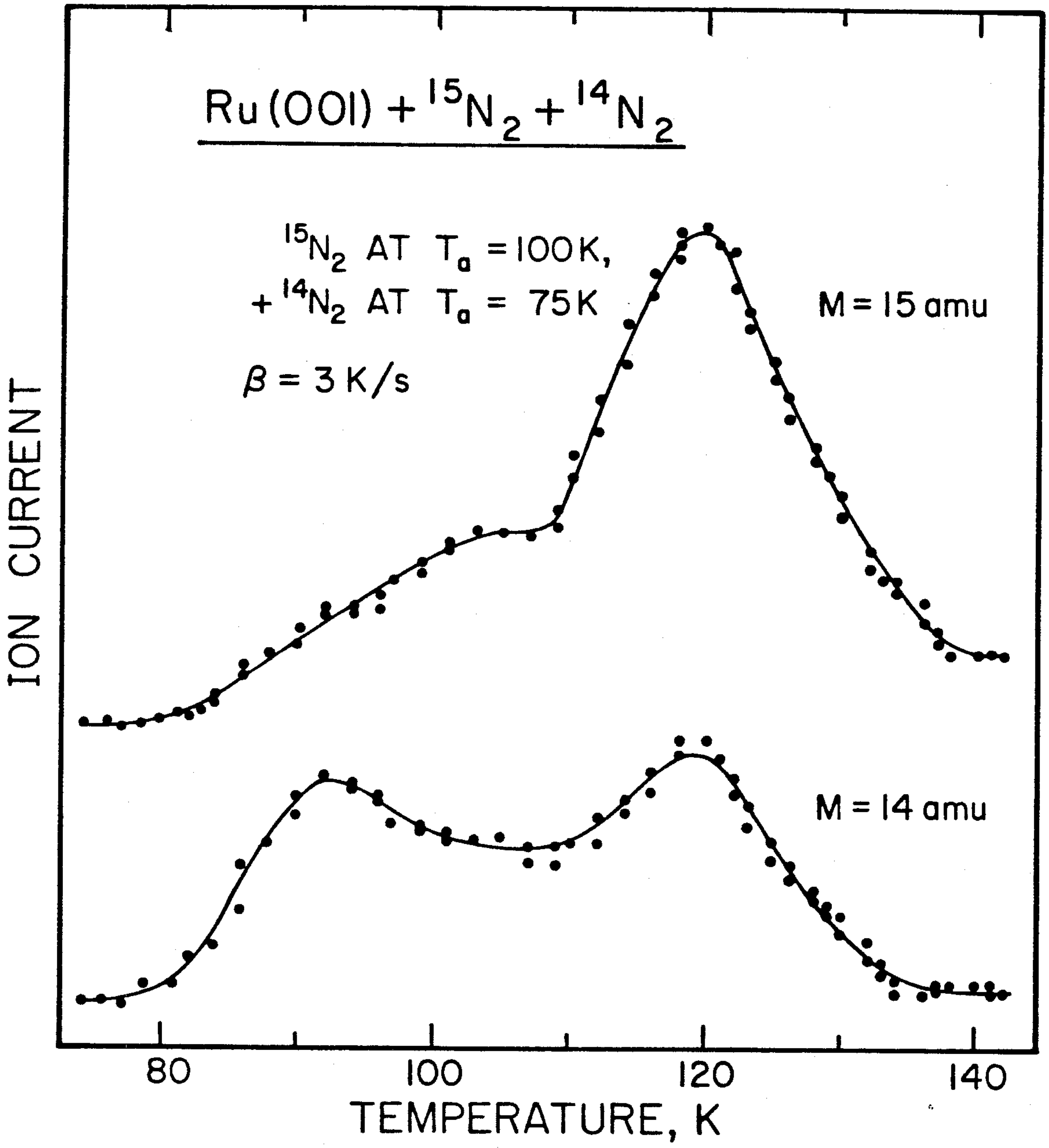
Ru(001) + $^{15}N_2$ + $^{14}N_2$
$^{15}N_2$ AT T_a = 100K,
+ $^{14}N_2$ AT T_a = 75K
β = 3 K/s
M = 15 amu
M = 14 amu
ION CURRENT
80
100
120
140
TEMPERATURE, K

Figure 2

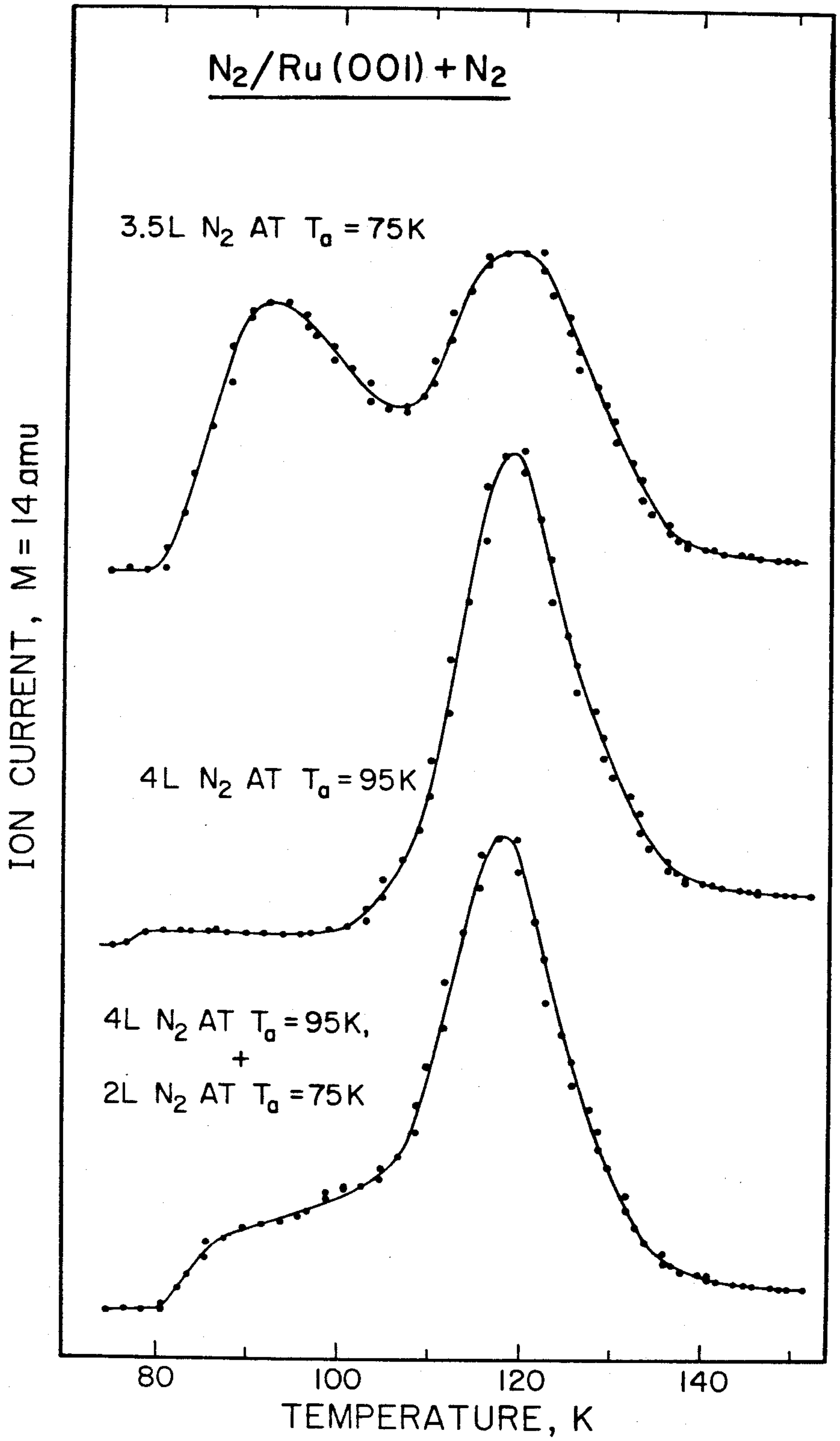
$N_2/Ru(001) + N_2$
3.5L N_2 AT $T_a = 75K$
4L N_2 AT $T_a = 95K$
4L N_2 AT $T_a = 95K$, + 2L N_2 AT $T_a = 75K$
ION CURRENT, M = 14 amu
80
100
120
140
TEMPERATURE, K

Figure 3

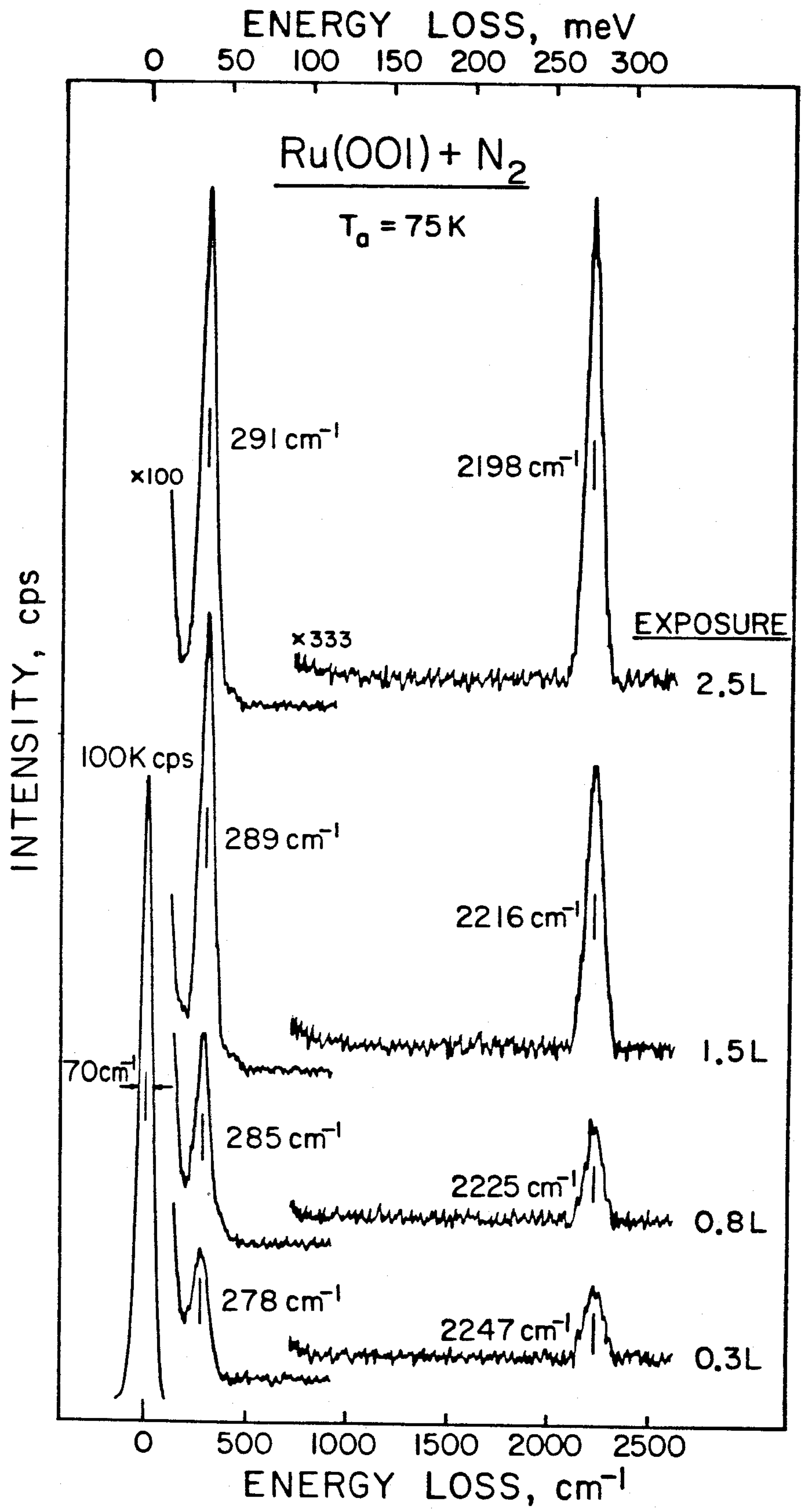
ENERGY LOSS, meV
0
50
100
150
200
250
300
Ru(001) + N2
Ta = 75 K
INTENSITY, cps
×100
291 cm⁻¹
2198 cm⁻¹
×333
EXPOSURE
2.5 L
100K cps
289 cm⁻¹
2216 cm⁻¹
1.5 L
70 cm⁻¹
285 cm⁻¹
2225 cm⁻¹
0.8 L
278 cm⁻¹
2247 cm⁻¹
0.3 L
0
500
1000
1500
2000
2500
ENERGY LOSS, cm⁻¹

Figure 4

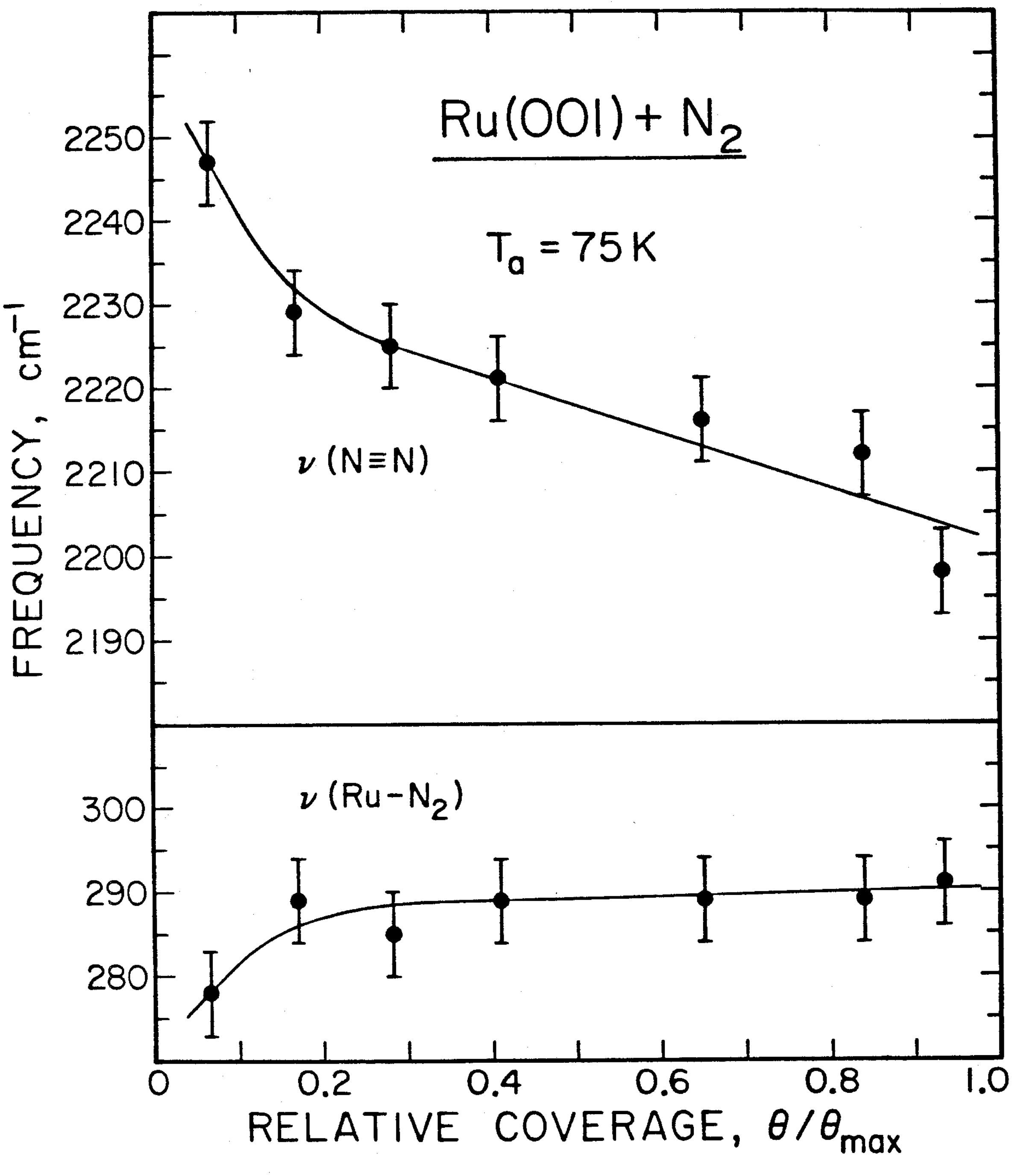
Ru(001) + N_2
T_a = 75 K
ν (N≡N)
ν (Ru-N_2)
FREQUENCY, cm^{-1}
2250
2240
2230
2220
2210
2200
2190
300
290
280
0
0.2
0.4
0.6
0.8
1.0
RELATIVE COVERAGE, θ/θ_{max}

Figure 5

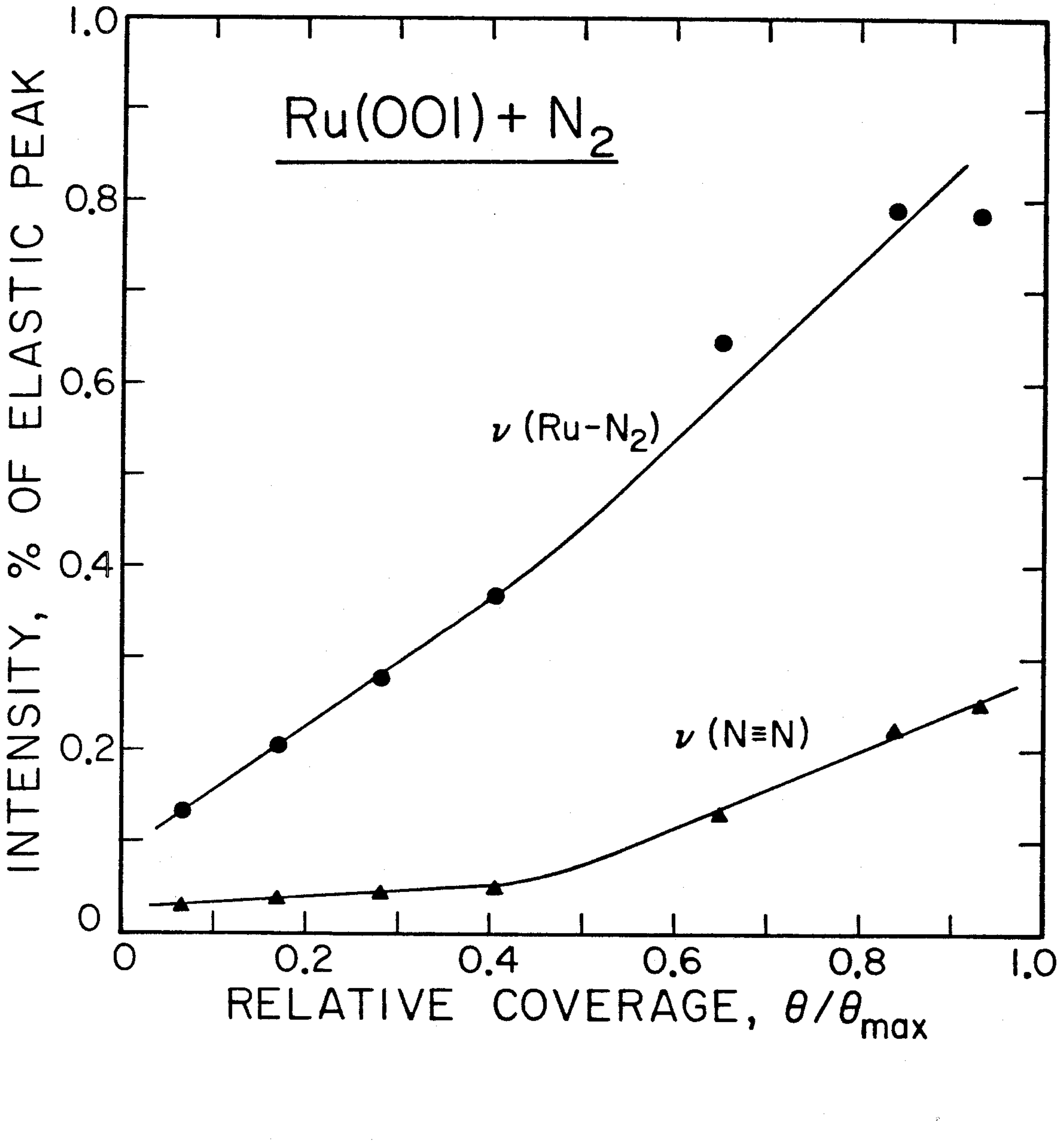
Ru(001) + N_2
ν (Ru-N_2)
ν (N≡N)
INTENSITY, % OF ELASTIC PEAK
RELATIVE COVERAGE, θ/θ_{max}
0
0.2
0.4
0.6
0.8
1.0

Figure 6

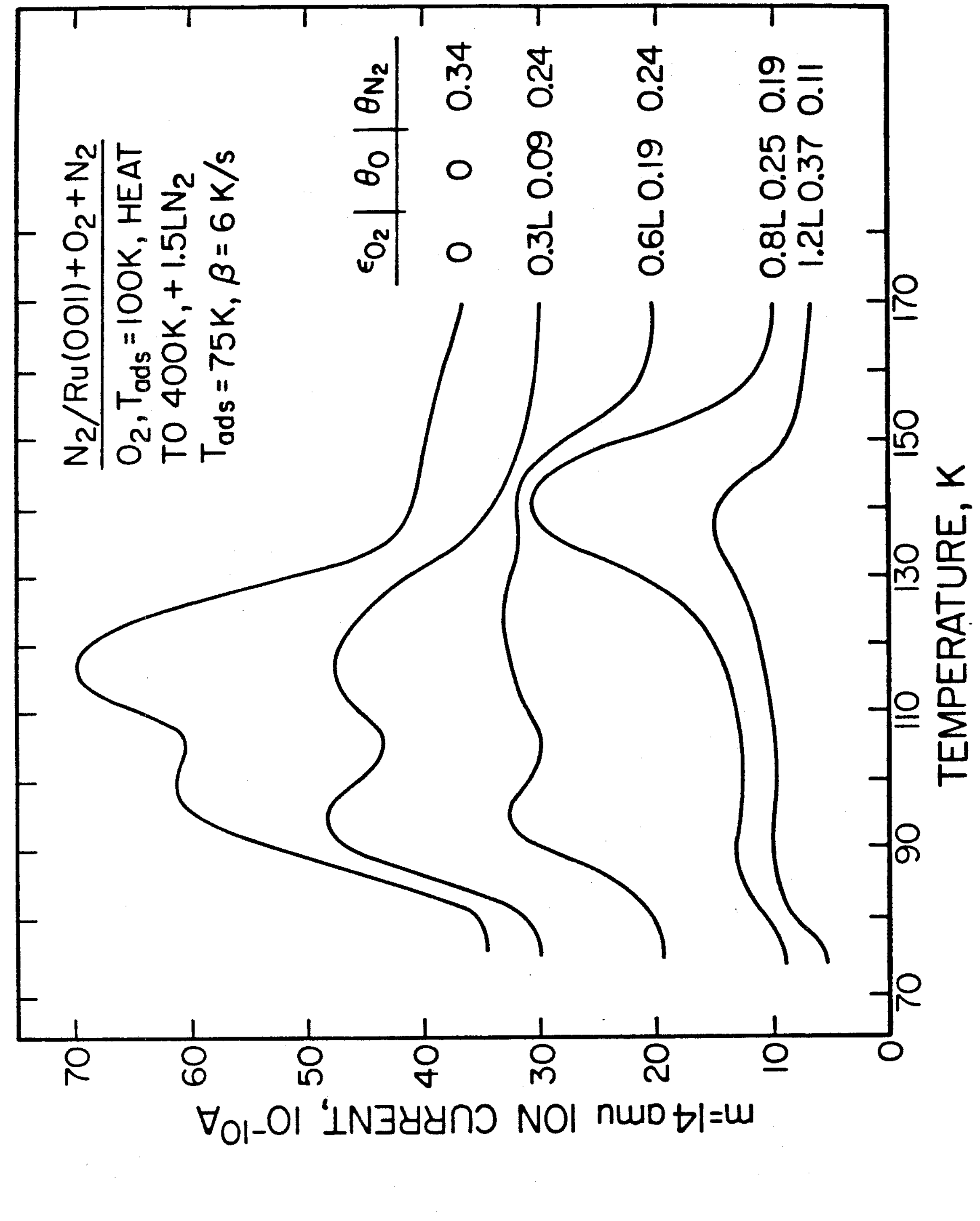
N2/Ru(001)+O2+N2
O2, Tads = 100K, HEAT
TO 400K, + 1.5L N2
Tads = 75K, β = 6 K/s
εO2 | θO | θN2
0 0 0.34
0.3L 0.09 0.24
0.6L 0.19 0.24
0.8L 0.25 0.19
1.2L 0.37 0.11
m=14 amu ION CURRENT, 10-10A
0
10
20
30
40
50
60
70
70
90
110
130
150
170
TEMPERATURE, K

Figure 7

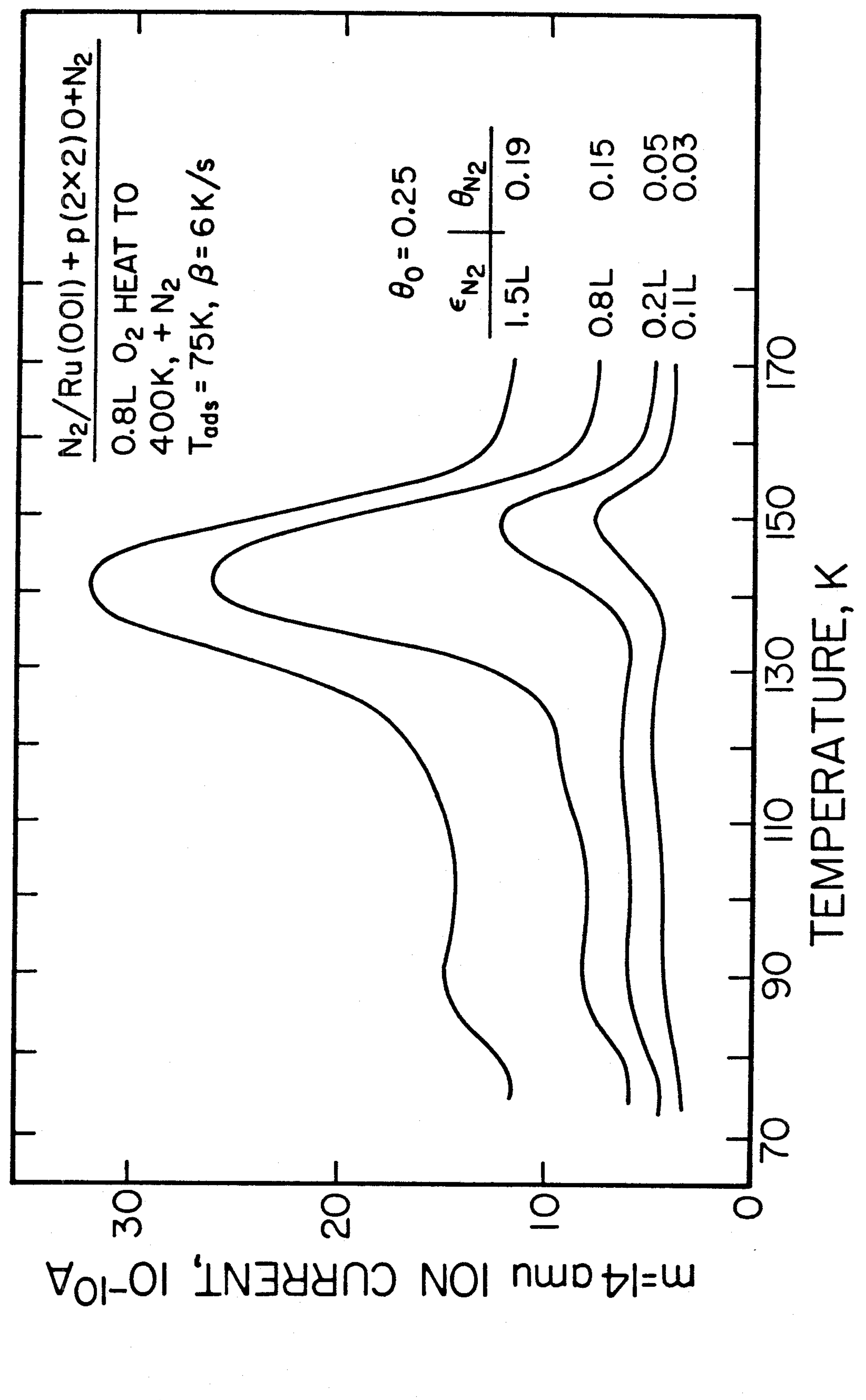
$N_2/Ru(001) + p(2\times2)O + N_2$
0.8L O_2 HEAT TO
400K, + N_2
T_{ads} = 75K, β = 6K/s
θ_O = 0.25
ϵ_{N_2}
θ_{N_2}
1.5L 0.19
0.8L 0.15
0.2L 0.05
0.1L 0.03
m=14 amu ION CURRENT, 10^{-10}A
0
10
20
30
70
90
110
130
150
170
TEMPERATURE, K

Figure 8

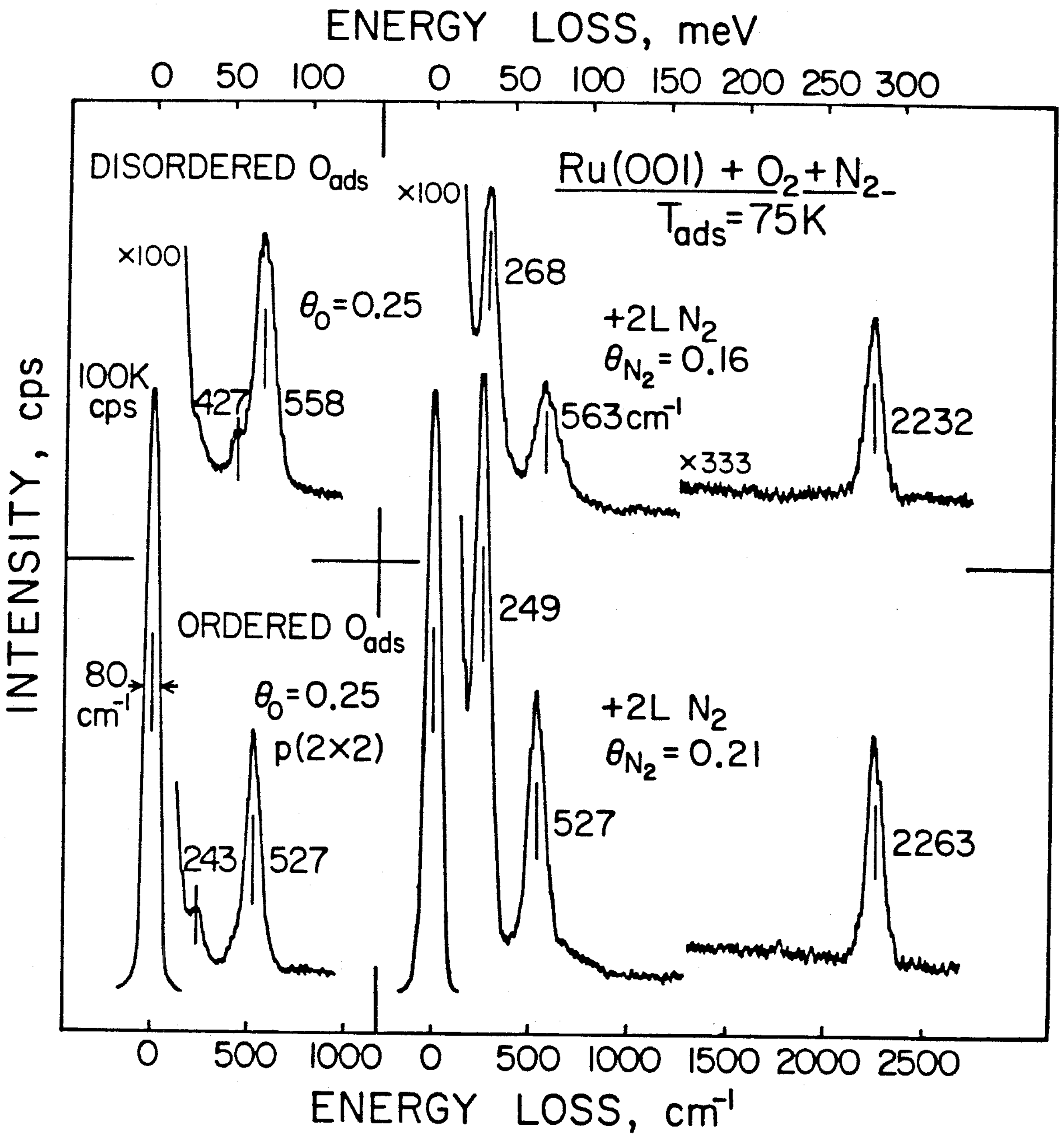
ENERGY LOSS, meV
0 50 100
0 50 100 150 200 250 300
DISORDERED O_{ads}
×100
θ_O=0.25
100K cps
427
558
×100
268
$\underline{Ru(001) + O_2 + N_2}$
T_{ads}=75K
+2L N_2
θ_{N_2}=0.16
563 cm^{-1}
×333
2232
ORDERED O_{ads}
80 cm^{-1}
θ_O=0.25
p(2×2)
243
527
249
+2L N_2
θ_{N_2}=0.21
527
2263
INTENSITY, cps
0 500 1000
0 500 1000 1500 2000 2500
ENERGY LOSS, cm^{-1}

Figure 9

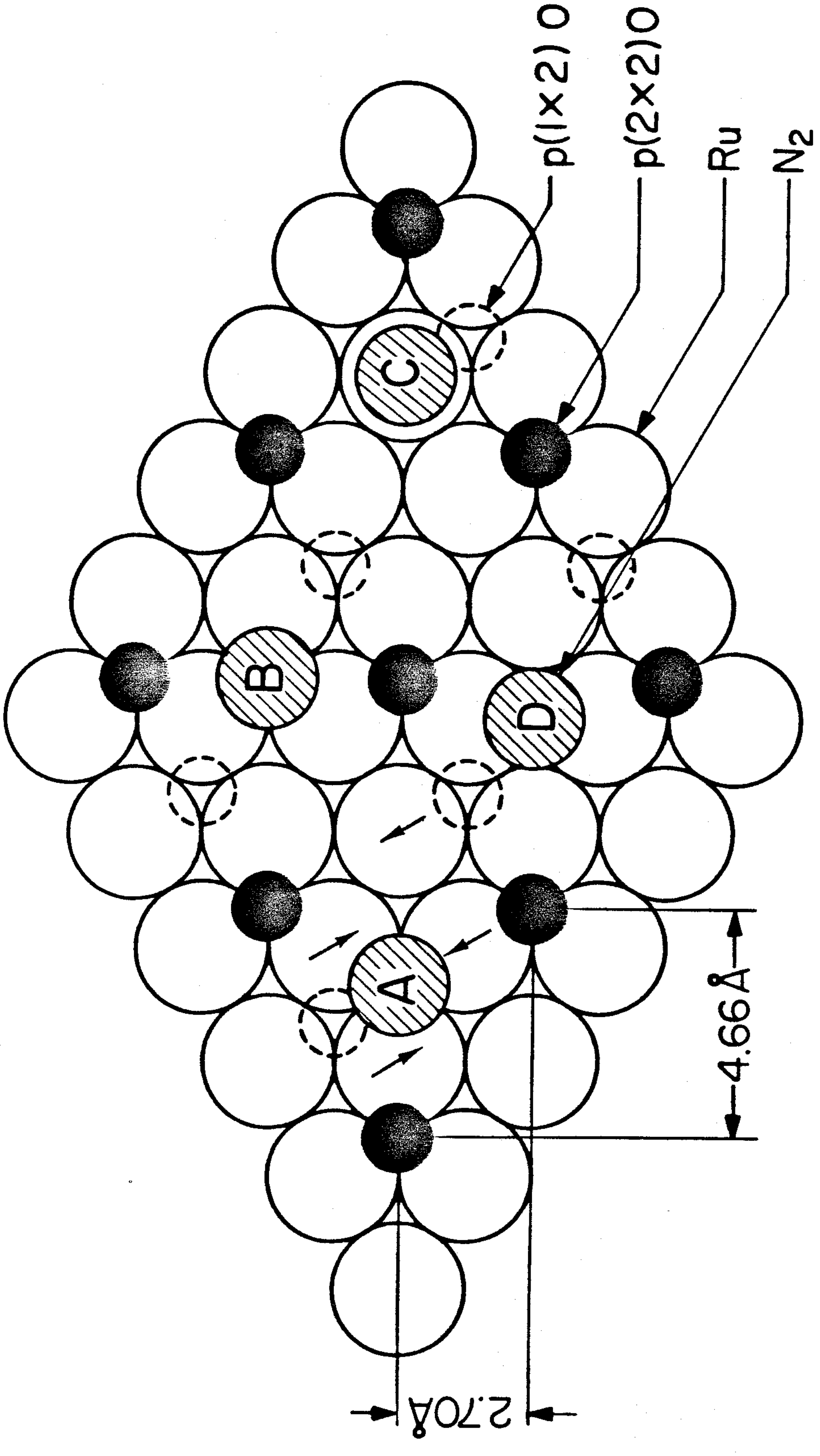

Figure 10

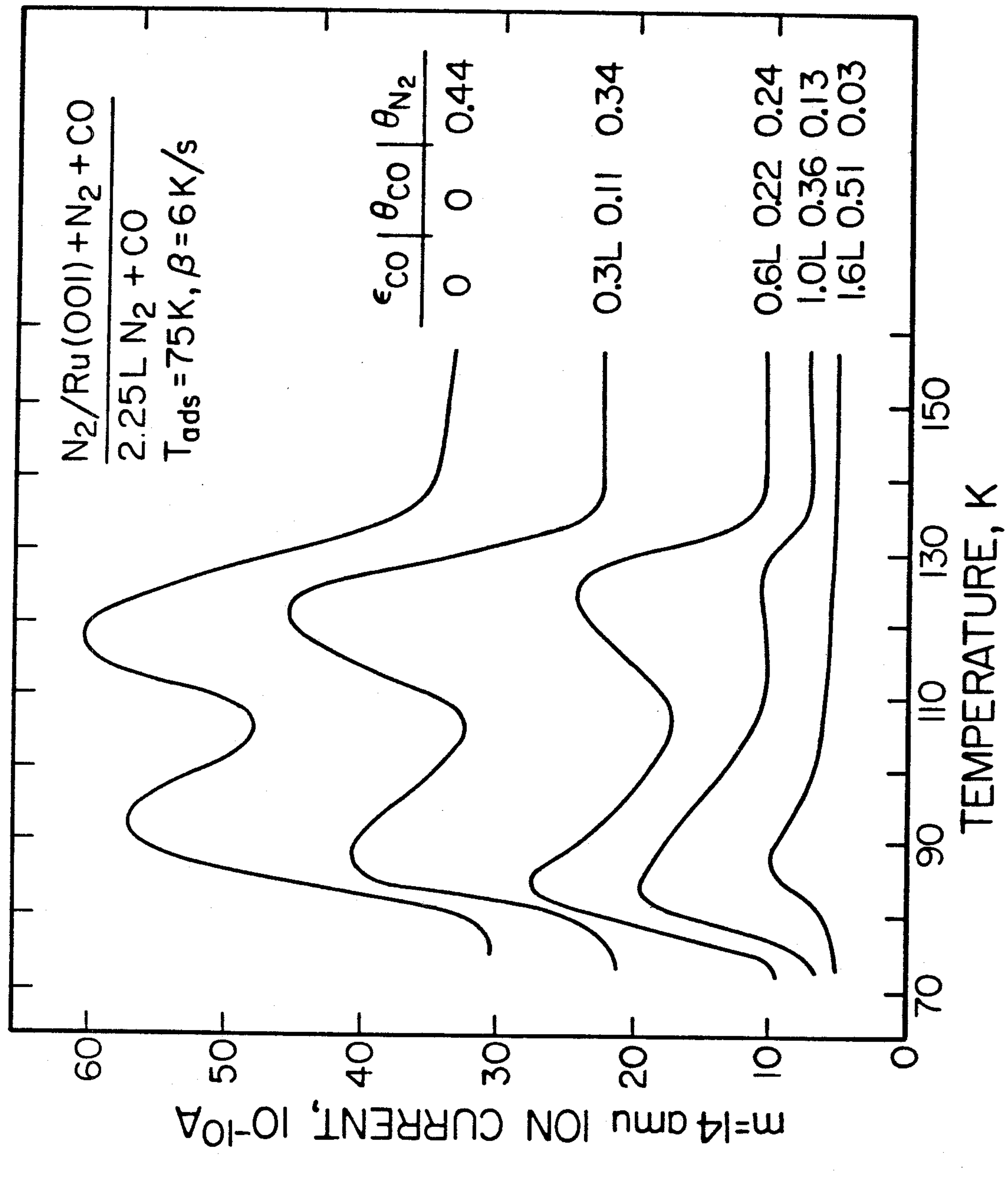
N_2/Ru(001) + N_2 + CO
2.25L N_2 + CO
T_{ads} = 75K, β = 6K/s
ϵ_{CO} | θ_{CO} | θ_{N_2}
0 0 0.44
0.3L 0.11 0.34
0.6L 0.22 0.24
1.0L 0.36 0.13
1.6L 0.51 0.03
m=14 amu ION CURRENT, 10^{-10}A
0
10
20
30
40
50
60
70
90
110
130
150
TEMPERATURE, K

Figure 11

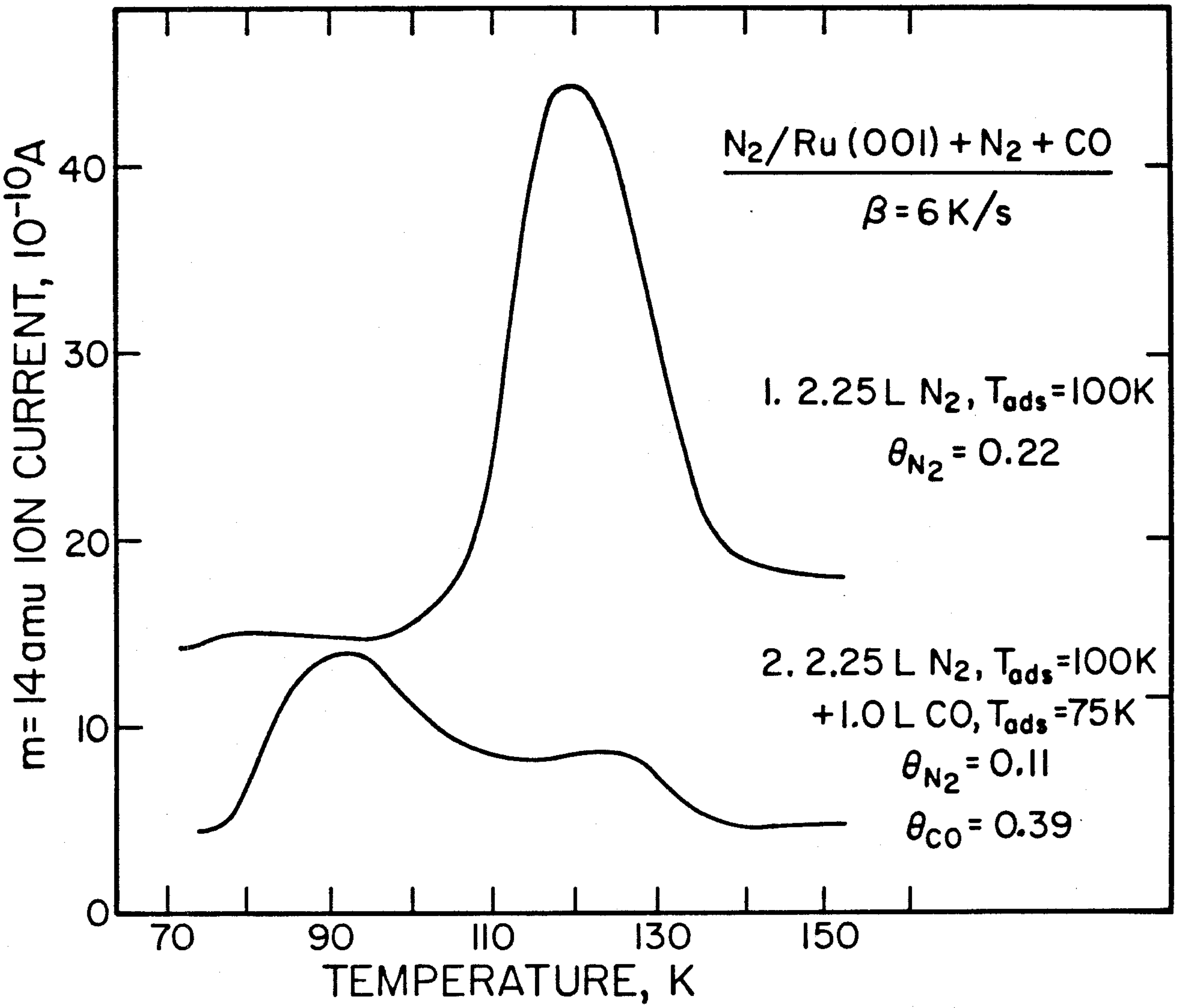
N2/Ru (001) + N2 + CO
β = 6 K/s
1. 2.25 L N2, Tads=100K
θN2 = 0.22
2. 2.25 L N2, Tads=100K
+1.0 L CO, Tads=75K
θN2 = 0.11
θCO = 0.39
m= 14amu ION CURRENT, 10⁻¹⁰A
0
10
20
30
40
70
90
110
130
150
TEMPERATURE, K

Figure 12

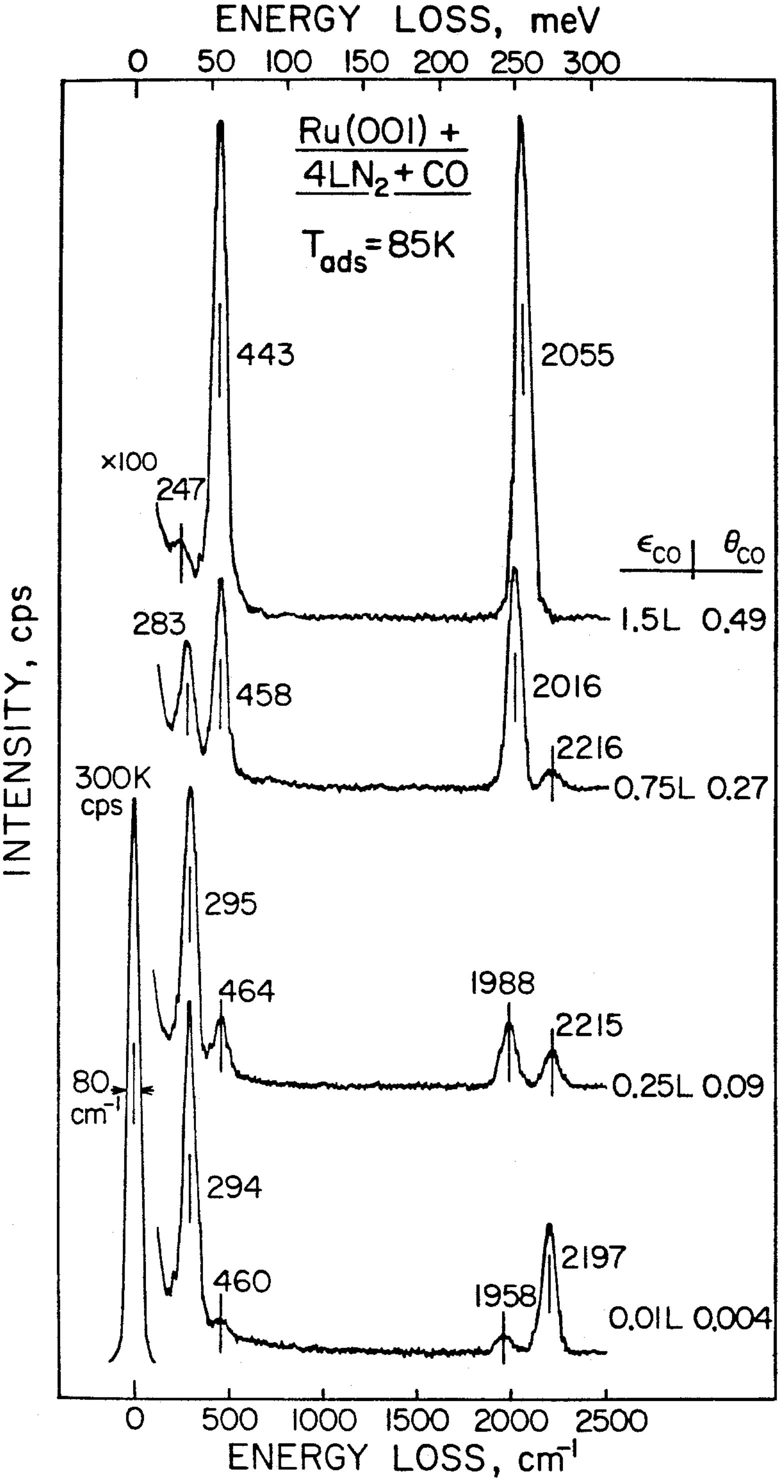
ENERGY LOSS, meV
0
50
100
150
200
250
300
Ru(001) +
4LN$_2$ + CO
T$_{ads}$=85K
443
2055
×100
247
ϵ_{CO} | θ_{CO}
1.5L 0.49
283
458
2016
2216
0.75L 0.27
300K
cps
295
464
1988
2215
0.25L 0.09
80
cm^{-1}
294
2197
460
1958
0.01L 0.004
INTENSITY, cps
0
500
1000
1500
2000
2500
ENERGY LOSS, cm^{-1}

Figure 13

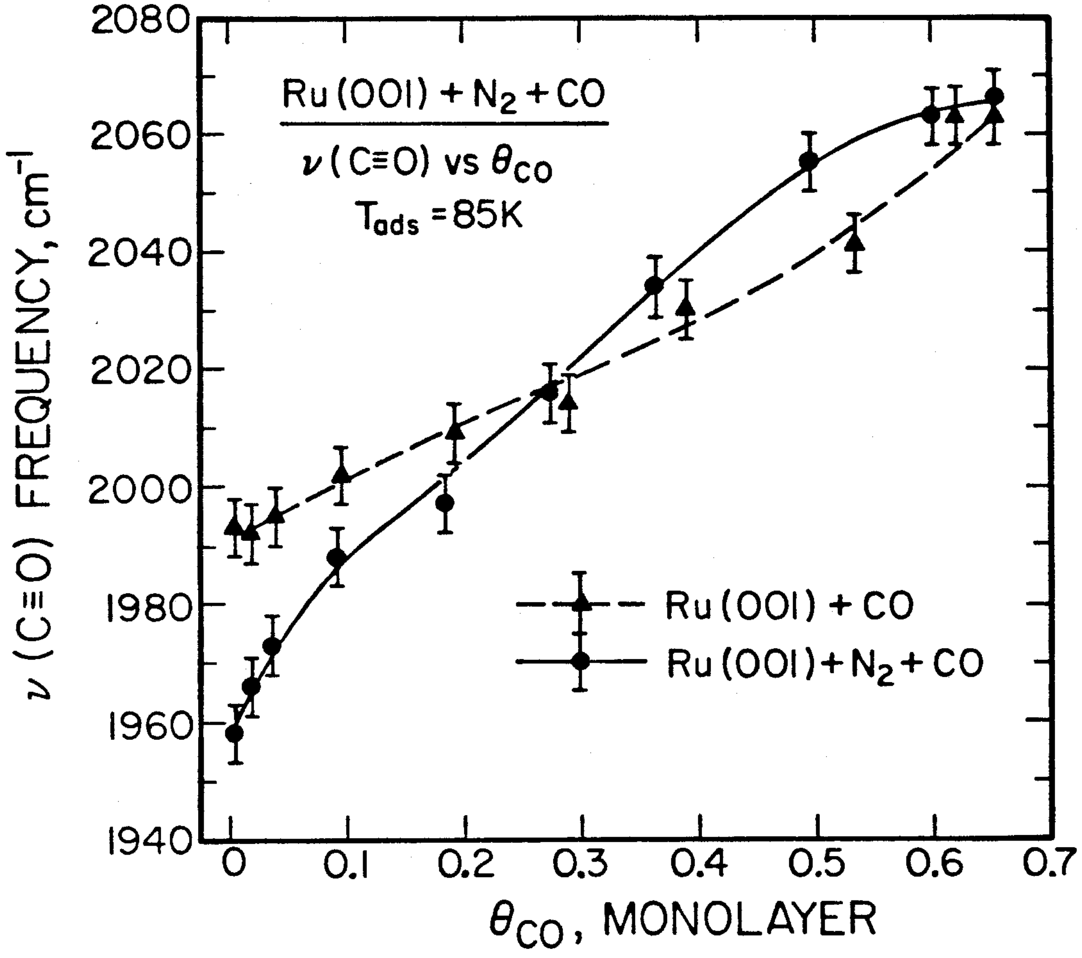

Ru (001) + N_2 + CO
ν (C≡O) vs θ_{CO}
T_{ads} = 85K
Ru (001) + CO
Ru (001) + N_2 + CO
ν (C≡O) FREQUENCY, cm^{-1}
2080
2060
2040
2020
2000
1980
1960
1940
0
0.1
0.2
0.3
0.4
0.5
0.6
0.7
θ_{CO}, MONOLAYER

Figure 14

Chapter V.

End-On and Side-On Bonding of Ketones to Surfaes: Acetone on the Ru(001) and Pt(111) Surfaces

VOLUME 51, NUMBER 8 PHYSICAL REVIEW LETTERS 22 AUGUST 1983

End-On and Side-On Bonding of Ketones to Surfaces: Acetone on the Ru(001) and Pt(111) Surfaces

N. R. Avery,[a] W. H. Weinberg, A. B. Anton, and B. H. Toby
Division of Chemistry and Chemical Engineering, California Institute of Technology, Pasadena, California 91125

(Received 10 February 1983)

High-resolution electron-energy-loss spectroscopy has verified the existence of two fundamentally different types of adsorbed acetone, η^1-bonded acetone on Pt(111) and η^2-bonded acetone on Ru(001). On a Ru(001) surface, the Lewis acidity of which has been increased by the presence of oxygen adatoms, the η^1 and η^2 forms of acetone coexist. The η^1-bonded acetone desorbs molecularly, whereas η^2-bonded acetone is a precursor to dissociation on the surface.

PACS numbers: 68.30.+z, 61.14.-x, 68.20.+t, 82.65.Jv

Previous investigations[1-15] concerning the bonding of prototypical ketones to metal centers in organometallic complexes have provided a qualitatively consistent picture of the effect of the Lewis acidity of a metal on its selectivity toward various possible configurations for the bonding of the ketonic ligands. The advent of high-resolution electron-energy-loss spectroscopy (EELS) for the vibrational analysis of adsorbed overlayers on solid surfaces has rendered feasible incisive studies of the organometallic chemistry of macroscopic, well-defined single-crystalline surfaces[16] and a rigorous comparison to the chemistry of analogous homogeneous complexes. In this Letter, new and unprecedented results are reported concerning the interaction of acetone (a weak donor ligand) with the close-packed Pt(111) and Ru(001) surfaces, as well as the Ru(001) surface on which an ordered $p(2\times 2)$ overlayer[17] of atomic oxygen is present.[18-20] The contrasting bonding configurations and the possible decomposition of acetone observed on these surfaces systematize the chemical effects of relative Lewis acidities of metals,[21] while clarifying the comparative chemistry of these surfaces and their relationship to analogous coordination complexes.

Descriptions of the EEL spectrometers (and the UHV chambers in which they are contained) used for the Ru (Ref. 22) and Pt (Ref. 23) studies have been published previously. A typical resolution in both spectrometers (for a disordered overlayer of low electron reflectivity) is 80 cm^{-1} (full width at half maximum of the elastically scattered electron beam), and optimum resolutions are below 40 cm^{-1}. Atomically clean single-crystalline surfaces were prepared by Ar$^+$ sputtering and chemical cleaning with oxygen followed by high-temperature reductive annealing.[24] The ordered $p(2\times 2)$ overlayer of atomic oxygen on Ru(001) was prepared by exposing the clean surface to 0.8 L of oxygen (1 L = 1 langmuir ≡ 10^{-6} Torr s) at 95 K, followed by thermal ordering at a temperature of approximately 350 K.[18-20] The Pt crystal was exposed to acetone with a directional beam doser consisting of a multichannel array of microcapillaries, whereas the Ru crystal was exposed to acetone by backfilling the UHV chamber. The acetone was degassed with multiple freeze-pump-thaw cycles before use, and its purity was verified *in situ* mass spectrometrically.

EEL spectra for acetone adsorbed on the three surfaces are shown in Fig. 1, and a summary of the surface structures, the measured vibrational frequencies, and the mode assignments is presented in Table I. Spectra obtained for adsorption of $(CD_3)_2CO$ rather than $(CH_3)_2CO$ are shown in Figs. 1(b) and 1(c), since they afford better clarity and resolution of the signature modes critical to the identification of the adsorbed species.

On the Pt(111) surface, the EEL spectrum of adsorbed acetone, shown in Fig. 1(a), exhibits (dipolar enhanced) modes of both A_1 and B_1 symmetry and a down-shifted carbonyl stretching frequency (relative to liquid acetone or acetone multilayers condensed on the Pt and Ru surfaces). Consequently, on Pt(111) acetone is bonded in an η^1 (end on) fashion through the oxygen atom with C_s symmetry (a mirror plane through the plane of the molecule, perpendicular to the surface), and a Pt-O=C bond angle that is less than 180°, as shown in Fig. 2(a). The bonding of the acetone to the Pt(111) surface is typical of a weak donor ligand since the temperature corresponding to the maximum rate of desorption of molecular ace-

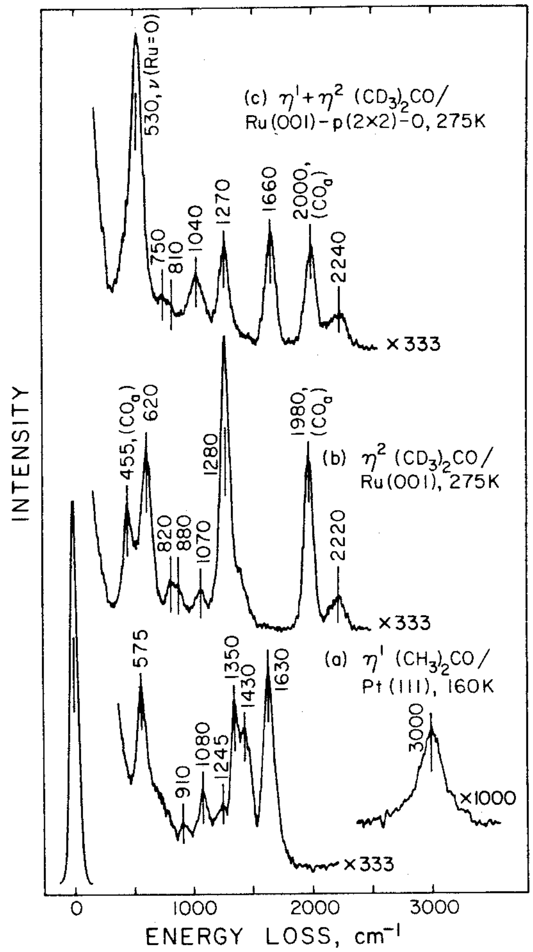

FIG. 1. EEL spectra for (a) a monolayer of $(CH_3)_2CO$ on the Pt(111) surface; (b) a monolayer of $(CD_3)_2CO$ on the Ru(001) surface; and (c) a monolayer of $(CD_3)_2CO$ on the Ru(001) surface with an ordered $p(2\times 2)$ overlayer of oxygen adatoms present. Features at 455 and 1980–2000 cm^{-1} in spectra (b) and (c) are due to adsorbed CO from the onset of decompsotion of the η^2 acetone. All spectra were recorded in the specular direction where dipolar scattering dominates the inelastic electron scattering cross section (Ref. 16).

tone is 185 K, suggesting a binding energy of approximately 11.5 kcal/mol.

It has been recognized for a number of years that acetone can bond coordinately in an η^1 configuration in various organometallic complexes.[1-8] The frequencies observed for η^1 acetone on the Pt surface are in good agreement with those reported previously for homogeneous (monometallic) complexes of η^1-bonded acetone.[1,7,8]. In x-ray diffraction crystallographic structural determinations of Ru complexes of η^1-bonded acetone, the Ru–O=C bond angle ranges from 135° to 153°, and the $Ru{-}O{=}C{-}C_2$ torsional angles are within 7° of planarity.[7,8] The frequency of the carbonyl stretching mode shifts from 1710 cm^{-1} in liquid acetone to approximately 1630 cm^{-1} on the Pt surface and is down shifted similarly in the organometallic complexes of Ru.[7,8] Consequently, especially since the acetone is adsorbed with C_s symmetry, quite similar bonding occurs in η^1-bonded acetone complexes and on the extended, close-packed surface of Pt.

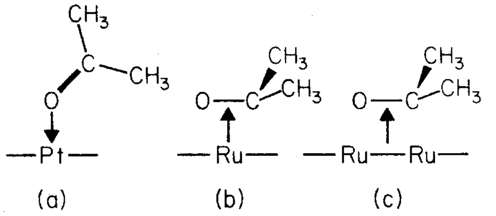

FIG. 2. Schematic bonding configurations for (a) η^1 acetone on Pt(111) and Ru(001) on which a $p(2\times 2)$ oxygen adatom superstructure exists; (b), (c) η^2 acetone on Ru(001).

At 275 K on the Ru(001) surface, a temperature at which all the acetone has desorbed reversibly from Pt, the acetone is bonded in an η^2 (side on) configuration as indicated schematically in Figs. 2(b) and 2(c).[27] This form of adsorbed acetone is identified by a substantially down-shifted carbonyl stretching mode at 1280 cm^{-1}, isopropyl-like rocking modes at 990 and 1170 cm^{-1}, and a skeletal mode at 670 cm^{-1} [at 1280, 820, and 880, and 620 cm^{-1} for $(CD_3)_2CO$, respectively; see Table I and Fig. 1(b)]. The feature at 670 cm^{-1} is due to the π(CO) mode of acetone which is transformed from B_2 to A' symmetry as the symmetry of the acetone skeleton is lowered from C_{2v} to C_s (a mirror plane through the C=O bond, perpendicular to the surface) with the rehybridization of the ketonic carbon atom from sp^2 to nearly sp^3 upon adsorption. This η^2 form of acetone on Ru is a stable intermediate in the decomposition of the acetone. The rapid decomposition of η^2 acetone to adsorbed CO, CH_x fragments ($x \leq 3$), and hydrogen adatoms occurs at temperatures slightly above 275 K.

A number of side-on bonded ketonic and related homogeneous complexes which resemble the η^2-bonded acetone on the Ru(001) surface have been reported.[9-15] In particular, the analogy with two zero-valent complexes of nickel are noteworthy, namely, (hexafluoroacetone)*bis*(triphenylphosphine) nickel(0),[9] and (benzophenone)*bis*(triethylphosphine) nickel(0).[13] An extension of the carbonyl bond length by approximately 0.1 Å in both

TABLE I. Vibrational frequencies (in inverse centimeters) observed with high-resolution electron-energy-loss spectroscopy of η^1 acetone on Pt(111), η^2 acetone on Ru(001), and a mixture of η^1 and η^2 acetone on Ru(001)$p(2\times 2)$-O. [Corresponding frequencies for deuterated acetone, $(CD_3)_2CO$, are given in brackets. The mode assignments, their symmetry types, and the ir and Raman frequencies of liquid acetone are listed as well.]

Mode	Symmetry		ir and Raman of liquid[a]	EELS on Pt(111)	EELS on Ru(001)	EELS on Ru(001)$p(2\times 2)$-O	
	C_{2v}	C_s		η^1	η^2	η^1	η^2
			3004[2255] (*s*)				
$\nu(CH_3)$			2964[2222] (*s*)	3000[2250]	2970[2220]	2970[2240]	2970[2240]
			2924[2111] (*s*)				
$\nu_s(CO)$	A_1	A'	1710[1701] (*vs*)	1630[1630]	1280[1280]	1660[1660]	1280[1270]
			1430[1085] (*s*)	1430		1420[1040]	
$\delta(CH_3)$			1361[1037] (*vs*)	1350[1030]	1370[1070]		1370[1040]
			1356[1036] (*w*)				
ν_a(Me-C-Me)	B_1	A''	1220[1245] (*vs*)	1245[1290]			
			1092 (*m*)		1170[880]	1090	
$\omega(CH_3)$			1066[890] (*m*)	1080	990[820]		960[810]
			902 (*m*)	910		890[750]	
ν_s(Me-C-Me)	A_1	A'	786[695] (*w*)				
$\delta(CO)$	B_1	A''	530[478] (*s*)	575[530]		b	
$\pi(CO)$	B_2	A'	393[331] (*w*)[c]		670[620]		b
δ(Me-C-Me)	A_1	A'	493[410] (*w*)[c]				

[a] Ref. 25.

[b] Obscured by the very strong ν_s (Ru=O) mode at 530 cm^{-1}.

[c] The original assignments of these modes (Ref. 25) have been reversed by Raman polarization measurements (Ref. 26).

complexes is strong evidence of π bonding to the nickel (i.e., π donation and π^* back-donation). If the bonding is thought of in terms of the Dewar-Chatt-Duncanson model,[28,29] then in view of the importance of back-bonding, side-on (π-bonded) ligands are stabilized by electronegative substituents on the ligand which serve to lower the energy of the π^* orbital. There is a concomitant need for "electron rich" metals, i.e., those in low formal oxidation states, to facilitate this type of bonding. This is the reason why only rather recently has η^2-bonded acetone been observed in a low-valent homogeneous Ta complex[15] compared to the earlier observation of an η^2-bonded hexafluoroacetone complex with Ni.[9] This is also the reason why the more "electron rich" Ru surface binds acetone in an η^2 configuration, whereas a geometrically identical surface of Pt does not. The degree of rehybridization of the ketonic carbon atom is similar in the Ta(η^5-C_5Me_5)(η^2-acetone)Me_2 complex ($Me = CH_3$)[15] compared to η^2 acetone on the Ru surface as judged by the carbonyl stretching frequencies, 1200 cm^{-1} in the former and 1280 cm^{-1} in the latter.

If the Lewis acidity of the Ru surface is increased by the adsorption of an ordered $p(2\times 2)$ overlayer of oxygen adatoms (corresponding to a quarter-monolayer surface coverage), the behavior of the (subsequently) chemisorbed acetone is *qualitatively different* from that of acetone on reduced Ru, as is evident from the EEL spectrum in Fig. 1(c). In the presence of the oxygen overlayer, a significant fraction of the adsorbed acetone exists as an η^1 ligand which desorbs *molecularly* near 300 K. This is a consequence of a through-metal depletion of the electron density on the surface Ru atoms due to the presence of the electronegative oxygen adatoms. On this modified Ru surface of greater Lewis acidity, the acetone adsorbs as a donor ligand with a binding energy considerably greater than on the reduced Pt surface. Consequently, the modified surface of Ru behaves similarly, but not identically, to the Pt surface. This fact is also apparent from the coexistence of η^1 and η^2 acetone on the Ru(001)$p(2\times 2)$-O surface [cf. Table I and Fig. 1(c)], whereas the η^2 form of acetone does not exist on reduced Pt.

To summarize, high-resolution EELS measurements have verified the existence of two fundamentally different types of adsorbed acetone, η^1-bonded acetone on Pt(111) and η^2-bonded acetone on Ru(001). On a Ru(001) surface, the Lewis acidity of which has been increased by the presence of oxygen adatoms, the η^1 and η^2 forms of acetone coexist. The η^1-bonded acetone desorbs molecularly, whereas η^2-bonded acetone is a precursor to dissociation to chemisorbed CO, CH_x fragments, and hydrogen. These results systematize the nature of the bonding of (ketonic) organometallic ligands to metal clusters and to metal surfaces, i.e., they provide a quantification of the so-called "metal-cluster, metal-surface analogy." More detailed descriptions and discussions of the results reported here are in preparation.[30, 31]

This research was supported by the National Science Foundation under Grant No. CHE82-06487.

---

[a] Permanent address: Division of Materials Science, CSIRO, Catalysis and Surface Science Laboratory, University of Melbourne, Parkville 3052 Victoria, Australia.

[1] W. L. Driessen and W. L. Groeneveld, Recl. Trav. Chim. Pays-Bas 88, 977–988 (1969).

[2] W. L. Driessen and W. L. Groeneveld, Recl. Trav. Chim. Pays-Bas 90, 258–264 (1971).

[3] K. Jackowski and Z. Kecki, J. Inorg. Nucl. Chem. 39, 1073–1078 (1977).

[4] C. White, S. J. Thompson, and P. M. Maitlis, J. Chem. Soc. Dalton Trans. 1977, 1654–1661.

[5] C. White, S. J. Thompson, and P. M. Maitlis, J. Organomet. Chem. 134, 319–325 (1977).

[6] S. J. Thompson, C. White, and P. M. Maitlis, J. Organomet. Chem. 136, 87–93 (1977).

[7] R. O. Gould, W. J. Sime, and T. A. Stephenson, J. Chem. Soc. Dalton Trans. 1978, 76–79.

[8] M. A. Bennett, T. W. Matheson, G. B. Robertson, W. L. Steffen, and T. W. Turney, J. Chem. Soc. Chem. Commun. 1979, 32–33.

[9] R. Countryman and B. R. Penfold, J. Cryst. Mol. Struct. 2, 281–290 (1972).

[10] D. Walther, Z. Chem. 15, 490–491 (1975).

[11] S. D. Ittel, J. Organomet. Chem. 137, 223–228 (1977).

[12] S. D. Ittel, Inorg. Chem. 16, 2589–2597 (1977).

[13] T. T. Tsou, J. C. Huffman, and J. K. Kochi, Inorg. Chem. 18, 2311–2317 (1979).

[14] W. R. Roper, G. E. Taylor, J. M. Waters, and L. J. Wright, J. Organomet. Chem. 182, C46-C48 (1979).

[15] C. D. Wood and R. R. Schrock, J. Am. Chem. Soc. 101, 5421–5422 (1979).

[16] See, for example, H. Ibach and D. L. Mills, *Electron Energy Loss Spectroscopy and Surface Vibrations* (Academic, New York, 1982); W. H. Weinberg, in *Experimental Methods of Surface Physics*, edited by R. L. Park and M. G. Lagally (Academic, New York, 1983).

[17] In a $p(2\times 2)$ overlayer, both edges of the primitive unit cell of the adsorbate lattice are twice the magnitude of those of the primitive unit cell of the substrate, i.e., the area of the former is four times that of the latter, and the fractional surface coverage is 0.25. For a detailed discussion of surface crystallography, see M. A. Van Hove, W. H. Weinberg, and C.-M. Chan, *Low-Energy Electron Diffraction* (Elsevier, Amsterdam, 1983).

[18] T. E. Madey, H. A. Englehardt, and D. Menzel, Surf. Sci. 48, 304–328 (1975).

[19] G. E. Thomas and W. H. Weinberg, J. Chem. Phys. 69, 3611–3613 (1978).

[20] T. S. Rahman, A. B. Anton, N. R. Avery, and W. H. Weinberg, to be published.

[21] P. C. Stair, J. Am. Chem. Soc. 104, 4044 (1982).

[22] G. E. Thomas and W. H. Weinberg, Rev. Sci. Instrum. 50, 497–501 (1979).

[23] N. R. Avery, Appl. Surf. Sci. 13, 171–179 (1982).

[24] G. E. Thomas and W. H. Weinberg, J. Chem. Phys. 70, 954–961 (1979).

[25] G. Dellepiane and J. Overend, Spectrochim. Acta 22, 593–614 (1966).

[26] J. R. Allkins and E. R. Lippincott, Spectrochim. Acta, Part A 25, 761–764 (1968).

[27] Whether the acetone is bound to a single ruthenium atom as in Fig. 1(b) or is bridging two (or three) ruthenium atoms as in Fig. 1(c) cannot be determined from the high-resolution EELS data.

[28] M. J. S. Dewar, Bull. Soc. Chim. Fr. 18, C74–C79 (1951).

[29] J. Chatt and L. A. Duncanson, J. Chem. Soc. 1953, 2939–2947.

[30] N. R. Avery, to be published.

[31] B. H. Toby, A. B. Anton, N. R. Avery, and W. H. Weinberg, to be published.

Chapter VI.

Adsorption of Acetone both on the Clean Ru(001) Surface and on the Ru(001) Surface Modified Chemically by the Presence of an Ordered Oxygen Adatom Overlayer

Adsorption of Acetone both on the Clean Ru(001) Surface and on the Ru(001) Surface Modified Chemically by the Presence of an Ordered Oxygen Adatom Overlayer

by

A. B. Anton, N. R. Avery,[a] B. H. Toby and W. H. Weinberg*
Division of Chemistry and Chemical Engineering
California Institute of Technology
Pasadena, CA 91125

Submitted to *The Journal of the American Chemical Society*

July 1985

---

[a] Current address: Division of Materials Science, C.S.I.R.O., Catalysis and Surface Science Laboratory, University of Melbourne, Parkville 3052, Victoria, Australia

Abstract

The adsorption of acetone on the clean Ru(001) surface and the Ru(001) surface on which an ordered p(2x2) overlayer of oxygen adatoms is present has been investigated via electron energy loss vibrational spectroscopy and thermal desorption mass spectrometry. On both surfaces two fundamentally different forms of adsorbed acetone coexist at temperatures below approximately 200 K — an η^1 species, bonded end-on through the oxygen atom, and an η^2 species, bonded side-on through both the oxygen atom and the acyl carbon atom. Both of these types of bonding have been identified previously in homogeneous organometallic complexes. On the clean Ru(001) surface, the η^2 species is dominant, with the η^1 species present only in low concentrations. Addition of the p(2x2)O overlayer increases the Lewis acidity of the Ru(001) surface, stabilizing η^1-acetone with respect to η^2-acetone. The η^1 species desorbs molecularly upon heating of the surface, whereas the more strongly bound η^2 species is an intermediate to dissociation. The results are compared with acetone adsorption on the Pt(111) surface and to the chemistry of analogous organometallic coordination complexes. The nature of the bonding on the two Ru(001) surfaces is interpreted in terms of the electronic structures of both the ketonic ligand and the metallic substrate.

I. Introduction

One of the principal aims of organometallic chemistry is to provide an interpretive framework in which the mechanistic details of metal-catalyzed reactions can be understood **(1)**. Reactions are conducted under carefully controlled conditions, and all reactants and products are thoroughly characterized with regard to their structural and chemical properties, both by spectroscopic techniques and by comparison to theoretical descriptions of the metal-ligand bonding interactions which govern their behavior. The stable coordination geometries for reactants, intermediates and products represent local minima on the potential energy surface which describes all the possible metal-ligand interactions for the particular system investigated, and both transition state structures and microscopic reaction mechanisms can often be inferred without ambiguity by this procedure. Our present understanding of metal-assisted chemical reactions in solution is a tribute to, and a direct result of, the success of this type of analysis.

One of the obvious goals of modern surface science research is to extend these results to the understanding of analogous reactions which occur under heterogeneous conditions, catalyzed by (extended) metal surfaces. A similar procedure must be followed, including careful control of reaction conditions and thorough characterization of the metal surface on which the reactions occur. Again, the structures of adsorbed (i.e. coordinated) intermediates can be used to delimit the transition state structure(s) and microscopic mechanism(s) which describe the surface reaction(s) observed. Within this context, it is clear that heterogeneous catalysis is in fact the organometallic chemistry of extended metal surfaces, and, as one might expect, results obtained for metal-ligand interactions in homogeneous systems prove to be very valuable in the interpretation of results obtained on metal surfaces.

The success of this approach for both homogeneous and heterogeneous systems relies on the ability to determine experimentally the structures of coordinated reaction intermediates. In homogeneous studies, stable products can often be separated, purified and crystallized, allowing detailed deduction of chemical bond lengths and bond angles via X-ray crystallography **(2)**. The surface sensitive analogue, low-energy electron diffraction (LEED) **(3)**, can be applied most easily to systems where a single reaction intermediate is formed in a translationally periodic, two-dimensional lattice on a single crystalline metal surface **(4)**. Even on single crystalline metal surfaces, more than one intermediate is frequently formed with no long-range order to facilitate a LEED analysis. Thus other approaches must be taken to identify surface structures. Of the various spectroscopic techniques available presently for the identification of reaction intermediates on surfaces, both the sensitivity and the wide spectral range of high resolution electron energy loss vibrational spectroscopy (EELS) make it arguably the most powerful tool for chemical analysis of adsorbed species on well characterized surfaces of low area **(5)**. Although the structural information provided by vibrational spectroscopy does not directly measure bond lengths and bond angles, it does identify both the nature of the bond and the bond order, and through application of the selection rules appropriate to EELS on metal surfaces **(6)**, the chemical identity and orientation of adsorbed species can be determined. With this type of information at hand, a rigorous comparison of the chemistry of extended metal surfaces to that of corresponding organometallic complexes can be made.

This paper reports results obtained via EELS and thermal desorption mass spectrometry for the interaction of acetone with the clean Ru(001) surface and the Ru(001) surface on which there is an ordered p(2x2) overlayer of oxygen adatoms **(7)**. The results help to quantify the relationship between the Lewis acidity of a metal surface and its selectivity toward both reactive and nonreactive bonding configurations of adsorbed acetone, providing an enlightening comparison of the chemistry of these surfaces to the chemistry of analogous organometallic complexes **(8)**.

The interaction of acetone and similar substituted ketones, R_1R_2CO, with metal centers in homogeneous systems has been the subject of a number of investigations. Two general classes of bonding configurations have been identified, characterized structurally, and correlated with the electronic properties of both the (R_1,R_2) substituents of the ketonic ligands and the metal centers to which they bond. Electron deficient metals (those in high formal oxidation states, for example) and weakly electronegative substituents (such as the CH_3 groups of acetone) generally facilitate bonding via σ-donation from the ligand to the metal to produce an η^1(O) configuration (bonded end-on to the metal through the oxygen atom and hereafter referred to as η^1) **(9-12)**. In this case, the metal serves as a weak Lewis acid and accepts an electron pair from the ketonic ligand. For metals weakly basic in the Lewis sense, i.e. those in a low formal oxidation state, or for ketonic ligands with more electronegative substituents (R_1,R_2 = H,CF_3,Ph), an η^2(O,C) configuration (bonded side-on to the metal through both the carbon and oxygen atoms and hereafter referred to as η^2) occurs **(13-20)**. This type of interaction, first described by Dewar, and by Chatt and Duncanson **(21)**, results from simultaneous donation of electrons from the π orbital of the ligand to the d orbitals of the metal and backdonation of metal d electrons to the π^* antibonding orbital of the ligand. This is a general feature of the interaction of many unsaturated ligands with metals **(22-24)**. The understanding of conditions prevailing at metal surfaces which yield selectively these two types of coordination interactions is an important and worthwhile pursuit. For example, η^1-carbonyl ligands are quite labile and nonreactive, exchanging easily in solution with other more tightly bound ligands **(10)**, whereas η^2 bonding is postulated to be important in the formation of reactive intermediates in heterogeneously catalyzed reactions such as Fischer-Tropsch synthesis **(25)**.

Although several investigations of acetone adsorption on metal surfaces have appeared in the literature **(26,27)**, only one report has presented an unequivocal determination of the binding configurations of acetone on a single crystalline metal surface **(27)**. In this case of acetone adsorption on the clean Pt(111) surface, EELS and thermal desorption mass spectrometry were used to identify an η^1 species which desorbed reversibly and a small concentration of an η^2 species, some of which decomposed upon heating the crystal. These results provide a particularly useful contrast and comparison to the results reported here for the adsorption of acetone on the Ru(001) and Ru(001)-p(2x2)O surfaces.

II. Experimental Procedures

A description of the EEL spectrometer and the ultrahigh vacuum (UHV) system in which it is contained has been published previously **(28)**. EEL spectra were recorded at a resolution of approximately 80 cm^{-1} (full-width at half-maximum) with a maximum count rate of 10^5 c.p.s. in the specularly reflected, elastically scattered electron beam. Beam kinetic energies at the sample were between approximately 5 and 6 eV.

The Ru(001) surface was cleaned by thermal cycling between 400 and 1100 K in 10^{-7} Torr of oxygen to remove surface impurities, followed by reductive annealing in vacuum at 1750 K **(29)**. Occasional Ar^+ sputtering was also used to clean the surface. Surface cleanliness was monitored via EELS and thermal desorption mass spectrometry, and the surface was judged clean when the EEL spectrum was featureless, and the peak positions and intensities in thermal desorption spectra for various coverages of CO were reproduced. The ordered p(2x2) overlayer of oxygen adatoms, with an ideal surface coverage of 0.25 monolayer, was prepared by exposing the clean surface to 0.8 L oxygen (1L = 10^{-6} Torr-s) at 95 K, followed by thermal ordering at a temperature of approximately 350 K **(7,30)**.

The $(CH_3)_2CO$ and $(CD_3)_2CO$ used in the experiments were degassed with multiple freeze-pump-thaw cycles, and their purities were verified *in situ* via mass spectrometry. The isotopically labeled compounds, $^{18}O_2$ and $(CD_3)_2CO$, were >99% purity in their specified isotopes. The crystal was exposed to all gases by backfilling the UHV chamber through leak valves, and exposures quoted in the text were measured with a Bayard-Alpert ionization gauge uncorrected for relative ionization cross sections.

Thermal desorption measurements were made in a line-of-sight mode with a UTI 100C quadrupole mass spectrometer, oriented approximately 40° from the surface normal. Surface coverages of hydrogen and CO reported for the (reaction product) thermal desorption measurements were obtained by comparing the time integrated ion current for the desorption spectra to those obtained for desorption of known coverages of hydrogen **(31)** and CO **(32)**. The accuracy in this comparison is approximately ±10%.

Since the adsorbed overlayers were prepared by backfilling the UHV chamber, exposing uniformly all cold surfaces in the chamber to the particular adsorbate, and since the mass spectrometer had no provision for selective sampling of the single crystalline surface, the features in the thermal desorption spectra associated with desorption from the crystal surface were superposed on a broad background signal due to desorption from all other chilled surfaces which are warmed during the collection of a thermal desorption trace. This is a particularly important consideration for a species such as acetone which condenses in

UHV at liquid nitrogen temperatures. In the apparatus used for the experiments reported here, the Ru(001) sample was supported by two 0.020 in. diameter tantalum wires which were spotwelded to its rear face and clamped by two 0.109 in. diameter copper wires to form an electrical current path through the sample. The copper wires were in contact with a liquid nitrogen reservoir to provide conductive cooling of the sample, and heating was accomplished by conduction of heat generated almost totally by the tantalum wires to the sample as an electric current was passed through the sample via the copper and tantalum support leads. The heavy copper leads were also warmed by conduction of heat from the tantalum support wires, but their temperature lagged well behind that of the Ru(001) sample. The net result of these effects, then, for a thermal desorption spectrum of mass spectrometer signal intensity versus sample temperature for acetone desorption, was to yield first a small, narrow signal burst at the beginning of the temperature ramp due to desorption from the rapidly heated tantalum leads, then features at their characteristic temperatures for desorption from the Ru(001) surface, superposed on a broad, slowly varying background due to desorption of condensed acetone from the slowly warming copper leads. For rather sharp desorption features, as were observed in the thermal desorption spectra for the H_2 and CO decomposition products, the background baselines in the spectra can be identified unambiguously, and the contribution due to desorption from the Ru(001) surface can be separated clearly. For broad features, however, as were observed for the desorption of molecular acetone from both the clean Ru(001) and the Ru(001)-p(2x2)O surfaces, the baselines were less certain. In all thermal desorption spectra presented below, the sharp burst at low temperatures and best estimates of the baselines due to background desorption have been subtracted for a more useful illustration of the experimental results. For the molecular acetone desorption spectra of Figs. 1 and 2, however, the uncertainty in the amplitudes of the broad feature which extends from approximately 200 to 450 K prevents a quantitative determination of the total amounts of acetone desorption in the spectra. The qualitative differences in the spectra, to be discussed later, namely the increased amount of molecular desorption from the Ru(001)-p(2x2)O surface for a given acetone exposure as compared to the clean surface, are reliable and are the most noteworthy results evident in Figs. 1 and 2.

III. Results

A. Thermal Desorption Spectra of Acetone from the Clean Ru(001) and the Ru(001)-p(2x2)O Surfaces

Thermal desorption spectra recorded after the indicated exposures of the clean Ru(001) surface to $(CH_3)_2CO$ at 80 K are shown in Fig. 1. For exposures below 4 L, almost no molecular acetone desorption is observed. For exposures of 4 L and above, however, a broad feature with a desorption rate maximum near 220 K, shifting with increasing exposure to 180 K for a monolayer saturation exposure, is observed. A peak due to the formation of a condensed multilayer appears at 140 to 150 K for exposures greater than 7 L. This multilayer state first appears at exposures below that necessary to saturate the monolayer state, suggesting that some "clustering" may occur, as has been observed in the thermal desorption spectra of H_2O from the Ru(001) surface **(33)**. No evidence for a "second layer" desorption state, like that observed for acetone adsorption on Pt(111) **(27)**, can be extracted unambigously from the thermal desorption spectra of Fig. 1, although some evidence for such a state is observed in the EELS results to be presented below.

Noteworthy is the "tailing" of the monolayer desorption feature from its desorption rate maximum near 200 K to approximately 400 K. This indicates a broad range of binding energies for the monolayer molecular species, due perhaps to repulsive interactions which lower its binding energy at high coverages and are relieved as desorption progresses, or to attractive interactions of acetone with surface species present at higher temperatures (and lower surface coverages).

A series of thermal desorption spectra for exposures equal to those of Fig. 1, but instead on the Ru(001)-p(2x2)O surface, are shown in Fig. 2. Although qualitatively similar, several quantitative differences are apparent: more molecular acetone is evolved in the temperature range between 200 and 450 K for all exposures; two rate maxima for monolayer desorption, near 180 and 200 K, are observed; and the multilayer feature is clearly evident for lower exposures, appearing first at 7 L.

B. Thermal Desorption Spectra of the Decomposition Products, CO and H_2, from the Clean Ru(001) and the Ru(001)-p(2x2)O Surfaces

Hydrogen and CO are the only products of the decomposition of $(CH_3)_2CO$ on the clean and the Ru(001)-p(2x2)O surfaces, as detected by thermal desorption spectra. The desorption spectra recorded for these products are shown in Figs. 3 and 4 following multilayer exposures (15 L) of both surfaces to $(CH_3)_2CO$ at 80 K. For comparison, spectrum (a) of Fig. 3 shows desorption of CO from the clean Ru(001) surface following exposure to 0.5 L CO [θ_{CO} adsorbed CO molecules per ruthenium surface = 0.20], and spectrum (a) of Fig. 4 shows desorption of H_2 from the clean Ru(001) surface following exposure to 4 L H_2 [θ_H = 0.85]. For spectra (c) of both Figs. 3 and 4, p(2x2)O overlayers were produced via adsorption of $^{18}O_2$ to allow separate detection of the CO produced by the decomposition of adsorbed $(CH_3)_2CO$, appearing at m = 28 amu, and that produced by reaction of adsorbed carbon from CH_3 decomposition with the ^{18}O of the p(2x2)O overlayer, appearing at m = 30 amu. Furthermore, this increases the sensitivity of the thermal desorption measurement to H_2O (m = 20 amu), which might be expected to be a product of the reaction of $(CH_3)_2CO$ with the Ru(001)-p(2x2)O surface. However, no $H_2{}^{18}O$ was detected under any circumstances.

The CO evolution from a saturated monolayer of $(CH_3)_2CO$ on the clean Ru(001) surface, shown in Fig. 3(b), yields $\theta_{CO} = 0.12$, and, since no CO_2, H_2O or other oxygen-containing desorption products were observed, this demonstrates that the clean surface is active for the decomposition of approximately one-eighth of a monolayer of adsorbed acetone. This is to be compared with the m = 28 amu spectrum below it for the same exposure on the Ru(001)-p(2x2)O surface, Fig. 3(c), where $\theta_{CO} = 0.02$. Obviously, the presence of the ordered oxygen overlayer decreases the decomposition activity of the Ru(001) surface by a factor of approximately six.

Proper stoichiometry in the overall surface decomposition reaction,

$$(CH_3)_2CO + 2{}^{18}O \rightarrow CO + 3H_2 + 2C^{18}O$$

would suggest that $\theta_{C^{18}O}$ for the m = 30 amu desorption spectrum of Fig. 3(d), should be equal to 0.04 rather than 0.03. This discrepancy may be a result of an inaccurate baseline determination in the spectra, or more likely is due to slight ($\theta_{CO} = 0.05$) adsorption of background CO (m = 28 amu) from the chamber ambient during exposure to $(CH_3)_2CO$, making θ_{CO} for the associated m = 28 amu spectrum [Fig. 3(c)] larger than the value of 0.015 necessary by stoichiometry to match the $\theta_{C^{18}O} = 0.03$ of the m = 30 amu spectrum.

The m = 30 amu desorption spectrum of Fig. 3(d) identifies the temperature range over which adsorbed carbon and oxygen react to form and evolve CO, i.e. between approximately 400 and 700 K. The absence of CO desorption in this temperature range for the m = 28 amu spectra confirms that no carbon-oxygen bond cleavage occurs in the decomposition of adsorbed acetone.

The m = 28 amu desorption spectra of Fig. 3(b) and (c) for the clean Ru(001) and the Ru(001)-p(2x2)O surfaces have the temperatures corresponding to their maximum desorption rates downshifted from 490 K, shown in the clean surface CO desorption spectrum of Fig. 3(a), to 470 and 455 K, respectively. This can be attributed to interactions between the adsorbed CO molecules and adsorbed hydrocarbon fragments **(34)** and the oxygen adatoms of the p(2x2)O overlayer **(35)**.

Comparison of the thermal desorption spectrum (b) of Fig. 4, which shows H_2 evolution from a saturated monolayer of $(CH_3)_2CO$ on the clean Ru(001) surface, to that of Fig. 4(c) for the same exposure on the Ru(001)-p(2x2)O surface shows an approximate sevenfold decrease in the amount of acetone decomposition upon the addition of the oxygen overlayer to the Ru(001) surface, a value that is consistent, within experimental uncertainties, with the results shown previously in Fig. 3. Furthermore, the hydrogen coverages, obtained by comparison to the spectrum of Fig. 4(a) for desorption from a saturation exposure of the clean surface to H_2, compare well with the values expected on the basis of the corresponding observed CO coverages and the stoichiometry expected from the aforementioned surface decomposition reaction, i.e. $\theta_H = 6 \times \theta_{CO} = 0.72$ and 0.12, respectively.

The peak shapes of the thermal desorption spectra shown in Figs. 4(b) and (c) are of particular interest. Comparison to results of thermal desorption measurements for coadsorbed overlayers of CO and hydrogen on Ru(001) **(36)** indicates that the H_2 desorption features appearing in Fig. 4(b) between 280 and 450 K are due solely to the recombination of hydrogen adatoms on the Ru(001) surface in the presence of coadsorbed CO. The series of weak features between approximately 450 and 750 K are due to the decomposition of adsorbed hydrocarbon fragments which result from the decomposition of adsorbed acetone. In Fig. 4(c), the sharp feature at 220 K is due to hydrogen adatoms recombining in the presence of adsorbed oxygen, its shape and peak temperature depending sensitively on the presence of the p(2x2)O overlayer **(37)**. Features above 250 K in this spectrum, representing slightly more than half of the total yield of hydrogen from the surface, are due to the decomposition of adsorbed hydrocarbon fragments from acetone decomposition in this temperature range.

Also noteworthy is the absence of H_2O production from the decomposition of $(CH_3)_2CO$ in the presence of the p(2x2)O overlayer. Although evidence for the reaction of ***disordered***, adsorbed oxygen with hydrogen on Ru(001) to evolve H_2O has been obtained in the thermal decomposition of adsorbed HCOOH **(38)**, thermal desorption measurements recorded following hydrogen adsorption on the Ru(001)-p(2x2)O surface produce no H_2O, only desorption of H_2 **(37)**. Thus, the relative probability of H_2O production versus H_2 desorption depends sensitively on the long-range order of the oxygen overlayer. This can be explained by consideration of two important effects of oxygen order on these reactions, both of which act to make hydrogen adatom recombination and desorption more likely. First, the formation of the ordered p(2x2)O overlayer upon the annealing of a disordered overlayer of adsorbed oxygen **(7,30)** indicates that attractive interactions which increase the Ru=O binding energy are maximized in the p(2x2) configuration, increasing the energy barrier to abstraction of adsorbed oxygen by reaction with hydrogen. Second, the p(2x2)O overlayer ***destabilizes*** adsorbed hydrogen into a new binding state with an activation energy of desorption below 9 kcal/mole, desorbing near 220 K, as compared with the clean surface state, desorbing near 400 K with an activation energy of desorption of approximately

17 kcal/mole **(31)**.

C. EELS of Acetone on the Clean Ru(001) Surface

Exposures of the Ru(001) surface to 15 L or more of acetone at 95 K produces EEL spectra typical of the condensed species and virtually identical to the multilayer spectra reported for acetone adsorption on Pt(111) **(27)**. The modes observed for multilayer $(CH_3)_2CO$ and their assignments based on a comparison with the IR and Raman spectra of liquid acetone **(39)** are listed in Table 1.

The EEL spectra for the monolayer states of acetone both on the clean Ru(001) and the Ru(001)-p(2x2)O surfaces show evidence for species coordinated both in η^1 and η^2 configurations. Before attempting to assign the spectra, however, a review of the vibrational structure expected for both of these species will be helpful.

Consideration of the σ-bonding interaction which leads to coordination in an η^1 configuration, to be discussed later, indicates that little perturbation of the structure of the acetone skeleton from that of the free molecule is expected in the η^1 configuration, depicted in Fig. 5(a). This is manifest in the vibrational spectra of η^1-acetone complexes by a preservation of the polarizations and only a weak perturbation of the frequencies of the methyl and nearly all of the skeletal vibrations of free acetone **(27)**. The only strongly affected mode is the ν(CO), which is red-shifted from its free acetone value of 1711 cm^{-1} to near 1650 cm^{-1} in a range of organometallic complexes of the type $\{[(CH_3)_2CO]_6M\}^{2+}$ **(9)**, to 1661 cm^{-1} **(11)** and 1665 cm^{-1} **(12)** in two η^1-acetone complexes of ruthenium, and to 1630 cm^{-1} for η^1–$(CH_3)_2CO$ adsorbed on the Pt(111) surface **(27)**. The presence of a carbonyl band in this frequency range and methyl vibrations at frequencies characteristic of free acetone in the EEL spectra identify unambiguously the presence of η^1-acetone. The appearance in the spectra of other unperturbed skeletal vibrations with polarizations well defined with respect to the symmetry properties of the acetone skeleton $-\nu_a(CCC)$, $\nu_s(CCC)$, $\delta(CO)$, $\delta(CCC)$ and $\pi(CO)$ — will depend on the orientation of the adsorbed acetone skeleton with respect to the surface plane through consideration of the "dipolar selection rules" for adsorbate vibrations **(40)**. Such considerations can be used to determine the symmetry of the η^1 surface complex **(27)**.

The vibrational spectrum expected for acetone coordinated in an η^2 configuration is not so well defined. Several η^2 configurations have been identified in the homogeneous chemistry of ketonic-like ligands with the general formula R_1R_2CO, including rigid three-membered rings with single metal centers, as in Fig. 5(b) [e.g. $R_1=R_2=H$, M=Os **(13)**, M=Fe **(14)**; $R_1=R_2=CF_3$, M=Pt **(15)**, M=Ni **(16,17)**; and $R_1=R_2=CH_3$, M=Ta **(18)**]; a rigid four-membered ring with two metal centers, as in Fig. 5(c) [$R_1=R_2=CF_3$ and $M_1=M_2=Pt$ **(19)**]; and a perpendicular bridge (μ–η^2) configuration where the carbon-oxygen bond of the ligand bisects the bond between the two metal atoms, as in Fig. 5(d) [e.g. $R_1=CH_3$, $R_2=H$ and $M_1=M_2=Mo$ **(20)**]. Any of these configurations must be considered a possible product of the interaction of acetone with the Ru(001) surface. Those complexes which have been characterized by vibrational spectroscopy show bands ascribed to $\nu(CO)$ in the range 1017 to 1220 cm^{-1} **(13,14,18)**, signifying in all cases a substantial lowering of the carbon-oxygen bond order of the free ligand from two to nearly one upon coordination and rehybridization of the ketonic carbon from sp^2 to nearly sp^3. Those complexes characterized by an X-ray structural analysis show C-O bond lengths between 1.32 and 1.59 Å and significant deviation of the R_1–C–R_2 plane and the C-O bond from the coplanar configurations of the free ligands **(13,17,19,20)**. This is indicative of the rehybridization of the ketonic carbon which occurs as a result of electron donation to the π^*_{CO} antibonding orbital of the ligand in all of these configurations. Consequently, an adsorbed η^2-acetone should display a C-O vibration that is red-shifted by several hundred wavenumbers from that of the η^1 species and skeletal vibrations that are consistent with the rehybridization of the ketonic carbon to nearly sp^3.

With this framework established, the results of the EELS experiments can now be interpreted. Figures 6 and 7 show EEL spectra recorded after exposure of the clean Ru(001) surface at 95 K to 6 L $(CH_3)_2CO$ and 6 L $(CD_3)_2CO$, respectively, followed by momentary annealing at the indicated temperatures and recooling to 95 K to record the spectra. Assignments of the surface species that are identified are listed in Table 1.

Spectrum (a) of Fig. 6, recorded immediately after adsorption at 95 K, shows strong modes at 2950, 1395, 1050 and 905 cm^{-1} due to the ν, δ and ω modes of the CH_3 groups of adsorbed $(CH_3)_2CO$. The shoulder at 1620 cm^{-1}, its apparent position red-shifted somewhat from its true position by overlap with the tail of the strong $\delta(CH_3)$ band, signifies the existence of some $(CH_3)_2CO$ adsorbed in an η^1 configuration. The ν, δ and ω modes of CH_3 appear with intensity too great to be attributed solely to the η^1 species identified by $\nu(CO)$ at 1620 cm^{-1}, however, and must therefore result from the presence of another adsorbed species which coexists with $\eta^1-(CH_3)_2CO$ at this temperature and exposure. The appearance of clustering in the monolayer, as evidenced by the thermal desorption results discussed previously, and the identification of a "second-layer" state in the thermal desorption spectra for acetone adsorption on Pt(111) **(27)** suggest that the "extra" intensity in these features may be due to the onset of adsorption into the multilayer (or alternatively, a second layer) state at this exposure. A correspondingly strong feature due to the $\nu(CO)$ mode of A_1 symmetry of the multilayer species, expected at 1720 cm^{-1} (cf. Table 1), is conspicuously absent, indicating via the dipolar selection rule that the molecules in this state are oriented with their molecular planes nearly parallel to the surface. This interpretation is substantiated by the presence of a weak mode at 400 cm^{-1}, which can be assigned most readily to the B_2 π(CO) vibration of the same second or multilayer species. The mode at 515 cm^{-1} and the poorly resolved feature labeled at 825 cm^{-1} are due to the B_1 δ(CO) and A_1 ν_s(CCC) vibrations of η^1–$(CH_3)_2CO$, respectively, and the feature at 655 cm^{-1} is the first indication of the presence of an η^2 species.

Annealing the surface to 200 K produces spectrum (b) of Fig. 6. Substantial desorption has occurred [note the change of scale between spectra (a) and (b)], but a small amount of η^1–$(CH_3)_2CO$ remains, as evidenced by the presence of ν(CO) near 1620 cm^{-1}, $\omega(CH_3)$ at 890 cm^{-1} and ν_s(CCC) at 780 cm^{-1}. New bands associated with η^2–$(CH_3)_2CO$ appear near 995 and 1130 cm^{-1}, the feature near 650 cm^{-1} gains intensity relative to the other modes in the spectra, and the broad band associated with $\delta(CH_3)$ shifts noticeably from 1395 to 1350 cm^{-1}. Some decomposition is evidenced by bands near 470 and 2000 cm^{-1} due to ν(RuC) and ν(CO) of adsorbed CO **(29)**.

Before proceeding further with the $(CH_3)_2CO$ spectra, the corresponding behavior in the $(CD_3)_2CO$ spectra of Fig. 7 should be addressed. The presence of η^1–$(CD_3)_2CO$ in spectrum (a) at 95 K is revealed by the ν(CO) mode at 1665 cm^{-1} and the A_1 ν_s(CCC) mode at 715 cm^{-1}. Again, the methyl vibrations — $\nu(CD_3)$ at 2210 and 2090 cm^{-1}, $\delta(CD_3)$ at 1030 cm^{-1}, and $\omega(CD_3)$ near 920 cm^{-1} — appear with anomalously high intensity compared to the ν(CO) mode at 1665 cm^{-1}, suggesting the presence of a second layer species, and the B_2 π(CO) of the latter is visible at 360 cm^{-1}. Other modes at 1260 and 495 cm^{-1} can be assigned to the B_1 ν_a(CCC) and B_1 δ(CO) modes of η^1–$(CD_3)_2CO$, respectively. Heating the surface to 200 K initiates decomposition, desorbs most of the η^1–$(CD_3)_2CO$, and reveals features due to η^2–$(CD_3)_2CO$ near 1260, 890, 800 and 590 cm^{-1}.

The EEL spectra of η^2–$(CH_3)_2CO$ and η^2–$(CD_3)_2CO$ are developed fully after annealing the surface to 275 K and are shown in Figs. 6(c) and 7(c), respectively, with assignments of these spectra listed in Table 1. The band at 1300 cm^{-1} in the $(CH_3)_2CO$ spectrum, which is barely resolved from the $\delta(CH_3)$ band at 1370 cm^{-1}, and the band at 1275 cm^{-1} in the $(CD_3)_2CO$ spectrum are assigned to the $\nu(CO)$ mode of η^2-acetone, red-shifted by over 400 cm^{-1} from $\nu(CO)$ for free acetone and implying considerable skeletal reorganization in this bonding configuration. This significant rehybridization of the ketonic carbon atom from sp^2 toward sp^3, analogous to that observed in the η^2 complexes of related ligands described earlier, reduces the C-C-C bond angle of acetone toward a tetrahedral configuration, which is manifest in two other features of the η^2-acetone spectra. First, the $\omega(CH_3)$ modes typical of free and η^1–$(CH_3)_2CO$, expected near 900 and 1100 cm^{-1} (cf. Table 1), are replaced by a strong band at 980 cm^{-1} and a weaker band at 1170 cm^{-1} in the spectrum of η^2–$(CH_3)_2CO$. This is a result of strong coupling between the methyl rocking modes and the C-C stretching mode of a CH_3 group bonded to an sp^3 carbon atom, and is typical of isopropyl and tertbutyl configurations **(41)**. In isopropyl alcohol, for example, similar coupling leads to a strong band at 950 cm^{-1} and a weaker band at 1140 cm^{-1} **(42)**. As a result of this coupling, CH_3 rocking modes often do not yield good group frequencies, and the disparity between the frequencies of the coupled rocking modes in isopropyl alcohol and in η^2–$(CH_3)_2CO$ is of lesser significance than the fact that a strong band in the 900-1000 cm^{-1} region is expected for this type of structural configuration. In the spectrum of η^2–$(CD_3)_2CO$, the difference in frequency between the $\omega(CD_3)$ modes and the C-C stretching vibrations precludes strong coupling, and the $\omega(CD_3)$ modes appear with low intensity at 820 and 880 cm^{-1}, close to the values obtained for the corresponding vibrations of free $(CD_3)_2CO$. The second manifestation of the skeletal reorganization in η^2-acetone is the appearance of the band at 655 cm^{-1} for η^2–$(CH_3)_2CO$ and at 610 cm^{-1} for η^2–$(CD_3)_2CO$, which develops concomitantly with the other features ascribed to the η^2 species. This band is assigned to an O-C-C_2 angle bending vibration, which may be regarded as being derived from the weak π(CO) mode of free acetone at 393 cm^{-1} for $(CH_3)_2CO$ and 331 cm^{-1} for $(CD_3)_2CO$, respectively. With both the oxygen and carbon atoms of the carbonyl function bonded to the ruthenium surface in the η^2 configuration, this mode corresponds to motion of the two methyls in unison up-and-down against the surface.

Further evidence justifying the assignment of bands near 655 and 1300 cm^{-1} in the η^2-acetone spectra to the signature skeletal vibrations can be obtained by consideration of the spectra shown in Fig. 8. The bottom spectrum, recorded in the specular direction where dipolar inelastic scattering is dominant, is identical to that shown in Fig. 6(c). The top spectrum, recorded with the EELS analyzer rotated 6° toward the surface normal from the specular direction, is expected to show enhancement of features which include a significant contribution from (short-range) impact inelastic scattering relative to the (long range) dipolar scattering. As has been shown previously, impact scattering is significant only for vibrational modes dominated by hydrogen or deuterium motion at the electron beam kinetic energy employed in these measurements **(6)**. Thus the top spectrum of Fig. 8 should show enhancement of the CH_3 modes relative to the skeletal modes. As may be seen, the ν(CO) and π(CO) modes at 1300 and 655 cm^{-1}, respectively, as well as the dipolar modes due to chemisorbed CO at 475 and 1970 cm^{-1}, have lost intensity relative to $\nu(CH_3)$ at 2955 cm^{-1}, $\delta(CH_3)$ at 1370 cm^{-1}, and $\omega(CH_3)$ at 1170 and 980 cm^{-1}, confirming the previous assignments and the correspondence indicated between the spectra for η^2–$(CH_3)_2CO$ and η^2–$(CD_3)_2CO$.

The dipolar selection rule for adsorbate vibrations indicates that only those vibrations which involve a component of motion perpendicular to the surface plane, i.e. only those modes which belong to the totally symmetric representation of the point symmetry group of the adsorbate-substrate complex, should couple to the incident EELS beam to produce inelastic scattering via the dipolar mechanism **(6)**. One might then ask why such a strong loss feature is observed for the ν(CO) mode of η^2-acetone, which for all possible η^2 configurations depicted in Fig. 5 is polarized nearly parallel to the surface. First, the highest point group symmetry attainable by each of the possible η^2-acetone configurations is C_s, which results when a mirror symmetry plane exists through the carbon-oxygen bond perpendicular to the surface. In this case, the A_1 ν(CO) mode of free acetone (point group C_{2v}) transforms to the A' representation of the C_s adsorbate complex and is dipolar active by symmetry considerations alone. Furthermore, the population of the π^*_{CO} orbital of η^2-acetone varies with the carbon-oxygen bond length, causing charge flow to-and-from the surface as the carbon-oxygen bond vibrates, producing the strong dynamic dipole which leads to the intense inelastic scattering observed for this mode. Comparable effects have been observed for similar parallel modes of C_2H_2 and C_2H_4 [ν(CC)] on Pt(111) **(43)**, $(CH_3)CN$ [ν(CN)] on Pt(111) **(44)**, and O_2 [ν(OO)] on Pt(111) **(45)** and Ag(110) **(46)**.

No distinction between configurations such as (b), (c) or (d) of Fig. 5 for η^2-acetone on Ru(001) can be made on the basis of the EELS results. Each would be expected to give methyl and skeletal vibrations similar to those observed and would differ only in the low frequency vibrations which represent motion of the bonds which coordinate the acetone molecule to the ruthenium surface atoms. These modes are not resolved in the EEL spectra, and no vibrational data in this frequency range for model complexes are available to allow a useful diagnostic comparison. The details of the η^2 coordination geometry are, of course, far less significant than the fact that η^2 coordination occurs.

Further heating of the Ru(001) surface to 310-315 K results in an attenuation of the features due to η^2-acetone and an increase in the intensities of the features due to adsorbed CO resulting from decomposition of η^2-acetone [cf. Figs. 6(d) and 7(d)]. Finally, after heating to 340 K, the EEL spectrum of the decomposition products of η^2–$(CH_3)_2CO$, shown in Fig. 6(e), displays broad, weak bands at 825, 1120, 1370 and 2945 cm^{-1} due to CH_x ($x \leq 3$) hydrocarbon fragments.

D. EELS of Acetone on the Ru(001)-p(2x2)O Surface

Exposure of the clean Ru(001) surface to 0.8 L O_2 at 95 K, followed by annealing to 400 K, produces the EEL spectrum of the p(2x2)O overlayer shown in Fig. 9(a). In addition to the feature at 530 cm^{-1} due to motion of the oxygen adatoms in threefold sites perpendicular to the surface, a mode appears at 250 cm^{-1} which results from coupling of the overlayer to a ruthenium surface phonon **(7)**. Addition of the p(2x2)O overlayer, with an ideal fractional surface coverage of 0.25, changes the work function of the Ru(001) surface by +0.20 eV **(30)**. Employing a Ru=O bond length of 2.05 Å **(7)** and ignoring depolarization effects, this change in work function can be shown **(47)** to be equivalent to the transfer of 0.02 electron from the ruthenium surface to each oxygen adatom of the p(2x2)O overlayer, producing a quantifiable increase in the Lewis acidity of the surface ruthenium atoms.

The effects of the addition of the p(2x2)O overlayer on the properties of acetone adsorbed on the Ru(001) surface are demonstrated dramatically in the EEL spectra of Figs. 9 and 10, recorded after exposure of the Ru(001)-p(2x2)O surface to 4 L $(CD_3)_2CO$ and 6 L $(CH_3)_2CO$ at 95 K, respectively, followed again by momentary annealing to the indicated temperatures.

The 95 K spectra, Figs. 9(b) and 10(a), are dominated by modes due to η^1-acetone and permit rather straightforward assignments (Table 1) and interpretation. In the $(CD_3)_2CO$ spectrum, modes at 1675 and 720 cm^{-1} are due to the A_1 $\nu(CO)$ and $\nu_s(CCC)$ modes of η^1–$(CD_3)_2CO$, while those at 2070 and 2240 cm^{-1} are due primarily to the $\nu(CD_3)$ modes of η^1–$(CD_3)_2CO$ and partly to similar modes of a small amount of η^2–$(CD_3)_2CO$. The feature at 1260 cm^{-1} contains contributions both from the B_1 $\nu_a(CCC)$ vibration of η^1–$(CD_3)_2CO$ and the $\nu(CO)$ mode of η^2–$(CD_3)_2CO$. The $\delta(CD_3)$ modes from both species are evident at 1045 cm^{-1}, and the broadened band at 505 cm^{-1} results from both the $\nu(Ru{=}O)$ mode of chemisorbed oxygen and the B_1 $\delta(CO)$ mode of η^1–$(CD_3)_2CO$. Although the strong $\omega(CH_3)$ and $\nu(CH_3)$ modes in the corresponding $(CH_3)_2CO$ spectrum may indicate the presence of some multilayer or second layer acetone from the slightly larger initial exposure in this spectrum, the observed features can be assigned confidently to η^1–$(CH_3)_2CO$ as follows: $\nu(CH_3)$ at 2995 cm^{-1}, A_1 $\nu(CO)$ at 1690 cm^{-1}, $\delta(CH_3)$ at 1440 cm^{-1}, $\omega(CH_3)$ at 1110 and 900 cm^{-1}, and B_1 $\delta(CO)$ unresolved from the mode due to adsorbed oxygen at 540 cm^{-1}.

Annealing to progressively higher temperatures attenuates the bands due to η^1–$(CH_3)_2CO$ and η^1–$(CD_3)_2CO$ concomitantly [cf. Fig. 9(c), (d) and (e); and Fig. 10(b), (c) and (d)] and reveals bands due to low concentrations of η^2–$(CH_3)_2CO$ and η^2–$(CD_3)_2CO$, the assignments of which parallel those given earlier for the clean surface spectra. The most significant aspect of these annealing sequences is the presence of η^1-acetone at temperatures approaching 300 K, correlating well with the increased stability of molecularly adsorbed acetone at higher temperatures evident in the thermal desorption spectra from the p(2x2)O overlayer in comparison to the clean Ru(001) surface. On the clean Ru(001) surface, η^1-acetone was barely detectable by EELS at 200 K, and it was not detected at 275

K. On the Pt(111) surface, η^1-acetone desorbs at 185 K. Consequently, the presence of the p(2x2)O overlayer serves to stabilize η^1-acetone compared to η^2-acetone, not only increasing the concentration of the η^1 bonded species, but also increasing its binding energy to the Ru(001) surface, as evidenced by the increased temperature of desorption.

Further heating attenuates the remaining bands due to η^2-acetone as it decomposes. Finally, heating to 750 K retrieves the spectrum of atomic oxygen [cf. Fig. 9(g)], the intensity of which is diminished due to depletion of the oxygen adatoms via reaction with the surface carbon from the decomposition of η^2-acetone.

E. EELS and the Orientations of the Adsorbed Species

The vibrational spectrum of free acetone contains 24 fundamental normal modes, six of which are due to motion of the C_2CO skeleton, and the remainder of which are due to internal motion of the methyl groups. The symmetry types of the six skeletal vibrations of free acetone (point group C_{2v}), as well as their frequencies for liquid $(CH_3)_2CO$ and $(CD_3)_2CO$ **(39)**, are listed in Table 1.

As was mentioned earlier, the polarizations of the acetone skeletal vibrations (i.e. the orientation of the transition dipole moment of each mode with respect to the symmetry elements of the acetone skeleton) are preserved when acetone is coordinated in an η^1 configuration. For simplicity in the analysis that follows, the surface is assumed to be a structureless flat plane. Inclusion of the effects of the surface structure on the symmetry of the adsorbed species is necessary only when the atoms of the adsorbate interact strongly with surface atoms other than those to which the adsorbate is coordinated, and is therefore superfluous in this analysis for adsorbed acetone. The dipolar activity of each of the acetone skeletal modes as a function of the orientation of the acetone skeleton with respect to the surface plane can be deduced by consideration of the possible coordination geometries shown schematically in Fig. 11. The results of this analysis are listed in Table 2.

Figure 11(a) shows the acetone skeleton coordinated to the surface plane in the η^1 configuration of highest possible symmetry (C_{2v}), preserving the C_2 rotational axis and both mirror planes of the free acetone molecule. The A_1 modes of the free acetone skeleton —ν(CO), ν_s(CCC) and δ(CCC) —are polarized parallel to the C_2 axis and strictly perpendicular to the surface plane in this configuration, and are therefore dipolar active. The B_1 modes — ν_a(CCC) and δ(CO) —are polarized in the σ_1 mirror plane strictly parallel to the surface, and are dipolar inactive. The B_2 mode —π(CO) —is polarized in the σ_2 plane, parallel to the surface, and is also dipolar inactive. Tilting the molecule in the σ_1 plane, as in Fig. 11(b), reduces the symmetry of the adsorbate complex from C_{2v} to C_s, transforming the A_1 and B_1 modes of C_{2v} to A' of C_s and the B_2 mode to A''. Only the A' modes are dipolar active. Tilting the molecule in the σ_2 plane produces the C_s configuration shown in Fig. 11(c), with the A_1 and B_2 modes transforming to A' and the B_1 modes to A''. In Fig. 11(d), the molecule has been tilted away from both mirror planes, reducing the symmetry to C_1. All modes transform to A of C_1 and are dipolar active. By the same reasoning as was applied in these examples, an acetone molecule lying flat on the surface could have symmetry no higher than C_s, as is shown for the η^2 configuration in Fig. 11(e). Note that in terms of symmetry arguments this configuration is formally equivalent to Fig. 11(c), and the differences in their vibrational spectra would depend on the effects of the skeletal rehybridization which accompanies the η^2 interaction depicted in Fig. 11(e).

Returning to the results listed in Table 1, obtained from the most clearly resolved spectra of the monolayer η^1 and η^2 species, only modes of A_1 and B_1

symmetry are observed for η^1-acetone on Ru(001), confirming as correct the configuration shown in Fig. 11(b). This is also the configuration that would be expected to result from the interaction of a single lobe of the oxygen lone pair orbital, a p-type orbital in the plane of the molecule **(48)**, with a single metal atom of the surface, and agrees with the results obtained for acetone adsorption on Pt(111) **(27)** and two structurally characterized η^1 complexes of ruthenium, where Ru-O-C bond angles of 153° **(11)** and 135° **(12)** have been reported. For the η^2 species, modes derived from the A_1 $\nu(CO)$ and $\nu_s(CCC)$ and the B_2 $\pi(CO)$ are observed, confirming (e) of Fig. 11 as the appropriate configuration.

IV. Discussion

The dramatic effect of oxygen preadsorption on the selectivity of the Ru(001) surface toward the nonreactive (η^1) and reactive (η^2) coordination geometries for adsorbed acetone has important implications in the understanding of more complex catalytic reactions. Two possibilities come immediately to mind. First, the ability to identify and modify selectively those properties of a heterogeneous catalyst which produce the adsorbed intermediate structures which ultimately lead to the desired products could be used to increase the rate and especially the yield for the catalytic reaction. Furthermore, these results may lead directly to a better understanding of how otherwise "inert" coadsorbed species can act as promoters or poisons to affect the product distribution in a heterogeneously catalyzed reaction. To appreciate these possibilities more fully, an understanding of the acetone-ruthenium bonding interaction with and without the effects of coadsorbed oxygen will be developed.

Three factors can be identified which control the type and strength of bonding which coordinate a ligand to a metal center or surface **(22)**. First, orbitals of the same symmetry must exist on both the ligand and the metal to allow their mixing; second, the spatial extent of the orbitals must be sufficient to facilitate significant overlap; and third, the energies of the interacting orbitals must be similar. Changes in the relative importance of these three factors make one coordination geometry favored over another for a particular ligand-metal system.

Let us first consider the η^1 and η^2 coordination geometries observed for acetone in terms of the "frontier" orbitals of the free acetone ligand **(48)**. The lowest unfilled orbital is the π^*_{CO} antibonding orbital, which lies at +4.4 eV with respect to the vacuum level and has its amplitude more strongly localized on the acyl carbon atom than on the oxygen atom. The highest filled molecular orbital is the nonbonding oxygen lone pair, resembling an atomic p-like orbital with lobes localized strongly on the oxygen atom and in the skeletal plane. Its energy lies at 11.2 eV below the vacuum level. The next highest filled level is the π_{CO} bonding orbital at -12.9 eV, the amplitude of which is slightly greater on the oxygen than on the acyl carbon atom.

An η^1 coordination geometry for organometallic complexes of acetone results from overlap of a single lobe of the nonbonding oxygen lone pair orbital of acetone with a d_σ acceptor orbital of the metal, resulting in a net transfer of electron density from the ligand to the metal. The bent M-O-C bond, identified for the two η^1-acetone complexes of ruthenium mentioned earlier **(11,12)** and for the orientation of η^1-acetone on both Pt(111) **(27)** and Ru(001), is a consequence of the spatial distribution of this lone pair donor orbital on acetone. Presumably due to the low amplitude of the π^*_{CO} antibonding orbital on the oxygen atom, little backdonation from the metal d_π levels to this ligand orbital occurs, as evidenced by the rather small (less than 100 cm^{-1}) red-shifts of the $\nu(CO)$ mode observed for homogeneous complexes **(9-12)** and metal surfaces

(27) which bind acetone in this configuration. The role of the metal in this type of interaction is that of a weak Lewis acid, and the purely dative metal-acetone bond which results is correspondingly weak. In many cases, depending on the metal and the properties of other ligands coordinated to it which affect its electronic structure, η^1-acetone complexes are too unstable to be isolated and characterized structurally **(9,10)**. Thermal desorption results suggest a binding energy of 11.6 kcal/mole for η^1-acetone on the Pt(111) surface **(27)**, and a similar analysis **(49)** of the thermal desorption data for Ru(001) suggests binding energies in the range of 10-15 kcal/mole on the clean surface and 10-19 kcal/mole on the Ru(001)-p(2x2)O surface.

An η^2 coordination geometry for organometallic complexes of acetone results from overlap of the π_{CO} bonding orbital of acetone with a d_σ or sp hybrid acceptor level of the metal, along with backdonation from metal d_π levels into the π^*_{CO} antibonding orbital of the acetone ligand **(21)**. The strength of this interaction, and therefore the probability of its occurrence relative to the η^1 interaction, depends critically on the ability of the ligand-metal bond to facilitate backdonation, since in the absence of backdonation the remaining π donor bond is particularly weak and unstable **(22)**. Indeed, each of the organometallic complexes isolated and characterized structurally which shows η^2 coordination of ligands similar to acetone **(13-20)** and the η^2-acetone identified on Ru(001) in this work display substantial rehybridization of the acyl carbon from sp^2 to nearly sp^3, giving clear evidence of efficient backdonation. The fact that backdonation dominates the η^2 interaction has been concluded in similar studies of olefin **(50)** and acetylene **(22,23)** bonding to transition metals and illustrates the function of the metal as a Lewis base in these cases **(50)**. Since transition metal atoms provide both orbitals of π symmetry to match the symmetry of the π^*_{CO} antibonding orbital and spatial extent to afford efficient overlap **(22)**, it is the energy match of the interacting orbitals which most strongly affects this backbonding interaction.

The effect of d_π and π^*_{CO} orbital energies on η^2 bonding is illustrated in the properties of the complexes with acetone-like ligands in η^2 coordination geometries. Recall that coordination of acetone to a number of transition metals, including rhodium and iridium **(10)**, and ruthenium **(11,12)**, produces η^1 complexes. Substitution of hydrogen for CH_3 in acetone, however, lowers the energy of the π^*_{CO} antibonding orbital from +4.4 eV to +3.1 eV **(48)**, decreasing the energy gap between the π^*_{CO} and d_π levels. This enhances d_π to π^*_{CO} backdonation, and η^2-formaldehyde complexes with a number of metals, including osmium **(13)** and iron **(14)**, result. Substitution of the more electronegative CF_3 for CH_3 depolarizes the carbon-oxygen bond of hexafluoroacetone relative to acetone, lowering its π^*_{CO} orbital energy dramatically and yielding η^2 complexes with electronegative metals such as platinum **(15,19)** and nickel **(16,17)**. Of particular significance with respect to these arguments is that the only unsubstituted η^2-acetone complex isolated to date is formed with a low valent and electropositive tantalum center **(18)**. The lower d-level occupancy of tantalum ($5d^3 6s^2$) relative to rhodium ($4d^8 5s^1$), iridium ($5d^7 6s^2$) and ruthenium ($4d^7 5s^1$) insures that its d levels have higher energy and therefore can more easily populate the π^*_{CO} level of acetone to facilitate η^2 bonding.

On the basis of these arguments, the formation of η^2-acetone on the Ru(001) surface can be understood. Interactions among metal atoms at a surface broaden the d levels to form bands which extend to higher energies than the d levels of isolated metal atoms (i.e. the Fermi level of a bulk metal is at a higher energy than the highest occupied level of an isolated metal center) **(51)**, causing the atoms of the surface to behave as isolated metal atoms of lower net d level occupancy. In effect, metal atoms at a surface are more electron rich than isolated atoms in a complex and can therefore raise their formal oxidation state more easily to yield backdonor bonding. The acetone π^*_{CO} orbital is apparently at the appropriate energy to allow a dramatic distinction between the behavior of the Ru(001) surface, where the Fermi level is at -5.4 eV **(52)** and where substantial η^2 bonding of acetone occurs, and the Pt(111) surface, the increased d level occupancy of which ($5d^9 6s^1$) lowers its Fermi level to -5.9 eV **(53)** and thus favors η^1 bonding.

It remains to explain in these same terms the effect of coadsorbed oxygen on the bonding of acetone on Ru(001). As was discussed previously, the p(2x2)O overlayer increases substantially both the concentration and the stability of η^1-acetone on the Ru(001) surface. We attribute this to a "short-range", through-metal electron deficiency at neighboring ruthenium surface sites, due to the presence of the electronegative oxygen adatoms, increasing the Lewis acidity of the former. The stability of other surface species coordinated to the Ru(001) surface via σ donor bonds shows a similar enhancement in the presence of coadsorbed oxygen, including N_2 **(54)**, N_2O **(55)** and bridge-bonded formate **(56)**.

Addition of the p(2x2)O overlayer increases the work function of the Ru(001) surface by 0.20 eV (i.e. lowers the Fermi level by 0.20 eV to -5.6 eV) **(30)**, increasing the disparity between the energy of the occupied d band of the metal and that of the π^*_{CO} acceptor level of acetone. This renders backdonation more difficult and causes Ru(001) to behave more like Pt(111). The implications of this for the effects of catalyst poisons and promoters are interesting: adsorption of electronegative substituents such as sulfur would produce an increase in the surface work function similar to oxygen and should therefore inhibit reactions which proceed through backbonded intermediates, whereas the adsorption of "cationic" species such as potassium would decrease the surface work function and should promote the formation of backbonded intermediates (based solely on the shift in energy difference between the donor and acceptor levels caused by each). The net effects of these bonding interactions on the surface chemistry of acetone adsorbed on both the clean Ru(001) and the Ru(001)-p(2x2)O surfaces may be illustrated by overall reaction schemes for the monolayer species adsorbed on both surfaces, which result from consideration of both the EELS and thermal desorption results discussed previously.

On the clean Ru(001) surface, both η^1- and η^2-acetone are produced upon adsorption of a saturated first layer of acetone at 95 K:

$$(CH_3)_2CO(g) \rightarrow \eta^1\text{-}(CH_3)_2CO$$

and

$$(CH_3)_2CO(g) \rightarrow \eta^2\text{-}(CH_3)_2CO \, .$$

Heating the surface causes η^1-acetone to desorb molecularly in the temperature range between approximately 150 and 250 K,

$$\eta^1\text{-}(CH_3)_2CO \rightarrow (CH_3)_2CO(g) \, ,$$

whereas η^2-acetone decomposes between approximately 200 and 320 K to adsorbed CO and CH_3 fragments:

$$\eta^2\text{-}(CH_3)_2CO \rightarrow CO(a) + 2CH_3(a) \, .$$

Decomposition of the CH_3 fragments follows rapidly through CH_x ($x<3$) intermediates

$$CH_3(a) \rightarrow CH_2(a) + H(a) \rightarrow CH(a) + 2H(a) \rightarrow C(a) + 3H(a) \, .$$

Adsorbed CO is evolved from the surface in a desorption rate-limited reaction near 470 K,

$$CO(a) \rightarrow CO(g) ,$$

and hydrogen adatoms from CH_x decomposition recombine on the surface to evolve H_2 in a desorption rate-limited reaction near 330 K and a series of reactions between 400 and 750 K which have their desorption rates limited by the rates of decomposition of the CH_x fragments on the surface in this temperature range:

$$2H(a) \rightarrow H_2(g) .$$

Adsorbed carbon from the methyl groups remains on the surface. The total amount of CO and H_2 evolution from the surface indicates that approximately one-eighth monolayer of η^2-acetone adsorbs and decomposes on the clean Ru(001) surface under these conditions.

On the Ru(001)-p(2x2)^{18}O surface, substantially more η^1-acetone and less η^2-acetone is formed upon adsorption at 95 K compared to the clean surface. Heating of the surface causes η^1-acetone to desorb molecularly in the temperature range between approximately 150 and 320 K, and the remaining η^2-acetone decomposes to adsorbed CO and CH_3 fragments in the temperature range between 200 and 350 K. The p(2x2) oxygen overlayer not only increases the yield of η^1-acetone and stabilizes it to higher desorption temperatures, but it also retards the rate of decomposition of η^2-acetone, as evidenced by its persistence in EEL spectra to higher temperatures on the Ru(001)-p(2x2)O surface than on the clean surface. Decomposition of the CH_3 fragments follows rapidly after their formation, producing H_2 in desorption rate-limited reactions near 220 K and a series of reactions between 250 and 550 K, the desorption rates of which are limited by the rates of decomposition of the adsorbed CH_x fragments. The CO produced from the decomposition of η^2-acetone (m = 28 amu) is evolved in a desorption rate-limited reaction at 450 K, and $C^{18}O$ produced by the reaction of adsorbed carbon from CH_3 decomposition with the oxygen adatoms (^{18}O) of the p(2x2) overlayer (m = 30 amu) is evolved between 400 and 700 K. The total amounts of CO (m = 28 amu), H_2 and $C^{18}O$ (m = 30 amu) evolution from the surface indicate that approximately 0.02 monolayer of η^2-acetone adsorbs and decomposes on the Ru(001)-p(2x2)O surface under these conditions.

Two pathways can be postulated for the decomposition of η^2-acetone on the Ru(001) surface. In one case, the acetone skeleton would decompose initially through C-C bond cleavage to produce CO and methyl groups on the surface. Since molecular dissociation in general proceeds through population of an antibonding molecular orbital **(51,57)**, the difference in reactivity of the Ru(001) surface toward η^1- and η^2-acetone would be a clear and obvious manifestation of the bonding interactions which lead to the formation of each species if C-C bond cleavage were the dominant dissociation channel. The reaction coordinate for this mechanism would be the ν(CO) vibration of η^2-acetone, since its amplitude controls most directly the population of the π^*_{CO} antibonding orbital, and this orbital in turn controls the integrity of the acetone skeleton. A second possible mechanism invokes first C-H bond cleavage, with decomposition of the destabilized acetone skeleton following rapidly thereafter. In this case, η^2-acetone, with its methyl groups in closer proximity to the ruthenium surface atoms than the η^1 species, would again be expected to be more reactive. Decomposition would proceed via population of the $\pi^*_{CH_3}$ antibonding orbital of acetone, and either the π(CO) vibration of η^2-acetone near 600 cm^{-1}, the motion of which controls the approach of the methyl groups to the surface, or the ν(CH) vibration would represent the reaction coordinate. A distinction between these possibilities could only be made if the experimental results showed clear evidence of a kinetic isotope effect. For example, if the decomposition of η^2–$(CD_3)_2CO$

occurred at higher temperatures than η^2–$(CH_3)_2CO$, this would identify $\nu(CH)$ as the reaction coordinate and C-H bond cleavage as the rate-limiting step in η^2-acetone decomposition. Such a kinetic isotope effect was not observed, however. Since the π^*_{CO} orbital of acetone is already partially populated in the stable η^2 configuration, and since the $\pi^*_{CH_3}$ orbital is at significantly higher energy than the π^*_{CO} orbital [16.5 eV versus 8.2 eV for free acetone **(48)**], decomposition of η^2-acetone via C-C bond cleavage would appear to be the favored mechanism.

V. Summary

The important conclusions of this work may be summarized as follows:

1. Acetone bonds molecularly to the Ru(001) surface at 95 K in two different configurations: an η^1 (end-on) configuration which desorbs reversibly and an η^2 (side-on) configuration which dissociates upon heating of the surface.
2. The η^2 configuration is the majority species on the clean Ru(001) surface. The appearance of a red-shifted $\nu(CO)$ vibration near 1300 cm^{-1} indicates significant rehybridization of the acyl carbon in this configuration, to that found for homogeneous organometallic complexes with η^2 ketonic ligands.
3. The η^1 configuration is adsorbed with C_s symmetry and a nonlinear Ru-O-C bond, as has been observed in analogous organometallic η^1 complexes of acetone.
4. Addition of an ordered p(2x2) overlayer of oxygen adatoms to the Ru(001) surface stabilizes the η^1 configuration of adsorbed acetone, rendering it the majority surface species and increasing its binding energy relative to the clean surface.
5. The selectivity of the Ru(001) and the Ru(001)-p(2x2)O surfaces toward the η^1- and η^2-acetone bonding configurations can be explained in terms of the

electronic properties of these surfaces and their effects on the bonding interactions which dictate the two coordination geometries.

Acknowledgments

The authors wish to thank Professors R. H. Grubbs and J. E. Bercaw for valuable discussions during the preparation of this manuscript. This research was supported by the National Science Foundation under Grant No. CHE82-06487.

References

1. See, for example, J. P. Collman and L. S. Hegedus, *Principles and Applications of Organotransition Metal Chemistry*, University Science, Mill Valley, 1980.
2. A. F. Wells, *Structural Inorganic Chemistry*, 4th ed., Clarendon Press, Oxford, 1975.
3. J. P. Pendry, *Low Energy Electron Diffraction*, Academic Press, London, 1974.
4. One notable example is the successful determination via LEED of the structure of the ethylidyne species which ethylene and acetylene form upon reaction with the Pt(111) surface. See L. L. Kesmodel, L. H. Dubois and G. A. Somorjai, J. Chem. Phys. **70**, 2180 (1979); H. Steininger, H. Ibach and S. Lehwald, Surface Sci. **117**, 685 (1982).
5. H. Ibach and D. L. Mills, *Electron Energy Loss Spectroscopy and Surface Vibrations*, Academic Press, 1982, Ch. 6.
6. *Ibid*, Ch. 3.
7. T. S. Rahman, A. B. Anton, N. R. Avery and W. H. Weinberg, Phys. Rev. Letters **51**, 1979 (1983).
8. N. R. Avery, W. H. Weinberg, A. B. Anton and B. H. Toby, Phys. Rev. Letters **51**, 682 (1983).
9. W. L. Driessen and L. Groeneveld, Recl. Trav. Chim. Pays-Bas **88**, 977 (1969).
10. S. J. Thompson, C. White and P. M. Maitlis, J. Organomet. Chem. **136**, 87 (1977).
11. R. O. Gould, W. J. Sime and T. A. Stephenson, J. Chem. Soc. Dalton **1978**, 76.
12. M. A. Bennett, T. W. Matheson, G. B. Robertson, W. L. Steffen and T. W. Turney,

J. Chem. Soc. Chem. Commun. **1979**, 32.

13. K. L. Brown, G. R. Clark, C. E. L. Headford, K. Marsden and W. R. Roper, J. Am. Chem. Soc. **101**, 503 (1979).
14. H. Berke, W. Bankhardt, G. Huttner, J. V. Seyerl and L. Zsolnai, Chem. Ber. **114**, 2754 (1981).
15. B. Clarke, M. Green, R. B. L. Osborn and F. G. A. Stone, J. Chem. Soc. A **1968**, 167.
16. J. Browning, C. S. Cundy, M. Green and F. G. A. Stone, J. Chem. Soc. A **1969**, 20.
17. R. Countryman and B. R. Penfold, J. Cryst. Mol. Struct. **2**, 281 (1972).
18. C. D. Wood and R. R. Schrock, J. Am. Chem. Soc. **101**, 5421 (1979).
19. M. Green, J. A. K. Howard, A. Laguna, L. E. Smart, J. L. Spencer and F. G. A. Stone, J. Chem. Soc. Dalton **1977**, 278.
20. H. Adams, N. A. Bailey, J. T. Gauntlett and M. J. Winter, J. Chem. Soc. Chem. Commun. **1984**, 1360.
21. M. J. S. Dewar, Bull. Soc. Chim. France **18**, C79 (1951); J. Chatt and L. A. Duncanson, J. Chem. Soc. **1953**, 2939.
22. E. O. Greaves, C. J. L. Lock and P. M. Maitlis, Can. J. Chem. **46**, 3879 (1968).
23. M. H. Chisholm and H. C. Clark, Acc. Chem. Res. **6**, 202 (1973).
24. S. D. Ittel, Inorg. Chem. **16**, 2589 (1977).
25. G. Henrici-Olive′ and S. Olive′, Agnew Chem. Int. Ed. Engl. **15**, 136 (1976), and references therein.
26. G. Blyholder and L. D. Neff, J. Phys. Chem. **70**, 893 (1966); R. P. Young and N. Sheppard, J. Catal. **7**, 223 (1967); G. Blyholder and D. Shihabi, J. Catal. **46**, 91

(1977); H. Lüth, G. W. Rubloff and W. D. Grobman, Surface Sci. **63**, 325 (1977).

27. N. R. Avery, Surface Sci. **125**, 771 (1983).

28. G. E. Thomas and W. H. Weinberg, Rev. Sci. Instrum. **50**, 497 (1979).

29. G. E. Thomas and W. H. Weinberg, J. Chem. Phys. **70**, 954 (1979).

30. T. E. Madey, H. A. Engelhardt and D. Menzel, Surface Sci. **48**, 304 (1975).

31. H. Shimizu, K. Christmann and G. Ertl, J. Catal. **61**, 412 (1980).

32. E. D. Williams and W. H. Weinberg, Surface Sci. **82**, 93 (1979).

33. P. A. Thiel, F. M. Hoffmann and W. H. Weinberg, J. Chem. Phys. **75**, 5556 (1981).

34. M. M. Hills and W. H. Weinberg, unpublished results.

35. H.-I. Lee, G. Praline and J. M. White, Surface Sci. **91**, 581 (1980).

36. D. E. Peebles, J. A. Schreifels and J. M. White, Surface Sci. **116**, 117 (1982).

37. A. B. Anton and W. H. Weinberg, unpublished results.

38. N. R. Avery, B. H. Toby, A. B. Anton and W. H. Weinberg, Surface Sci. **122**, L574 (1982); B. H. Toby, N. R. Avery, A. B. Anton and W. H. Weinberg, J. Electron Spect. **29**, 233 (1983).

39. G. Dellepiane and J. Overend, Spectrochimica Acta **22**, 593 (1966); J. R. Allkins and E. R. Lippincott, Spectrochimica Acta **25A**, 761 (1968).

40. *Ibid*, Ch. 4.

41. N. B. Coltup, L. H. Daly and S. E. Wiberley, *Introduction to Infrared and Raman Spectroscopy*, Academic Press, New York, 1975, Ch. 5.

42. *Ibid*, p. 458.

43. H. Ibach, H. Hopster and B. Sexton, Appl. Surface Sci. **1**, 1 (1977).

44. B. A. Sexton and N. R. Avery, Surface Sci. **129**, 21 (1983).

45. J. L. Gland, B. A. Sexton and G. B. Fisher, Surface Sci. **95**, 587 (1980).

46. C. Backx, C. P. M. DeGroot and P. Biloen, Surface Sci. **104**, 300 (1981).

47. J. Topping, Proc. Roy. Soc. London A **114**, 67 (1927).

48. B. Hess, P. J. Bruna, R. J. Buenker and S. D. Peyerimhoff, Chem. Phys. **18**, 267 (1980).

49. P. A. Redhead, Vacuum **12**, 203 (1962).

50. R. Ugo, Coordin. Chem. Rev. **3**, 319 (1968).

51. J.-Y. Saillard and R. Hoffmann, J. Am. Chem. Soc. **106**, 2006 (1984).

52. F. J. Himpsel, K. Christmann, P. Heimann and D. E. Eastman, Phys. Rev. B **23**, 2546 (1981).

53. B. E. Nieuwenhuys and W. H. M. Sachtler, Surface Sci. **34**, 317 (1973).

54. A. B. Anton, N. R. Avery, T. E. Madey and W. H. Weinberg, in preparation.

55. T. E. Madey, A. B. Anton, N. R. Avery and W. H. Weinberg, in preparation.

56. B. H. Toby, N. R. Avery, A. B. Anton and W. H. Weinberg, in preparation.

57. S.-S. Sung and R. Hoffmann, J. Am. Chem. Soc. **107**, 578 (1985).

Table 1. Assignments of vibrational bands (in cm^{-1}) observed with high-resolution electron energy loss spectroscopy of $(CH_3)_2CO$ and $(CD_3)_2CO$ on Ru(001) and Ru(001)-p(2x2)O. Also listed are the Raman and IR bands of liquid acetone and their symmetry types for the free acetone molecule.

Mode	Liquid Acetone (39)			EELS — Acetone on Ru(001)				
	Symmetry (C_{2v})	$(CH_3)_2CO$	$(CD_3)_2CO$	$(CH_3)CO$			$(CD_3)_2CO$	
				Multilayer	η^1 (95 K)	η^2 (275 K)	η^1 (95 K)	η^2 (275 K)
ν(CO)	A_1	1711(vs)	1701(vs)	1720	1690	1300	1665-1675	1275
ν_a(C-C-C)	B_1	1221(vs)	1249(vs)	1240			1260	
ν_s(C-C-C)	A_1	787(w)	696(m)		780-825		715-720	
δ(CO)	B_1	530(m)	478(s)	535	515-540[a]		495-505[a]	
δ(C-C-C)	A_1	493(w)	410(w)					
π(CO)	B_2	393(w)	331(w)			655		610
$\nu(CH_3)$		3006(s) 2967(s) 2922(s)	2257(s) 2222(s) 2109(s)	3030	2950-2995	2955	2210-2240 2070-2090	2220
$\delta(CH_3)$		1430(s) 1361(vs) 1356(w)	1088(s) 1037(vs) 1006(w)	1380	1395-1440	1370	1030-1045	1075
$\omega(CH_3)$		1092(m) 1066(m) 902(m)	889(m)	905	1050-1110 890-905	1170 980	920	880 820

[a] Not resolved from the mode at 530 cm^{-1} due to oxygen adatoms of the p(2x2)O overlayer.

Table 2. Point groups and symmetry types of acetone skeletal vibrations for free acetone and the adsorbed configurations shown in Fig. 11.

Configuration	Point Group	Skeletal Mode					
		ν(CO)	ν_s(CCC)	δ(CCC)	ν_a(CCC)	δ(CO)	π(CO)
free	C_{2v}	A_1	A_1	A_1	B_1	B_1	B_2
(a) η^1	C_{2v}	A_1	A_1	A_1	B_1	B_1	B_2
(b) η^1	C_s	A'	A'	A'	A'	A'	A''
(c) η^1	C_s	A'	A'	A'	A''	A''	A'
(d) η^1	C_1	A	A	A	A	A	A
(e) η^2	C_s	A'	A'	A'	A''	A''	A'

Figure Captions

Figure 1: Thermal desorption spectra for increasing exposures of $(CH_3)_2CO$ on the clean Ru(001) surface at 80 K. The most abundant cracking fragment of $(CH_3)_2CO$, m = 43 amu, was monitored, and the average heating rate β was 15 K/s.

Figure 2: Thermal desorption spectra recorded under conditions identical to those of Fig. 1 except for adsorption on the Ru(001)-p(2x2)O surface.

Figure 3: Thermal desorption spectra for the CO decomposition product from 15 L exposures of the clean Ru(001) and the Ru(001)-p(2x2)^{18}O surfaces to $(CH_3)_2CO$. The top spectrum shows CO desorption following exposure of the clean surface to 0.5 L CO for comparison.

Figure 4: Thermal desorption spectra for the H_2 decomposition products from 15 L exposures of the clean Ru(001) and the Ru(001)-p(2x2)O surfaces to $(CH_3)_2CO$. The top spectrum shows H_2 desorption following exposure of the clean surface to 4 L H_2 for comparison.

Figure 5: Schematic η^1 [(a)] and η^2 [(b), (c) and (d)] bonding configurations for ketonic ligands observed in homogeneous complexes.

Figure 6: EEL spectra recorded after exposure of the clean Ru(001) surface to 6 L $(CH_3)_2CO$ at 95 K. The symbol "Δ" signifies momentary heating to the indicated temperatures, followed by cooling to 95 K to record the spectra.

Figure 7: EEL spectra recorded after exposure of the clean Ru(001) surface to 6 L $(CD_3)_2CO$ at 95 K, heating to the indicated temperatures, and recooling to 95 K.

Figure 8: EEL spectra recorded in the specular direction (a), and 6° out of the

specular direction (b), after exposure of the clean Ru(001) surface to 6 L $(CH_3)_2CO$ at 95 K, heating to 275 K, and recooling to 95 K.

Figure 9: EEL spectra recorded after preparation of a p(2x2)O overlayer on the Ru(001) surface (a), followed by exposure to 4 L $(CD_3)_2CO$ at 95 K, heating to the indicated temperatures, and recooling to 95 K.

Figure 10: EEL spectra recorded after exposure of the Ru(001)-p(2x2)O surface to 6 L $(CH_3)_2CO$ at 95 K, heating to the indicated temperatures, and recooling to 95 K.

Figure 11: Schematic bonding configurations for η^1-acetone on a structureless flat surface (a-d), illustrating the symmetry elements preserved in each configuration. The η^2 configuration (e) is shown for comparison. In each case, the larger circles represent methyl groups and the smaller circles represent the carbon and oxygen atoms.

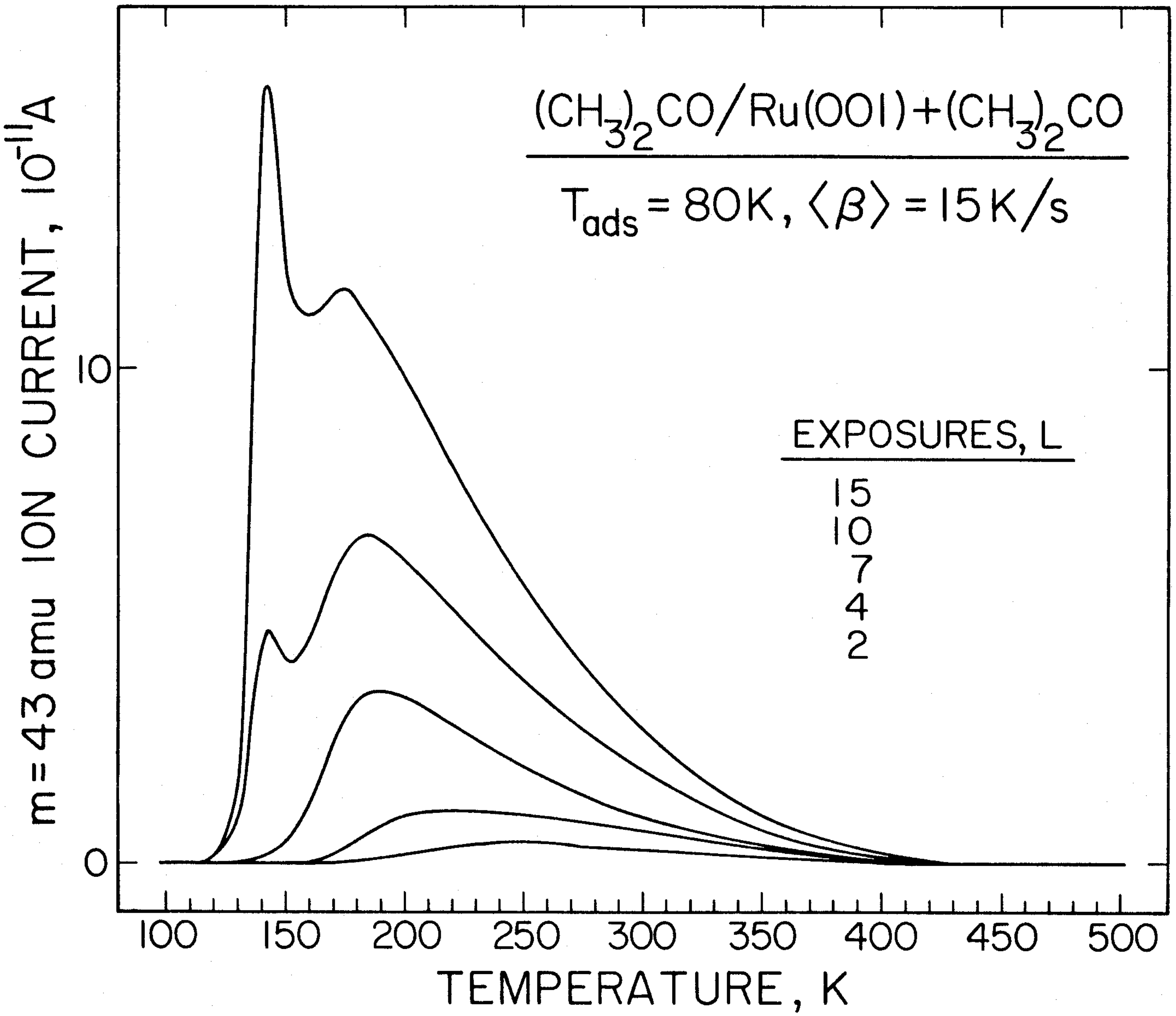
$(CH_3)_2CO/Ru(001)+(CH_3)_2CO$
$T_{ads} = 80K, \langle\beta\rangle = 15K/s$
EXPOSURES, L
15
10
7
4
2
m = 43 amu ION CURRENT, 10^{-11}A
10
0
100
150
200
250
300
350
400
450
500
TEMPERATURE, K

Figure 1

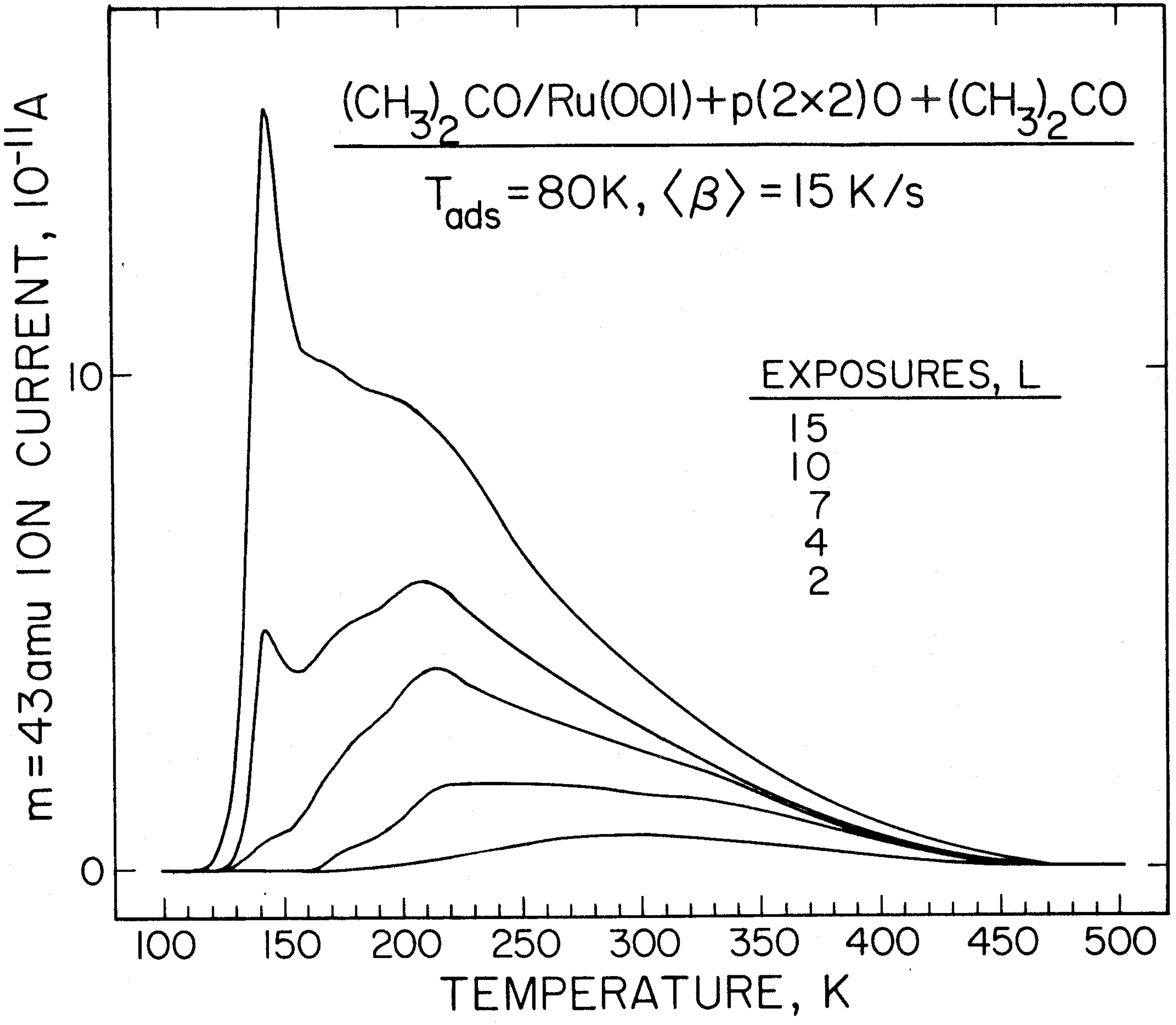

$(CH_3)_2CO/Ru(001)+p(2\times2)O+(CH_3)_2CO$
$T_{ads}=80K, \langle\beta\rangle=15\ K/s$
EXPOSURES, L
15
10
7
4
2
10
0
m=43amu ION CURRENT, 10^{-11}A
100
150
200
250
300
350
400
450
500
TEMPERATURE, K

Figure 2

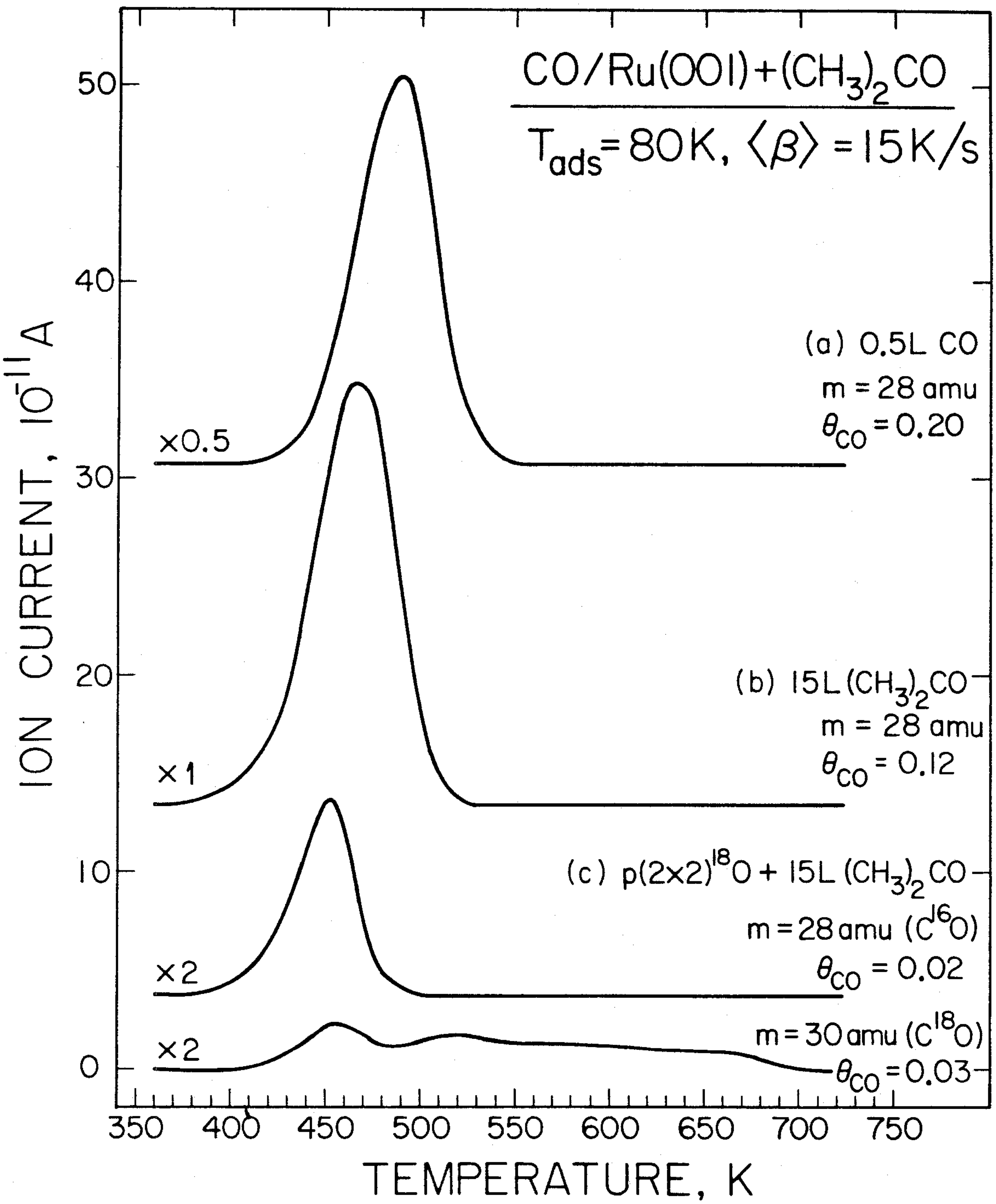
CO/Ru(001)+$(CH_3)_2CO$
T_{ads}=80K, ⟨β⟩ =15K/s
ION CURRENT, 10^{-11}A
TEMPERATURE, K
0
10
20
30
40
50
350
400
450
500
550
600
650
700
750
×0.5
×1
×2
×2
(a) 0.5L CO
m = 28 amu
θ_{CO} = 0.20
(b) 15L $(CH_3)_2CO$
m = 28 amu
θ_{CO} = 0.12
(c) p(2×2)^{18}O + 15L $(CH_3)_2CO$
m = 28 amu ($C^{16}O$)
θ_{CO} = 0.02
m = 30 amu ($C^{18}O$)
θ_{CO} = 0.03

Figure 3

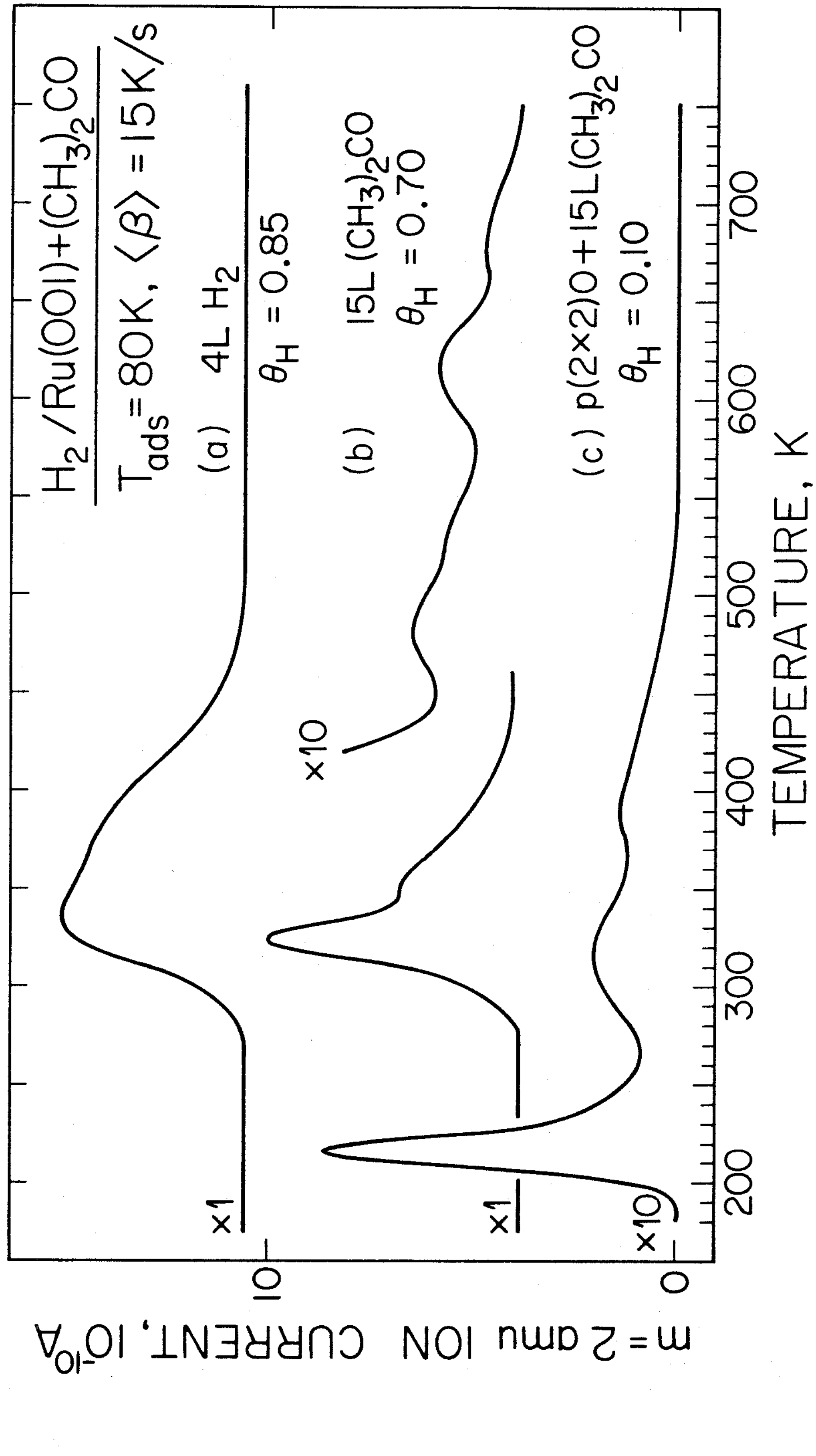
H_2 /Ru(001)+$(CH_3)_2CO$
T_{ads} = 80K, ⟨β⟩ = 15K/s
(a) 4L H_2
θ_H = 0.85
(b) 15L $(CH_3)_2CO$
θ_H = 0.70
(c) p(2×2)O+15L$(CH_3)_2CO$
θ_H = 0.10
×1
×1
×10
×10
0
10
m = 2 amu ION CURRENT, 10^{-10}A
200
300
400
500
600
700
TEMPERATURE, K

Figure 4

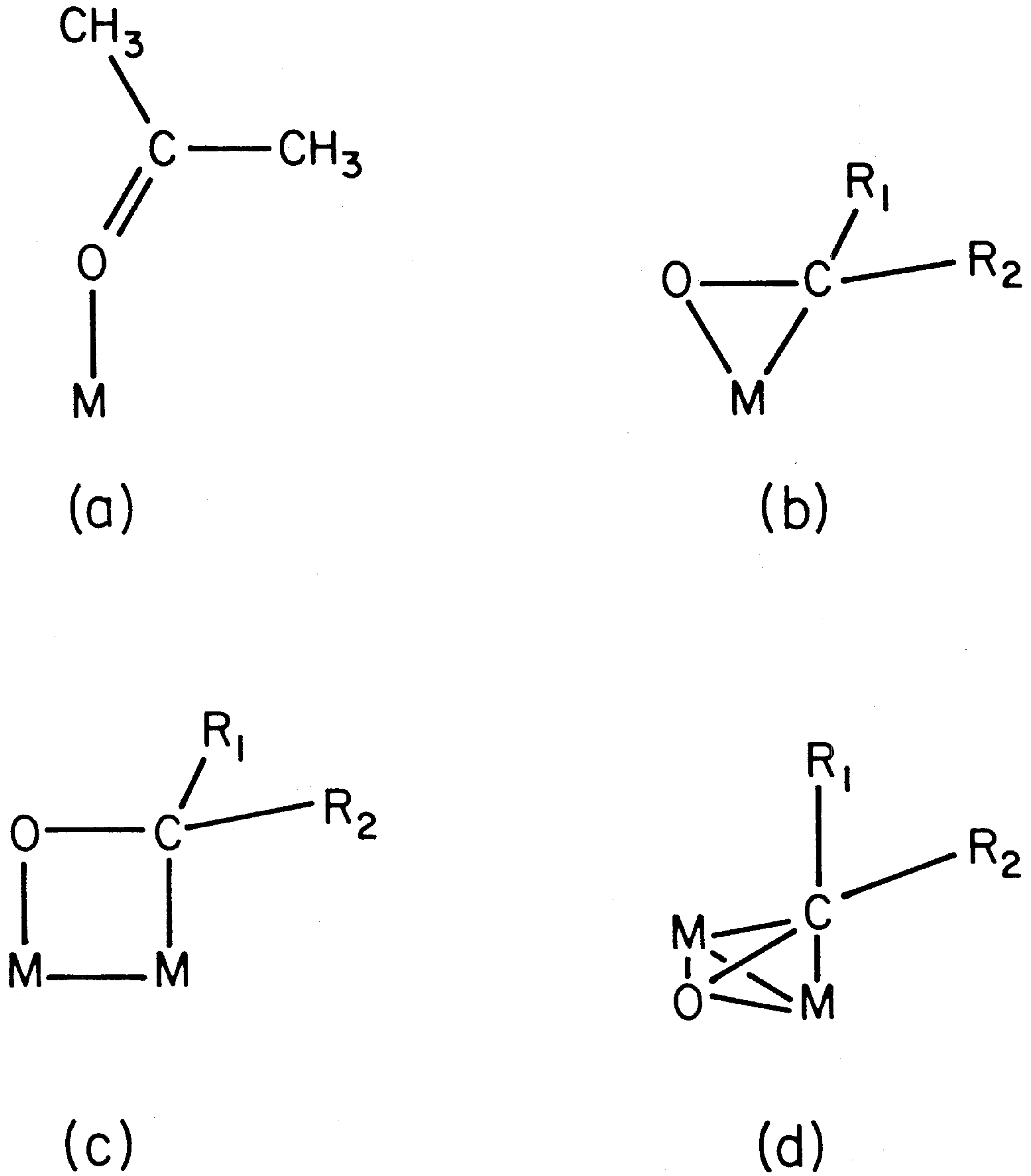

Figure 5

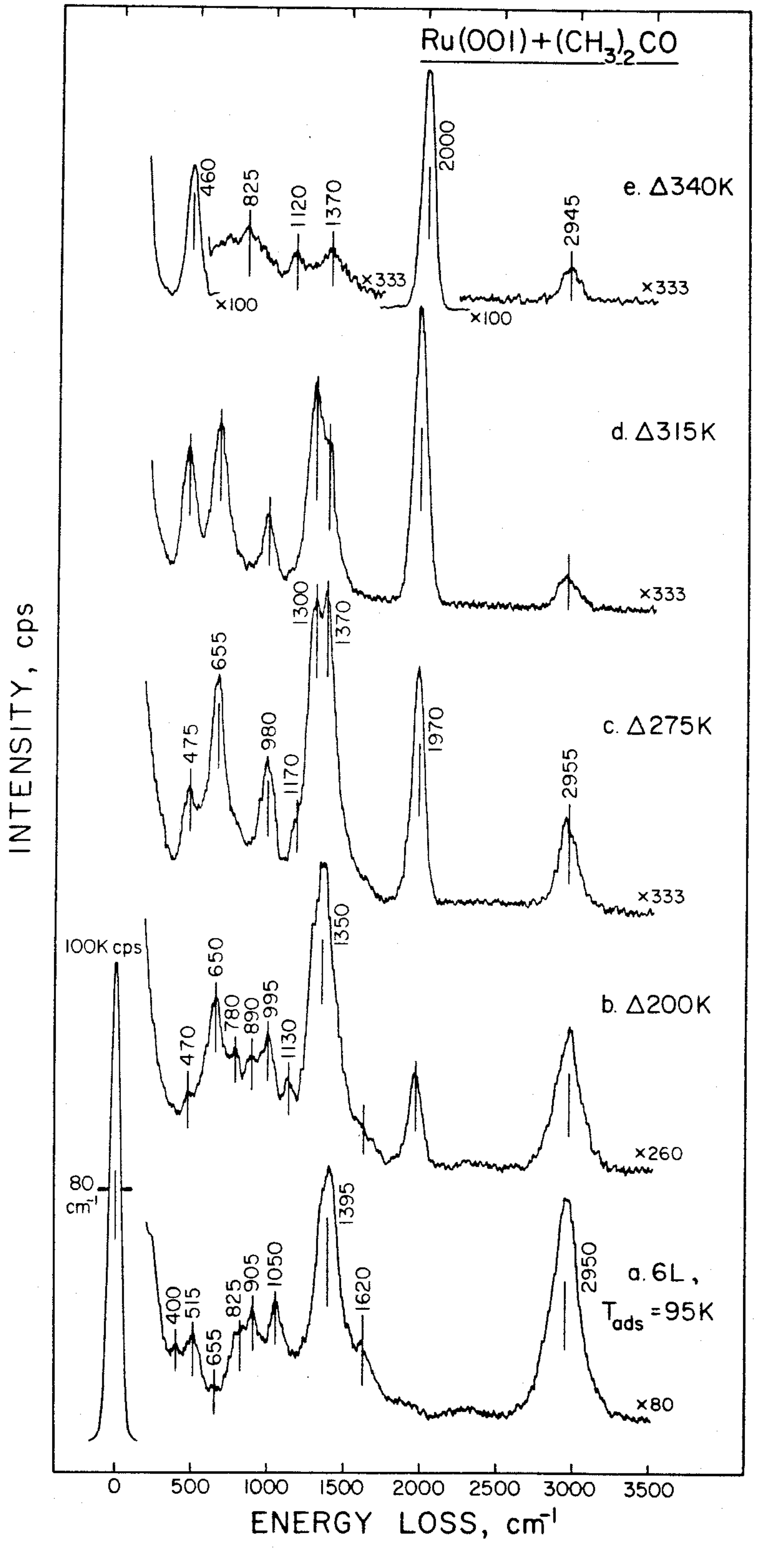
Ru(001)+(CH$_3$)$_2$CO
e. Δ340K
460
825
1120
1370
×333
×100
2000
×100
2945
×333
d. Δ315K
×333
c. Δ275K
475
655
980
1170
1300
1370
1970
2955
×333
b. Δ200K
100K cps
470
650
780
890
995
1130
1350
×260
a. 6L, T$_{ads}$ =95K
80 cm^{-1}
400
515
655
825
905
1050
1395
1620
2950
×80
INTENSITY, cps
0
500
1000
1500
2000
2500
3000
3500
ENERGY LOSS, cm^{-1}

Figure 6

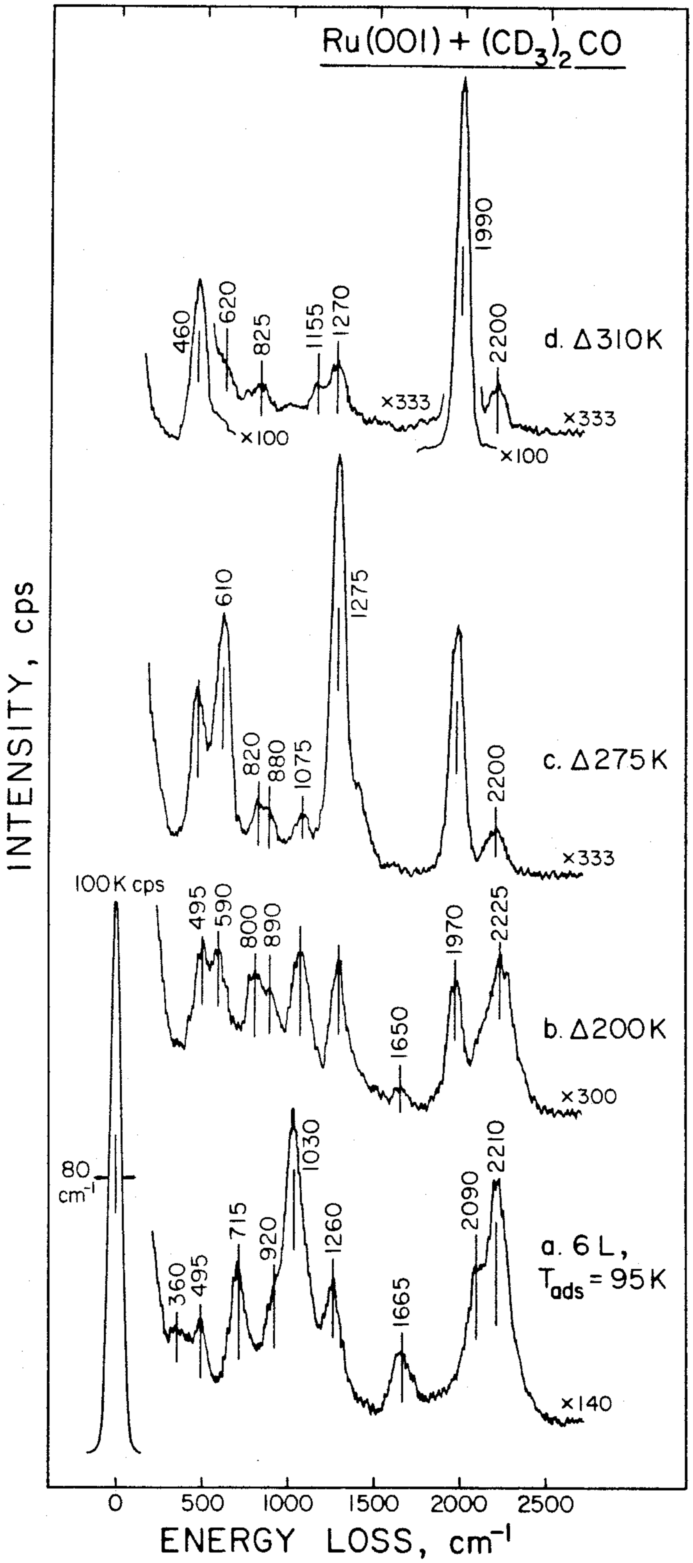
Ru(001) + (CD3)2 CO
d. Δ310K
460
620
825
1155
1270
1990
2200
×100
×333
×333
×100
c. Δ275K
610
1275
820
880
1075
2200
×333
b. Δ200K
100K cps
495
590
800
890
1970
2225
1650
×300
a. 6L, Tads = 95K
80 cm⁻¹
360
495
715
920
1030
1260
1665
2090
2210
×140
INTENSITY, cps
0
500
1000
1500
2000
2500
ENERGY LOSS, cm⁻¹

Figure 7

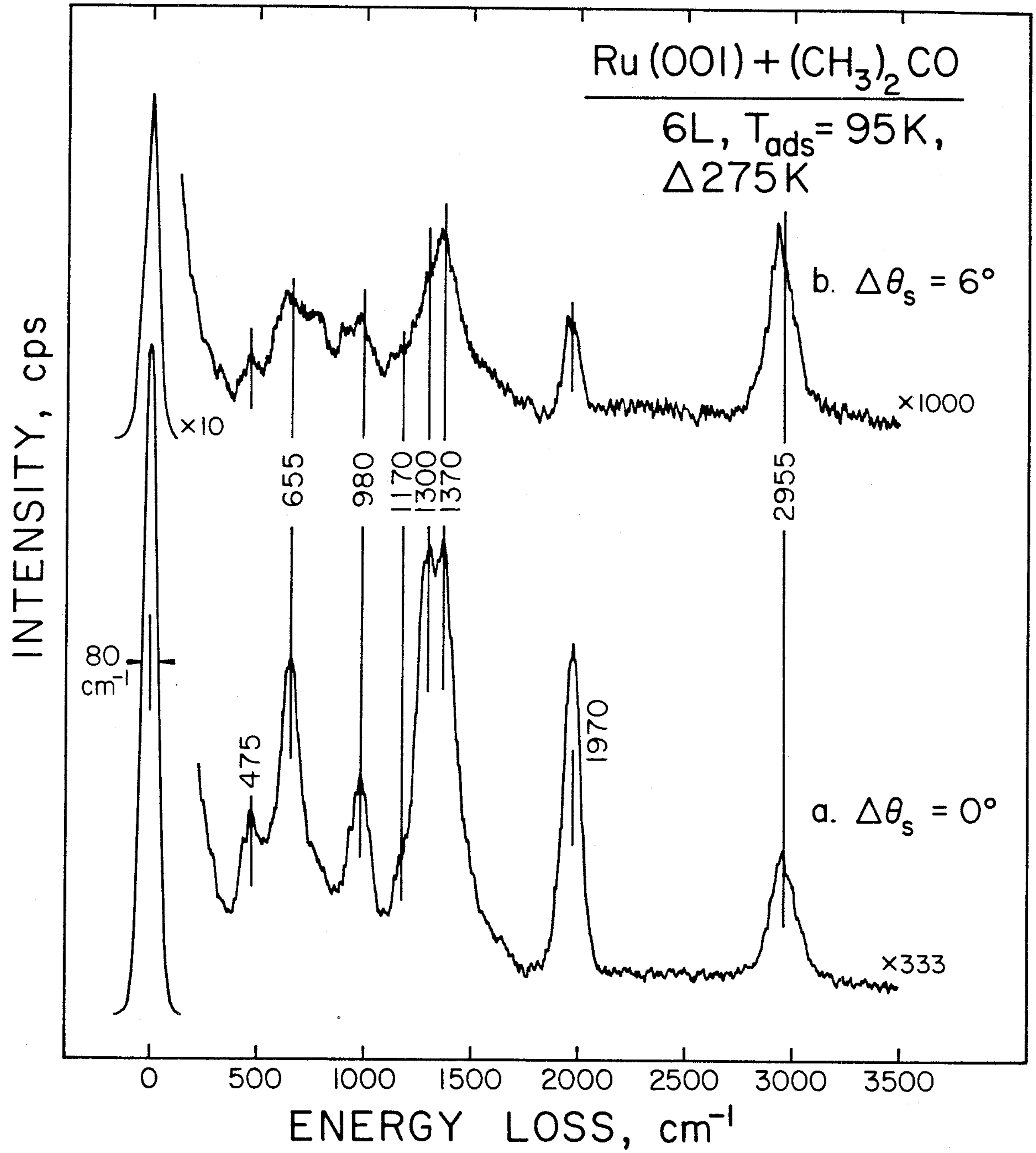
Ru (001) + $(CH_3)_2CO$
6L, T_{ads}= 95 K,
Δ275 K
b. $\Delta\theta_s$ = 6°
a. $\Delta\theta_s$ = 0°
×10
×1000
×333
80 cm^{-1}
475
655
980
1170
1300
1370
1970
2955
INTENSITY, cps
ENERGY LOSS, cm^{-1}
0
500
1000
1500
2000
2500
3000
3500

Figure 8

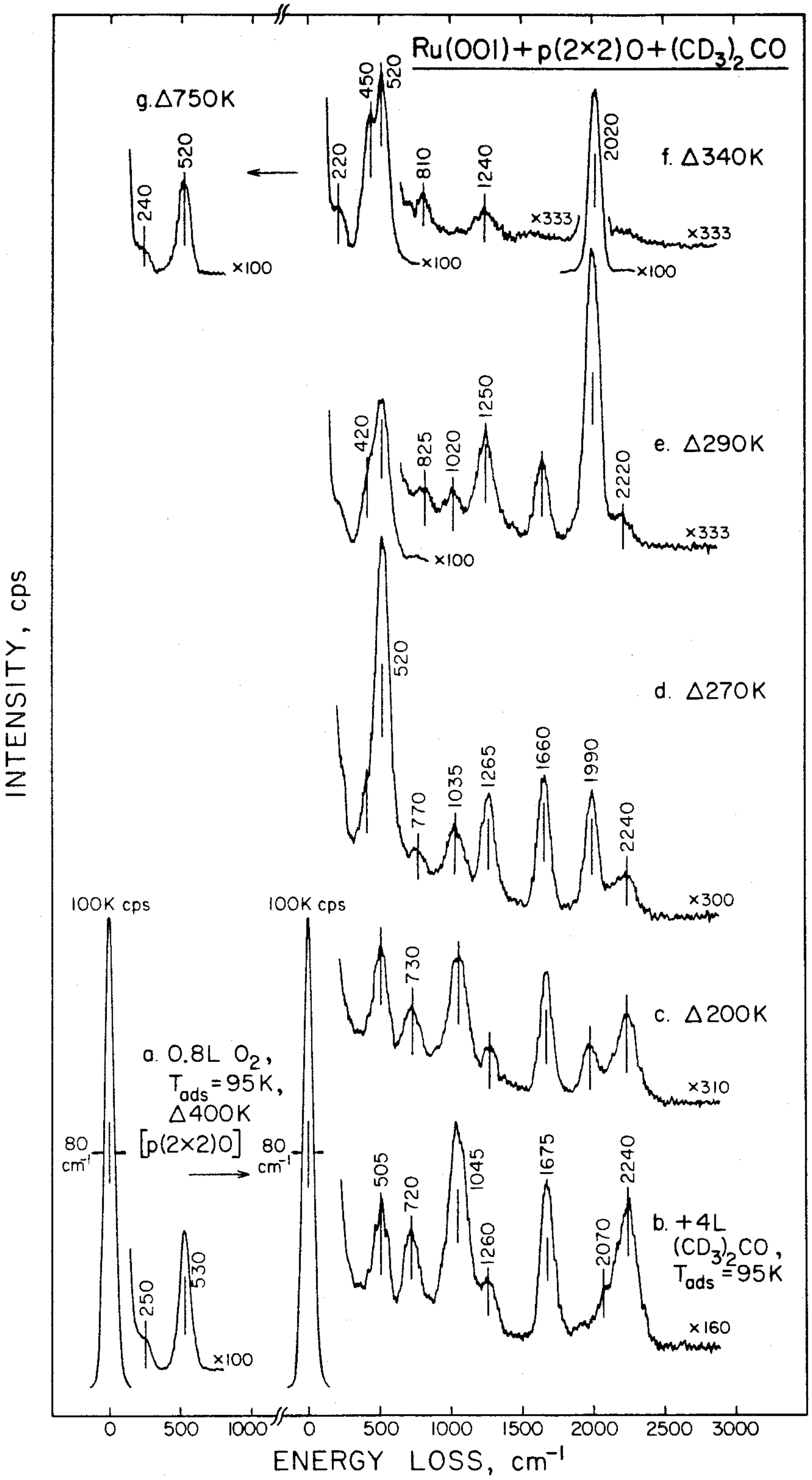
Ru(001)+p(2×2)O+(CD$_3$)$_2$CO
g. Δ750K
240
520
×100
f. Δ340K
220
450
520
810
1240
×333
2020
×100
×333
×100
e. Δ290K
420
825
1020
1250
2220
×100
×333
d. Δ270K
520
770
1035
1265
1660
1990
2240
×300
100K cps
100K cps
c. Δ200K
730
×310
a. 0.8L O$_2$,
T$_{ads}$=95K,
Δ400K
[p(2×2)O]
80 cm^{-1}
80 cm^{-1}
250
530
×100
505
720
1045
1260
1675
2070
2240
b. +4L
(CD$_3$)$_2$CO,
T$_{ads}$=95K
×160
INTENSITY, cps
0
500
1000
0
500
1000
1500
2000
2500
3000
ENERGY LOSS, cm^{-1}

Figure 9

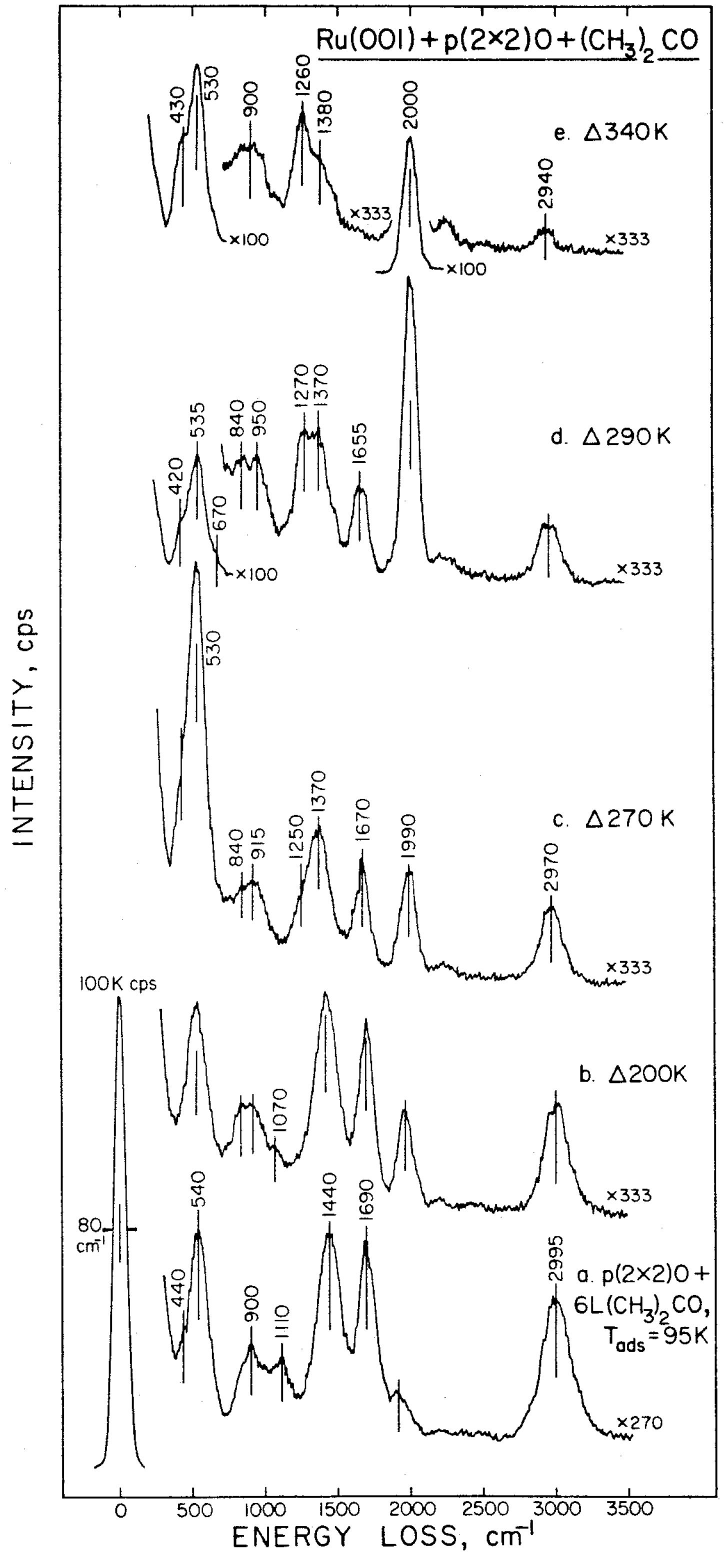
Ru(001) + p(2×2)O + $(CH_3)_2CO$
e. Δ340 K
430
530
900
1260
1380
2000
2940
×333
×100
×100
×333
d. Δ290 K
420
535
670
840
950
1270
1370
1655
×100
×333
c. Δ270 K
530
840
915
1250
1370
1670
1990
2970
×333
100K cps
b. Δ200K
1070
×333
80 cm⁻¹
a. p(2×2)O + 6L $(CH_3)_2CO$, T_{ads} = 95K
440
540
900
1110
1440
1690
2995
×270
INTENSITY, cps
0
500
1000
1500
2000
2500
3000
3500
ENERGY LOSS, cm⁻¹

Figure 10

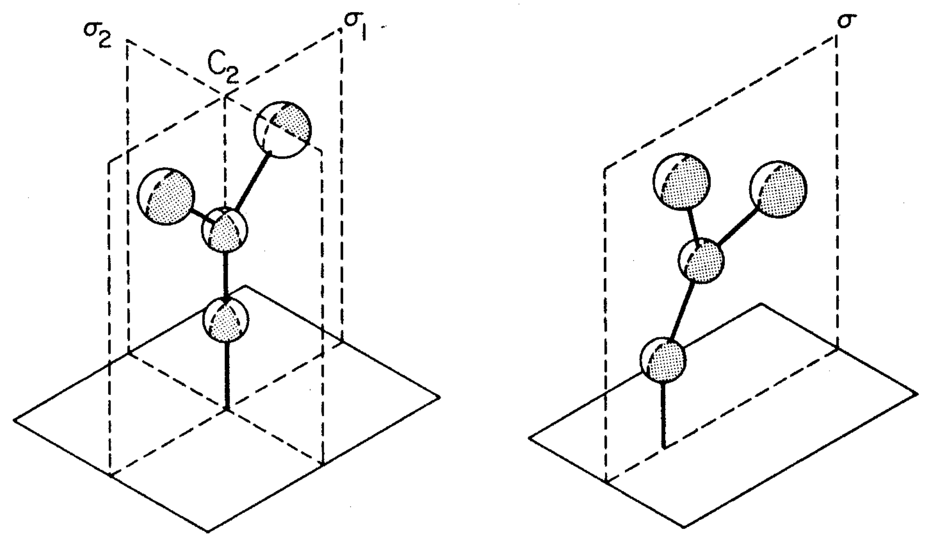

(a) η^1-C_{2v} (b) η^1-C_s

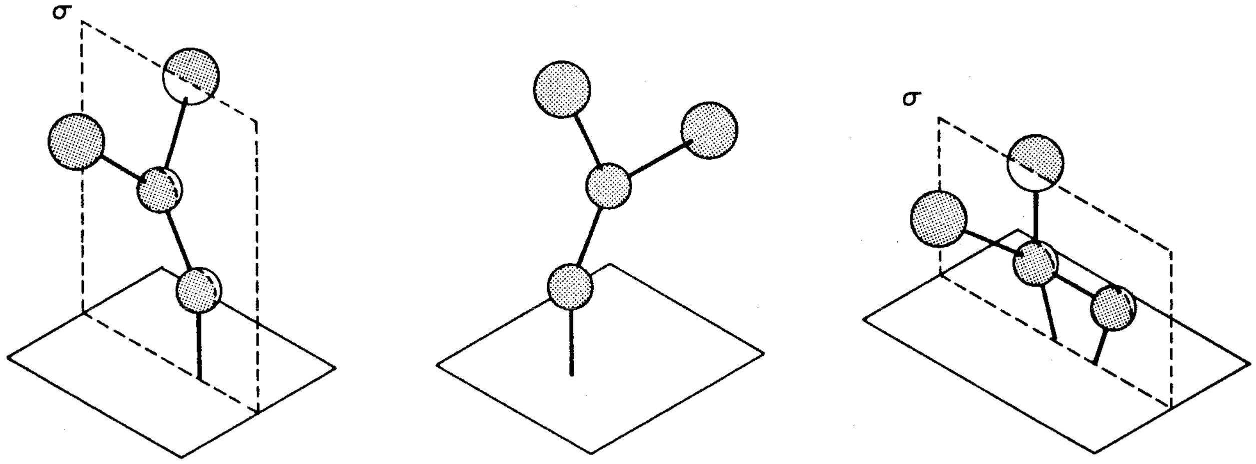

(c) η^1-C_s (d) η^1-C_1 (e) η^2-C_s

Figure 11

Chapter VII.

Adsorption and Decomposition of Formaldehyde on the Ru(001) Surface:

The Spectroscopic Identification of η^2–H_2CO and η^2-HCO

Adsorption and Decomposition of Formaldehyde on the Ru(001) Surface: The Spectroscopic Identification of η^2–H_2CO and η^2-HCO

by

A. B. Anton, J. E. Parmeter and W. H. Weinberg*

Division of Chemistry and Chemical Engineering
California Institute of Technology
Pasadena, CA 91125

April 1985

To be submitted as a Communication to the *Journal of the American Chemical Society*

Abstract

The adsorption of formaldehyde on the Ru(001) surface has been investigated using high-resolution electron energy loss spectroscopy. At coverages approaching a saturated monolayer, an η^2-formaldehyde species is identified. Lower coverage spectra reveal the presence of an η^2-formyl species. Pre-adsorption of hydrogen inhibits the formation of η^2-formyl, and η^2-formaldehyde becomes the majority species at low coverage. This work represents the first spectroscopic identification of either η^2-formaldehyde or η^2-formyl on any metal surface.

The interaction of formaldehyde with transition metal surfaces is of obvious importance in view of the fact that species such as M-CH_2O and M-CHO may play a key role in the catalytic hydrogenation of carbon monoxide **(1-3)**. Recently, several organometallic complexes have been identified in which both formaldehyde **(4-7)** and the formyl group **(8)** function as dihapto (η^2-) ligands. In this Communication, we report the results of high-resolution electron energy loss (HREELS) measurements of formaldehyde adsorbed on the hexagonally close-packed Ru(001) surface that demonstrate the existence of both η^2–H_2CO and η^2-HCO. This represents the first spectroscopic identification of either species on any metal surface.

The ultrahigh vacuum (UHV) system in which the experiments were performed has been described previously **(9)**. HREELS was used to identify surface reaction products after adsorption at 80 K, subsequent annealing up to 600 K, and recooling to 80 K to record the spectra. Gaseous H_2CO and D_2CO were produced by thermal dehydration and depolymerization of their parent polyoxymethylene glycols (paraformaldehyde) and were introduced into the UHV chamber through a leak valve. The H_2CO (D_2CO) produced by this method contains 3-5% H_2O (D_2O) impurity **(10)**, and, consequently, spectra recorded after heating below 170 K are expected to show vibrational features attributable to small amounts of coadsorbed water **(11)**.

Exposing the Ru(001) surface at 80 K to 7 L (1 L = 1 Langmuir = 10^{-6} Torr-s) or more of H_2CO or D_2CO results in the formation of molecular multilayers of formaldehyde, as evidenced by a comparison of the observed vibrational spectra to the IR spectrum of gaseous formaldehyde **(12)**. Annealing the surface to 140 K desorbs the multilayer, leaving adsorbed carbon monoxide (θ = 0.20 CO molecules/Ru surface atom) **(13)**, hydrogen adatoms (θ = 0.40) **(14)**, and another surface species (θ = 0.10) which is stable to approximately 250 K. This new species is identified as η^2-formaldehyde. The spectra for H_2CO and D_2CO are shown at the top of Fig. 1, and mode assignments are given in Table I. The observed CO stretching frequency of approximately 1000 cm^{-1} is consistent with a reduction in bond order of the CO bond from double to single and is in good agreement with the CO stretching frequency of 1017 cm^{-1} for η^2–H_2CO in the organometallic compound $(PPh_3)_2(CO)_2Os(\eta^2-H_2CO)$ **(4)**. The observed frequencies and deuteration shifts for the various CH_2 modes agree well with those observed for sp^3 -CH_2- groups in various molecules **(15)**.

Spectra of lower coverages of H_2CO or D_2CO on Ru(001) at 80 K reveal a species which is fundamentally different from the η^2-formaldehyde that results after annealing the formaldehyde multilayer. The spectra obtained after clean Ru(001) is exposed to 0.8 L H_2CO (or D_2CO) at 80K are shown at the bottom of Fig. 1. Although there is significant decomposition to adsorbed carbon monoxide (θ = 0.15) and hydrogen (θ = 0.30), additional loss features due to another adsorbed species (θ = 0.05) are observed at 2900, 1400, 1180, 1065 and 590 cm^{-1} for H_2CO, and at 1160, 980, 825 and near 550 cm^{-1} for D_2CO. Heating to 100 K causes these features to disappear as this species decomposes to carbon monoxide admolecules and hydrogen adatoms. Weak features at 800 and 1590 cm^{-1} in the H_2CO spectrum and at 360 and 1150 cm^{-1} (obscured by the stronger mode at 1160 cm^{-1} associated with D_2CO adsorption in the spectrum of Fig. 1) in the D_2CO spectrum persist to 170 K, the desorption temperature of water from the Ru(001) surface, and can be identified readily with librational and scissoring modes of small amounts of coadsorbed H_2O and D_2O, respectively **(11)**. The spectra in the bottom panel of Fig. 1 can be identified unambiguously as an η^2-HCO (η^2-DCO) adspecies **(8)**, and the mode assignments are given in Table II. The presence of the η^2-formyl is perhaps not surprising in view of the fact that there is substantial decomposition of the formaldehyde to adsorbed carbon monoxide and hydrogen at low surface coverages, and η^2-formaldehyde exists at saturation monolayer coverage. The formyl ligand, although not heretofore identified on a surface, has been observed as a product of the interaction of formaldehyde with metal centers in organometallic compounds **(1,4,5)**. As would be expected, there is excellent agreement between the vibrational frequencies of the η^2-HCO (η^2-DCO) bonded to the Ru(001) surface and the corresponding vibrational frequencies of the HCO (DCO) function of the "model compound" $HCOOCH_3$ ($DCOOCH_3$) **(15)**, of which the latter are listed also in Table II. The mode at 590 cm^{-1} (550 cm^{-1}) for η^2-HCO (η^2-DCO) is assigned to the frustrated translation of the formyl perpendicular to the surface, its rather high frequency a natural consequence of the relatively low mass of HCO (DCO) and the stiffness of the (one) Ru-O and (two) Ru-C bonds which coordinate it to the surface.

The conditions that lead to the formation of η^2-HCO and η^2–H_2CO provide a consistent picture of the mechanism of H_2CO decomposition on the Ru(001) surface. The η^2-HCO is favored over η^2–H_2CO at low surface coverages because there exist vacant sites at which a hydrogen atom from the decomposing η^2–H_2CO may bind. At higher coverages the absence of such vacant sites inhibits decomposition and favors the formation of η^2–H_2CO. Indeed, precoverage of the Ru(001) surface by a saturation exposure (3L) of H_2, followed by exposure to H_2CO at 80 K, results in the formation of η^2–H_2CO at all submonolayer coverages, with essentially no dissociation to adsorbed CO and hydrogen at 80 K.

The spectroscopic identifications put forward in this Communication have been confirmed by off-specular HREELS measurements, thermal desorption mass spectrometry results, and complementary experiments concerning H_2CO and D_2CO adsorption on the Ru(001) surface modified by the presence of a p(2x2) ordered overlayer of oxygen adatoms. A complete discussion of all of these results will be presented separately **(16)**.

Acknowledgment: This research was supported by the National Science Foundation under Grant No. CHE-8206487. The assistance of Dr. Neil Avery in the early stages of this work is very much appreciated.

References

1. Muetterties, E. L.; Stein, J., *Chem. Rev.* **1979**, 79, 479-490.
2. Eisenberg, R.; Hendricksen, D. E. *Advan. Catal.* **1979**, 28, 79-172.
3. Dombek, B. D., *Advan. Catal.* **1983**, 32, 325-416.
4. Brown, K. L.; Clark, G. R.; Headford, C. E. L.; Marsden, K.; Roper, W. R., *J. Am. Chem. Soc.* **1979**, 101, 503-505.
5. Gambarotta, S.; Floriani, C.; Chiesi-Villa, A.; Guastini, C., *J. Am. Chem. Soc.* **1982**, 104, 2019-2020.
6. Buhro, W. E.; Patton, A. T.; Strouse, C. E.; Gladysz, J. A.; McCormick, F. B.; Etter, M. C., *J. Am. Chem. Soc.* **1983**, 105, 1056-1058.
7. Kropp, K.; Skibbe, V.; Erker, G.; Krüger, C., *J. Am. Chem. Soc.* **1983**, 105, 3353-3354.
8. Belmonte, P. A.; Cloke, F. G. N.; Schrock, R. R., *J. Am. Chem. Soc.* **1983**, 105, 2643-2650.
9. Thomas, G. E.; Weinberg, W. H., *Rev. Sci. Instrum.* **1979**, 50, 497-501.
10. Walker, J. F., "Formaldehyde", Reinhold, New York, p. 142, 1964.
11. Thiel, P. A.; Hoffmann, F. M.; Weinberg, W. H., J. Chem. Phys. **1981**, 75, 5556-5572.
12. Herzberg, G., "Infrared and Raman Spectra", p. 300, D. Van Nostrand Co., New York, 1945.
13. Thomas, G. E.; Weinberg, W. H., *J. Chem. Phys.* **1979**, 70, 954-961, 1437-1439. Weinberg, W. H., *Methods of Experimental Physics* **1985**, 22, 23-125.
14. Barteau, M. A.; Broughton, J. Q.; Menzel, D., *Surface Sci.* **1983**, 133, 443-452.
15. Shimanouchi, T., "Tables of Vibrational Frequencies", Consolidated Vol. I, NSRDS-NBS 39; Vol. II.

16. A. B. Anton, J. E. Parmeter and W. H. Weinberg, to be published.

Table I. Mode assignments for η^2–H_2CO (η^2–D_2CO) on Ru(001).

Mode	η^2–H_2CO cm^{-1}	η^2–D_2CO cm^{-1}	Frequency Ratio (H_2CO/D_2CO)
ν(CO)	980	1020	0.96
$\nu_a,\nu_s(CH_2)$	2940	2225	1.32
$\delta(CH_2)$	1450	1190	1.22
$\omega(CH_2)$	1160	865	1.34
$\rho(CH_2)$	840	620	1.35

Table II. Mode assignments for η^2-HCO (η^2-DCO) on Ru(001), with corresponding assignments from the model compound $HCOOCH_3$ ($DCOOCH_3$) (see Ref. 15).

Mode	η^2-HCO cm^{-1}	$HCOOCH_3$ cm^{-1}	η^2-DCO cm^{-1}	$DCOOCH_3$ cm^{-1}
ν(CH)	2900	2943	†	2216
δ(CH)	1400	1371	980	1048
ν(CO)	1180	1207	1160	1213
π(CH)	1065	1032	825	870
ν(Ru-HCO)	590	-	550	-

†Weak and not resolved from the tail of the strong feature due to adsorbed CO at 1990 cm^{-1}.

Figure Caption

Figure 1. High resolution electron energy loss spectra of (1) a multilayer exposure (10 L) of H_2CO (D_2CO) adsorbed on Ru(001) at 80 K and annealed to 250 K, and (2) a submonolayer exposure (0.8 L) of H_2CO (D_2CO) on Ru(001) at 80 K. The spectra in (1) are characteristic of η^2-formaldehyde, and those in (2) are characteristic of η^2-formyl. In all these spectra, intense modes near 450 and 2000 cm^{-1} are due to adsorbed CO from formaldehyde decomposition, as is the weak combination band occasionally observed near 2450 cm^{-1} **(13)**. Adsorbed hydrogen adatoms from formaldehyde decomposition are not observed due to their extremely small scattering cross section **(14)**. Features at 800 and 1590 cm^{-1} in the H_2CO spectrum of (2) and near 360 cm^{-1} in the D_2CO spectrum of (2) are due to H_2O and D_2O **(11)**, respectively, to which the crystal is exposed unavoidably during the adsorption of H_2CO and D_2CO at 80 K.

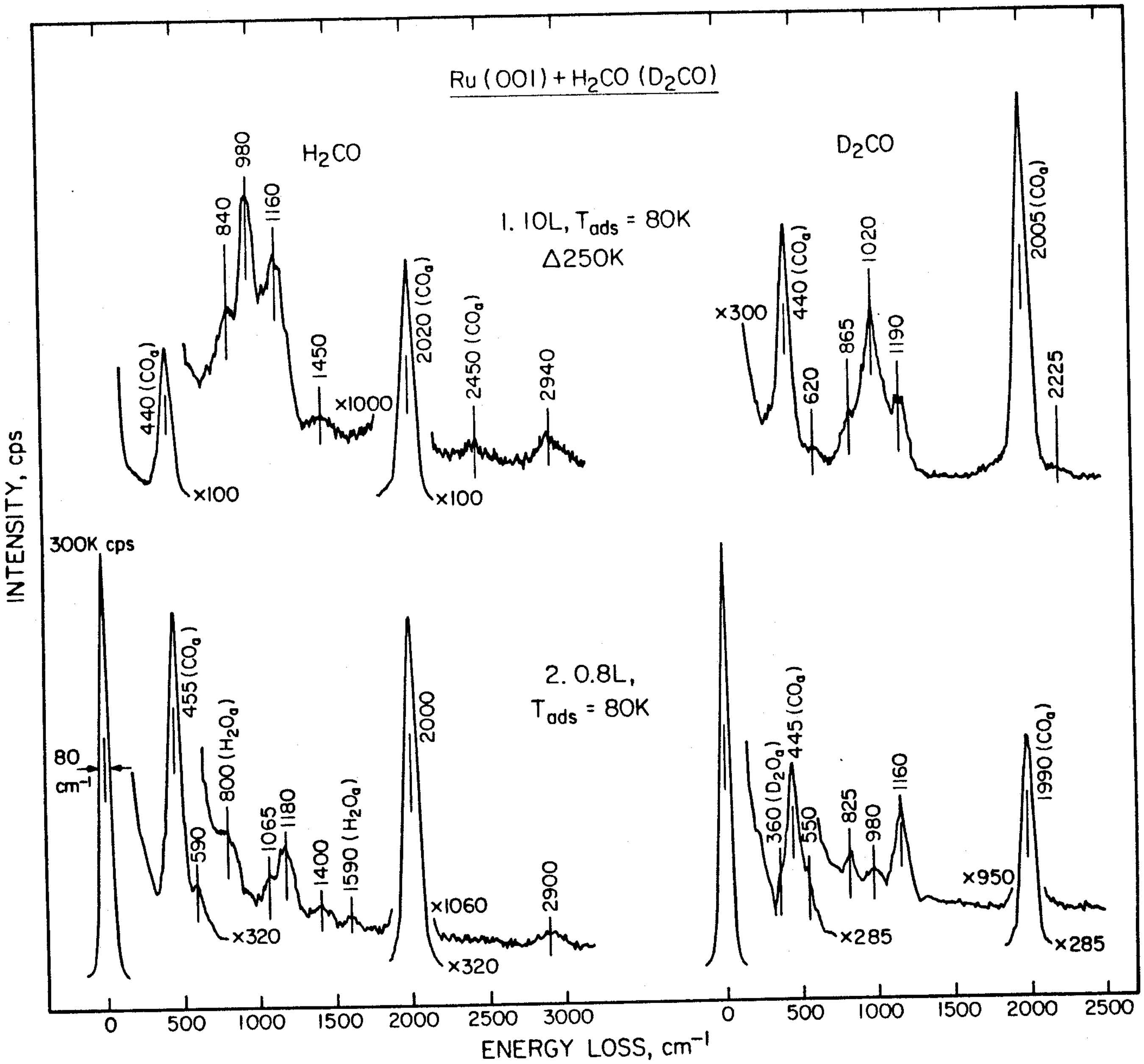
Ru (001) + H_2CO (D_2CO)
H_2CO
D_2CO
1. 10L, T_{ads} = 80K
Δ250K
2. 0.8L,
T_{ads} = 80K
440 (CO_a)
840
980
1160
1450
x1000
x100
2020 (CO_a)
2450 (CO_a)
2940
x100
x300
440 (CO_a)
620
865
1020
1190
2005 (CO_a)
2225
300K cps
80 cm^{-1}
455 (CO_a)
590
800 (H_2O_a)
1065
1180
1400
1590 (H_2O_a)
x320
2000
x1060
2900
x320
360 (D_2O_a)
445 (CO_a)
550
825
980
1160
x285
x950
1990 (CO_a)
x285
INTENSITY, cps
0
500
1000
1500
2000
2500
3000
0
500
1000
1500
2000
2500
ENERGY LOSS, cm^{-1}

Figure 1

Chapter VIII.

The Adsorption of Formaldehyde on the Ru(001) and Ru(001)-p(2x2)O Surfaces

Adsorption of Formaldehyde on the Ru(001) and Ru(001)-p(2x2)O Surfaces

by

A. B. Anton, J. E. Parmeter and W. H. Weinberg*

Division of Chemistry and Chemical Engineering
California Institute of Technology
Pasadena, CA 91125

Submitted to *The Journal of the American Chemical Society*

July 1985

Abstract

The adsorption of formaldehyde on the clean Ru(001) surface and a Ru(001) surface on which an ordered p(2x2) overlayer of oxygen adatoms is present has been investigated via high resolution electron energy loss vibrational spectroscopy (EELS) and thermal desorption mass spectrometry (TDMS). On the clean Ru(001) surface, the formaldehyde-surface bonding interaction at 80 K is primarily via π_{CO} donation and π^*_{CO} backdonation, leading to decomposition to adsorbed hydrogen and CO for low exposures. With subsequent exposure to formaldehyde, a small fractional surface coverage (θ = 0.02-0.03) of η^2-formyl is observed, followed by formation of η^2-formaldehyde (θ = 0.10) and η^1-formaldehyde at saturation (monolayer) coverage. Upon heating, the η^2-formyl decomposes to adsorbed hydrogen and CO by 120 K, and the η^1-formaldehyde desorbs molecularly between 130 and 180 K. After annealing the surface to 250 K, the EEL spectrum of the η^2-formaldehyde (θ = 0.03) is obtained (together with adsorbed CO from decomposition). Further heating decomposes the remaining η^2-formaldehyde, and thermal desorption measurements indicate that a total of a quarter-monolayer of formaldehyde decomposes on the Ru(001) surface under these conditions. The presence of the p(2x2)O overlayer (θ = 0.25) withdraws charge from the surface ruthenium atoms, increasing their Lewis acidity and making σ lone pair donation the dominant formaldehyde-surface bonding interaction. Under these conditions, only η^1–formaldehyde can be identified via EELS for all submonolayer coverages after adsorption at 80 K. After annealing the surface to 300 K to desorb η^1–formaldehyde, EEL spectra show weak bands due to small amounts of η^2–formaldehyde (θ = 0.01) and η^2-formate (θ = 0.04). Compared to the clean surface, more molecular desorption of formaldehyde is observed in the 130-180 K temperature range, and the decomposition activity, as evidenced by the amount of CO and H_2 evolved from the surface, is decreased by

a factor of two from a quarter to an eighth of a monolayer.

I. Introduction

Although the study of surface reactions under ultrahigh vacuum (UHV) conditions allows the application of powerful spectroscopic techniques such as high resolution electron energy loss spectroscopy (EELS) for the identification of stable adsorbed intermediates, the absence of a significant pressure of gas phase reactants renders practical only investigations of surface reactions in which the activation energy of the reaction is on the order of, or less than, the activation energy of desorption of the reactants. For this reason, studies which seek to elucidate the mechanistic details of technologically important heterogeneously catalyzed synthesis reactions under these conditions usually must proceed via adsorption of the reaction products of interest and investigate the reverse decomposition reactions. Surface species that are observed as stable intermediates in the decomposition reactions identify the minimum energy configurations for the adsorbate/surface interaction and therefore the plausible channels through which the reverse synthesis reactions should proceed.

A number of investigations have sought to elucidate the details of the heterogeneously catalyzed reaction of CO with H_2 to form methanol via studies of methanol adsorption and thermal decomposition on single crystalline metal surfaces. Studies on Ni(111) **(1)**, Cu(100) **(2)**, Pt(111) **(3)**, Pd(100) **(4)** and Ru(001) **(5)**, which have included results of EELS experiments to identify surface intermediates during the annealing of adsorbed overlayers of methanol, have demonstrated the formation of an adsorbed methoxy intermediate [(g) denotes gaseous species and (a) adsorbed species], i.e.

$$CH_3OH(g) \rightarrow CH_3OH(a)$$

and

$$CH_3OH(a) \rightarrow CH_3O(a) + H(a)\ .$$

Heating of the surfaces to temperatures near 300 K resulted in decomposition of the adsorbed methoxy to yield H(a) and CO(a):

$$CH_3O(a) \rightarrow 3H(a) + CO(a)\ .$$

No stable intermediates other than the methoxy could be isolated, indicating that intermediates in the methoxy decomposition, e.g. $H_2CO(a)$ or HCO(a), are less stable and decompose rapidly compared to the methoxy. The study of the chemisorption and thermal decomposition of formaldehyde on these metal surfaces may afford an opportunity to investigate the structures of adsorbed formaldehyde [$H_2CO(a)$] and formyl [HCO(a)] intermediates, providing a more complete mechanistic picture of methanol decomposition [and by inference, methanol synthesis from H_2 and CO **(6)**] in terms of elementary surface reactions. Pursuit of this information provides the motivation for the present study of formaldehyde adsorption on the Ru(001) surface **(7)**.

Several investigations of the adsorption and reaction of formaldehyde on single crystalline metal surfaces under UHV conditions have been reported, and a wide variety of surface reaction products have been observed via thermal desorption mass spectrometry (TDMS). Spectroscopic information necessary to identify adsorbed reaction intermediates is sparse, however, and the details of the surface reaction mechanisms which provide the observed products have yet to be delineated unequivocally. In particular, the surface intermediates pertinent to an understanding of methoxy decomposition and CO hydrogenation reactions were not isolated and observed. The results of these investigations do, however, provide interesting comparisons and contrasts to those reported here for the adsorption of formaldehyde on the clean Ru(001) and the Ru(001)-

p(2x2)O surfaces.

An early investigation of formaldehyde adsorption on W(100) and W(111) surfaces employing TDMS demonstrated the evolution of H_2 and CO as the principal reaction products, with small amounts of CO_2 and methane produced only at coverages approaching a saturated monolayer **(8)**. A more recent TDMS study of formaldehyde adsorption on clean and carbided W(100) surfaces showed qualitatively similar results, but also indicated minority evolution of a small amount of methanol from the clean surface and the evolution of methyl formate together with enhanced formation of methanol and methane from the carbided, as compared to the clean, W(100) surface **(9)**. On Ni(110), formaldehyde adsorption yielded H_2, CO, CO_2, H_2O and methanol as reaction products **(10)**, and a more recent investigation of the same system **(11)**, which also included EELS results to identify surface intermediates, qualitatively duplicated the TDMS results of the previous investigation and showed that, in addition to hydrogen and CO from formaldehyde decomposition, methoxy is the primary surface intermediate, and mixed multilayers of solid formaldehyde and polymeric paraformaldehyde are formed at high coverages. Products similar to those observed for the reaction of formaldehyde with tungsten and nickel surfaces were also reported for clean and sulfided Pt(111) surfaces **(12)**. On an oxygen precovered Ag(110) surface **(13)**, EEL spectra showed condensed multilayers of solid formaldehyde at 100 K, spectra consistent with an η^2-dioxymethylene species or paraformaldehyde after annealing to 200 K, and decomposition to evolve H_2 and CO_2 through a formate intermediate upon heating the surface to 500 K. Similar results were obtained in a more recent investigation of formaldehyde adsorption on clean and oxygen precovered Cu(110) surfaces **(14)**, where EELS identified paraformaldehyde as the only monolayer species on both surfaces at low temperatures. Depolymerization of adsorbed paraformaldehyde released formaldehyde from both surfaces at 225 K. However, EEL spectra for the oxygen precovered surface showed that a reaction of formaldehyde with coadsorbed oxygen also occurred, producing some adsorbed formate which decomposed to yield CO_2 and H_2 near 470 K.

More pertinent to the results reported here are studies of the homogeneous chemistry and structures of coordinated formaldehyde and formyl intermediates and their potential importance in metal catalyzed CO hydrogenation reactions **(15-17)**. Several stable compounds displaying η^2(O,C) coordination geometries [bonded to the metal atom(s) through both the oxygen and carbon atoms of the carbonyl function, hereafter referred to simply as η^2] for formaldehyde **(18,21)** and acetaldehyde **(22)** have been synthesized and characterized structurally. Furthermore, evidence for η^1(O) coordination [bonded end-on to the metal atom through only the oxygen atom, hereafter referred to simply as η^1] has been obtained for a formaldehyde complex of ruthenium **(23)**. Structures analogous to both of these have been observed for the adsorption of the structurally similar acetone molecule on the Ru(001) surface **(24)**. Finally, η^1-formyl **(23,25-29)**, η^2-formyl **(30-32)** and similar η^1-acyl complexes **(33-37)** have also been synthesized and characterized structurally.

This paper presents an EELS and TDMS investigation of the adsorption and reactions of formaldehyde on both the clean Ru(001) surface and a Ru(001) surface modified chemically by the presence of an ordered p(2x2) overlayer of oxygen adatoms. The results of the experiments conducted on the clean Ru(001) surface differ from those described earlier for other single crystalline metal surfaces in that no evidence for associative reactions on the surface is obtained. Instead, only reversible molecular adsorption and decomposition to hydrogen and CO through intermediates similar to those observed in the homogeneous chemistry of model CO hydrogenation reactions are observed. For this reason, extensive comparison to the structural and spectroscopic properties of the model homogeneous compounds mentioned previously will be made to facilitate interpretation of the EELS results for adsorption of formaldehyde on the clean Ru(001) surface. Addition of the p(2x2) oxygen overlayer not only provides an adsorbed reactant which may open surface reaction channels that did not exist on the clean surface, but it also withdraws charge from the surface ruthenium atoms, increasing their Lewis acidity and altering their reactivity toward the reactions identified on the clean surface. In all EELS results reported here, spectra for both H_2CO and D_2CO are included to verify the vibrational assignments and the conclusions concerning the structures of the adsorbed species. The results provide an interesting and chemically consistent comparison to those obtained previously for the adsorption of acetone on the same clean and oxygen modified surfaces **(24)**.

II. Experimental Procedures

A description of the EEL spectrometer and the UHV system in which it is contained has been published previously **(38)**. EEL spectra were recorded at a resolution of 80 cm^{-1} (full-width at half-maximum) with a count rate of 3 x 10^5 c.p.s. in the specularly reflected, elastically scattered electron beam. Incident electron beam kinetic energies at the sample were 5-6 eV.

The Ru(001) surface was cleaned by thermal cycling between 400 and 1100 K in 10^{-7} Torr of oxygen to remove surface impurities, followed by reductive annealing in vacuum at 1750 K **(39)**. Occasional Ar^+ sputtering was also used to clean the surface. Surface cleanliness was monitored via both EELS and TDMS, and the surface was judged clean when the EEL spectrum was featureless and the peak intensities and temperatures for thermal desorption spectra of various coverages of CO were reproduced. The ordered p(2x2) overlayer of oxygen adatoms, with an ideal surface coverage of 0.25 monolayer, was prepared by exposing the clean surface to 0.8 L of O_2 ($1L \equiv 10^{-6}$ Torr-s) at 95 K, followed by thermal ordering at a temperature of approximately 350 K **(40,41)**.

Gaseous H_2CO and D_2CO were produced by thermal dehydration and depolymerization of their parent polyoxymethylene glycols (paraformaldehyde), and the crystal surface was exposed to these gases by backfilling the UHV chamber through leak valves. Exposures quoted in the text were measured with a Bayard-Alpert ionization gauge, uncorrected for relative ionization cross sections.

Preparation of pure monomeric formaldehyde from paraformaldehyde is in general quite difficult, as has been discussed by Walker **(42)**. Water is an unavoidable product of the thermal depolymerization reaction (n = degree of polymerization)

$$H(H_2CO)_nOH \rightarrow nH_2CO(g) + H_2O(g) ,$$

and high grade paraformaldehydes as were used in this work [H_2CO from Aldrich Chemical Co., and D_2CO from U.S. Services Inc. (98 atom % D)] have an average degree of polymerization near 30. Thus the vapor produced by thermal depolymerization is expected to contain approximately 3 mole % water. Further purification of the vapor, for example by treatment with standard chemical drying agents, is in general fruitless, since these materials also catalyze the decomposition and polymerization of formaldehyde **(42)**. The formaldehyde used in these experiments was purified by extensive pumping on the solid paraformaldehyde prior to thermal depolymerization. Storage lines which held formaldehyde prior to introduction into the UHV chamber were cleaned and refilled frequently, and the composition of the vapor introduced into the UHV chamber was checked *in situ* via mass spectrometry. More elaborate means for producing dry monomeric formaldehyde **(42)** were not attempted. Fortunately, the adsorption properties of water on both the clean **(43)** and oxygen precovered **(44)** Ru(001) surfaces have been characterized thoroughly by both TDMS and EELS, allowing extraction from the EEL spectra for formaldehyde adsorption those features attributable to the presence of small amounts of coadsorbed water after annealing of the surface to temperatures below 170 K [the low coverage desorption temperature for water on Ru(001)].

Another impurity in formaldehyde that is produced from depolymerization of paraformaldehyde is methyl formate, which is formed by the Tischenko reaction **(42)**:

$$2H_2CO \rightarrow HCOOCH_3 .$$

The problem of methyl formate contamination in formaldehyde vapor has been discussed in Ref. 8, where mass spectra for both purified and methyl formate contaminated formaldehyde are shown for comparison. Mass spectra for the H_2CO and D_2CO used in the experiments reported here showed only trace levels of $HCOOCH_3$ and $DCOOCD_3$ contaminants.

Although formaldehyde used in the experiments reported in Refs. 8 through 14 was prepared by methods nearly identical to those employed here, in most cases little or no mention is made of the presence of water and methyl formate impurities and their potential importance on the chemistry of the surfaces investigated. For example, small amounts of methane, carbon dioxide and methyl formate evolution in TDMS after large formaldehyde exposures **(8,9,12)** may be attributable to the adsorption and/or reaction of a methyl formate contaminant. Furthermore, the polymerization of formaldehyde to give adsorbed paraformaldehyde **(11,13,14)** may not result from the interaction of formaldehyde with the clean metal surface but rather from the interaction of formaldehyde with adsorbed water, which is known to catalyze formaldehyde polymerization rapidly on rather nonreactive surfaces below 100°C **(42)**.

Thermal desorption measurements were made in a line-of-sight mode with a UTI 100C quadrupole mass spectrometer, oriented approximately 40° from the surface normal. Surface coverages of H_2 and CO reported for the reaction product TDMS measurements were obtained by comparing the time integrated ion current for the desorption spectra to those obtained for desorption of known coverages of H_2 **(45)** and CO **(46)** and are accurate to approximately 10%.

Since adsorbed overlayers were prepared by backfilling the entire UHV chamber, exposing all surfaces which were chilled by contact with the liquid nitrogen reservoir which cooled the sample, and since the mass spectrometer had no provision for selective sampling of the desorption flux from the oriented crystal surface, the features in the thermal desorption spectra associated with desorption from the crystal surface were superposed on a broad background signal due to desorption from all other chilled surfaces which were warmed during the collection of a TDMS trace. For sharp desorption features, as were observed in the thermal desorption spectra for the H_2 and CO decomposition products, the background baselines in the spectra can be identified unambiguously, and the contribution due to desorption from the Ru(001) surface can be separated clearly. For molecular formaldehyde, which condenses on all surfaces at liquid nitrogen temperatures and produces broad monolayer desorption features, the baselines were less certain. In all thermal desorption spectra shown here, best estimates of the baselines due to background desorption have been subtracted for a more useful presentation of the experimental results.

Temperature dependent changes in the vibrational spectra of adsorbed overlayers of formaldehyde were monitored by momentary annealing of the surfaces, followed by rapid cooling to 80 K to record the spectra. It should be noted that the surface spends more net time at each "peak" temperature during this type of thermal cycling than during the TDMS experiments, where a constant monotonic increase of temperature with time is employed. For this reason, thermally activated surface reactions or thermal desorption are expected to have proceeded to further conversion for a given annealing temperature in EELS experiments than the corresponding temperature in a TDMS experiment, and surface species identified by EELS following annealing correspond to those which exist at a slightly higher temperature in TDMS. The exact magnitude of this discrepancy is difficult to estimate, although results of previous experiments indicate that it is less than 50 K **(24)**.

III. Results

A. Thermal Desorption Spectra of Formaldehyde from the Clean Ru(001) and the Ru(001)-p(2x2)O Surfaces

Thermal desorption spectra of D_2CO (m = 32 amu), recorded after the indicated exposures of the clean Ru(001) surface and the Ru(001)-p(2x2)O surface to D_2CO at 80 K are shown at the left and right of Fig. 1, respectively. For exposures of 0.8 L or less of D_2CO on both surfaces, no molecular formaldehyde desorption is observed. For exposure of the clean surface to 1.5 L or more of D_2CO, desorption rate maxima associated with monolayer adsorbed states appear near 130 and 155 K. These features saturate, and the apparent temperatures of their desorption rate maxima shift slightly to lower temperatures for exposures of 5 L or more. Another feature appears near 110 K, the amplitude of which grows without saturation for increasing exposures, indicating that it is associated with multilayers of formaldehyde condensed on the surface. Also evident is a broad, weak feature near 250 K and a small sharp feature near 275 K with constant amplitudes for all exposures of 3 L or more. Binding energies for the monolayer states desorbing at 130, 155 and 275 K, estimated for first-order desorption kinetics via the method of Redhead with $\nu = 10^{13}$- s^{-1} **(47)**, are 7.3, 8.8 and 16.0 kcal/mole, respectively. Similar results are obtained for desorption from the Ru(001)-p(2x2)O surface, although desorption from the monolayer states near 130 and 155 K is enhanced for equivalent exposures compared to the clean surface, and the state at 275 K is extinguished.

Experimental values obtained for the endothermic heat of the formaldehyde depolymerization reaction, i.e.

$$H(H_2CO)_nOH \rightarrow H(H_2CO)_{n-1}OH + H_2CO(g)$$

range between 14.6 and 17.3 kcal/mole **(48)**. In the absence of an activation barrier to depolymerization other than the endothermicity of the reaction, depolymerization of paraformaldehyde on the surface should yield formaldehyde at a temperature near that which would result from first-order desorption kinetics with an activation energy equal to the heat of depolymerization, i.e. 250-300 K. On Ag(110) **(13)** and Cu(110) **(14)**, for example, depolymerization of surface paraformaldehyde evolved formaldehyde from the surface at 250 and 225 K, respectively. (The corresponding activation energies are 15.0 and 13.9 kcal/mole.) This suggests that the desorption state at 275 K for formaldehyde adsorption on Ru(001) may be due to depolymerization of a very small amount of paraformaldehyde at this temperature. It is of course also possible that this feature results from desorption of a small amount of another molecularly adsorbed formaldehyde species at high surface coverages which is bonded more strongly to the clean Ru(001) surface (the binding energy corresponding to desorption at 275 K is 16.0 kcal/mole) than that which desorbs between 130 and 155 K. The relative merits of these two possibilities will be considered further after the surface reactions and intermediates accompanying formaldehyde adsorption and desorption are identified through the results of the EELS measurements.

B. Thermal Desorption Spectra of the Decomposition Products, CO and H_2, from Formaldehyde on the Clean Ru(001) and the Ru(001)-p(2x2)O Surfaces

To check for the possible formation of surface reaction products like those identified in earlier studies of formaldehyde adsorption on single crystalline metal surfaces, thermal desorption spectra were recorded at m = 20 amu (D_2O^+, CD_4^+), m = 34 amu (CD_3O^+, the principal cracking fragment of CD_3OH), m = 44 amu (CO_2^+) and m = 64 amu ($DCOOCD_3^+$), in addition to m = 4 amu and m = 28 amu for the principal reaction products, D_2 and CO. No desorption at m = 44 and m = 64 amu could be detected for monolayer saturation exposures of both the clean Ru(001) and the Ru(001)-p(2x2)O surfaces to D_2CO at 80 K, and only weak features with intensities lower than those observed for D_2 and CO by factors of 100 to 1000 were observed at 160 to 180 K for D_2O (m = 20 amu) and 280 to 320 K for CD_3OD (m = 34 amu). It is therefore reasonable to attribute all D_2O and CD_3OD evolved from both the clean Ru(001) and the Ru(001)-p(2x2)O surfaces to impurities in the adsorbed D_2CO and to identify D_2CO, D_2 and CO as the only desorption products resulting from the interaction of D_2CO with both surfaces.

Noteworthy in these results is the absence of significant D_2O production from the reaction of deuterium adatoms from D_2CO decomposition with the oxygen adatoms of the p(2x2)O overlayer. Although evidence for the reaction of adsorbed oxygen with hydrogen on Ru(001) to evolve H_2O has been obtained in the thermal decomposition of adsorbed formic acid **(49)**, the relative likelihood of H_2O (D_2O) production versus H_2 (D_2) desorption depends critically on the ordering of the oxygen overlayer. This can be explained by consideration of two different effects of oxygen ordering on these processes, both of which act to make hydrogen adatom recombination and desorption more likely. First, the formation of the ordered p(2x2)O overlayer upon annealing a disordered overlayer of adsorbed oxygen **(40,41)** indicates that attractive interactions which increase the Ru=O binding energy are maximized in the p(2x2) configuration, increasing the energy barrier to abstraction of adsorbed oxygen by reaction with hydrogen. In addition, and probably of more significance, the p(2x2)O overlayer destabilizes adsorbed hydrogen into a new binding state with a reduced activation energy for desorption, to be discussed below, decreasing the barrier to hydrogen adatom recombination and desorption.

Thermal desorption spectra of CO recorded after exposure at 80 K of both the clean Ru(001) and the Ru(001)-p(2x2)O surfaces to 0.8, 1.5 and 5.0 L (monolayer saturation) of D_2CO are shown at the top of Fig. 2. Also shown for comparison at the bottom of Fig. 2 are spectra recorded after the adsorption of CO. In all these spectra, fractional surface coverages are assigned by comparison to spectra recorded for saturation exposures of the clean surface to CO, where θ_{CO} = adsorbed CO molecules per rutheium surface atom = 49/75 at saturation **(46)**. Since no other reaction products were observed, the CO coverages obtained indicate directly the amount of D_2CO decomposition for each experiment. For 0.8 L exposures of both surfaces to D_2CO, comparable amounts of decomposition are observed, 0.08 monolayer on the clean Ru(001) surface and 0.07 monolayer on the Ru(001)-p(2x2)O surface. As the D_2CO exposure is increased, however, decomposition on the clean surface increases relative to that on the oxygen precovered surface, and for 5 L (monolayer saturation) exposures on both surfaces, the decomposition activity of the clean surface [θ_{CO} = 0.26] is twice that of the Ru(001)-p(2x2)O surface [θ_{CO} = 0.13]. The peak shapes and positions are unperturbed compared to those resulting from adsorption of CO on the same surfaces, suggesting that the surface is free of other adsorbed species which could affect the CO desorption rate.

Thermal desorption spectra of D_2 from the decomposition of adsorbed D_2CO, following exposures of both surfaces to D_2CO equal to those used to generate the CO thermal desorption spectra of Fig. 2, are shown at the top of Fig. 3. For comparison, thermal desorption spectra after D_2 adsorption on both surfaces are shown at the bottom of Fig. 3. Coverages for all the spectra are assigned by comparison to the 4.0 L (monolayer saturation) exposure of D_2 on the clean surface where $\theta_D = 0.85$ **(45)**.

Of particular interest are the spectra recorded for the adsorption of D_2 on the Ru(001)-p(2x2)O surface, shown at the bottom of Fig. 3. Comparison to the 0.2 L spectrum for D_2 adsorption on the clean surface immediately above shows that the average probability of adsorption up to a coverage of approximately $\theta(D) = 0.15$ is increased by a factor of two on the Ru(001)-p(2x2)O surface relative to the clean surface. Desorption of D_2 is complete by 250 K, indicating that the activation energy for desorption is less than 9 kcal/mole [estimated for second-order desorption kinetics via the method of Redhead with $\nu = 10^{-4}$ cm^2s^{-1} **(47)**], as compared to 17.0 kcal/mole on the clean surface **(45)**. The feature near 200 K has the temperature corresponding to its maximum rate of desorption shifting downward with coverage, indicative of second-order desorption kinetics, and at saturation this state contains 0.23 monolayer of deuterium adatoms. The state at lower temperature, which fills after the state at 200 K and is shown expanded by a factor of 0.5 in Fig. 3, contains an additional 0.45 monolayer of deuterium adatoms, and its peak temperature remains constant at 150 K from its initial appearance to the exposure necessary for its saturation (0.4 L). The appearance of a 2:1 stoichiometry for these two states, plus the near match of their populations to the 0.25 monolayer ideal coverage of the p(2x2)O overlayer, suggests that occupation of the state at 200 K contributes stoichiometrically one deuterium atom per p(2x2)O unit cell, and occupation of the state at 150 K contributes an additional two deuterium atoms per p(2x2)O unit cell. Other experiments **(50)** have shown that the appearance of both these states is intimately related to the presence of the p(2x2)O overlayer. As the ordered oxygen coverage is increased past 0.25 monolayer, the resulting overlayer is a combination of local regions of both the p(2x2) and the p(1x2) overlayer **(40)**, which is developed fully at an oxygen coverage of 0.50 monolayer and does not chemisorb hydrogen at these temperatures. The thermal desorption spectra which result after subsequent D_2 adsorption show the states associated with the p(2x2)O overlayer attenuated proportionally to the fraction of the surface expected to be populated by the p(1x2) rather than the p(2x2)O overlayer. For ordered oxygen adatom coverages below 0.25 monolayer, the thermal desorption spectra of adsorbed D_2 are a linear combination of the clean surface and the surface on which the p(2x2)O overlayer is present.

The stoichiometry of the overall decomposition reaction for formaldehyde,

$$D_2CO(a) \rightarrow CO(a) + 2D(a)$$

indicates that, in the absence of other surface reactions which consume deuterium, the coverages obtained for the thermal desorption spectra of D_2 at the top of Fig. 3 should be twice the coverages obtained for the CO TDMS data of Fig. 2. Agreement is obtained within experimental error.

For the thermal desorption spectra obtained after adsorption of D_2CO on the clean Ru(001) surface, all D_2 evolution can be attributed to desorption from the surface after D_2CO decomposition at lower temperature, since the peak shapes and positions match very closely those obtained for the coadsorption of H_2 and CO on Ru(001) **(51)**. On the Ru(001)-p(2x2)O surface, however, features at temperatures above approximately 250 K are clearly due to the decomposition of adsorbed species in this temperature range, as can be deduced by comparison to the spectra for the Ru(001)-p(2x2)O surface shown in Fig. 3(a) and (c).

The decreased decomposition activity of the Ru(001)-p(2x2)O surface compared to the clean Ru(001) surface could be attributed reasonably to a decreased amount of formaldehyde adsorption into monolayer states on the oxygen precovered surface, resulting from blocking by the oxygen adatoms of the p(2x2) overlayer of formaldehyde adsorption sites which would otherwise be available on the clean surface. Since the temperature of formaldehyde adsorption, 80 K, is well below the temperature of desorption of condensed multilayers of formaldehyde, 110 K, formaldehyde molecules striking either the clean or the Ru(001)-p(2x2)O surface during exposure at 80 K are expected to adsorb with a probability near unity. Then, the exposures necessary to initiate formation of the multilayer state on each surface in the thermal desorption spectra for formaldehyde give a relative measure of how much formaldehyde is adsorbed into the monolayer states on both surfaces. As may be seen in Fig. 1, no desorption from the multilayer state is observed for 3 L exposures of both the clean Ru(001) and the Ru(001)-p(2x2)O surfaces to D_2CO, whereas 5 L exposures produce multilayer desorption from both surfaces. The multilayer state shows greater population for a 5 L exposure of the clean Ru(001) surface to formaldehyde than the Ru(001)-p(2x2)O surface, indicating that more adsorption into monolayer states occurs on the oxygen precovered surface than on the clean Ru(001) surface. Thus, the decreased decomposition activity of the Ru(001)-p(2x2)O surface, compared to the clean Ru(001) surface, must be due to differences in the reactivity of the adsorbed formaldehyde present on the two surfaces and not due simply to differences in the amounts of formaldehyde adsorbed.

C. EELS of Formaldehyde on the Clean Ru(001) Surface

EEL spectra recorded after increasing exposures of the clean Ru(001) surface to both H_2CO and D_2CO are shown in Fig. 4. For exposures below approximately 0.5 L, total decomposition at 80 K is evidenced by the appearance of only strong vibrational features near 450 and 2000 cm^{-1} due to approximately 0.10 monolayer of adsorbed CO **(39)**. Features attributable to hydrogen or deuterium adatoms from formaldehyde decomposition are not detected clearly due to the extremely small inelastic scattering cross section of these species on the Ru(001) surface **(52)**. After a 0.8 L exposure, however, the EEL spectrum of H_2CO shows modes due to other surface species at 590, 800, 1065, 1180, 1400, 1590 and 2900 cm^{-1}. Heating the surface to 120 K causes the modes at 590, 1065, 1180, 1400 and 2900 cm^{-1} to disappear, leaving features at 800 and 1590 cm^{-1} and increasing the intensities of the features due to adsorbed CO by an amount consistent with an increase of the CO coverage of 0.02 to 0.03 monolayer. Similar results are observed for identical experiments for the adsorption of D_2CO: heating the surface to 120 K removes features near 550 (shoulder), 825, 980 and 1160 cm^{-1}, leaving the shoulder near 360 cm^{-1} and a weak feature at 1150 cm^{-1}. A feature for D_2CO corresponding to that at 2900 cm^{-1} for H_2O should appear near 2100 cm^{-1}, but would be expected to be quite weak and is not resolved from the tail of the strong feature due to $\nu(CO)$ at 1990 cm^{-1}. Spectra which were extended to higher loss energies (not shown) also showed very weak features at 3500 cm^{-1} for H_2CO and 2500 cm^{-1} for D_2CO which were present both before and after annealing to 120 K. By comparison to EEL spectra obtained for water adsorption on Ru(001) **(43)**, the modes at 800 (360), 1590 (1150) and 3500 (2500) cm^{-1} can be readily assigned to librational modes (frustrated translation), $\delta(H_2O)$ [$\delta(D_2O)$] and $\nu(OH)$ [$\nu(OD)$], respectively, of less than 0.01 monolayer of adsorbed H_2O (D_2O) from paraformaldehyde depolymerization. The other features are due to a weakly stable species which is an intermediate in the formaldehyde decomposition to hydrogen adatoms and adsorbed CO.

The structure of this intermediate can be deduced from its vibrational spectrum by comparison to the structural properties of species obtained in the analogous chemistry of homogeneous organometallic complexes, where precedent for the formation of coordinated formyls has been obtained both from the reaction of metal centers with formaldehyde and from reactions of CO with hydrogen at metal centers. For example, the reaction of formaldehyde with ruthenium **(23)** and iridium **(25)** compounds and the thermally activated decomposition of a coordinated formaldehyde complex of osmium **(18)** have been shown to give hydrido formyl complexes in which the formyl ligand is coordinated in an η^1 configuration like that in (a) in the top panel of Fig. 5 (R=H). The same configuration has been observed for η^1-formyl produced by the hydrogenation of coordinated CO at rhenium **(26,27)**, nickel **(28)** and iron **(29)** centers. At a more oxophilic thorium center, insertion of CO into a hydride to give an η^2-formyl like that of (b) in the top panel of Fig. 5 has been observed **(30)**. Also, a tantalum hydride complex reacts with CO to form a ditantalum hydrido formyl product with η^2-formyl coordination analogous to that shown in (c) **(31)**, and reaction of a tungsten carbonyl compound with a zirconium hydride yields formyl in a bridging geometry like that of (d), where the carbon atom of the formyl is coordinated to the tungsten center through a double bond and the oxygen atom to the zirconium center through a single bond **(32)**. Similar acyl compounds (R = CH_3, C_6H_5, etc.) with structures analogous to those of (b) **(33)**, (c) **(34)**, and (d) **(35-37)** of Fig. 5 *(top panel)*, have also been synthesized and characterized structurally. In all cases, the carbon-oxygen double bond is preserved in the η^1-formyl complexes, as evidenced by carbon-oxygen bond lengths near 1.2 Å and ν(CO) values near 1600 cm^{-1}. For the η^2-formyl and similar η^2-acyl complexes, however, carbon-oxygen bond lengths range between 1.2 and 1.5 Å, depending on the strength of the metal-oxygen bonding interaction. Only those with structures like (b), where the carbon-oxygen bond order is near two and the carbon-oxygen bond length is near 1.2 Å, have been characterized by vibrational spectroscopy, and these compounds show ν(CO) between 1450 and 1600 cm^{-1}. Structures like (c) and (d) have carbon-oxygen bond orders near one and should have ν(CO) in the range 1000 to 1200 cm^{-1}. Any of these structures for coordinated formyl, plus others which would involve more than two metal atoms, must be considered as possible products of the reaction of formaldehyde with the Ru(001) surface, and it remains to test the correspondence between these candidates and the structure evidenced by the features in the EEL spectra shown in (a) of Fig. 4.

First, a comparison of the spectra in Fig. 4(a) for H_2CO and D_2CO allows immediate identification of the modes at 1180 and 1160 cm^{-1} as being due to the carbon-oxygen stretching vibration. The low frequency indicates that the carbon-oxygen bond order is lowered to nearly one, signifying η^2 coodination to at least two surface metal atoms by comparison to the formyl structures just described. With this established, the remaining skeletal vibrations for η^2-HCO can be assigned as follows: δ(HCO), the in-plane deformation at 1400 cm^{-1}; π(CH), the out of plane deformation at 1065 cm^{-1}; and ν(CH) at 2900 cm^{-1}. The corresponding modes for η^2-DCO are at 980, 825 and near 2100 cm^{-1} (not resolved). Substantial justification for these assignments and the postulated η^2 coordination geometry for formyl on Ru(001) can be obtained by comparison to the normal mode frequencies and their assignments for the model compounds $HCOOCH_3$ and $DCOOCH_3$ **(53)**, where the HCO and DCO functions of each compound mimic in carbon-oxygen bond order and structural arrangement the geometry expected for η^2-formyl on the Ru(001) surface. As may be seen from the results listed in Table 1, the correspondence is excellent. Finally, the mode at 590 cm^{-1} for H_2CO, appearing as a shoulder near 550 cm^{-1} in the D_2CO spectrum, is assigned to the frustrated translation of the formyl perpendicular to the surface, its rather high frequency a natural consequence of the relatively low mass of formyl and the stiffness of the multiple bonds which coordinate it to the surface.

Although the low frequency of ν(CO) for η^2-formyl on Ru(001) allows a structure like that of (b) to be excluded, no distinction between configurations such as (c) or (d) in the top panel of Fig. 5 for η^2-formyl on the Ru(001) surface can be made on the basis of the EELS results. Each would be expected to give similar ν(CH), δ(CH), π(CH) and ν(CO) vibrations and would differ only in the low frequency vibrations due to motion of the bonds which coordinate the formyl to the surface ruthenium atoms. Only one of these modes, at 590 cm^{-1} for η^2-HCO and 550 cm^{-1} for η^2-DCO, is observed, and no vibrational data in this frequency range for model complexes are available to allow a useful diagnostic comparison. The details of the η^2 coordination geometry are of less importance, however, than the definitive result that formyl exists on the surface and is bound with η^2 coordination.

It should be noted that a detailed analysis of the point group symmetry properties of the adsorbate complex, as was carried out successfully for η^1- and η^2-acetone on Ru(001) **(24)**, cannot be done in a straightforward manner for adsorbed formyl or the adsorbed formaldehyde structures which will be identified later. Since the dominant contribution to inelastic electron scattering from hydrogenic vibrations is expected to be via an impact rather than a dipolar mechanism at the electron beam energy employed for the EELS measurements reported here, all vibrations involving hydrogenic motion are, in principle, active in both specular and off-specular EELS measurements **(54)**. For a molecule like formaldehyde in which the skeletal configuration is defined by the orientations of C-H bonds, the polarizations of skeletal vibrations with respect to the symmetry elements of the adsorbate-surface complex cannot be determined by the standard technique of noting the dipolar activity (or inactivity) of signature skeletal modes for specular scattering and applying the "dipolar selection rule" **(58)** to determine bond orientations. For example, the appearance of the π(CH) vibration in the spectra for η^2-formyl does not rule out the possibility that the η^2-formyl is adsorbed in a configuration with C_s symmetry (with the carbon, hydrogen and oxygen atoms lying in a mirror symmetry plane perpendicular to the surface), even though the π(CH) mode would be dipolar inactive in this configuration.

Returning to the EEL spectra of Fig. 4, one can see that exposure of the clean surface to 3.0 L of H_2CO or D_2CO [cf. Fig. 4(b)] adds new features to the EEL spectra which signify the presence of surface species other than η^2-formyl. The appearance of a carbonyl band at 1660 cm^{-1} in both spectra, by analogy to the results obtained for adsorption of the structurally similar acetone molecule on Ru(001) **(24)**, indicates the presence of molecular formaldehyde coordinated to the surface in an η^1 configuration. This bonding configuration, shown schematically in (a) in the bottom panel of Fig. 5, results from overlap of a single lobe of the nonbonding lone pair orbital of formaldehyde, localized strongly on the oxygen atom, with a ds hybrid acceptor orbital of the metal, resulting in a net transfer of electron density from the formaldehyde ligand to the metal surface. This σ-donation interaction leaves the skeleton of the formaldehyde molecule unperturbed other than the red-shift of ν(CO) to 1660 cm^{-1} from its value of 1744 cm^{-1} for free H_2CO and 1700 cm^{-1} for free D_2CO **(55)**. Since the remaining features in both spectra cannot all be attributed to η^1–formaldehyde, another surface species is also present under these conditions. The features at 345 and 780 cm^{-1} in the spectrum for H_2CO are due to the frustrated translation and librational modes of coadsorbed H_2O, respectively **(43)**, and the corresponding modes in the spectrum of D_2CO are not resolved from the tail of the elastic peak or the strong feature due to adsorbed CO near 450 cm^{-1}. Having identified η^1–formaldehyde by the presence of ν(CO) at 1660 cm^{-1}, the assignments of the remaining features in these spectra and the structural identification of other species present is best left for the discussion of subsequent spectra, where each species is isolated and characterized unambiguously.

The addition of another 7 L of formaldehyde to the clean Ru(001) surface to give a total exposure of 10 L at 80 K produces condensed multilayers of formaldehyde, as was shown in the TDMS results of Fig. 1. EEL spectra recorded for H_2CO and D_2CO under these conditions are shown in Fig. 4(c), and assignments and corresponding frequencies for solid H_2CO and D_2CO **(56)** are listed in Table 2. As was observed for multilayer adsorption of formaldehyde on Ag(110) **(13)**, a strong lattice vibration appears at 170 cm^{-1} for H_2CO (160 cm^{-1} for D_2CO), and the frequencies for all other vibrations correspond more closely to those of solid formaldehyde **(56)** than to those of gaseous formaldehyde **(55)**. The intensity of ν(CO) due to adsorbed CO in these spectra indicate that decomposition of approximately 0.15 monolayer of formaldehyde occurs upon adsorption at 80 K.

Shown in Fig. 6 are EEL spectra recorded after exposure of the clean Ru(001) surface to 10 L of H_2CO *(left)* and 10 L of D_2CO *(right)*, followed by annealing to the indicated temperatures. After annealing to 150 K, the mode at 1660 cm^{-1} evident in the 3.0 L spectra of Fig. 4(b) for both H_2O and D_2CO is absent, indicating that η^1–formaldehyde has desorbed by this temperature and correlating well with the evolution of formaldehyde from the clean surface between 120 and 160 K in the thermal desorption spectra of Fig. 1. In the spectrum for H_2CO, Fig.

6(a), features which may be ascribed to librations or the frustrated translation of coadsorbed water are observed as shoulders on both the low and high frequency sides of the mode due to adsorbed CO at 450 cm^{-1}. A broad envelope of poorly resolved bands extends from 750 to 1250 cm^{-1}, a band due to C-H deformation vibrations is evident at 1420 cm^{-1}, and a band due to C-H stretching vibrations is evident at 2925 cm^{-1}. In the corresponding spectrum for D_2CO, a shoulder at 375 cm^{-1} on the low frequency side of the CO vibration at 450 cm^{-1} is observed, which again is due to the frustrated translation of D_2O perpendicular to the surface **(43)**. Also observed are a weak mode at 600 cm^{-1}, a broad, poorly resolved envelope of bands between 750 and 1250 cm^{-1}, and a weak feature due to C-D stretching modes at 2200 cm^{-1}. Also, the increase in the intensity of ν(CO) at 1995-2000 cm^{-1} in these spectra indicates that an additional 0.07-0.08 monolayer of formaldehyde decomposition has occurred upon annealing to 150 K.

Further heating to 250 K frees the surface of the adsorbed formaldehyde which produced the features between 240 and 280 K in the TDMS results of Fig. 1. The EEL spectra recorded after annealing to 250 K, Fig. 6(b), show no change in the intensities of the features due to adsorbed CO, indicating that decomposition has not proceeded in the temperature range of 150 to 250 K. The remaining bands sharpen and decrease in intensity, consistent not only with desorption of the adsorbed species which contributes these bands, but also with ordering of the remaining 0.03 monolayer of adsorbed species which has not decomposed. Results of other experiments for annealing temperatures between 250 and 300 K (not shown) verify that the features in Fig. 6(b) at 840, 980, 1160, 1450 and 2940 cm^{-1} for H_2CO; and at 620, 865, 1020, 1190 and 2225 cm^{-1} for D_2CO maintain their relative intensities and decrease in intensity in unison as the surface is annealed to progressively higher temperatures. As these vibrational features attenuate, those due to adsorbed CO increase in intensity. Consequently, these features are readily ascribable to a single adsorbed species which decomposes to yield CO in this temperature range.

Comparison of the frequencies observed in Fig. 6(b) to those expected for paraformaldehyde [630, 900-930, 1090-1100, 1235, 1470 and 2900-2980 for para-H_2CO and 620, 835, 970, 1050-1080, 1130-1160 and 2235 for para-D_2CO **(57)**] confirms that paraformaldehyde is not the majority species formed and does not produce the spectra observed after annealing to 250 K. Similar comparisons allow species such as methoxy **(5,11)** and η^2-dioxymethylene **(13)**, which have been observed as adsorbed products of the interaction of formaldehyde with other metal surfaces, to be excluded. The presence of a small amount of paraformaldehyde at lower temperatures, however, may explain the poor resolution in the envelope of bands between 750 and 1250 cm^{-1} for both H_2CO and D_2CO in the spectra recorded after annealing to 150 K. As was argued earlier, the depolymerization of a small amount of paraformaldehyde may also contribute to the desorption of formaldehyde between 240 and 280 K in the TDMS results of Fig. 1.

The spectra of Fig. 6(b) are consistent with an η^2 configuration for adsorbed formaldehyde, analogous to that obtained for the adsorption of acetone on the Ru(001)-surface **(24)**. Precedent for this type of coordination geometry for formaldehyde has also been established in the homogeneous chemistry of organometallic complexes. For example, the interaction of formaldehyde with single osmium **(18)** and vanadium **(19)** centers and the oxidation of coordinated methylene at a rhenium center **(20)** produces the η^2–formaldehyde configuration shown schematically in (b) in the bottom panel of Fig. 5 (R=H). On the other hand, the carbonylation of a zirconium hydride forms a bridging configuration for η^2–formaldehyde **(21)**, as in (c) in the bottom panel of Fig. 5.

Also of interest is a configuration like that of (d), which has been observed for η^2-acetaldehyde (R=CH_3) synthesized by the hydrogenation of coordinated acetyl in a dimolybdenum complex **(22)**. All these compounds have carbon-oxygen bond lengths between 1.35 and 1.59 Å, and those that have been characterized by vibrational spectroscopy **(18,19,21)** have ν(CO) between 1012 and 1160 cm^{-1}, compared to 1.23 Å and 1744 cm^{-1} for free formaldehyde **(55)**. These results are indicative of extensive rehybridization of the acyl carbon from sp^2 to nearly sp^3 upon coordination in an η^2 configuration. As was discussed earlier in connection with η^2-formyl, a distinction among these possible configurations for η^2–formaldehyde on the Ru(001) surface cannot be made on the basis of the EELS data, since the vibrational spectra would differ only in the unresolved, low frequency vibrations which involve motion of the bonds which coordinate the η^2–formaldehyde to the ruthenium surface. As in the case of η^2-acetone on Ru(001), however, C_s symmetry is expected for η^2–formaldehyde (a mirror plane through the carbon-oxygen bond perpendicular to the surface), but this cannot be substantiated by the EELS results due to the presence of impact scattering from the hydrogenic modes.

Assignments of each of the observed vibrational modes for both η^2–H_2CO and η^2–D_2CO are listed in Table 2. The ν(CO) frequency near 1000 cm^{-1} agrees well with those observed in analogous η^2–formaldehyde complexes **(18,19,21)**. In addition, the frequencies of the $\nu(CH_2)$, $\omega(CH_2)$ and $\rho(CH_2)$ modes agree well with assignments for methylene groups with sp^3 hybridization in other compounds, as do the frequency shifts upon deuteration [(ν for H_2CO)/(ν for D_2CO) = 1.32 to 1.35] **(53-55)**. Noteworthy, however, is the slight increase from 980 to 1020 cm^{-1} of ν(CO) upon deuteration and the less-than-expected **(58)** decrease from 1450 to 1190 cm^{-1} of $\delta(CH_2)$ upon deuteration [$\delta(CH_2)/\delta(CD_2)$ = 1.22]. The origin of these effects can be explained in terms of a strong interaction between the

ν(CO) and δ(CD_2) motions of η^2–D_2CO. As has been discussed in Refs. 55 and 59, the description of molecular vibrational motion in terms of bending and stretching of isolated units [e.g. δ(CH_2), ν(CO), ω(CH_2), etc.] fails when two (or more) vibrational modes involving motion of (a) common atom(s) and belonging to the same symmetry type have nearly equal frequencies. In this circumstance, the resulting normal modes of the molecule are combinations of the two (or more) types of motion, which may produce frequencies substantially different than are expected for vibrations of the isolated units. Such an interaction was observed in the EEL spectra of η^2-acetone on Ru(001), where the coupling of the methyl rocking motion to the carbon-carbon stretching motion of η^2–$(CH_3)_2CO$ produced strong ρ(CH_3) modes at 980 and 1170 cm^{-1}, but substitution of deuterium for hydrogen shifted the ρ(CD_3) frequency away from the ν(C-C) frequency, reducing the strength of this coupling and producing weak ρ(CD_3) modes at 880 and 820 cm^{-1}. The anomalous shift of the lower frequency mode upon deuteration [$\rho(CH_3)/\rho(CD_3) = 980\ cm^{-1}/820\ cm^{-1} = 1.18$] and the dramatic decrease in the intensities of the ρ(CD_3) modes compared to the ρ(CH_3) modes were clear and obvious manifestations of this decoupling effect. For η^2–H_2CO, the ν(CO) mode at 980 cm^{-1} and the δ(CH_2) mode at 1450 cm^{-1}, both of which are A' symmetry for η^2–formaldehyde in the expected C_s configuration and derived from A_1 modes of free formaldehyde (see Table 2), are largely decoupled due to their disparity in frequency. Thus, the δ(CH_2) vibration involves almost exclusively relative motion of the hydrogen atoms, and the ν(CO) vibration involves only relative motion of the carbon and oxygen atoms. When deuterium is substituted for hydrogen, however, the frequency of isolated δ(CD_2) motion would shift to approximately $1450/1.41 = 1030\ cm^{-1}$, where coupling with the ν(CO) motion would be strong. Thus, the resulting normal mode for η^2–CD_2O identified as δ(CD_2) actually involves substantial ν(CO) motion, and the mode identified as

ν(CO) correspondingly contains substantial $\delta(CD_2)$ motion.

Vibrational interactons of this type are not unique to η^2–D_2CO. For example, normal mode calculations **(57)** for para-H_2CO show that the ν(CO), $\delta(CH_2)$ and $\omega(CH_2)$ motions are nearly decoupled, producing ν(CO) modes at 919, 932, 1091 and 1097 cm^{-1}, $\delta(CH_2)$ modes near 1480 cm^{-1}, and $\omega(CH_2)$ modes near 1410 cm^{-1}. Substitution of deuterium for hydrogen lowers the frequencies of the ω and δ modes to produce strong symmetry allowed coupling with the ν(CO) vibrations, and normal modes due to combinations of ν(CO), $\delta(CD_2)$ and $\omega(CD_2)$ motion result at 970, 1050, 1078, 1120, 1128 and 1156 cm^{-1}.

In dipolar inelastic scattering, the electrons of the EELS beam incident upon the surface interact with the time dependent electric field above the surface which results from the oscillation of separated charges in the adsorbed species, exiting the surface in the near specular direction after losing energy to excite a surface vibration **(54)**. Since the charge separation between the carbon and hydrogen (or deuterium) atoms of the C-H [or (C-D)] bonds is small with respect to that between carbon and oxygen of the C-O bond, strong dipolar scattering is only expected to occur for those vibrational modes of adsorbed formaldehyde which involve motion of the carbon and oxygen atoms with respect to each other. Since the cross section for dipolar inelastic scattering is strongly peaked in the specular direction, rotation of the electron energy analyzer away from the specular collection geometry where dipolar scattering is dominant attenuates features due to dipolar scattering, i.e. those vibrations which involve C-O motion for adsorbed formaldehyde, with respect to features due primarily to short-range impact scattering, i.e. those vibrations which involve C-H (or C-D) motion for adsorbed formaldehyde **(54)**. This is clearly illustrated in Fig. 7 for both η^2–H_2CO and η^2–D_2CO. Comparison of the top spectrum for η^2–H_2CO, at the left of Fig. 7, that was recorded with the electron energy analyzer rotated 5° in the scattering plane away from the specular direction and toward the surface normal, to that below it for specular scattering shows that the $\nu(CO)$ mode at 980 cm^{-1} is attenuated sharply with respect to the ρ, ω, δ and $\nu(CH_2)$ modes of η^2–H_2CO at 840, 1165, 1450 and 2940 cm^{-1}, which maintain their relative intensities. In the spectra at the right for η^2–D_2CO, however, both $\nu(CO)$ at 1020 cm^{-1} and $\delta(CD_2)$ at 1190 cm^{-1} are attenuated in unison upon changing from the specular to the off-specular scattering geometry, maintaining their intensities relative to each other but decreasing uniformly with respect to the ρ, ω and $\nu(CD_2)$ modes at 620, 865 and 2225 cm^{-1}. The $\delta(CD_2)$ mode of η^2–D_2CO at 1190 cm^{-1} shows much stronger dipolar scattering than the corresponding $\delta(CH_2)$ mode of η^2–H_2CO at 1450 cm^{-1}, illustrating the strong coupling of C-O and C-D motion in this vibrational mode of η^2–D_2CO.

Returning to the spectra of Fig. 6, the most notable effect of annealing the Ru(001) surface, upon which η^2–formaldehyde and CO and hydrogen from the decomposition of formaldehyde are adsorbed, to 350 K [Fig. 6(c)] is to decompose completely the remaining 0.03 monolayer of η^2–formaldehyde. The CO coverage in spectra (c) of Fig. 6 is approximately 0.25 monolayer, and, for coverages of CO above approximately 0.20 monolayer, the vibrational spectrum of adsorbed CO on Ru(001) not only shows modes at 455 and 2020 cm^{-1} due to $\nu(RuC)$ and $\nu(CO)$, respectively, but also shows weak features at 2450 to 2490 cm^{-1} due to the combination loss of $\nu(RuC) + \nu(CO)$ and at 835 to 840 cm^{-1} due to the overtone of $\nu(RuC)$, downshifted from twice the $\nu(RuC)$ frequency due to anharmonicity of the ruthenium-carbon bond **(39)**. In addition to these features from adsorbed CO, the spectrum for H_2CO shows a weak feature at 2900 cm^{-1} due to a small amount of an unidentifiable hydrocarbon fragment on the surface. Some spectra for both H_2CO and D_2CO recorded after annealing to temperatures between 250 and 350 K *(not shown)* also showed bands clearly attributable to small amounts (less than 0.01 monolayer) of coadsorbed η^2-formate **(49)**. These bands are probably due to small amounts of impurities in the adsorbed formaldehyde and are insignificant with regard to the important formaldehyde chemistry evidenced in these EEL spectra.

D. EELS of Formaldehyde on the Ru(001)-p(2x2)O Surface

Exposure of the clean Ru(001) surface to 0.8 L of O_2 at 80 K, followed by annealing to 400 K, produces the EEL spectrum of the p(2x2)O overlayer shown in the inset of Fig. 8. In addition to the feature at 540 cm^{-1} due to motion of the oxygen adatoms in threefold hollow sites perpendicular to the surface, a mode appears at 240 cm^{-1} which results from coupling of the overlayer to a ruthenium surface phonon **(40)**. The presence of the p(2x2)O overlayer, with an ideal fractional surface coverage of 0.25, changes the work function of the Ru(001) surface by +0.20 eV **(41)**. Employing a Ru=O bond length of 2.05 Å **(40)** and ignoring depolarization effects, this change in the work function can be shown to be equivalent to the transfer of 0.02 electron from the ruthenium surface to each oxygen adatom of the p(2x2)O overlayer **(60)**, producing a quantifiable increase in the Lewis acidity of the surface ruthenium atoms.

Spectra recorded after adsorption of 0.6 L of H_2CO and D_2CO on the Ru(001)-p(2x2)O surface at 80 K are shown in Fig. 8(a). The strong mode due to adsorbed oxygen of the p(2x2) overlayer is visible at 540 cm^{-1}, and a broad, weak feature due to librational modes of a small amount of coadsorbed H_2O can be seen at 750 cm^{-1} in the spectrum of H_2CO. Modes due to adsorbed CO from formaldehyde decomposition or background adsorption of CO are present in both spectra with intensities indicative of coverages near 0.01 monolayer. The remaining features in both spectra can be identified easily with the presence of only η^1–formaldehyde. The band locations and assignments for η^1–H_2CO and

η^1–D_2CO are listed in Table 2. The strong band at 270 cm^{-1} in the spectrum of H_2CO and the band at 245 cm^{-1} in the spectrum of D_2CO are due to the frustrated translation of the η^1–formaldehyde molecules perpendicular to the surface.

Spectra for 3 L exposures of H_2CO and D_2CO under the same conditions are shown in Fig. 8(b). Other than shifts in the apparent frequencies of the ρ and ω, and δ modes (from 1240 to 1195 cm^{-1} and 1490 to 1465 cm^{-1} for H_2CO; and from 1020 and 1190 cm^{-1} to a single band at 1025 cm^{-1} for D_2CO) and some changes in the relative intensities of the bands due to η^1–formaldehyde, no clear evidence for any species on the Ru(001)-p(2x2)O surface other than η^1–formaldehyde and carbon monoxide is present in the spectra of Fig. 8.

This conclusion is in agreement with the results of a previous investigation of acetone adsorption on the clean Ru(001) and the Ru(001)-p(2x2)O surfaces **(24)**, where preadsorption of oxygen stabilized the η^1 form of adsorbed acetone, analogous to the η^1–formaldehyde identified here, with respect to the η^2 form, which existed in much greater concentration on clean Ru(001) compared to the Ru(001)-p(2x2)O surface. Furthermore, only η^2-acetone was an intermediate to decomposition, while η^1-acetone desorbed molecularly. This correlates well with the appearance of only slight decomposition of formaldehyde after adsorption on the Ru(001)-p(2x2)O surface, whereas initial adsorption of formaldehyde on the clean Ru(001) surface is almost completely dissociative.

Figure 9 shows spectra recorded after exposure of the Ru(001)-p(2x2)O surface to 10 L of H_2CO and D_2CO, an exposure that is more than sufficient to provide a saturated monolayer of formaldehyde at 80 K, followed by annealing to the indicated temperatures. The decrease in the intensities of the modes due to η^1–formaldehyde in the spectra of Fig. 9(a), taken after annealing to 150 K, compared to the spectra of Fig. 8(b), indicates that approximately 80% of the η^1–formaldehyde has desorbed by this temperature. This correlates with the thermal desorption features at 130 and 150 K for formaldehyde on the Ru(001)-p(2x2)O surface, shown in Fig. 1. The attenuation of the bands due to η^1–formaldehyde reveals bands in the frequency range expected for η^2–formaldehyde, at 875, 1005, 1130 and 1440 cm^{-1} in the spectrum for H_2CO and a single, broad band centered at 985 cm^{-1} in the spectrum for D_2CO.

Spectra recorded for annealing temperatures between 150 and 300 K (not shown) demonstrate the broad envelope of bands between 750 and 1250 cm^{-1} in the spectra for both H_2CO and D_2CO changing shape as a surface reaction proceeds which forms the products evident in the spectra of Fig. 9(b). Significant decomposition of η^2–formaldehyde occurs in this temperature range, as evidenced by the increase in the intensities of the modes due to adsorbed CO. Furthermore, the bands attributable to η^1–formaldehyde decrease in intensity in this temperature range, and bands near 800 and 1300 cm^{-1} grow concomitantly with the disappearance of the last η^1–formaldehyde for annealing temperatures between 200 and 250 K. These bands are due to η^1-formate **(49)** produced by the reaction of η^1–formaldehyde with the oxygen adatoms of the p(2x2) overlayer. Slight desorption of η^1–formaldehyde also occurs in this temperature range, producing the very weak desorption rate maxima between approximately 180 and 300 K in the thermal desorption spectra of Fig. 1 *(right)*. No η^1–formaldehyde is evident in the EEL spectra for annealing temperatures greater than 250 K. At 300 K [Fig. 9(b)], bands due to 0.04 monolayer of η^2-formate are present at 800 and 1330 cm^{-1} for H_2CO and at 795 and 1305 cm^{-1} for D_2CO. In addition, bands due to 0.01 monolayer of η^2–formaldehyde are evident at 990, 1145 and 2960 cm^{-1} for H_2CO and 1010 and 1150 cm^{-1} for D_2CO. The high intensity of the ν(CO) mode in these spectra (990 and

1010 cm^{-1}) relative to the other modes of η^2–formaldehyde is probably a result of the perturbation of its bonding interaction with the surface due to the presence of the coadsorbed oxygen of the p(2x2)O overlayer. This perturbation is also evidenced in the increased stability of η^2–formaldehyde on the Ru(001)-p(2x2)O surface; on the clean Ru(001) surface, decomposition of η^2–formaldehyde is complete by 300 K.

Annealing to 400 K decomposes the remaining η^2–formaldehyde, decomposes a fraction of the η^2-formate, and desorbs a fraction of the CO from the surface. The remaining η^2-formate persists to 450 K on the Ru(001)-p(2x2)O surface, and its decomposition produces the broad, weak desorption feature for hydrogen between 400 and 470 K in Fig. 3(c) **(61)**.

EEL spectra recorded after annealing to temperatures sufficient to desorb all the hydrogen and CO from the surface show the features at 240 and 540 cm^{-1} due to the p(2x2)O overlayer with intensities unchanged from those observed prior to the adsorption of formaldehyde at 80 K. This verifies that little or no consumption of the oxygen adatoms of the p(2x2) overlayer by reactions with formaldehyde or its dissociation products occurs under the conditions prevailing in these experiments.

IV. Discussion

The η^1 and η^2 coordination geometries identified for formaldehyde in the EELS results reported here can be understood qualitatively in terms of the interaction of the valence orbitals of the surface metal atoms with the highest occupied and lowest unoccupied molecular orbitals of free formaldehyde **(24)**. An η^1 coordination geometry results from overlap of a single lobe of the nonbonding oxygen lone pair orbital of formaldehyde [at 12.0 eV below the vacuum level for free formaldehyde **(62)**] with a ds hybrid acceptor orbital of the metal, resulting in a net transfer of electron density from the ligand to the metal surface. Presumably due to the low amplitude on the oxygen atom of the π^*_{CO} antibonding orbital of formaldehyde [at 3.1 eV above the vacuum level **(62)**], little backdonation from the metal d levels to this orbital occurs, as is evidenced by the weak perturbation of the vibrational frequencies for η^1–formaldehyde relative to the frequencies of free formaldehyde (cf. Table 2). The role of the metal in this type of interaction is that of a weak Lewis acid, and the resulting metal-formaldehyde bond is correspondingly weak. For example, the thermal desorption spectra of Fig. 1 indicate binding energies between 7 and 9 kcal/mole **(47)** for the desorption features attributable to η^1–formaldehyde at 130 and 155 K.

An η^2 coordination geometry results from overlap of the π_{CO} bonding orbital of formaldehyde [at 14.6 eV below the vacuum level **(62)**] with a ds hybrid acceptor level of the metal, along with backdonation from metal d levels into the π^*_{CO} antibonding orbital of the formaldehyde ligand **(63)**. The strength of this interaction, and therefore the probability of its occurrence relative to the η^1 interaction, depends critically on the ability of the ligand-metal bond to facilitate backdonation, since in the absence of backdonation the π donor bond is weaker than the lone pair donor bond which produces η^1 coordination. The importance of backdonation and the function of the metal as a Lewis base in this type of interaction is evidenced in the results obtained in structural studies of η^2-aldehyde complexes **(18-22)**, where in all cases nearly complete rehybridization of the acyl carbon from sp^2 to sp^3 occurs, and the carbon-oxygen bond order for the aldehyde ligands is lowered to nearly one.

The π^*_{CO} antibonding orbital of free formaldehyde is approximately 1.3 eV lower in energy than the corresponding orbital of free acetone [π^*_{CO} at 4.4 eV above the vacuum level for acetone **(62)**]. This decreases the disparity in energy between this orbital for formaldehyde and the d band of the metal with which it interacts in η^2 bonding, facilitating increased backdonation for formaldehyde with respect to acetone. Several aspects of the comparative chemistry of these two compounds can be correlated with this difference. First, the only η^2-acetone complex isolated thus far has the acetone coordinated to an electropositive tantalum center **(64)**, whereas η^2–formaldehyde complexes have been synthesized with more electronegative osmium **(18)** and rhenium **(20)** centers. Furthermore, η^2–formaldehyde on Ru(001) shows ν(CO) near 1000 cm^{-1}, whereas ν(CO) for η^2-acetone on Ru(001) is near 1300 cm^{-1} **(24)**, indicating more extensive rehybridization of the acyl carbon due to backdonation for η^2–formaldehyde than for η^2-acetone. Finally, the more extensive rehybridization evident for η^2–formaldehyde on Ru(001) results in a lower barrier to its dissociation, explaining the fact that significant decomposition of formaldehyde, presumably through short-lived η^2–formaldehyde and η^2-formyl intermediates, occurs on the clean Ru(001) surface at 80 K (cf. Fig. 4), whereas decomposition of η^2-acetone on the same surface begins near 200 K **(24)**.

The conditions that lead to the formation of η^2-formyl and η^2–formaldehyde provide a consistent picture of the mechanism of formaldehyde decomposition on the clean Ru(001) surface. For low exposures of formaldehyde to Ru(001) at 80 K, total decomposition to adsorbed CO and hydrogen occurs. This indicates that the activation energy for dissociation of η^2–formaldehyde on Ru(001) at low coverages is less than 4.8 kcal-mol^{-1} **(65)**. As binding sites for the hydrogen from decomposition are occupied, further decomposition is inhibited sterically, stabilizing both the partial decomposition product η^2-formyl over a small exposure range [Fig. 4(a)], and η^1- and η^2–formaldehyde at coverages approaching a saturated monolayer [Fig. 4(b)]. Annealing to temperatures below the onset of hydrogen desorption renders probable the additional decomposition of η^2–formaldehyde as η^1–formaldehyde is desorbed and hydrogen adatoms become mobile, exposing the necessary binding sites for the products of η^2–formaldehyde decomposition. For example, the *apparent* activation energy for the decomposition of η^2–formaldehyde at 150 K, 9 kcal-mol^{-1}, represents the steric barrier which η^2–formaldehyde must overcome under these conditions to find binding sites to accommodate decomposition products, hydrogen and CO, on the surface. These conclusions are supported by the results of EELS measurements for adsorption of formaldehyde at 80 K on the Ru(001) surface precovered with a saturated monolayer of hydrogen adatoms **(50)**. Only η^1- and η^2–formaldehyde are observed at 80 K for all submonolayer coverages, and very little decomposition is observed until hydrogen desorption commences near 275 K, whereupon decomposition of η^2–formaldehyde proceeds rapidly.

The effect of hydrogen coverage on the rate of dissociation of η^2–formaldehyde has another important consequence for the interpretation of the experimental results reported here. If η^2–formaldehyde has a characteristic activation energy for *molecular desorption* (i.e. heat of adsorption) less than the activation energy for recombination and desorption of hydrogen from the Ru(001) surface, at high surface coverages, where the binding sites for the products of the decomposition of η^2–formaldehyde on the Ru(001) surface are filled and further decomposition is unfavorable, molecular desorption of η^2–formaldehyde would occur. Consequently, the EELS results, which show that decomposition and adsorption of η^1- and η^2–formaldehyde are clearly favored over polymerization of adsorbed formaldehyde on Ru(001), suggest that the desorption of molecular formaldehyde from the clean surface at 275 K for high surface coverages (cf. Fig. 1) is in fact attributable to the desorption of η^2–formaldehyde and not to depolymerization of adsorbed paraformaldehyde. The very high binding energy of this adsorbed species on Ru(001) (approximately 115 kcal-mol^{-1}) makes the formation of η^2–formaldehyde far more favorable than the formation of paraformaldehyde on the Ru(001) surface.

The results of these considerations for the surface chemistry of formaldehyde adsorbed on both the clean and Ru(001)-p(2x2)O surfaces may be illustrated by overall reaction schemes for the monolayer species adsorbed on both surfaces, which result from a consideration of both the TDMS and EELS results discussed earlier. Initial exposure of the clean Ru(001) surface to formaldehyde at 80 K produces adsorbed CO and hydrogen from decomposition,

$$H_2CO(g) \rightarrow CO(a) + 2H(a) .$$

Once decomposition has progressed to approximately 0.15 monolayer of formaldehyde, subsequent exposure produces 0.02 to 0.03 monolayer of η^2-formyl,

$$CH_2O(g) \rightarrow \eta^2\text{–}HCO(a) + H(a) .$$

Heating the surface upon which η^2-formyl is adsorbed to 120 K decomposes the η^2-formyl [the *apparent* activation energy for dissociation is 7.1 kcal/mole **(65)**]. Further exposure to formaldehyde produces both η^1–formaldehyde and 0.10 monolayer of η^2–formaldehyde,

$$H_2CO(g) \rightarrow \eta^1\text{–}H_2CO(a)$$

$$H_2CO(g) \rightarrow \eta^2\text{–}H_2CO(a) .$$

The η^1–formaldehyde desorbs molecularly between 120 and 160 K,

$$\eta^1\text{–}H_2CO(a) \rightarrow H_2CO(g) ,$$

exposing binding sites for the products of the decomposition of 0.07 to 0.08 monolayer of η^2–formaldehyde,

$$\eta^2\text{-}H_2CO(a) \rightarrow CO(a) + 2H(a) .$$

As the surface is heated to 300 K, hydrogen desorption commences, and decomposition of the remaining 0.03 monolayer of η^2–formaldehyde follows rapidly. Hydrogen is evolved from the surface in a desorption rate-limited step between 250 and 350 K, and CO is evolved from the surface in a desorption rate-limited step at 480 K,

$$2H(a) \rightarrow H_2(g)$$

$$CO(a) \rightarrow CO(g) .$$

Exposure of the Ru(001)-p(2x2)O surface to formaldehyde at 80 K produces η^1–formaldehyde,

$$H_2CO(g) \rightarrow \eta^1\text{-}H_2CO(a) .$$

Negligible decomposition of formaldehyde is observed under these conditions. Heating the surface to 150 K desorbs approximately 80% of the η^1–formaldehyde,

$$\eta^1\text{-}H_2CO(a) \rightarrow H_2CO(g) ,$$

revealing the presence of η^2–formaldehyde. Further heating of the surface to 300 K produces approximately 0.08 monolayer of CO from the decomposition of η^2–formaldehyde and produces approximately 0.04 monolayer of η^2-formate from the reaction of η^1–formaldehyde with the oxygen adatoms of the p(2x2)O overlayer,

$$\eta^1\text{-}H_2CO(a) + O(a) \rightarrow \eta^2\text{-}HCOO(a) + H(a) .$$

This reaction, as well as the decomposition of η^2–formaldehyde, produces hydrogen above its characteristic temperature of desorption from the Ru(001)-p(2x2)O surface, thus hydrogen atom recombination and desorption follow rapidly in the temperature range between 250 and 300 K. Approximately 0.01 monolayer of η^2–formaldehyde also remains on the surface at 300 K. Further heating decomposes the remaining η^2–formaldehyde, and decomposition of the η^2-formate occurs between 400 and 450 K,

$$\eta^2\text{–HCOO(a)} \rightarrow \text{O(a)} + \text{CO(a)} + \text{H(a)} .$$

Again, hydrogen desorption follows rapidly. The CO from decomposition is evolved from the surface in a desorption rate-limited step at 450 K. The p(2x2) oxygen overlayer is left intact on the surface.

The appearance of η^2-formyl as an intermediate to the decomposition of adsorbed formaldehyde on Ru(001) has important implications for the mechanistic understanding of surface catalyzed CO hydrogenation reactions **(15,66)**. Although the reaction of coordinated CO with hydrogen from borohydride donors has been shown to produce η^1-formyl complexes of rhenium **(26,27)** and iron **(29)** under homogeneous conditions, this reaction, represented schematically as [R = alkyl or alkoxide, L = Cp, PPh_3, NO, CO and/or $P(OC_6H_5)_3$],

$$BR_3H^- + L_xM^N(CO) \rightarrow BR_3 + L_xM(\eta^1\text{–HCO})^{N-1} ,$$

involves direct nucleophilic attack by the electron-rich hydrogen atom of the hydride donor at the carbonyl carbon. The resulting compounds are either neutral [N = +1 **(26,27)**] or are negatively charged [N = 0 **(29)**]. At no point is molecular hydrogen, nor an intermediate *metal* hydride, involved in this elementary reaction. Furthermore, the resulting η^1-formyl is only weakly stable, and the weakened carbon-oxygen bond of η^1-formyl relative to that of the CO which can be formed by its decomposition to the hydrido-carbonyl product drives the equilibrium for the decomposition reaction, represented below, to the right **(15,27,30,32)**

$$L_xM(\eta^1\text{–}HCO) \overset{\leftarrow}{\rightarrow} L + L_{x-1}M(H)(CO) \, .$$

A more realistic model of the elementary CO reduction reaction which must occur under heterogeneous catalytic conditions involves migratory insertion of CO into a metal hydride bond **(66)**,

$$CO + L_xMH \rightarrow L_xM(HCO) \, .$$

Thus far, only one such reaction has been observed under homogeneous conditions, where the reaction of CO with an oxophilic thorium hydride $[(\eta^5\text{–}C_5Me_5)_2Th(H)(OR)$, OR = alkoxide ligand **(30)**] produces an η^2-formyl like that shown in Fig. 5(b) *(upper panel)* . The ability of the single metal center to coordinate the formyl product in an η^2 configuration was considered crucial to the occurrence of this reaction, since the metal-oxygen bond which is formed increases the stability of the formyl product, shifting the equilibrium for the formyl decomposition reaction toward the desired η^2-formyl product and away from the hydrido-carbonyl product **(30,32,66)**. Another route to stabilization of the formyl product involves the use of multiple coordination centers for the CO hydrogenation reaction. Two such reactions have been observed under homogeneous conditions, one involving the reaction of CO with a tantalum hydride dimer **(31)**,

$$[(\eta^5\text{–}C_5Me_4Et)Ta(Cl)_2H]_2 + CO \rightarrow (\eta^5\text{–}C_5Me_4Et)_2(Cl)_4Ta_2(H)(\eta^2\text{–}HCO)$$

to produce an η^2-formyl product, the structure of which is like that of Fig. 5(c) *(upper panel)*, and another involving the reaction of a tungsten carbonyl compound with a zirconium hydride **(32)**,

$$(Cp)_2W(CO) + (\eta^5\text{–}C_5Me_5)_2Zr(H)_2 \rightarrow (Cp)_2W{=}CHOZr(H)(\eta^5\text{–}C_5Me_5)_2$$

to produce a "carbene-like" η^2-formyl complex, the structure of which is like that of Fig. 5(d) *(upper panel)*. The η^2 interaction not only stabilizes the η^2-formyl intermediate, increasing the likelihood of its formation, but also increases the likelihood of subsequent attack by hydrogen to form formaldehyde intermediates, leading to oxygenated products, and to carbon-oxygen bond cleavage, leading to hydrocarbon products **(66)**.

From these results concerning the mechanism of CO activation and reduction under homogeneous conditions, the importance of the η^2-formyl observed in the decomposition of formaldehyde on Ru(001) is clearly evident. This result illustrates the ability of an extended metal surface to provide the proper coordination geometry for this species and supports strongly a surface reaction mechanism for CO hydrogenation which proceeds through an η^2-formyl intermediate. This, coupled with the isolation of stable η^2–formaldehyde on Ru(001), supports also the following reaction mechanism for methanol decomposition on Ru(001) **(5)** and suggests that the reverse reactions may well represent a plausible path for methanol synthesis on Ru(001):

$$CH_3OH(g) \rightarrow CH_3O(a) + H(a)$$

$$CH_3O(a) \rightarrow \eta^2\text{–}H_2CO(a) + H(a)$$

$$\eta^2\text{–}H_2CO(a) \rightarrow \eta^2\text{–}HCO(a) + H(a)$$

$$\eta^2\text{–}HCO(a) \rightarrow CO(a) + H(a)\,.$$

It is interesting to note that a reaction sequence analogous to the reverse of the above set of reactions has been postulated to explain the formation of methanol from CO and hydrogen by $Ru_3(CO)_{12}$ under homogeneous reaction conditions **(17)**. Our observations should be interpreted as lending support to this proposition.

V. Summary

The important conclusions of this work may be summarized as follows:

1. Initial adsorption of formaldehyde on the clean Ru(001) surface at 80 K is dissociative, producing adsorbed CO and hydrogen. As binding sites for hydrogen adatoms become occupied, the total decomposition is inhibited, leading first to the formation of η^2-formyl and then to molecular adsorption of formaldehyde in both η^1 and η^2 configurations.
2. Heating of the clean surface after a monolayer saturation exposure to formaldehyde at 80 K causes the η^1–formaldehyde to desorb molecularly and the η^2–formaldehyde to decompose (to adsorbed CO and hydrogen). The clean Ru(001) surface is active for the decomposition of approximately a quarter-monolayer of formaldehyde under these conditions.
3. The presence of a p(2x2) oxygen overlayer on the Ru(001) surface increases the Lewis acidity of the surface ruthenium atoms, and adsorption of formaldehyde at 80 K on the Ru(001)-p(2x2)O surface produces vibrational spectra characteristic of η^1–formaldehyde for all submonolayer coverages.
4. Heating of the Ru(001)-p(2x2)O surface after a monolayer saturation exposure to formaldehyde at 80 K causes the η^1–formaldehyde to desorb molecularly, revealing the presence of η^2–formaldehyde. In addition to decomposition of the η^2–formaldehyde to CO and hydrogen, reaction of η^1–formaldehyde with the oxygen adatoms of the p(2x2)O overlayer to produce η^2-formate also occurs between 150 and 300 K. The Ru(001)-p(2x2)O surface is

active for approximately one-half as much formaldehyde decomposition via both η^2–formaldehyde and η^2-formate intermediates) as the clean surface under these conditions.

5. The appearance of η^2-formyl and η^2–formaldehyde as stable intermediates in the decomposition of formaldehyde on Ru(001) supports a reaction mechanism for CO hydrogenation to methanol under heterogeneous conditions which includes these species as important intermediates.

Acknowledgment

This research was supported by the National Science Foundation under Grant No. CHE82-06487.

References

1. J. E. Demuth and H. Ibach, Chem. Phys. Letters **60**, 395 (1979).
2. B. A. Sexton, Surface Sci. **88**, 299 (1979).
3. B. A. Sexton, Surface Sci. **102**, 271 (1981).
4. K. Christmann and J. Demuth, J. Chem. Phys. **76**, 6308 (1982).
5. J. Hrbek, R. A. de Paola and F. M. Hoffmann, J. Chem. Phys. **81**, 2818 (1984).
6. G. Henrici-Olive′ and S. Olive′, Agnew. Chem. Int. Ed. Engl. **15**, 136 (1976).
7. A. B. Anton, J. E. Parmeter and W. H. Weinberg, J. Am. Chem. Soc., submitted.
8. J. T. Yates, T. E. Madey and M. J. Dresser, J. Catal. **30**, 260 (1973).
9. J. B. Benziger, E. I. Ko and R. J. Madix, J. Catal. **64**, 132 (1980).
10. J. T. Dickinson and R. J. Madix, Int. J. Chem. Kinetics, Vol. X, 871 (1978).
11. L. J. Richter and W. Ho, submitted.
12. N. M. Abbas and R. J. Madix, Appl. Surface Sci. **7**, 241 (1981).
13. E. M. Stuve, R. J. Madix and B. A. Sexton, Surface Sci. **119**, 279 (1982).
14. B. A. Sexton, A. E. Hughes and N. R. Avery, Surface Sci. **155**, 366 (1985).
15. E. L. Muetterties and J. L. Stein, Chem. Rev. **79**, 479 (1979).
16. C. Masters, Advan. Organomet. Chem. **17**, 61 (1979).
17. B. D. Dombek, J. Am. Chem. Soc. **102**, 6855 (1980).
18. K. L. Brown, G. R. Clark, C. E. L. Headford, K. Marsden and W. R. Roper, J. Am. Chem. Soc. **101**, 503 (1979).
19. S. Gambarotta, C. Floriani, A. Chiesi-Villa and C. Guastini, J. Am. Chem. Soc. **104**, 2019 (1982); **107**, 2985 (1985).

20. W. E. Buhro, A. T. Patton, C. E. Strouse and J. A. Gladysz, J. Am. Chem. Soc. **105**, 1056 (1983).

21. K. Kropp, Y. Skibbe, G. Erker and K. Krüer, J. Am. Chem. Soc. **105**, 3353 (1983).

22. H. Adams, N. A. Bailey, J. T. Gauntlett and M. J. Winter, J. Chem. Soc. Chem. Commun. **1984**, 1360.

23. B. N. Chaudret, D. J. Cole-Hamilton, R. S. Nohr and G. Wilkinson, J. Chem. Soc. Dalton **1977**, 1546.

24. N. R. Avery, W. H. Weinberg, A. B. Anton and B. H. Toby, Phys. Rev. Letters **51**, 682 (1983); A. B. Anton, N. R. Avery, B. H. Toby and W. H. Weinberg, J. Am. Chem. Soc., submitted.

25. D. L. Thorn, J. Am. Chem. Soc. **102**, 7109 (1980); Organomet. **1**, 197 (1982).

26. W.-K. Wong, W. Tam, C. E. Strouse and J. A. Gladysz, J. Chem. Soc. Chem. Commun. **1979**, 530.

27. C. P. Casey, S. M. Neumann, M. A. Andrews and D. P. McAlister, Pure and Appl. Chem. **52**, 625 (1980).

28. J. R. Morton and K. F. Preston, Chem. Phys. Letters **111**, 611 (1984).

29. C. P. Casey, M. W. Meszaros, S. M. Neumann, I. G. Cesas and K. J. Haller, Organomet. **4**, 143 (1985).

30. K. G. Moloy and T. J. Marks, J. Am. Chem. Soc. **106**, 7051 (1984); T. J. Marks, Science **217**, 989 (1982).

31. P. A. Belmonte, F. G. N. Clarke and R. R. Schrock, J. Am. Chem. Soc. **105**, 2643 (1983); M. R. Churchill and H. J. Wasserman, Inorg. Chem. **21**, 226 (1982).

32. P. T. Wolczanski and J. E. Bercaw, Acc. Chem. Res. **13**, 121 (1980).

33. W. R. Roper, G. E. Taylor, J. M. Waters and L. J. Wright, J. Organomet. Chem. **182**, C46 (1979).

34. K. Sükel, K. Schloter, W. Beck, K. Ackerman and U. Schubert, J. Organomet. Chem. **241**, 333 (1983).

35. S. Merlino, G. Montagnoli, G. Braca and G. Sbrana, Inorg. Chim. Acta **27**, 233 (1978).

36. B. Longato, J. R. Norton, J. C. Huffmann, J. A. Marsella and K. G. Caulton, J. Am. Chem. Soc. **103**, 209 (1981).

37. G. S. Bristow, P. B. Hitchcock and M. F. Lappert, J. Chem. Soc. Chem. Commun. **1982**, 462.

38. G. E. Thomas and W. H. Weinberg, Rev. Sci. Instrum. **50**, 497 (1979).

39. G. E. Thomas and W. H. Weinberg, J. Chem. Phys. **70**, 954 (1979).

40. T. S. Rahman, A. B. Anton, N. R. Avery and W. H. Weinberg, Phys. Rev. Letters **51**, 1979 (1983).

41. T. E. Madey, H. A. Engelhardt and D. Menzel, Surface Sci. **48**, 304 (1975).

42. J. F. Walker, *Formaldehyde*, 3rd ed., Reinhold, New York, 1964, pp. 44-45 and p. 215.

43. P. A. Thiel, F. M. Hoffmann and W. H. Weinberg, J. Chem. Phys. **75**, 5556 (1981).

44. P. A. Thiel, F. M. Hoffmann and W. H. Weinberg, Phys. Rev. Letters. **49**, 501 (1982).

45. H. Shimizu, K. Christmann and G. Ertl, J. Catal. **61**, 412 (1980).

46. E. D. Williams and W. H. Weinberg, Surface Sci. **82**, 93 (1979).

47. P. A. Redhead, Vacuum **12**, 203 (1962).

48. Ibid 42, p. 148.

49. N. R. Avery, B. H. Toby, A. B. Anton and W. H. Weinberg, Surface Sci. **122**, L574 (1982).

50. A. B. Anton and W. H. Weinberg, unpublished results.

51. D. E. Peebles, J. A. Schreifels and J. M. White, Surface Sci. **116**, 117 (1982).

52. M. A. Barteau, J. Q. Broughton and D. Menzel, Surface Sci. **133**, 443 (1983).

53. T. Shimanouchi, *Tables of Vibrational Frequencies*, Consolidated Vol. I, NSRDS-NBS 39; Vol. II.

54. H. Ibach and D. L. Mills, *Electron Energy Loss Spectroscopy and Surface Vibrations*, Academic Press, New York, 1982.

55. G. Herzberg, *Infrared and Raman Spectra of Polyatomic Molecules*, Van Nostrand, New York, 1945.

56. H. Khoshkoo, S. T. Hemple and E. R. Nixon, Spectrochim. Acta **30A**, 863 (1974).

57. H. Tadokoro, M. Kobayashi, Y. Kawaguchi, A. Kobayashi and S. Murahashi, J. Chem. Phys. **38**, 703 (1963).

58. If hydrogen motion is decoupled from other vibrational motion of a molecule, substitution of deuterium for hydrogen decreases the frequencies of hydrogenic modes by the square root of the H/D mass ratio, and $\nu(H)/\nu(D) = 1.41$ **(55,56)**.

59. N. B. Colthup, L. H. Daly and S. E. Wiberley, *Introduction to Infrared and Raman Spectroscopy*, Academic Press, New York, 1975.

60. J. Topping, Proc. Roy. Soc. London A **114**, 67 (1927).

61. B. H. Toby, N. R. Avery, A. B. Anton and W. H. Weinberg, in preparation.

62. B. Hess, P. J. Bruna, R. J. Buenker and S. D. Peyerimhoff, Chem. Phys. **18**, 267 (1980).

63. M. J. S. Dewar, Bull. Soc. Chim. France **18**, C79 (1951); J. Chatt and L. A. Duncanson, J. Chem. Soc. **1953**, 2939.

64. C. D. Wood and R. R. Schrock, J. Am. Chem. Soc. **101**, 5421 (1979).

65. The activation energies for these surface reactions are estimated by assuming first order kinetics, which is appropriate for unimolecular decomposition reactions, and assuming a preexponential factor of the reaction rate coefficient of 10^{13} s^{-1}. The activation energy, E_a is then obtained by assuming that the characteristic time of the reaction is approximately one second, i.e. $10^{-13} \exp(-|E_a|/kT)$.

66. C. Masters, Adv. Organomet. Chem. **17**, 61 (1979).

Table 1. Assignments of vibrational bands (in cm^{-1}) observed with high resolution electron energy loss spectroscopy of η^2-HCO and η^2-DCO on Ru(001). Also listed for comparison are the IR bands for the HCO and DCO functions of the model compounds $HCOOCH_3$ and $DCOOCH_3$.

Mode	η^2-HCO	$HCOOCH_3$ **(53)**	η^2-DCO	$DCOOCH_3$ **(53)**
ν(CH)	2900	2943	-	2216
δ(CH)	1400	1371	980	1048
ν(CO)	1180	1207	1160	1213
π(CH)	1065	1032	825	870
ν(Ru-HCO)	590		550	

Table 2. Assignments of vibrational bands (in cm^{-1}) observed with high resolution electron energy loss spectroscopy of H_2CO and D_2CO on Ru(001) and Ru(001)-p(2x2)O. Also listed are the IR bands of solid H_2CO and D_2CO.

Mode and Symmetry for Free Formaldehyde	Solid **(56)**		Ru(001) and Ru(001)-p(2x2)O					
			H_2CO			D_2CO		
	H_2CO	D_2CO	multi-layer	η^1(80K)	η^2(250K)	multi-layer	η^1(80K)	η^2(250K)
$\nu_a(CH_2)(B_1)$	2843	2214	2840	2970	2940	2210	2200-2255	2225
$\nu_s(CH_2)(A_1)$	2831	2095		2850		2100		
$\nu(CO)(A_1)$	1700	1660	1720	1660-1680	980	1690	1640-1660	1020
$\delta(CH_2)(A_1)$	1490	1096	1500	1465	1450	1110	1190	1190
$\rho(CH_2)(B_1)$	1250	990	1215	1195-1240	840	1015	1025	620
$\omega(CH_2)(B_2)$	1179	942			1160			865
lattice	161	152	170			160		

Figure Captions

Figure 1: Thermal desorption spectra for increasing exposures of D_2CO on the clean Ru(001) *(left)* and Ru(001)-p(2x2)O *(right)* surfaces at 80 K. The average heating rate, $<\beta>$, for these spectra and the spectra of Figs. 2 and 3 was 15 K/s.

Figure 2: Thermal desorption spectra showing the evolution of CO from Ru(001) following exposure (a) of the clean surface to 0.5 L of CO, (b) of the Ru(001)-p(2x2)O surface to 0.4 L of CO, and (c) of the clean and (d) the Ru(001)-p(2x2)O surfaces to the indicated exposures of D_2CO.

Figure 3: Thermal desorption spectra showing the evolution of D_2 from Ru(001) following the indicated exposures of (a) the Ru(001)-p(2x2)O and (b) the clean Ru(001) surfaces to D_2CO.

Figure 4: EEL spectra recorded after the indicated exposures of the clean Ru(001) surface to H_2CO *(left)* and D_2CO *(right)* at 80 K.

Figure 5: Schematic η^1 [(a)] and η^2 [(b), (c) and (d)] bonding configurations observed in homogeneous complexes with acyl *(top)* and aldehyde *(bottom)* ligands.

Figure 6: EEL spectra recorded after exposure of the clean Ru(001) surface to 10 L of H_2CO *(left)* and D_2CO *(right)* at 80 K. The symbol "Δ" signifies momentary heating of the surface to the indicated temperatures, followed by cooling to 80 K to record the spectra.

Figure 7: EEL spectra of η^2-H_2CO *(left)* and η^2-D_2CO *(right)* recorded in the specular direction *(bottom)* and 5° out of the specular direction *(top)*.

Figure 8: EEL spectra recorded after the indicated exposures of the Ru(001)-p(2x2)O surface to H_2CO *(left)* and D_2CO *(right)* at 80 K. Also shown in the inset is the EEL spectrum of the p(2x2) oxygen overlayer.

Figure 9: EEL spectra recorded after exposure of the Ru(001)-p(2x2)O surface to 10 L of H_2CO *(left)* and D_2CO *(right)* at 80 K, followed by annealing to the indicated temperatures.

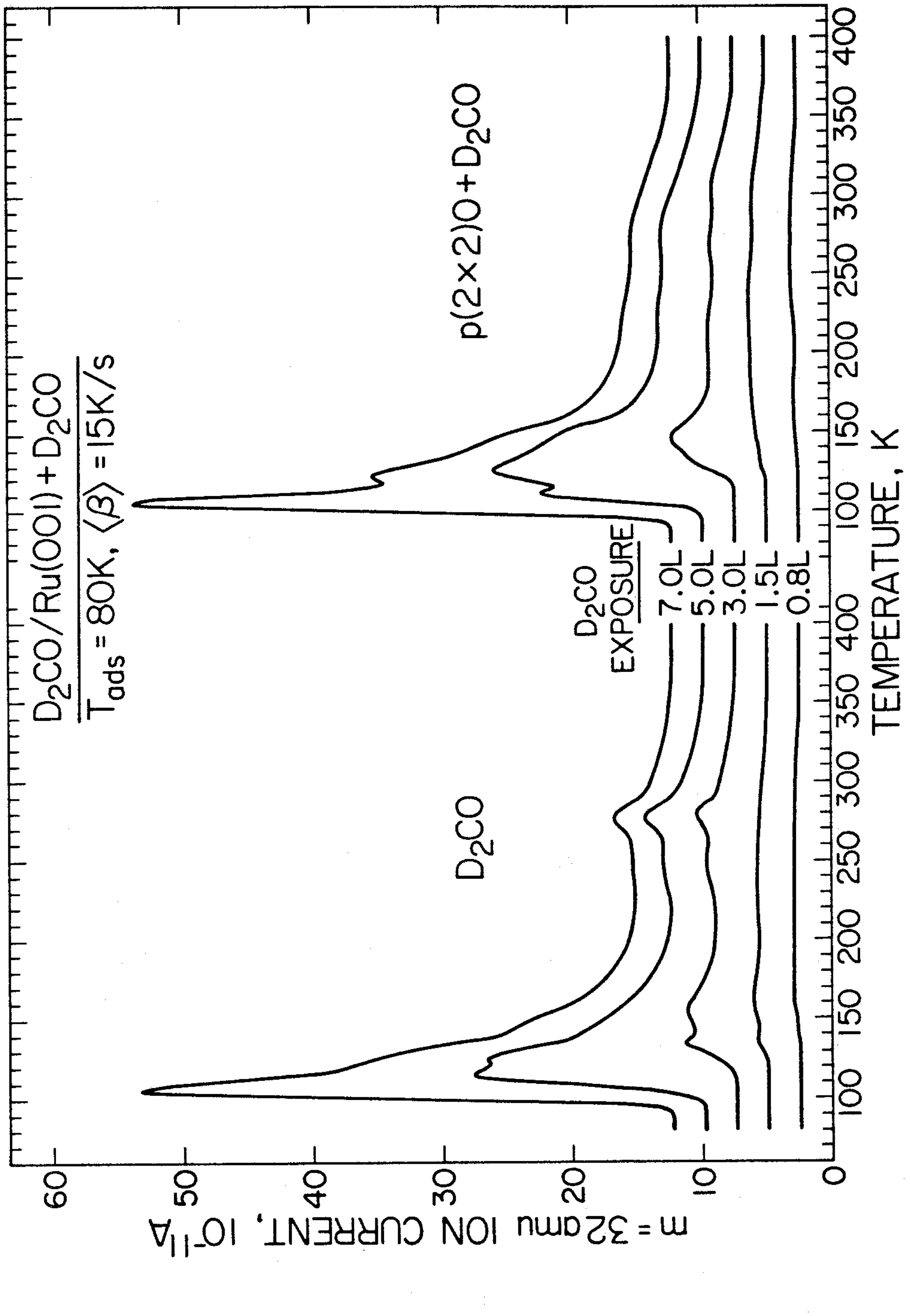
D₂CO/Ru(001) + D₂CO
T_ads = 80K, ⟨β⟩ = 15K/s
D₂CO
p(2×2)O + D₂CO
D₂CO EXPOSURE
7.0L
5.0L
3.0L
1.5L
0.8L
0
10
20
30
40
50
60
m = 32amu ION CURRENT, 10⁻¹¹A
100
150
200
250
300
350
400
100
150
200
250
300
350
400
TEMPERATURE, K

Figure 1

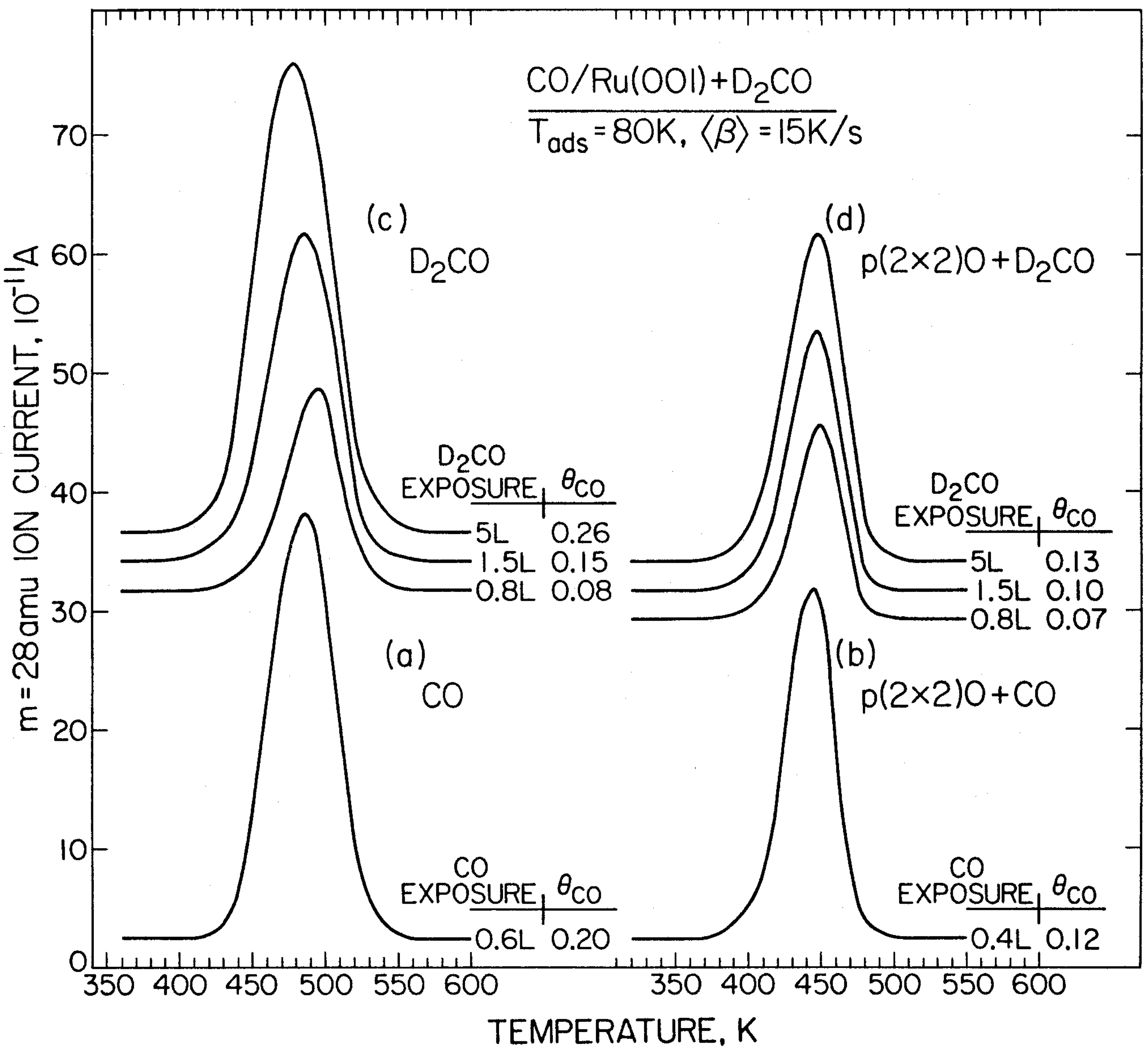
CO/Ru(001)+D_2CO
T_{ads}=80K, ⟨β⟩=15K/s
(c)
D_2CO
(d)
p(2×2)O+D_2CO
(a)
CO
(b)
p(2×2)O+CO
D_2CO EXPOSURE | θ_{CO}
5L 0.26
1.5L 0.15
0.8L 0.08
D_2CO EXPOSURE | θ_{CO}
5L 0.13
1.5L 0.10
0.8L 0.07
CO EXPOSURE | θ_{CO}
0.6L 0.20
CO EXPOSURE | θ_{CO}
0.4L 0.12
m=28amu ION CURRENT, 10^{-11}A
0
10
20
30
40
50
60
70
350
400
450
500
550
600
350
400
450
500
550
600
TEMPERATURE, K

Figure 2

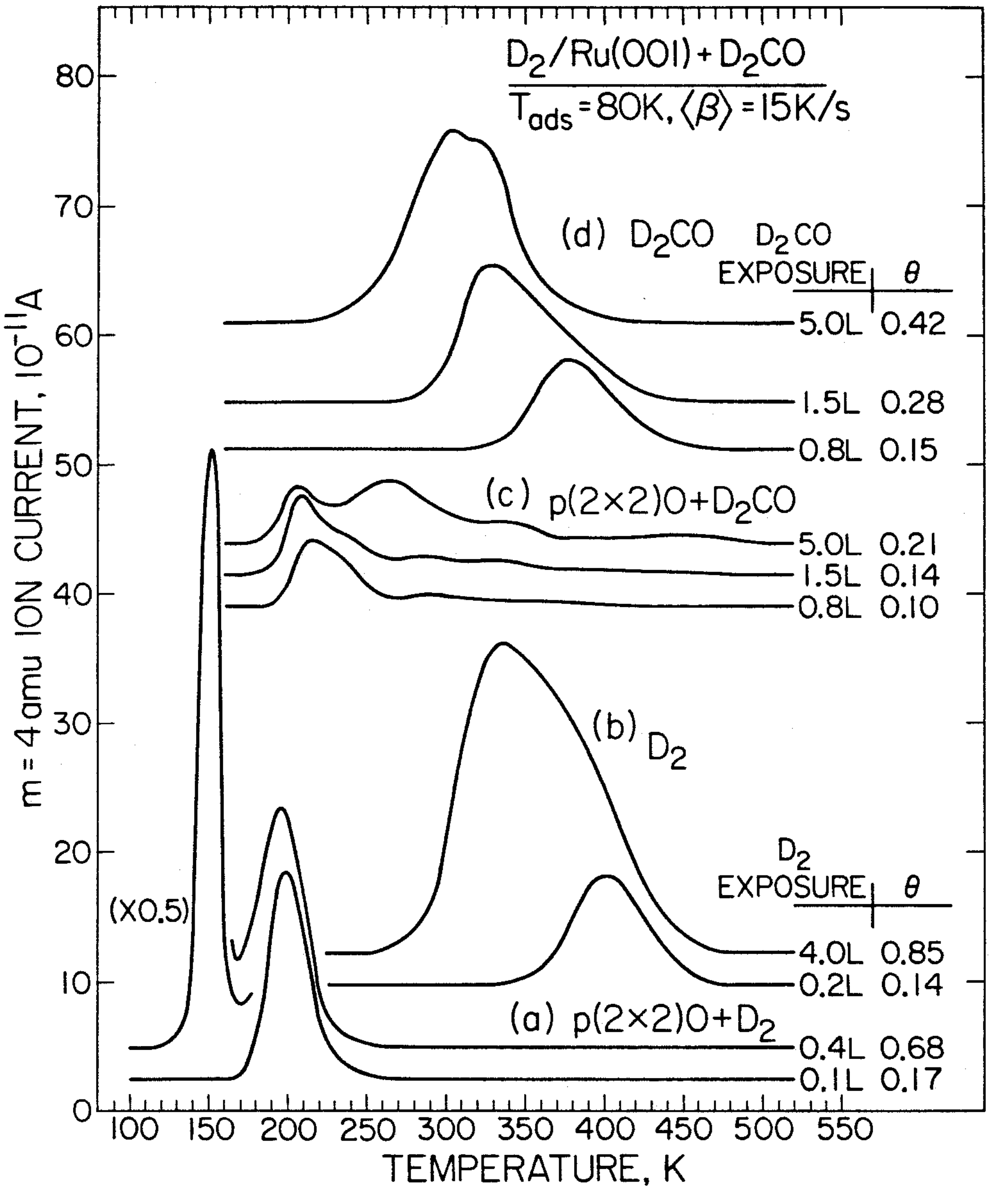
$D_2/Ru(001)+D_2CO$
$T_{ads}=80K, \langle\beta\rangle=15K/s$
(d) D_2CO
D_2CO EXPOSURE θ
5.0L 0.42
1.5L 0.28
0.8L 0.15
(c) $p(2\times2)O+D_2CO$
5.0L 0.21
1.5L 0.14
0.8L 0.10
(b) D_2
D_2 EXPOSURE θ
4.0L 0.85
0.2L 0.14
(a) $p(2\times2)O+D_2$
0.4L 0.68
0.1L 0.17
(X0.5)
m = 4 amu ION CURRENT, 10^{-11}A
0 10 20 30 40 50 60 70 80
100 150 200 250 300 350 400 450 500 550
TEMPERATURE, K

Figure 3

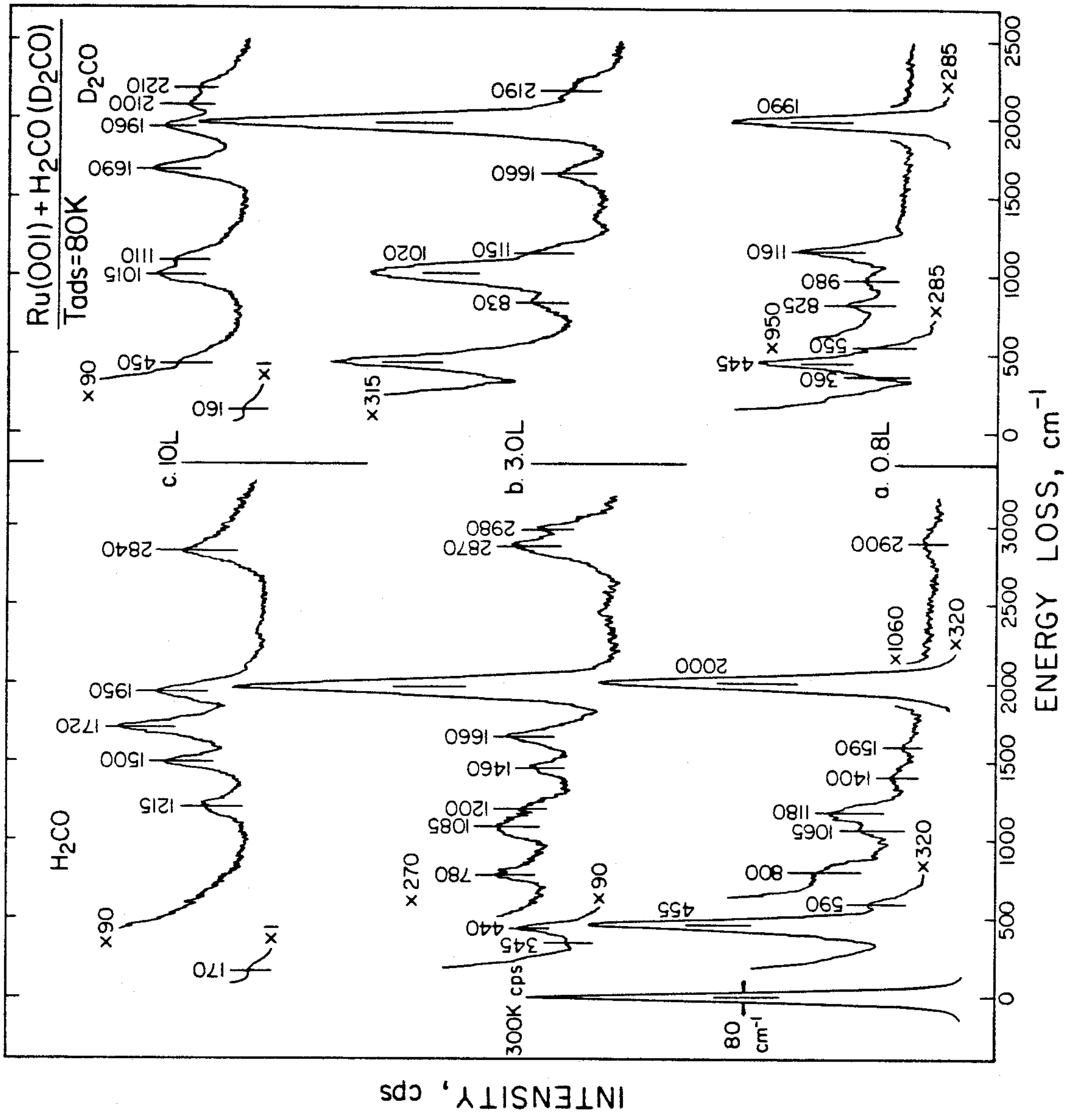
Ru(001) + H$_2$CO (D$_2$CO)
Tads=80K
H$_2$CO
D$_2$CO
c. 10L
b. 3.0L
a. 0.8L
x90
170
x1
1215
1500
1720
1950
2840
x270
345
440
x90
780
1085
1200
1460
1660
2870
2980
300K cps
80 cm^{-1}
455
590
x320
800
1065
1180
1400
1590
2000
x1060
x320
2900
x90
160
x1
450
1015
1110
1690
1960
2100
2210
x315
830
1020
1150
1660
2190
360
445
x950
550
825
x285
980
1160
1990
x285
0
500
1000
1500
2000
2500
3000
INTENSITY, cps
ENERGY LOSS, cm^{-1}

Figure 4

ACYL:

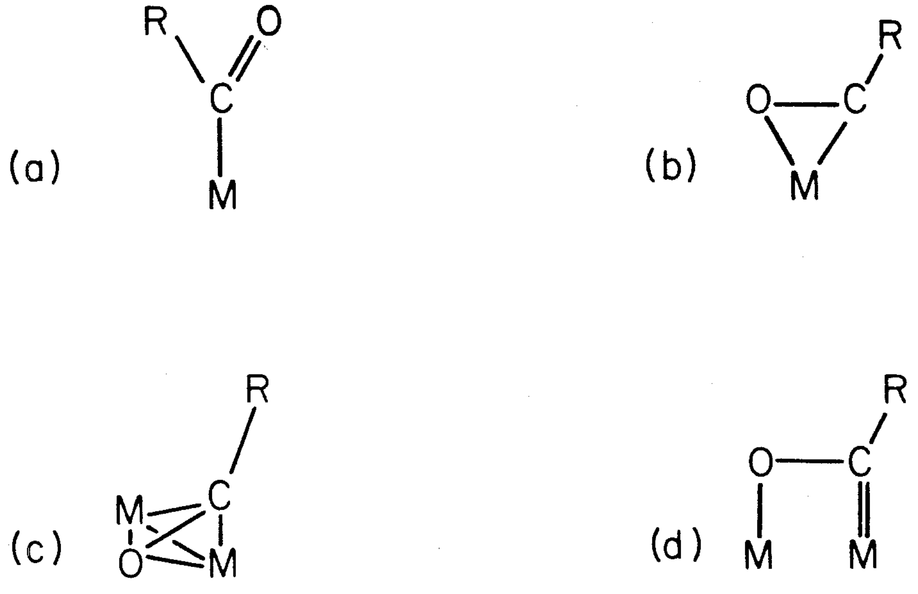

ALDEHYDE:

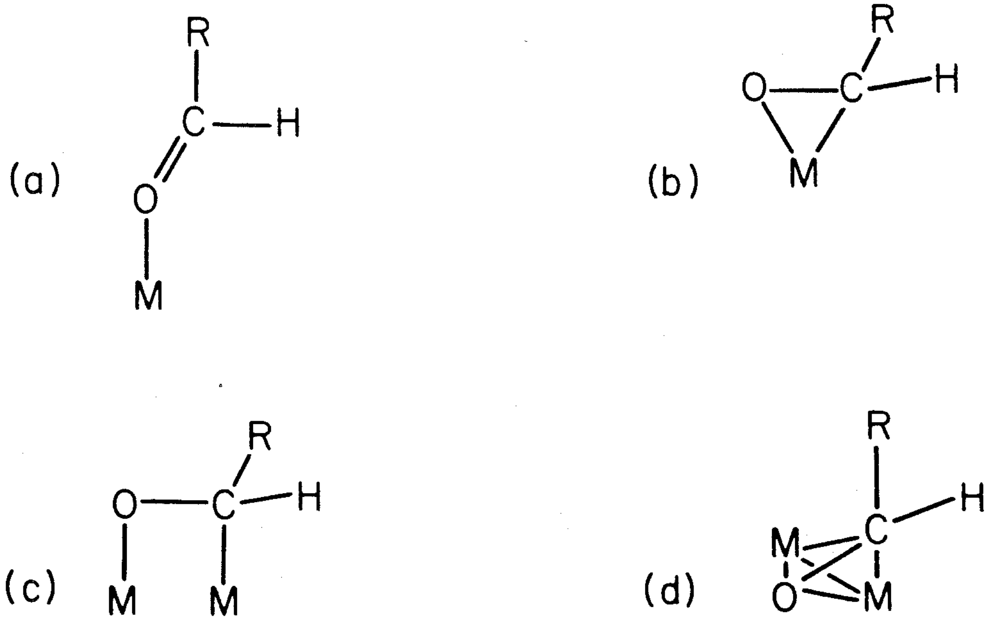

Figure 5

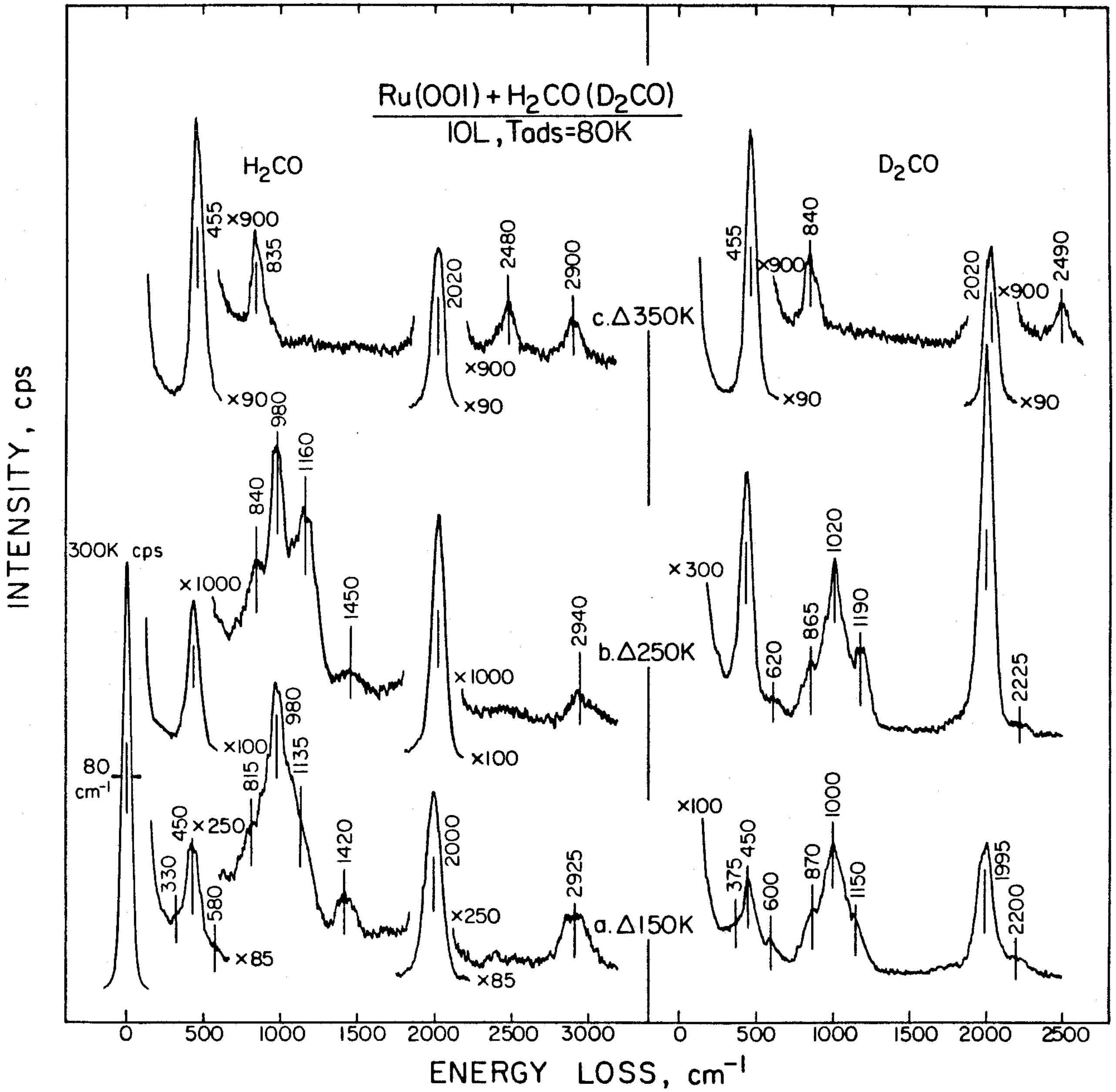
Ru(001) + H_2CO (D_2CO)
10L, Tads=80K
H_2CO
D_2CO
c.Δ350K
b.Δ250K
a.Δ150K
300K cps
80 cm^{-1}
455
×900
835
×90
2020
×900
2480
2900
×90
×1000
840
980
1160
1450
×100
×1000
2940
×100
330
450
×250
815
980
1135
1420
580
×85
2000
×250
2925
×85
455
×900
840
×90
2020
×900
2490
×90
×300
620
865
1020
1190
2225
×100
375
450
600
870
1000
1150
1995
2200
INTENSITY, cps
ENERGY LOSS, cm^{-1}
0
500
1000
1500
2000
2500
3000
0
500
1000
1500
2000
2500

Figure 6

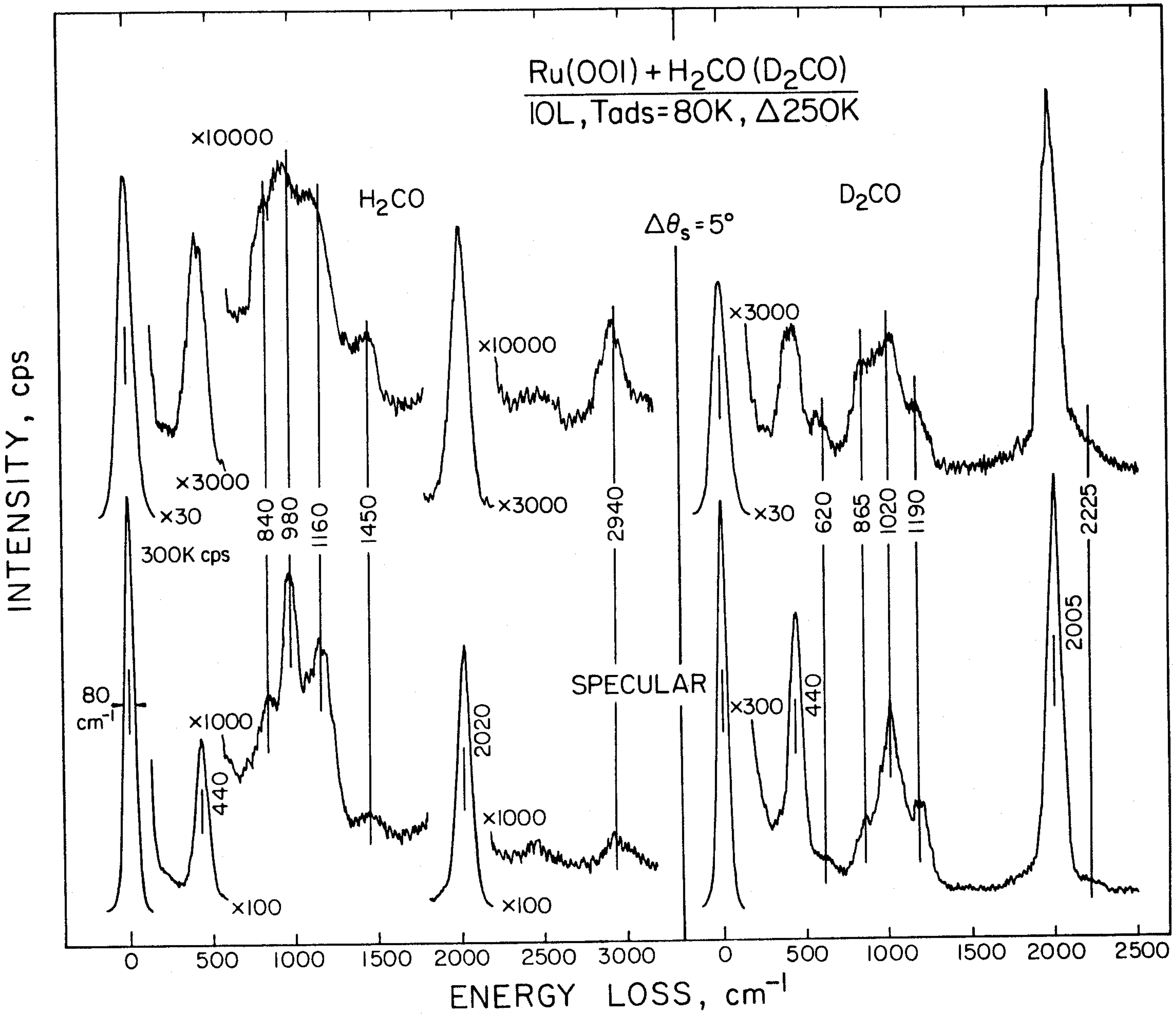
Ru(001) + H2CO (D2CO)
10L, Tads=80K, Δ250K
INTENSITY, cps
ENERGY LOSS, cm-1
H2CO
D2CO
Δθs = 5°
SPECULAR
×10000
×3000
×30
300K cps
80 cm-1
×1000
×100
440
840
980
1160
1450
2020
2940
×300
620
865
1020
1190
2005
2225
0
500
1000
1500
2000
2500
3000

Figure 7

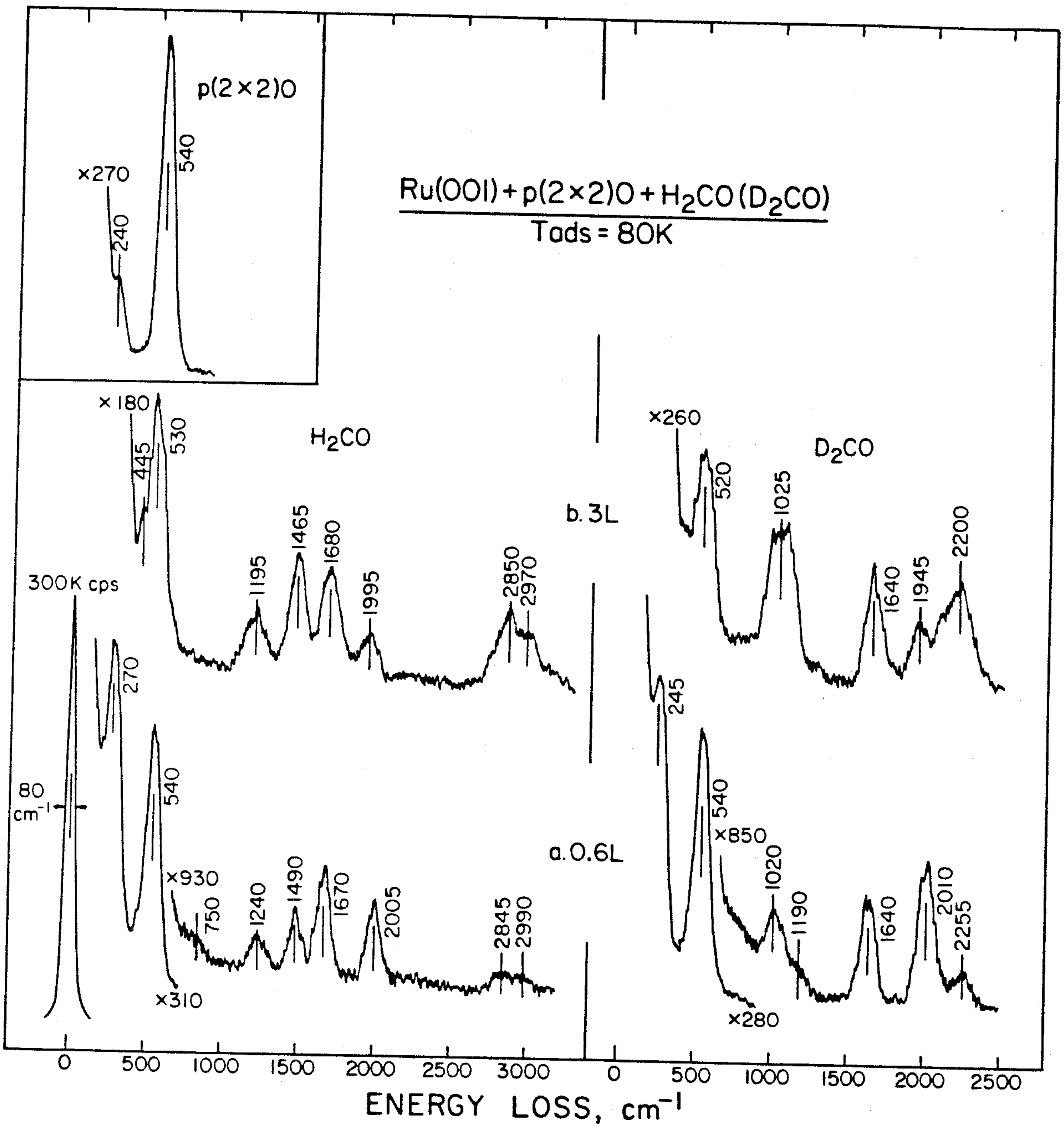

Ru(001) + p(2×2)O + H_2CO (D_2CO)
Tads = 80K
p(2×2)O
×270
240
540
×180
445
530
H_2CO
1195
1465
1680
1995
2850
2970
b. 3L
×260
520
D_2CO
1025
1640
1945
2200
300K cps
270
540
80 cm⁻¹
×930
750
1240
1490
1670
2005
2845
2990
×310
a. 0.6L
245
540
×850
1020
1190
1640
2010
2255
×280
INTENSITY, cps
ENERGY LOSS, cm⁻¹
0
500
1000
1500
2000
2500
3000

Figure 8

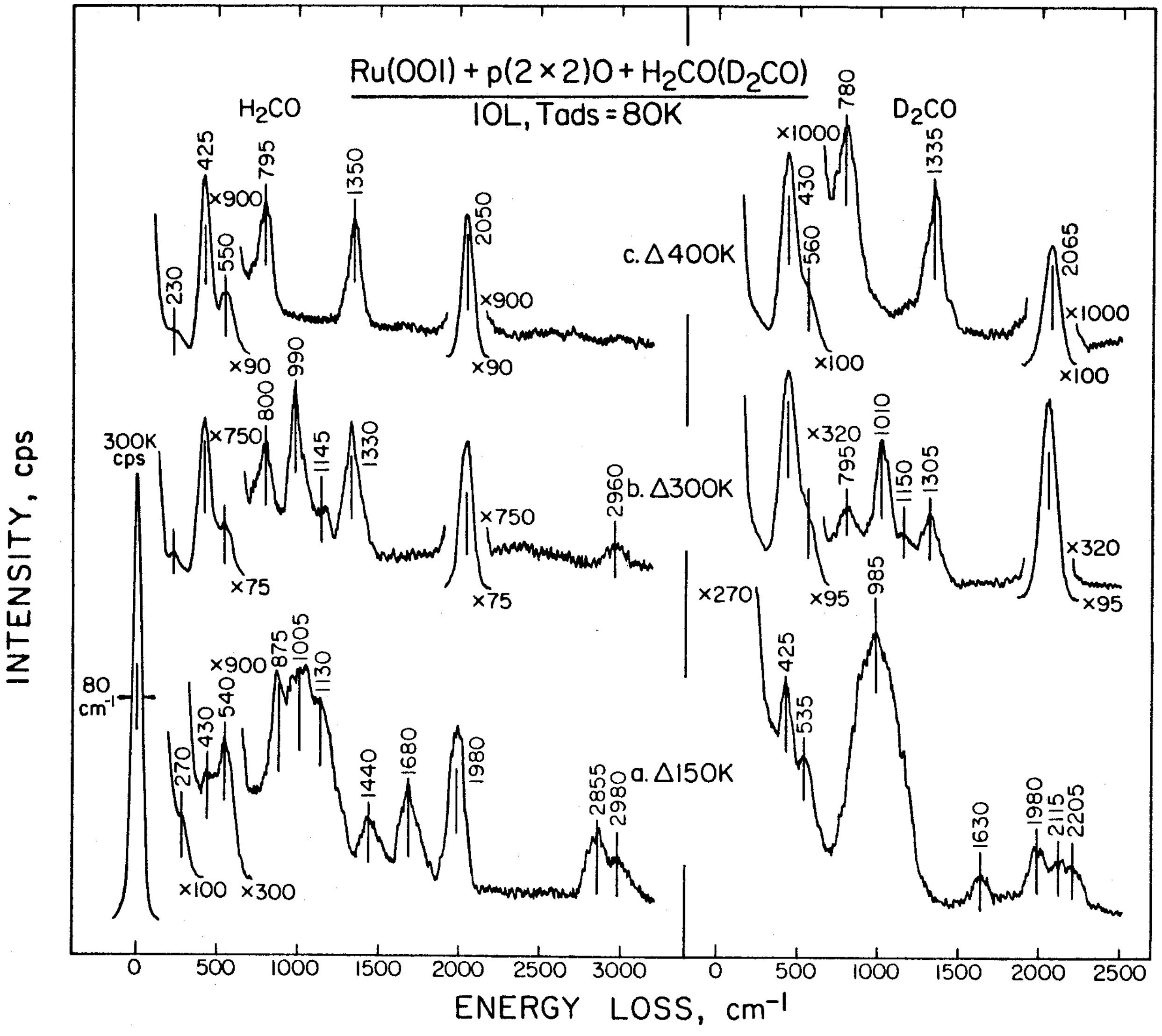
Ru(001) + p(2 × 2)O + H2CO(D2CO)
10L, Tads = 80K
H2CO
D2CO
c. Δ400K
b. Δ300K
a. Δ150K
300K cps
80 cm-1
425
×900
795
550
230
×90
1350
2050
×900
×90
×750
800
990
1145
1330
×75
×750
×75
2960
×900
875
1005
1130
270
430
540
×100
×300
1440
1680
1980
2855
2980
×1000
780
430
560
×100
1335
2065
×1000
×100
×320
1010
795
1150
1305
×95
×320
×95
×270
985
425
535
1630
1980
2115
2205
INTENSITY, cps
ENERGY LOSS, cm-1
0
500
1000
1500
2000
2500
3000
0
500
1000
1500
2000
2500

Figure 9

Chapter IX.

Appendices

Appendix 1.

Decomposition of Formic Acid on Ru(001): An EELS Search for a Formic Anhydride Intermediate

Surface Science 122 (1982) L574–L578
North-Holland Publishing Company

SURFACE SCIENCE LETTERS

DECOMPOSITION OF FORMIC ACID ON Ru(001): AN EELS SEARCH FOR A FORMIC ANHYDRIDE INTERMEDIATE *

N.R. AVERY **, B.H. TOBY, A.B. ANTON and W.H. WEINBERG

Division of Chemistry and Chemical Engineering, California Institute of Technology, Pasadena, California 91125, USA

Received 21 June 1982

High resolution electron energy loss spectroscopy has demonstrated the existence of a symmetrical bidentate bridging formate as a stable intermediate in the decomposition of formic acid on the Ru(001) surface. This formate decomposes with two pathways – via C–H bond cleavage to give CO_2 and adsorbed hydrogen, and via C–O bond cleavage to give adsorbed hydrogen, oxygen and CO. Thermal desorption demonstrates the evolution of H_2, H_2O, CO and CO_2. The observation of this product distribution from Ru(100), Ni(100) and Ni(110) had prompted the proposal of a formic anhydride intermediate. The spectroscopic results reported here bring the presence of this postulated, normally unstable species into question.

Thermal desorption mass spectrometry (TDMS) studies of the decomposition of formic acid on clean, well characterized (110) and (100) surfaces of nickel have shown that an initial low temperature dehydration is followed by the evolution of CO_2, H_2 and CO at higher temperatures [1–3]. The CO_2 and H_2 appear in a common reaction-limited step between 350 and 370 K, whereas CO is evolved from the surface in a desorption-limited step at approximately 440 K. The ratio of CO_2 to CO evolved has been reported to be close to unity, and these results have been rationalized as a bimolecular dehydration to an adsorbed intermediate with the stoichiometry [HCOO · HCO], which subsequently decomposes in a single autocatalytic step to the observed products, viz. gaseous CO_2 and H_2, and adsorbed CO. In a comparable study of the decomposition of formic acid on the prismatic (100) surface of ruthenium, a similar dehydration, followed by the evolution of CO_2, H_2 and CO has been reported and similarly associated with a decomposition intermediate of stoichiometry [HCOO · HCO] [4]. In each of these cases, the investigators have postulated that the metal surface has stabilized the dehydration of formic acid to formic anhydride, normally an unstable species.

---

* Supported by the National Science Foundation under Grant No. CHE82-06487.

** Permanent address: Division of Materials Science, CSIRO, University of Melbourne, Parkville, Victoria, Australia 3052.

By contrast, the decomposition of formic acid on Cu(100) [5], Ag(110) [6] and Pt(111) [7] yields only CO_2 and H_2 in a simple unimolecular dehydrogenation of an adsorbed formate intermediate. In each of these instances, Brönsted deprotonation of the adsorbed formic acid to the adsorbed formate intermediate has been *confirmed* spectroscopically by electron energy loss spectroscopy (EELS).

In this Letter we report some pertinent aspects of a TDMS and EELS study of the decomposition of formic acid on the close-packed (001) surface of ruthenium [8]. Although this is not the same surface of ruthenium for which TDMS has *implied* the existence of a formic anhydride intermediate [4], we expect that the fundamental chemistry of the two ruthenium surfaces will be quite similar, as is the case for the (100) and (110) surfaces of nickel [3]. The aim of this study is to determine unequivocally, via EELS, the structure of the

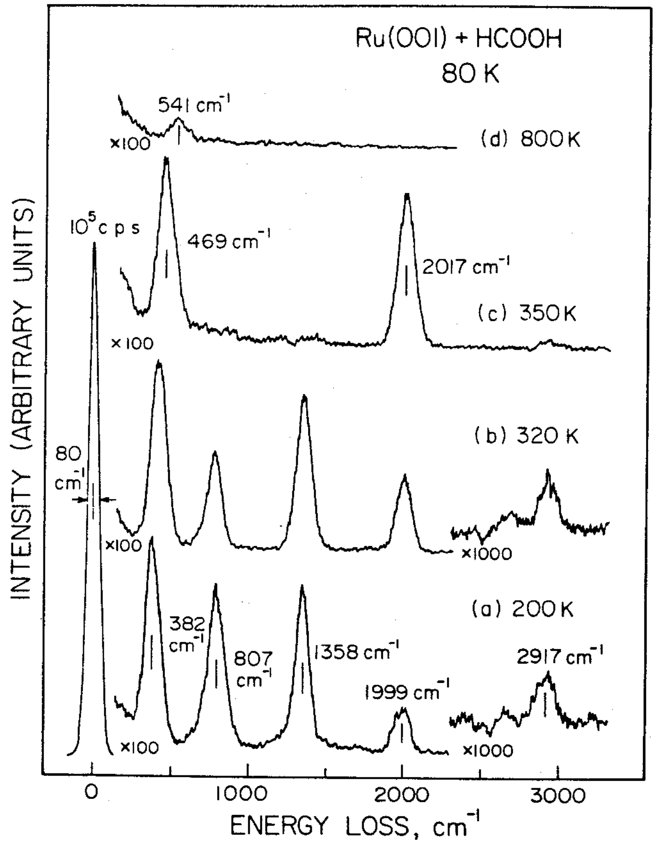

Fig. 1. EEL spectra obtained after adsorption of formic acid on a clean Ru(001) surface at 80 K followed by annealing to the indicated temperatures.

prominent adsorbed intermediate formed by decomposition of formic acid on Ru(001) and to reevaluate the feasibility of a decomposition scheme which proceeds through formation of a normally unstable formic anhydride intermediate. The electron energy loss spectrometer used in this work and the ultrahigh vacuum apparatus in which it is housed have been described in detail previously [9].

Fig. 1 shows a sequence of EEL spectra which were obtained after the adsorption at 80 K of slightly in excess of one monolayer of formic acid on a clean Ru(001) surface, followed by annealing to the indicated temperatures. Annealing to 200 K causes molecularly adsorbed (multilayer) formic acid to desorb, and the resulting EEL spectrum (fig. 1a) shows four conspicuous bands at 382, 807, 1358 and 2917 cm^{-1} which are easily assigned to the ν(Ru–O), δ(OCO), ν_s(OCO) and ν(CH) modes of an adsorbed formate, respectively [5–7]. Note also the absence of vibrational bands at 1040–1175 and 1700–1775 cm^{-1} in this spectrum, as would be seen for the ν_s(COC) and ν_s(CO) modes of an adsorbed anhydride, respectively [10]. The inherently strong ν_s(OCO) mode, expected at 1600 cm^{-1} for an adsorbed formate, has B_1 symmetry and could not be detected. This indicates, according to the surface selection rule for dipole excitations, an equivalence of the two oxygen atoms. Furthermore, the similarity between the frequencies of the ν_s(OCO) mode for the adsorbed formate (1358 cm^{-1}) and the free formate ion (1366 cm^{-1}) suggests a symmetric bidentate bridging configuration, as shown below [7,11]:

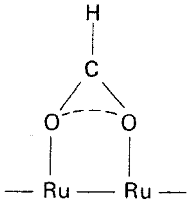

The only other surface species which could be detected is a weak band at 1999 cm^{-1} (fig. 1a) due to adsorbed CO [12]. This CO, representing less than 0.05 monolayer, is due to the onset of decomposition of the adsorbed formate and correlates with the evolution of H_2O below 200 K. Further annealing to 320 K (fig. 1b) causes the intensities of the bands due to the adsorbed formate to decrease and those due to adsorbed CO to increase, At 350 K (fig. 1c), the decomposition of the adsorbed formate is complete. Annealing to 800 K (fig. 1d) resulted in the desorption of CO, revealing a weak band at 541 cm^{-1} which could be removed by further annealing to 1630 K. This band is due to a small residual concentration of oxygen adatoms [13].

TDMS results demonstrate the evolution of HCOOH, H_2O, H_2, CO_2 and CO from the Ru(001) surface and reveal a complicated mechanism of decomposition. For initial coverages in excess of one monolayer, molecular formic acid from condensed multilayers desorbs with a peak temperature of 195 K. A second molecular formic acid desorption feature is seen at 350 K for low coverages, shifting to 375 K and saturating for all initial coverages of a monolayer or greater. No molecular formic acid is detected by EELS above 200 K, suggesting that the desorption of formic acid at 350–375 K is due to recombination of adsorbed hydrogen and formate. For submonolayer initial coverages, H_2O desorbs in two peaks with maxima at 160 and 275 K. As mentioned earlier, this H_2O results from decomposition of the adsorbed formate and correlates with the appearance of CO in the EEL spectra. Carbon dioxide is evolved in a single reaction-limited step with a peak temperature of 300 K for low initial coverages, shifting to 365 K for saturation coverage. This temperature shift results from increased stability of the adsorbed formate at higher coverage [8]. Hydrogen is evolved in a single desorption-limited step with a peak temperature of 455 K for low initial coverages, shifting to 375 K at saturation. In this case the temperature shift probably results from repulsive interactions among hydrogen adatoms and other adsorbed species, the net effect of which increases with total surface coverage [14]. Carbon monoxide is evolved in a single desorption-limited step with a peak temperature of 480 K, and a trace of adsorbed oxygen remains to approximately 1600 K.

Since the probability of CO oxidation to CO_2 on Ru(001) under the conditions prevailing in these experiments is on the order of 0.1% of the probability of CO desorption [15], the appearance of both CO_2 and CO in TDMS results indicates that formic acid decomposes by two competing mechanisms on Ru(001). Initial dehydrogenation of formic acid to an adsorbed formate intermediate is followed by decomposition of the formate through dehydrogenation *or* through C–O bond cleavage. The integrated intensities of the CO_2 and CO desorption peaks, corrected for the relative sensitivity of the quadrupole mass spectrometer to each species, yield a ratio of CO to CO_2 evolution of approximately three to one, indicating that formate decomposition through C–O bond cleavage is more rapid than by simple dehydrogenation. An overall reaction scheme consistent with all EELS and TDMS results for formic acid decomposition on Ru(001) can be written as follows ((a) denotes an adsorbed species, (g) denotes a gaseous species):

Following adsorption of formic acid in excess of one monolayer, molecules in multilayers desorb intact near 195 K, while those in contact with the surface decompose to yield an adsorbed formate. Some recombination occurs on the surface to yield molecular formic acid near 375 K;

$$\mathrm{HCOOH(g)} \rightleftharpoons \mathrm{HCOOH(a)}, \quad \mathrm{HCOOH(a)} \rightleftharpoons \mathrm{HCOO(a)} + \mathrm{H(a)}.$$

The formate species decomposes by two competing mechanisms to yield adsorbed CO over a broad temperature range (150–400 K) and gaseous CO_2 between 300 and 365 K. Mechanism (1) is more rapid than mechanism (2):

$$\mathrm{HCOO(a)}\begin{array}{l}\nearrow \mathrm{H(a)+CO(a)+O(a)}, \qquad (1)\\ \searrow \mathrm{H(a)+CO_2(g)}. \qquad (2)\end{array}$$

Hydrogen adatoms and oxygen adatoms from formate decomposition recombine to yield water at 160 and 275 K:

$$\mathrm{H(a)+O(a)\rightarrow OH(a)}, \quad \mathrm{OH(a)+H(a)\rightarrow H_2O(g)}.$$

Hydrogen and CO are evolved in desorption-limited steps at 375–455 K and 480 K, respectively. The oxygen adatoms, present in low concentration, are dissolved into the bulk of the Ru at approximately 1600 K,

$$\mathrm{2\,H(a)\rightarrow H_2(g)}, \quad \mathrm{CO(a)\rightarrow CO(g)}, \quad \mathrm{O(a)\rightarrow O(dissolved)}.$$

In conclusion, the products of the decomposition of formic acid on Ru(001) are the same as those observed on Ru(100), Ni(100) and Ni(110), yet only a *formate intermediate* is present on Ru(001) as *verified* by EELS. The adsorbed formate intermediate present on Ru(001) does not decompose exclusively by dehydrogenation, as observed for formate intermediates on Cu(100) [5], Ag(110) [6] and Pt(111) [7], but also by C–O bond cleavage. These results bring into question earlier *speculation* of the presence of a formic anhydride intermediate on Ru(100), Ni(100) and Ni(110) which was *inferred* from the distribution of desorbing products of the decomposition reaction [1–4].

References

[1] R.J. Madix and J.L. Falconer, Surface Sci. 51 (1975) 546.
[2] J.B. Benzinger and R.J. Madix, Surface Sci. 79 (1979) 394.
[3] R.J. Madix, Advan. Catalysis 29 (1980) 1.
[4] L.A. Larsen and J.T. Dickinson, Surface Sci. 84 (1979) 17.
[5] B.A. Sexton, Surface Sci. 88 (1979) 319.
[6] B.A. Sexton and R.J. Madix, Surface Sci. 105 (1981) 177.
[7] N.R. Avery, Appl. Surface Sci. 11/12 (1982) 774.
[8] B.H. Toby, N.R. Avery, A.B. Anton and W.H. Weinberg, in preparation; also, B.H. Toby, N.R. Avery, A.B. Anton and W.H. Weinberg, in: Proc. 3rd Intern. Conf. on Vibrations at Surfaces, Asilomar, CA, 1982, to be published.
[9] G.E. Thomas and W.H. Weinberg, Rev. Sci. Instr. 50 (1979) 497.
[10] N.B. Colthup, J. Opt. Soc. Am. 40 (1950) 397.
[11] K. Nakamoto, Infrared and Raman Spectra of Inorganic and Coordination Compounds (Wiley, New York, 1978) p. 232.
[12] G.E. Thomas and W.H. Weinberg, J. Chem. Phys. 70 (1979) 1437.
[13] G.E. Thomas and W.H. Weinberg, J. Chem. Phys. 69 (1978) 3611.
[14] This effect has been demonstrated for the coadsorption of H_2 and CO on Ru(001). See: D.E. Peebles, J.A. Schreifels and J.M. White, Surface Sci. 116 (1982) 117.
[15] H.I. Lee, G. Praline and J.M. White, Surface Sci. 91 (1980) 581.

Appendix 2.

Electron Energy Loss Spectroscopy of the Decomposition of Formic Acid On Ru(001)

Journal of Electron Spectroscopy and Related Phenomena, 29 (1983) 317—321
Elsevier Scientific Publishing Company, Amsterdam — Printed in The Netherlands

ELECTRON ENERGY LOSS SPECTROSCOPY OF THE DECOMPOSITION OF FORMIC ACID ON Ru(001)*

B.H. TOBY[1], N.R. AVERY[2], A.B. ANTON[1] and W.H. WEINBERG[1]

[1]Division of Chemistry and Chemical Engineering, California Institutue of Technology, Pasadena, California 91125 U.S.A.

[2]Division of Materials Science, C.S.I.R.O., University of Melbourne, Parkville, Victoria, Australia 3052.

ABSTRACT

Electron energy loss spectroscopy has demonstrated the existence of both a monodentate and a symmetric bidentate bridging formate as stable intermediates in the decomposition of formic acid on the Ru(001) surface. The monodentate formate converts upon heating to the bidentate formate which decomposes via two pathways: C-H bond cleavage to yield CO_2 and adsorbed hydrogen; and C-O bond cleavage to yield adsorbed hydrogen, oxygen and CO. Thermal desorption spectra demonstrate the evolution of H_2, H_2O, CO and CO_2 as gaseous products of the decomposition reaction. The observation of this product distribution from Ru(100), Ni(100) and Ni(110) had prompted the proposal of a formic anhydride intermediate, the existence of which is rendered questionable by the spectroscopic results reported here.

INTRODUCTION

Recently, electron energy loss spectroscopy (EELS) has shown clearly that a formate is the stable surface intermediate in the decomposition of formic acid on (100)Cu (ref.1,2), Ag(110) (ref.3) and Pt(111) (ref.4) surfaces. However, based on *indirect* evidence, namely the product distribution in thermal desorption spectra, formic anhydride has been postulated to be a stable intermediate in the decomposition of formic acid on Ni(100) and (110)(ref.5-7) and Ru(100) (ref.8) surfaces. The present work was undertaken in order to decide whether a formic anhydride species exists on the (001) surface of Ru under any circumstances.

EXPERIMENTAL PROCEDURES

All relevant experimental details including a description of the EEL spectrometer (ref.9), the preparation of the clean Ru(001) surface (ref.10) and the handling of formic acid in the UHV system (ref.11) have been described previously.

---

*Supported by the National Science Foundation under Grant No. CHE82-06487.

RESULTS AND DISCUSSION

Electron energy loss spectra corresponding to exposures of formic acid greater than 4L at 80 K show bands characteristic of the molecular species, indicating multilayer condensation. Annealing to 200 K causes the multilayers of formic acid to desorb, and the resulting EEL spectrum [Fig. 1(a)] shows four bands at 382, 807, 1358 and 2917 cm^{-1} which are assigned easily to the ν_s(Ru-O), δ(OCO), ν_s(OCO) and ν_s(CH) modes of an adsorbed formate, respectively (ref.1-4,11). The inherently strong ν_a(OCO) mode, expected near 1600 cm^{-1} for an adsorbed formate, has B_1 symmetry and could not be detected. This indicates, according to the surface selection rule for dipolar excitations, an equivalence of the two oxygen atoms. Furthermore, the similarity between the frequencies of the ν_s(OCO) mode for the adsorbed formate (1358 cm^{-1}) and the free formate ion (1366 cm^{-1}) suggests a symmetric bidentate bridging configuration of C_{2v} symmetry as shown schematically in (a) below (ref.12).

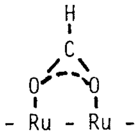

(a)

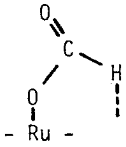

(b)

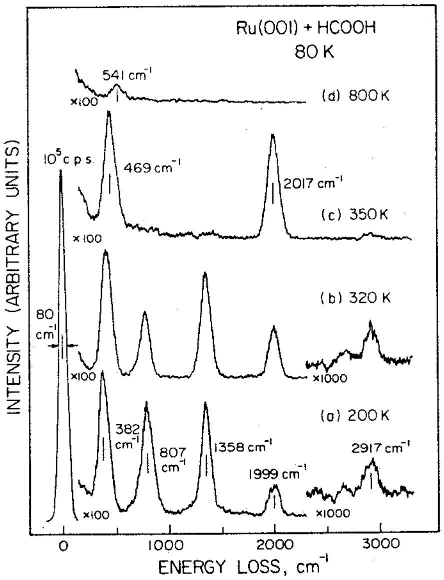

Fig. 1. EEL spectra obtained after the adsorption at 80 K of slightly in excess of one monolayer of formic acid on a clean Ru(001) surface, followed by annealing to the indicated temperatures.

The weak band at 1999 cm^{-1} in Fig. 1(a) is due to adsorbed CO (ref.13). This CO, representing less than 0.05 monolayer, is due to the onset of decomposition of the adsorbed formate and correlates with the evolution of H_2O below 200 K. Further annealing to 320 K [Fig. 1(b)] causes the intensities of the bands due to the adsorbed formate to decrease and those due to adsorbed CO to increase. At 350 K [Fig. 1(c)], the decomposition of the adsorbed formate is complete. Annealing to 800 K [Fig. 1(d)] results in the desorption of CO, revealing a weak band at 541 cm^{-1} which could be removed by further annealing to 1630 K. This band is due to a small residual concentration of oxygen adatoms (ref. 10).

An EEL spectrum corresponding to a submonolayer coverage of dissociatively adsorbed formic acid at 80 K is shown in Fig. 2. In addition to those modes observed in Fig. 1(a), there are additional bands at 1158, 1681, and 2357 cm^{-1}. The latter are assigned to the π(CH), the ν_a(OCO), and a "softened" ν_s(CH) mode [verified with DCOOD (ref.14)], respectively, for a monodentate formate, shown schematically in (b) above. Since both the π(CH) mode of B_2 symmetry and the ν_a(OCO) mode of B_1 symmetry are dipolar allowed, the formate is of C_1 symmetry, i.e. tilted with respect to the page in (b) above. The "softening" of the ν_s(CH) mode, which is manifest by a decrease of its frequency by over 500 cm^{-1}, indicates an H-Ru interaction in the chemisorbed monodentate formate. Below 200 K, both the monodentate and bidentate formates coexist on the Ru surface. Annealing the surface with both types of formate present to 200 K causes the bands corresponding to the monodentate species to disappear, and those

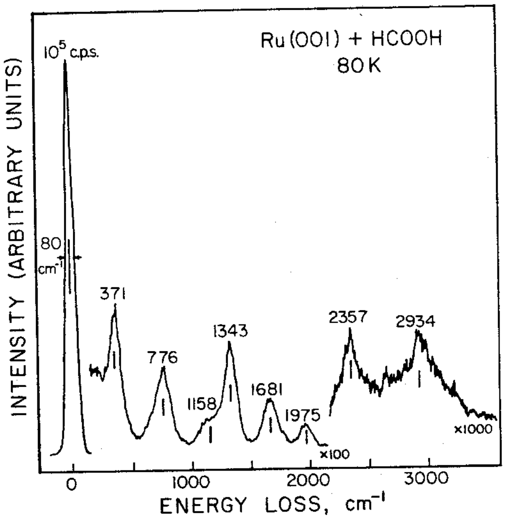

Fig. 2. EEL spectrum obtained after the adsorption at 80 K of a submonolayer amount of formic acid on a clean Ru(001) surface.

corresponding to the bidentate species to increase in intensity. This is clear evidence of the *irreverible* conversion of a monodentate to a bidentate bridging formate on the Ru(001) surface.

Thermal desorption results demonstrate the evolution of HCOOH, H_2O, H_2, CO_2 and CO from the Ru(001) surface and reveal a complicated mechanism of decomposition. For initial coverages in excess of one monolayer, molecular formic acid from condensed multilayers desorbs with a peak temperature of 195 K. A second molecular formic acid desorption feature is seen at 350 K for low coverages, shifting to 375 K and saturating for all initial coverages of a monolayer or greater. No molecular formic acid is detected by EELS above 200 K, suggesting that the desorption of formic acid at 350-375 K is due to recombination of adsorbed hydrogen and formate. For submonolayer initial coverages, H_2O desorbs in two peaks with maxima at 160 and 275 K. As mentioned earlier, this H_2O results from decomposition of the adsorbed formate and correlates with the appearance of CO in the EEL spectra. Carbon dioxide is evolved in a single reaction-limited step with a peak temperature of 300 K for low initial coverages, shifting to 365 K for saturation coverage. This temperature shift results from an increased stability of the adsorbed formate at higher coverage (ref.11,14). Hydrogen is evolved in a single desorption-limited step with a peak temperature of 455 K for low initial coverages, shifting to 375 K at saturation. Carbon monoxide is evolved in a single desorption-limited step with a peak temperature of 480 K.

Since the probability of CO oxidation to CO_2 on Ru(001) under the conditions prevailing in these experiments is on the order of 0.1 percent of the probability of CO desorption (ref.15), the appearance of both CO_2 and CO in the thermal desorption spectra indicates that formic acid decomposes by two competing mechanisms on Ru(001). Initial dehydrogenation of formic acid to an adsorbed formate intermediate is followed by decomposition of the formate *either* through dehydrogenation *or* through C-O bond cleavage with the latter favored somewhat, as judged by relative areas of thermal desorption peaks, i.e.,

$$\begin{tikzcd}
HCOO(a) \arrow[r, "①"] \arrow[dr, "②"] & H(a) + CO(a) + O(a) \\
& H(a) + CO_2(g)
\end{tikzcd}$$

Reaction ① is not only slightly favored kinetically over reaction ②, it is also (marginally) favored thermodynamically, by approximately 6 kcal/mol (ref.16).

Formic acid dehydrogenates upon adsorption on Cu(100)(ref.1,2), Ag(110)(ref.3), and Pt(111)(ref.4) to yield a chemisorbed formate intermediate which decomposes via C-H bond cleavage exclusively. However, on Ni(110), Ni(100)(ref.5-7) and Ru(100)(ref.8), the same distribution of the products of decomposition was observed as that reported here. On these surfaces, a formic anhydride intermediate was postulated to explain the observed product distribution. The fact that the formic anhydride intermediate does not exist on Ru(001) under any circumstances brings into considerable doubt its existence on Ni(110), Ni(100), and Ru(100).

REFERENCES

1 B.A. Sexton, Surface Sci. 88, 319 (1979).
2 B.E. Hayden and A.M. Bradshaw (private communication).
3 B.A. Sexton and R.J. Madix, Surface Sci. 105, 177 (1981).
4 N.R. Avery, Appl. Surface Sci. 11/12, 774 (1982).
5 R.J. Madix and J.L. Falconer, Surface Sci. 51, 546 (1975).
6 J.B. Benzinger and R.J. Madix, Surface Sci. 79, 394 (1979).
7 R.J. Madix, Advan. Catal. 29, 1 (1980).
8 L.A. Larsen and J.T. Dickinson, Surface Sci. 84, 17 (1979).
9 G.E. Thomas and W.H. Weinberg, Rev. Sci. Instrum. 50, 497 (1979).
10 G.E. Thomas and W.H. Weinberg, J. Chem. Phys. 69, 3611 (1978); 70, 954 (1979).
11 N.R. Avery, B.H. Toby, A.B. Anton and W.H. Weinberg, Surface Sci. (in press).
12 K. Nakamoto, *Infrared and Raman Spectra of Inorganic and Coordination Compounds*, Wiley, New York, 1978.
13 G.E. Thomas and W.H. Weinberg, J. Chem. Phys. 70, 1437 (1979).
14 B.H. Toby, N.R. Avery, A.B. Anton and W.H. Weinberg (in preparation).
15 H.I. Lee, G. Praline and J.M. White, Surface Sci. 91, 581 (1980).
16 W.H. Weinberg, unpublished results.

Appendix 3.

Contrasting Bonding Configurations of Acetone on Pt(111) and Ru(001) Surfaces

Journal of Electron Spectroscopy and Related Phenomena, 29 (1983) 233—237
Elsevier Scientific Publishing Company, Amsterdam — Printed in The Netherlands

CONTRASTING BONDING CONFIGURATIONS OF ACETONE ON Pt(111) AND Ru(001) SURFACES.

N.R. AVERY,[1] A.B. ANTON,[2] B.H. TOBY[2] and W.H. WEINBERG[2]

[1]CSIRO Division of Materials Science, University of Melbourne, Parkville, 3052, Victoria, Australia.

[2]Division of Chemistry and Chemical Engineering, California Institute of Technology, Pasadena, CA 91125, USA.

ABSTRACT

The comparative chemistry of acetone adsorption on Pt(111) and Ru(001) has been studied by EELS. On the more easily oxidized Ru(001) surface, acetone bonded in a side-on, η^2(O,C) configuration, whereas on the well-defined, close-packed regions of the Pt(111) surface acetone adopted a weak adduct-like, end-on, η^1(O) configuration. On Pt(111), some η^2(O,C) was also observed and associated with adsorption at low coordination accidental step sites.

INTRODUCTION

As part of a continuing study of the organometallic chemistry of weak donor ligands on metal surfaces, we have studied the interaction of acetone with two single crystal metal surfaces viz. Pt(111) and Ru(001). In this way, it has been shown that acetone bonds either through the oxygen in an end-on or η^1(O) configuration or through the oxygen and ketonic carbon atoms in a lying-down or η^2(O,C) configuration.

EXPERIMENTAL

Descriptions of the EEL spectrometers used for the Pt(111) (ref.1) and Ru(001) (ref.2) work have been given previously. All spectra were taken in the specularly reflected beam. Clean surfaces were prepared by well-established Ar^+ sputtering and oxidation techniques. Thoroughly degassed acetone was adsorbed either by back-filling the vacuum chamber in the Ru(001) work or with a movable doser located in front of the Pt(111) crystal. Base pressures of $<10^{-10}$ torr were routinely obtained with both systems.

RESULTS AND INTERPRETATION

Multilayer acetone. The EEL spectrum from multilayer acetone on Pt(111) at 130 K (Fig. 1) may be assigned according to Dellepiane and Overend (ref.3). Acetone (C_{2v} point group) has 24 normal modes which may be divided into 18 internal methyl modes and 6 modes involving the Me_2CO (Me ≡ methyl) skeleton. The skeletal modes involve dynamic dipole moments along the two-fold axis (A_1)

0368-2048/83/0000—0000/$03.00

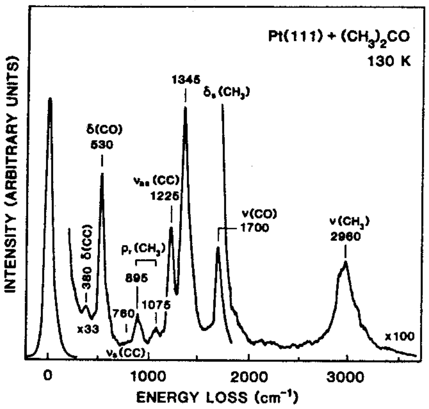

Fig. 1. EEL spectrum from multilayer acetone on Pt(111) at 130 K.

or perpendicular to the two-fold axis but either in the molecular plane (B_1) or perpendicular to it (B_2). There are three A_1 modes viz. ν(C=O), ν_s(MeCMe) and δ(MeCMe), two strong B_1 modes viz. ν_{as}(MeCMe) and δ(CO) and a single weak B_2 mode viz π(CO) which could not be resolved from the δ(CO) in the present spectrum.

Monolayer acetone on Ru(001). Heating the Ru(001) surface, which had previously been covered with multilayer acetone, to 190 K desorbed the excess adsorbate and revealed the spectrum of monolayer acetone (Fig. 2a). This spectrum showed a systematic absence of the intrinsically strong A_1 and B_1 modes, indicating, according to the surface selection rule for dipole excitations, that the CO bond is parallel, or almost so, to the surface. Instead, conspicuous bands at 3000 cm^{-1}, 1385 cm^{-1} and 990 cm^{-1} are seen and assigned to methyl stretching, deformation and rocking modes, respectively. The 675 cm^{-1} band is assigned to a skeletal angle deformation mode.

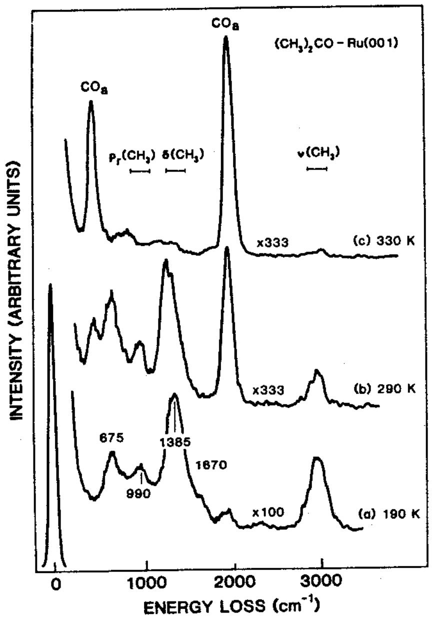

Fig. 2. EEL spectra from (a) monolayer acetone on Ru(001) at 190 K and after heating to (b) 290 K and (c) 330 K.

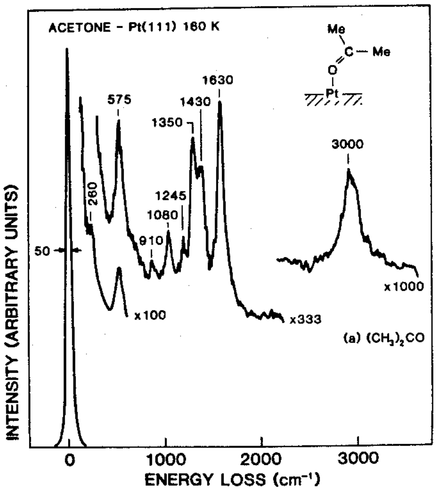

Fig. 3. EEL spectrum from monolayer acetone on Pt(111) at 160 K.

In the absence of a clearly detectable $\nu(CO)$ mode or the ability to measure the C-O bond length, it is not possible to estimate the bond-order and with it the extent of rehybridization of the ketonic carbon atom. Conceivable bonding configurations include I, II and III. In I it is envisaged that the ketonic carbon atom retains its sp^2 character whereas in II and III substantial rehybridization to sp^3 occurs. The real structure of adsorbed acetone on Ru(001) probably lies between these extremes. The resulting species is designated $\eta^2(O,C)$ acetone to signify the involvement of both the oxygen and carbon atoms in bonding to the metal atom.

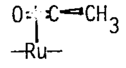
I

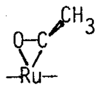
II

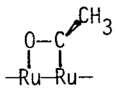
III

With further heating to 290 K (Fig. 2c), EEL bands due to adsorbed CO appear and dominate the spectrum after a further flash to 330 K (Fig. 2d). Molecular acetone does not desorb in this temperature regime suggesting that instead, $\eta^2(O,C)$ acetone decomposes to adsorbed CO and by inference adsorbed H and C thus:

$$\eta^2(O,C)\ \text{acetone} \xrightarrow{300\ K} CO_a + C_a + H_a \qquad (1)$$

Monolayer acetone on Pt(111). An EEL spectrum of acetone adsorbed on Pt(111) at 160 K is shown in Fig. 3. This spectrum shows the presence of methyl stretching, deformation and rocking modes which are essentially unperturbed from their free acetone frequencies indicating that the methyl groups are inert and play no role in the bonding to the surface. Of greater diagnostic significance is the presence of the two B_1 modes viz. $\delta(CO)$ (575 cm^{-1}) and $\nu_{as}(CC)$ (1245 cm^{-1}) both slightly blue-shifted from their free acetone frequencies and a $\nu(CO)$ band (A_1 symmetry) which is similarly red-shifted by 80 cm^{-1}. This indicates that the adsorbed species on Pt(111) is bonded through the oxygen atom and from the surface selection rule for dipole excitations, that the Pt-O-C bond must be bent significantly from 180°, as in IV. The bands in this spectrum are attenuated, in unison, after heating to 180-190 K corresponding to a thermal desorption pulse of molecular acetone seen in the same temperature range. When regions of crystal closer to the edge were probed by the EELS beam weak residual methyl stretching, deformation and rocking bands were seen after the $\eta_1(O)$ species was desorbed at 190 K. No adsorbed CO bands arising from acetone decomposition were seen. These bands are attributed to a small concentration of $\eta^2(O,C)$ acetone, analogous to that which forms the majority species on Ru(001), confined to the accidental step sites which inevitably contribute to a real

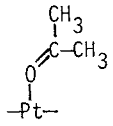
IV

crystal surface, particularly near the edges. The η^2(O,C) species on Pt(111) is a minority state and its properties will be discussed more fully elsewhere (ref.1b). By inference, the η_1(O) species is associated with adsorption on the well-defined, close-packed regions of the Pt(111) surface and is the majority species.

DISCUSSION

In summary, EELS has identified two basically different forms of adsorbed acetone which have been designated η^1(O) and η^2(O,C) for end-on and side-on bonding configurations, respectively. On Ru(001), the η^2(O,C) form is the majority species. On Pt(111), the η^1(O) form has been identified as the majority species on the well-defined, close-packed regions of the surface whereas a small contribution from the η^2(O,C) form has been associated with accidental step sites.

In inorganic coordination compounds, acetone bonded in an end-on η^1(O) configuration are well known. Labile donor ligands of this kind are easily exchanged for other ligands and consequently are widely exploited in synthesis reactions. In X-ray structure analysis of two ruthenium complexes, the Ru-O-C bond has been shown to be bent at angles of 153^o (ref.5) and 138^o (ref.6) in, or close to, the molecular acetone plane. A bonding scheme for both these complexes and η^1(O) adsorbed acetone may be devised by reference to the frontier orbitals of acetone (ref.7). The highest filled orbital is a non-bonding atomic p-like orbital located on the oxygen atom and oriented in the molecular plane. If one lobe of this orbital is regarded as a Lewis base and interacts with an empty Pt orbital, the desired bent Pt-O-C bond is formed. Clearly, there is a strong similarity between η^1(O) acetone and these inorganic acetone complexes.

Inorganic compounds with acetone bonded in an η^2(O,C) configuration have not been isolated. However, comparable compounds with the more electrophillic $(CF_3)_2CO$ are well known in both three (ref.8) and four (ref.9) membered heterocyclic ring configurations analogous to the surface structure II and III. In these compounds, almost complete rehybridization of the ketonic carbon to sp^3 has occurred, whereas in a nickel $(CF_3)_2CO$ complex (ref.10) only partial rehybridization occurs and bonding must be regarded as being more π-like. In the latter case, the $(CF_3)_2CO$ skeleton is much less distorted from the plannar free $(CF_3)_2CO$ configuration than in the ruthenium complexes. The nickel complex is the organic analog of I whereas the ruthenium complexes correspond to II and III.

The ability of the Ru(001) surface to adsorb acetone in the η^2(O,C) configuration would indicate that the solid surface is more easily able to raise its oxidation state than the isolated atoms in the inorganic compounds. Similarly, the close-packed regions of the Pt(111) surface will be less easily oxidized and therefore failed to form a comparable species but instead adsorb acetone in a weak donor ligand, or adduct configuration. The minority component of η^2(O,C) acetone on the Pt(111) surface is confined to the low coordination and therefore more easily oxidized step sites.

REFERENCES

1 N.R. Avery, (a) Appl Surface Sci. 13 (1982) 171; and (b) Surface Sci. (submitted).
2 G.E. Thomas and W.H. Weinberg, Rev. Sci. Instrum. 50 (1979) 497.
3 G. Dellepiane and J. Overend, Spectrochimica Acta 22 (1966) 593.
4 Introduction to Infrared and Raman Spectroscopy, 2nd Edition (Academic Press) 1975.
5 R.D. Gould, W.J. Sime and T.A. Stephenson, J.C.S. Dalton (1978) 76.
6 M.A. Bennett, T.W. Matheson, G.B. Robertson, W.L. Steffen and T.W. Turney, J.C.S. Chem. Comm. (1979) 32.
7 W.L. Jorgensen and C. Salem, The Organic Chemist's Book of Orbitals (Academic Press) 1973.
8 B. Clarke, M. Green, R.B.L. Osburn, F.G.A. Stone, J. Chem. Soc. (A) (1969) 20.
9 M. Green, J.A.K. Howard, A. Laguna, L.E. Smart, J.L. Spencer and F.G.A. Stone, J. Chem. Soc. (Dalton)(1977) 278.
10 R. Countryman and B.R. Penfold, J. Crys. Molec. Structure 2 (1972) 281.

Appendix 4.

A User's Guide to the Operation of the Electron Energy Loss Spectroscopy

Table of Contents

I. Introduction

Of the numerous electron beam techniques applied presently in experimental chemical physics, EELS of adsorbate vibrations places the most stringent demands on apparatus design and performance. In a typical EEL experiment, a low energy (typically <10 eV) beam of electrons is generated by a thermionic emitter, accelerated and passed through a dispersive electrostatic energy selector, and focused on the surface of a metal crystal sample. This beam scatters from the surface with some fraction of the electrons losing discrete amounts of energy to excite surface vibrations, and the scattered beam is subsequently collected, counted, and energy analyzed by a second dispersive electrostatic selector to give an intensity vs. energy loss spectrum. The power of this technique, as measured by its ability to detect weak vibrational features (sensitivity) and to distinguish between distinct features of nearly equal loss energy (resolution), depends critically on the careful control of the physical parameters which affect the instrument's performance.

The purpose of this Manual is threefold. First, a description of the basic physical principles which govern the experiment is provided, with particular reference to those points which are critical to the optimum performance of the spectrometer. Second, the purpose and design of the control electronics is described. And third, some important points concerning experimental technique, particularly regarding the tuning of the spectrometer and the collection of energy loss spectra, is presented. This information should serve as a useful primer for future users of the machine, and the emphasis on basic physics should provide a framework for the design of useful trouble-shooting methods and modifications which improve the machine's performance.

II. Electron Potential and Kinetic Energies in the Spectrometer

Crucial to proper operation and maintenance of the EEL spectrometer and the interpretation of EELS data is a thorough understanding of the relationship between externally controlled electrostatic potentials applied to optical elements in the spectrometer and their resulting effects on the trajectories of electrons in the EELS beam. This understanding is also helpful when considering the design and effective operation of the EELS optics control system, to be discussed in Section VII of this Manual. As a basis for this discussion, consider the following fundamental points:

1. In the absence of magnetic fields (as is the case in a μ-metal shielded chamber such as ours), the equation of motion of a charged particle in a region of spatially varying electrostatic potential is

$$m \frac{dv}{dt}(\bar{r}) = -q\nabla\Phi(\bar{r}) \tag{1}$$

   where m = mass, v = velocity, q = charge, Φ = electrostatic potential, and $\bar{r}$ = position coordinates. The electrostatic potential in free space is a solution of Laplace's equation, i.e.

$$\nabla^2\Phi(\bar{r}) = 0\ , \tag{2}$$

   subject to conditions specified at boundary surfaces where the electrostatic potential is held constant. All functions of the EEL optical system, including focusing, energy analysis, and deflection of the electron beam make use of these concepts.

2. For a single electron in a scalar electrostatic potential field (or a non-interacting ensemble of electrons, i.e. a beam of sufficiently low current density), the Hamiltonian

$$H = T + V = \frac{1}{2} mv^2 + q\Phi \, , \tag{3}$$

where T = kinetic energy and V = potential energy, is a constant. Using eV energy units,

$$H' = T' - \Phi \, . \tag{4}$$

If a reference potential is chosen such that $H' = 0$, then $T' = \Phi$, and an applied electrostatic potential is a direct measure of the kinetic energy of an electron in that region of potential **(1)**.

Now that the importance of applied electrostatic potentials has been described, material properties which relate the value of a potential applied by an external source (i.e. power supply) to the true surface potential, and therefore the free space electrostatic potential distribution in electron optical elements, must be addressed. To this end, consider the following concepts:

1. Two dissimilar conducting materials in electrically nonresistive contact with each other align their conduction band edges (Fermi levels) at equal electrostatic potentials. Then the vacuum potentials existing at the surfaces of the two conductors differ by $\Delta\varphi$, the contact potential difference (or work function difference) between the two conductors. Since a power supply used to control externally the potential of a conducting element does so by fixing the potential of the conductor's Fermi level, the potential at the conductor's surface differs from the applied potential by φ, the work function of the conducting material.

2. The measured work function of a given conducting material varies by as much as 1.0 eV depending on which crystalline face of the material forms its exposed surface **(2)**. Then, machined metal surfaces or metal plated surfaces, which are constituted of randomly oriented microcrystallites, have

surface potentials which vary by such amounts over microscopic distances, producing spatially varying electric fields which can adversely affect the trajectories of low energy electrons in a sensitive electron optical system. To combat this effect in our spectrometer, the electron optics have been coated carefully with graphite via brush and aerosol painting with a liquid colloidal suspension of graphite in isopropanol ("dag") **(3)**. Graphite particles tend to adsorb with their hexagonal planes oriented preferentially parallel to their exposed surfaces **(4)**, producing a microscopically uniform effective work function and surface potential. The surface potential of this graphite coating, however, changes in a nonuniform way ("patch fields") upon adsorption of contaminants from the chamber background, again adversely affecting the optical properties of the electron lens system. Bakeout of the optics with the internal spectrometer ovens at 150-200°C for several hours after each day of experiments desorbs reversibly adsorbed contaminants and returns stable operation of the EELS optical system. Occasionally, particularly after long sequences of experiments with hydrocarbons, a tenacious brown residue collects on the first few optical elements following the cathode, presumably due to electron impact dissociation of gas molecules and irreversible adsorption of their dissociation fragments onto the graphite coating. Formation of this residue necessitates periodic (yearly) cleaning and recoating of the affected lens elements.

The net results of these considerations are illustrated in the energy vs. applied potential diagram shown in Fig. 1. First note that the zero of external potential is the common ground circuit to which all grounded elements in the vacuum chamber and control racks are attached. Conservation of total energy, as described earlier, guarantees that positive changes in external potential lead to increased kinetic energy and decreased potential energy of the electron beam, thus the "External Potential" and "Electron Kinetic (Potential) Energy" axes at the left side of the diagram. Also, since excitation of a conduction electron in a material from the Fermi level to a state near but below the vacuum level corresponds to an increase in the electron's potential energy, the various elements of the spectrometer (cathode, graphite-coated optics and crystal sample) are shown with their Fermi levels (μ_C, μ_{GR} and μ_S, respectively) at higher external potential than their vacuum levels (identified with respect to their Fermi levels by their positive work functions, φ_C, φ_{GR} and φ_S, respectively). Then, for example, the potential at the surface of the grounded sample is $-\varphi_S$ with respect to the zero of external potential. V' represents voltage measured with respect to the zero of external potential (i.e. as measured with a grounded voltmeter), and V represents voltage measured with respect to an arbitrary fixed internal potential (V'_{RAIL}), the significance of which will be described in Section VII of this Manual discussing the optics control system. In this configuration, the beam energy (the kinetic energy of electrons emitted from the cathode and striking the sample) is $E = -V'_{CATHODE} + \varphi_C + kT_c - \varphi_S = -V'_{RAIL} + \varphi_{GR} - \varphi_S$, and the contact potential difference between the cathode and the graphite coated optics is $\Delta V = \varphi_C + kT_c - \varphi_{GR}$ **(5)**.

III. Electron Emitter

The current for the EELS beam is produced by thermionic emission of electrons from a heated cathode. Basic statistical thermodynamical considerations **(6)** demonstrate that the saturation electron current, $I_0(T_c)$, obtainable from a thermionic emitter with a work function φ_C at a temperature T_c is given by

$$I_0(T_c) = AT_c^2\exp[-\varphi_C/kT_c] \tag{5}$$

where $A = 120\ \text{A/cm}^2 - \text{K}^2$. Furthermore, the electrons in the resulting current have their kinetic energies, E, distributed according to

$$I(E,T_c) = \frac{I_0(T_c)E}{kT_c^2}\exp[-E/kT_c]\,. \qquad (6)$$

This distribution has a full-width at half-maximum $\Delta E = 2.54kT_c$, and both its mean and maximum lie at $E = kT_c$. Combining Eqs. (5) and (6) yields

$$I(E,T_c) = \frac{A}{k^2}E\exp[-(\varphi_C + E)/kT_c]\,. \qquad (7)$$

This equation has several very important practical implications.

First, insertion of suitable values for all parameters shows that temperatures in excess of 1000 K must be used to provide adequate current density. At 1000 K, $\Delta E = 2.54kT_c \approx 220$ mV, whereas the desired energy width in the incident EELS beam is less than 10 mV to allow resolution of closely spaced adsorbate vibrational modes. The function of the monochromator, then, is to select a small energy slice of this kinetic energy distribution, discarding all electrons from the beam whose kinetic energies fall outside this slice. The actual temperature at which the cathode is to be operated is determined by φ_C and the minimum beam current required to do EELS experiments through the $\exp[-\varphi_C/kT_c]$ term of Eq. (7). In practice, directly heated W filament cathodes, with $\varphi_C \approx$ 4.5 eV, must be operated near 1600 K where $\Delta E \approx$ 350 mV, and indirectly heated oxide cathodes, with $\varphi_C \approx 2$ eV, are best operated near 1100 K where $\Delta E \approx 240$ mV.

These considerations also bear on operating problems associated with "space charge" spreading of the electron beam. Briefly, "space charge" applies to beam conditions where high current densities and low kinetic energies cause electrons in the beam to be in sufficiently close proximity to each other to feel the effects of their mutual electrostatic repulsion, producing electron trjectories different than would be imposed by the applied electrostatic lens potentials, i.e. beam spreading. This reduces the throughput and resolution of the spectrometer. The severity of space charge effects, which are of course expected to be greatest at the cathode surface where electron kinetic energies are at their minimum prior to acceleration, depends on the total flux of electrons leaving the cathode. Clearly, the higher φ_C is, the higher the operating temperature must be to produce the desired maximum current at $E = kT_c$, and therefore the broader the kinetic energy distribution of emitted electrons will be, producing a greater net electron flux which can contribute to space charge problems.

With these problems in mind, our spectrometer has been equipped with a low work function cathode, consisting of a porous W matrix impregnated with BaO and coated with Os (Spectra-Mat STD134, type M) and heated indirectly with a ceramic coated W coil. Addition of the BaO lowers the effective work function of the cathode from approximately 4.5 eV, the expected value for pure W, to approximately 2 eV, an effect first explained by Langmuir **(7)**, and more recently addressed in theoretical calculations for a "jellium" surface model by Lang **(8)**. Addition of the ionic BaO species to the W surface produces strong dipoles oriented with their positive ends directed away from the surface, decreasing the net surface work function. When in use at an operating temperature of 1000-1100 K, an equilibrium is established between Ba and BaO on the cathode surface, and the actual nature of the resulting "active" cathode structure is still a source of controversy **(9)**, even though cathodes of this design have been used commercially for more than 30 years. Furthermore, the performance (i.e. work function) of such oxide cathodes is a sensitive function of the concentrations of the Ba, BaO and Os constituents, and the gradual increase in the work function of oxide cathodes with time correlates with the slow evaporation of these species from the surface of the cathode at normal operating temperatures.

Although oxide cathodes provide operational advantages due to their low work functions, there are several difficulties associated with their use of which all operators should be aware. First, the normal operating temperature of 1000-

1100 K is well below the desorption temperatures of some atomic species from W surfaces, particularly C and O, thus chemisorption of these species can occur from the ambient environment in which the cathode resides. However, the temperature of the cathode is sufficient to activate reaction of these adsorbed species with the W support or with the Ba, BaO and Os species adsorbed on the cathode surface, forming high work function species which poison and deactivate the cathode **(10)**. The problem is exacerbated in our system by the accelerating field which typically exists in the cathode region due to the +30 V bias of the anode extractor with respect to the cathode. Emitted electrons have approximately 30 eV of kinetic energy at the anode, sufficient to impact ionize ambient gas molecules, and the resulting reactive positive ions are accelerated back to the cathode to poison its surface.

With proper care, however, the deleterious effects of these phenomena can be minimized. First, spare cathodes should be maintained in evacuated ($<10^{-3}$ Torr) glass tubes as supplied by the manufacturer to avoid slow poisoning by O_2 in air at room temperature and pressure. Cathodes which have endured atmospheric pressure for more than three days (in storage or during vacuum break to service the spectrometer) should not be used. Second, heating of the cathode to its normal operating temperature in gas pressures greater than 10^{-7} torr can activate surface reactions which permanently poison the cathode and should be avoided. Third, the anode bias voltage should be set to zero (i.e. set $V_{CATHODE} = V_{ANODE}$) when O_2 cleaning the crystal or when doing experiments which require exposure to pressures greater than 5×10^{-8} Torr for extended periods of time. This will minimize backstreaming of reactive ions to the cathode surface. Finally, the cathode (and heater) should be replaced without hesitation when the chamber is opened for any repairs to the spectrometer, etc. The Spectra-Mat cathodes are relatively inexpensive (1985 price, thirty-five dollars each), and an improvement in the performance of the spectrometer will always be realized.

IV. Hemispherical Electrostatic Energy Analyzer

To select an appropriately narrow kinetic energy distribution of electrons to probe the vibrational structure of the sample surface in EELS experiments and to determine the kinetic energy distribution of the scattered electrons, hemispherical electrostatic energy analyzers are used in both the monochromator and analyzer of the spectrometer. An excellent review of the pertinent properties of spherical analyzers is available in Ref. 11 and should be studied by all users of the EELS system. A brief review of some of the important results is presented in the following paragraphs with emphasis on those points which bear directly on the resolution of the spectrometer.

An analysis of electron trajectories in a transverse electrostatic field demonstrates that the force exerted by the field on the moving electrons produces curved trajectories whose radii of curvature are indicative of the electron's velocities. An energy selector, then, passes only those electrons having a distribution of well-defined trajectories centered on some ideal trajectory which represents the desired pass energy of the selector, and it is the characteristic width of this distribution which defines the energy selector's resolving power. These considerations will be discussed in reference to the quantities illustrated in Fig. 2, where a sectional view of the hemispherical analyzer in the plane of the electron beam, bisecting the hemispheres, is shown. It is assumed that the electron optics preceding the hemispherical analyzer (not shown) feed a cylindrically symmetrical beam with a distribution of velocities and entrance angles, broad with respect to the resolving power of the analyzer, to a focal point at a radius R_0 in the equatorial plane of the analyzer, as shown at the top of Fig. 2. In this diagram, R_1 and R_2 are the inner and outer sphere radii, $R_0 = (R_1 + R_2)/2$,

V_1 and V_2 are the inner and outer sphere surface potentials, and θ is the angle which measures the arc swept by the sample electron trajectories T_0, T_1 and T_2 as they pass through the hemispherical field. As shown in the enlarged view at the bottom of Fig. 2, T_0 is an "ideal" trajectory, entering the hemispherical field at $r = R_0$ and normal to the equatorial plane, and T_1 and T_2 are trajectories entering also at $r = R_0$ but deviating from T_0 by a small angle α. ΔS is the characteristic width at the equatorial plane of the distribution of trajectories in the feed beam, or, alternatively, the width of the bundle of trajectories leaving the hemispherical analyzer which are selectively collected by the electron optics following the analyzer to form the energy-resolved beam. This quantity is also known as the "slit width".

Rather than follow the more complicated three-dimensional analysis of Ref. 11, the relationship between the potentials V_1 and V_2 and the pass energy E_0 (i.e. the kinetic energy of the electrons which follow the ideal trajectory T_0) can be obtained via a two-dimensional force balance in the plane of T_0. If $\hat{r}$ is a radially directed unit vector in the plane of T_0, $\Phi(r)$ is the electrostatic potential distribution between the hemispheres, and -e, m and v are the charge, mass and speed of the electron along T_0, respectively, then a radial force balance yields

$$\frac{mv^2}{r}\hat{r} = e\nabla\Phi(r) \quad (\text{at } r = R_0)\ . \tag{8}$$

Then the pass energy, E_0, is

$$E_0 = \frac{mv^2}{2} = \frac{er}{2}\,|\nabla\Phi(r)| \quad (\text{at } r = R_0)\ . \tag{9}$$

The potential, $\Phi(r)$, is obtained by solving Laplace's equation

$$\nabla^2\Phi(r) = 0\ , \tag{10}$$

subject to the boundary conditions

$$\Phi(r = R_1) = V_1$$

$$\Phi(r = R_2) = V_2 \,. \tag{11}$$

The results for $\Phi(r)$ and $|\nabla\Phi(r)|$ at $r = R_0$ are

$$\Phi(r = R_0) = \left[\frac{R_1R_2}{R_2 - R_1}\right]\left[\frac{2}{R_1 + R_2} - \frac{1}{R_1}\right](V_1 - V_2) + V_1 \tag{12}$$

$$|\nabla\Phi(r)|_{r=R_0} = -\frac{4R_1R_2}{(R_2 - R_1)(R_1 + R_2)^2}(V_1 - V_2) \,. \tag{13}$$

Substituting Eq. (13) into Eq. (9) gives the following expression for E_0:

$$E_0 = -\frac{R_1R_2}{(R_2 - R_1)(R_1 + R_2)}(V_1 - V_2) \,. \tag{13}$$

One important conclusion can be drawn immediately from the form of Eqs. (1) and (2). In a region of fixed potential gradient, the radius of curvature of the trajectory of an electron varies linearly with its kinetic energy. In the hemispherical analyzer, for example, electrons with kinetic energy E_0, entering along trajectory T_0, exit the analyzer at point A of Fig. 2. Those with kinetic energy slightly greater than E_0 exit at C, and those with slightly less at B. Also, electrons with kinetic energies other than E_0 entering parallel to but displaced from T_0 may also exit at point A. Then, as ΔS at both the entrance and exit increase, the ability of the analyzer two discriminate between electrons of different kinetic energies, and therefore the resolution, decreases.

The more complete three-dimensional analysis of Ref. 11 reveals some other important characteristics of the hemispherical analyzer. First, trajectories such as T_1 and T_2, entering at R_0 with energy E_0 and deviating from T_0 only by a small change in entrance angle, α, cross T_0 as shown in Fig. 2 after traversing an angle of $\theta = \pi$. Similar results are obtained for small deviations of entrance angle out of the plane of T_0, and the hemispherical configuration is chosen to take advantage of the enhanced beam throughput produced by this focusing effect. Second, the transmission function of the hemispherical analyzer can be shown to be very nearly Gaussian. Thus, lineshapes obtained in experimental spectra are convolution products of the natural lineshape of the excitation probed and the Gaussian transmission function of the spectrometer. Furthermore, the net transmission function of two such analyzers operating in series, as is the case in an EEL spectrometer where one operates at fixed energy to produce the electron beam and one scans the scattered energy loss spectrum, is the Gaussian convolution product of the two individual analyzer transmission functions. Its full-width at half-maximum, $\Delta E(\text{net})$ is given in forms of those of the constituent analyzers, ΔE_1 and ΔE_2, by

$$\Delta E(\text{net}) = \sqrt{(\Delta E_1)^2 + (\Delta E_2)^2} \tag{15}$$

Finally, a sensitivity analysis of the response of the analyzer to variations in the various parameters which characterize its performance, measured in terms of their effect on ΔE, yields

$$\frac{\Delta E}{E_0} = \frac{\Delta S}{2R_0} + \frac{\alpha^2}{2}. \tag{16}$$

Then, high resolution, as quantified by low ΔE, results from large R_0 and the smallest simultaneously obtainable values of E_0, ΔS and α. In practice, R_0 is fixed by the mechanical design of the electrostatic analyzer and is chosen to be the largest value consistent with the space limitations in the vacuum system in which it is housed. ΔS and α are controlled by the focal properties of the electrostatic lens systems which feed the beam to and extract the beam from the hemispherical analyzer and are therefore determined by the voltages applied to the various lens elements and by the apertures which are strategically dispersed throughout the optical system to control the electron beam diameter. E_0 is also controlled by externally applied potentials [see Eq. (14)], but in practice the minimum E_0 that can be used is limited by the approach of the difference in voltage of the inner and outer spheres to a value characteristic of the local variation of the surface potentials of the spheres due to inhomogeneities in the work function of their graphite coatings. No apparent gain in resolution is observed for $(V_1 - V_2) < 0.20$ V, limiting minimum useful pass energies to approximately 0.30 eV.

V. Electron Optics

In the brief description of the electron optical system to follow, use will be made of the lens numbering system shown in Fig. 3. Note that this differs from the number designations for the various lens elements provided in Ref. 12, but is current with that of the spectrometer control panel. Also, voltages applied to the lens elements are measured with respect to the -RAIL potential illustrated in Fig. 1 unless mentioned otherwise. With this notation, the applied potentials represent the kinetic energy of the electron beam at the respective lens elements.

Several basic points must first be addressed to provide a proper framework in which to discuss the purposes of the various elements of the electron optical system.

First, the kinetic energy of the electron beam arriving at the sample should be on the order of 10 eV for EELS vibrational measurements, thus V'_{RAIL} of Fig. 1 is at approximately -10 V with respect to the grounded sample. As shown in the previous section of this Appendix, however, the kinetic energy of the electron beam while passing through the hemispherical energy selectors of the monochromator and analyzer is to be of the order of 0.5 eV for acceptable energy resolution. Then, one important function of the electron optics is to accelerate and decelerate the beam as it passes through the spectrometer, delivering the beam at the desired kinetic energies both to the hemispherical analyzers and to the sample. As was shown by Eq. (4) and in Fig. 1, the applied lens potentials are equal (within an additive constant) to the beam kinetic energy along its path and therefore exhibit directly this acceleration-deceleration function of the electron optics.

Also, several desired operating properties of the spectrometer depend critically on the ability of the electron optical system to deliver a focused beam to a point in space with a minimized image diameter and angular divergence. This consideration affects the intensity of the beam (and therefore the sensitivity of the spectrometer) throughout its path, the ability of the spectrometer to resolve the angles through which electrons scatter from the sample (and therefore the magnitude of their momentum exchange with the surface), and the resolution of the hemispherical energy selectors through the ΔS and α^2 terms of Eq. (16).

To avoid interference of fringing, inhomogeneous fields at the entrance and exit planes of the hemispherical analyzers and their possible detrimental effects on ΔS and α^2, "Herzog elements" **(13)** are provided as the last lens element preceding and first following each set of spheres. Once a pass energy is chosen for each set of spheres according to Eq. (14) and the expressions given in Table 1, the corresponding Herzog potentials are to be set to match the potential of the ideal, centerline trajectory (see Fig. 2) through the spheres, as given by Eq. (12) and again listed in Table 1. This insures a homogeneous potential in these critical resolution-defining regions of the spectrometer.

As was alluded to previously, apertures ("slits") of carefully chosen diameter are dispersed throughout the electron optics at strategic locations to "skim" the electron beam, defining either its maximum diameter (via a single slit at or near a focal point) or its angular divergence (via a pair of slits operating in tandem between two focal points). The current aperture locations and diameters are listed in Table 2. Although the optimum locations and diameters for the apertures can in principle be chosen by calculation of beam trajectories through the lenses with well-developed ray-tracing computer programs **(1,14)**, improvements in the performance of the spectrometer can often be realized through experiment with various aperture configurations. One should keep in mind, however, that patch and fringing fields at the machined edge of an aperture can produce local potential variations which may distort or deflect the beam as it passes through the aperture, particularly if the aperture is located in a region where the electron beam has a kinetic energy comparable to the contact potential variation expected at a machined surface, i.e. less than one eV. In practice the graphite coating seems to control this problem, and the apertures used in elements 12 and 32 of the spectrometer are placed contrary to this concern but have had a profoundly positive effect on the resolution of the spectrometer. Also, possible deflection by patch fields at apertures or by patch fields at the surfaces of the lenses themselves requires that beam deflectors be available between any pair of apertures to insure that the beam can be guided through the apertures. For this reason, only one aperture can be installed per matching pair of Herzog elements, as no deflectors are provided to guide the beam while it passes through the hemispheres.

The first stage of electron optics shown in Fig. 3 serves to produce a well-collimated beam from the electron source and to focus that beam at a point on the entrance plane of the monochromator hemispheres. Element 0 supports the dispenser cathode, and its potential defines the electron beam energy. Element 3, the anode, is biased 20-30 eV positive with respect to the cathode to provide initial acceleration of emitted electrons from the cathode surface, and the

0.020 in. aperture it supports defines the initial size and angular divergence of the beam. Element 6 operates at a high positive potential (80-100 V), and its purpose is twofold: first, penetration of its high positive potential into the aperture of element 3 forms an attractive potential well which "extracts" the source beam through the aperture, and second, it operates in conjunction with element 7 to form a two-element, 10:1 decelerating lens which forms a focused image of the source on the equatorial plane of the monochromator hemispheres. The 0.020 in. apertures of element 7 limit the angular divergence of the beam entering the spheres. Typical operating voltages for these and other lens elements for operation of the spectrometer in the usual mode for high-resolution electron energy loss vibrational spectroscopy are listed in Table 3.

The second stage of electron optics serves to form an image of the exit pupil of the monochromator hemispheres at the sample surface. Element 15 accelerates the beam, its 0.020 in. aperture limiting the angular divergence of the beam eminating from the spheres, and works in unison with element 16 to form a focused image at an intermediate point in this optical stage. Elements 16, 17 and 22 form a three element "zoom" lens, the purpose of which is to pass this image to the sample surface with controlled beam diameter and angular divergence for a broad range of beam kinetic energies. Element 60 is grounded to form a nearly field-free region between the monochromator and the sample, and its 0.10 in. slit helps prevent protrusion of the field from element 22 into this region. With element 60 grounded and element 12 at a potential fixed by the chosen pass energy, the other four elements with only one real slit at element 15 afford sufficient flexibility to meet the needs for beam focus at the sample in the energy range 5-100 eV.

The first element of the next stage of electron optics, number 62, is grounded to form a nearly field-free region between the sample and the analyzer, and it contains two 0.030 in. apertures to define the acceptance angle of the analyzer of roughly 2°. The functions of elements 24, 25, 26 and 27 mirror those of elements 22, 17, 16 and 15, as described previously, imaging a point on the crystal surface to a pupil at the entrance plane of the analyzer spheres. Element 23 has been included to allow corrections to the focal properties of this optical stage for experiments where the energy range scanned to generate a loss spectrum represents a significant fraction of the incident beam energy, for example in EELS of valence electronic excitations, where scan widths of 30 eV are necessary in conjunction with an incident beam energy of approximately 100 eV. For this purpose, the potential of 23 can be ramped in proportion to the ramp applied to the other analyzer lens elements to maintain a fixed image size and location, independent of the acceptance energy of the analyzer.

The last stage of opics images a point in the exit plane of the analyzer hemispheres to the entrance cone of the electron multiplier, which is supported in element 40. The pair of apertures, one each in elements 32 and 35, serve two purposes: first, they limit the angular speed of the beam cone reaching the multiplier, enhancing the energy resolving power of the spheres; and second, they reduce the chance that electrons of anomolous energy will reach the multiplier after scattering elastically from the surfaces of the spheres **(15)**, a problem which plagued the spectrometer prior to the addition of the aperture in element 32.

The focal properties of the stage of electron optics which passes the scattered beam from the sample surface to the entrance plane of the analyzer spheres are by design rather insensitive to the kinetic energy of the scattered beam. For vibrational measurements in particular where the spectral range to be scanned is approximately 0.5 eV wide (compared to an incident beam kinetic energy of 5-10 eV), the transmission of the analyzer is essentially constant throughout the scan. For this reason the energy scan is most readily accomplished by fixing all potentials in the electron analyzer with respect to each other and ramping the ensemble with respect to the monochromator (or ground) to generate the loss spectrum. This method has the advantage that the analyzer energy resolution remains constant during the scan.

VI. Electron Counting

As the acceptance of energy of the analyzer is ramped to generate an EEL spectrum, the scattered electrons transmitted by the analyzer are counted by an electron multiplier, operating through a sensitive chain of pulse counting electronic devices. In the paragraphs that follow, the purpose, pertinent specifications and optimum operating conditions for each element of the electron counting chain will be described. A block diagram of the electron counting system is shown in Fig. 4.

The heart of the electron counting system is the Channeltron Electron Multiplier, model CEM 4028, manufactured by Galileo Electo-Optics, Inc. **(16)**. It is a rather simple device, consisting only of a glass tube of approximately 0.05 in. inside diameter, several inches long and coiled into a pigtail configuration with an acceptance cone at its entrance end and a metal cap at its exit end. The inside of the tube is coated with a lead oxide semiconducting layer, the secondary electron emission characteristics of which are tailored to meet the specific needs of the multiplier's application. The cone of the multiplier is held at a low positive potential with respect to the electrons to be counted, insuring that they strike the multiplier surface with kinetic energies on the order of several eV or less, while the tail of the multiplier is held at a high (2.6-3.0 kV) positive potential, as is depicted schematically in Fig. 1. An electron incident on the multiplier's entrance ejects several secondary electrons from the lead oxide coating, and the potential gradient which exists along the multiplier's length accelerates these electrons to impact again with the coating. This process continues along the length of the multiplier, culminating in a charge pulse of approximately 10^8 electrons at the multiplier end cap as a result of the single electron which initially struck the entrance. Although this pulse has a time width of approximately 20 ns, suggesting a theoretical maximum electron count rate of 50 MHz for the multiplier, its gain drops severely at high count rates and maximum count rates on the order of 1 MHz are the practically obtainable maximum **(16)**.

The tail of the multiplier is connected to the Ortec 459 HV power supply through a 100 KΩ resistor, the purpose of which is to produce a voltage transient at the tail of the multiplier as the negative charge pulse is collected by the positive terminal of the HV power supply. This voltage pulse passes through the 2200 pF decoupling capacitor, as shown in Fig. 4, producing a charge pulse which is detected by the Ortec 113 Scintillation Preamplifier for further signal processing at ground potential. The load resistor and decoupling capacitor are wired to terminals which have been added to the Preamplifier chassis, allowing them to be shielded and enclosed with the Preamplifier electronics. The Preamp serves as an impedance matcher, detecting the charge pulse produced at the decoupling capacitor with nearly infinite input impedance and producing a proportional voltage pulse of approximately 50 mV amplitude with no shaping at low output impedance to the amplifier. The Ortec 460 Amplifier shapes, inverts and amplifies the pulses it receives with a gain of 100-200 to produce output pulses with positive polarity and amplitudes of 4-8 V. These pulses are fed to the Ortec 553 Single Channel Analyzer, the purpose of which is to discriminate between those input pulses which have peak amplitudes falling within an adjustable "window" of voltage and those which do not. For this detection configuration, the upper limit of the voltage window is set at its maximum value, 10 V, and the lower limit is chosen to exclude low amplitude noise pulses from the multiplier and low level, externally produced signals which have been picked up by the transmission cables leading from the chamber to the Single Channel Analyzer. This lower limit of the voltage window can be chosen most easily by looking at the output of the amplifier with a triggered, time base oscilloscope and measuring the amplitude of the background noise signals which are superimposed upon and clearly distinguishable from the true electron pulses generated by the multiplier circuit. In most circumstances, a setting of 0.030 V is acceptable. For each input pulse which falls in this voltage window, the Single Channel Analyzer produces a 5 V TTL pulse at its output, and the Ortec 449-2 Log/Lin Ratemeter produces a 0-10 V analog output whose magnitude is proportional to the time rate of arrival (or its logarithm, if desired) of TTL pulses from the Single Channel Analyzer. The Ratemeter sensitivity (in pulses per second, full scale) can be adjusted over 5 orders of magnitude from 10/s to 10^6/s, and damping of the output signal with an internal integrator having time constants between 0.03 and 30 s is also provided. The output of the Ratemeter can be input either to an oscilloscope with the 0.03 s time constant for spectrometer tuning purposes or to an X-Y Recorder with a longer time constant for EEL spectrum collection.

The performance of the multiplier, and consequently the entire electron counting system, is sensitive to the physical condition of the its lead oxide coating. Although exposure to air at atmosphere pressure has no apparent effect, its secondary emission characteristics can be altered drastically by some adsorbed contaminants, thus care must be taken to avoid contact with oils or exposure to high pressures of contaminants during bakeout **(17)**. If contamination is suspected, the multiplier should be rinsed thoroughly with methanol.

Also, the gain of the multiplier degrades slowly with use **(16)**, and the high voltage applied to the multiplier, the amplifier gain, and the lower voltage window level of the Single Channel Analyzer must in unison be adjusted periodically to return proper detection of electron pulses over interfering noise. When multiplier voltages in excess of 3 KV must be used to obtain adequate pulse heights or when the height of a significant fraction of the pulses at high (10^5 Hz) count rates falls below the minimum acceptable lower window level, a new multiplier is needed. Experience has shown this condition to prevail about once every two years under ordinary circumstances.

VII. Electron Optics Control Panel

The purpose of the optics control system, as shown in the schematic wiring diagram of Fig. 5 for the EELS monochromator and Fig. 6 for the analyzer, is to provide stable, ripple-free control of the potentials of the spheres, Herzogs, and all lens elements in the spectrometer. These potentials define the beam kinetic energy at the sample, the pass energies of the hemispherical analyzers, the focal properties of the various electron lens stages, and the acceptance energy of the EELS analyzer as it is ramped for spectrum collection. The following paragraphs will first describe the important hardware used in the control system, and then the design and operating principles which led to the particular circuit configuration chosen.

In addition to the Lambda LH124B power supply which operates the cathode heater circuit (not shown in Fig. 5), five separate power supplies are required to operate the optics control system. "PS #1" and "PS #3" (both Kepco PCX 100-0.2) provide a (fixed) 100 V of potential difference between the -RAIL and +RAIL of the monochromator and analyzer, respectively, and the potentials for all the lens elements except the cathode and anode are obtained from variable resistance voltage dividers which span these rails. The supply labeled "EMITTER" (Kepco PCX-MAT 100-0.2) has a 0-100 V variable output and provides a 20-30 V bias potential between the anode and cathode. The supplies marked "OFFSET" and "RAMP" are identical to that used for "EMITTER" and are used to drive the -RAIL of the monochromator and analyzer from ground, effectively controlling the beam kinetic energy. The output of the "RAMP" supply is actually summed to the output of an Exact 7260 Function Generator (grounded), which provides a positive sawtooth ramp output, variable in amplitude from 0 to 7.5 V and in period from 10^{-7} to 10^{3} s. This function generator provides the voltage ramp which sweeps the acceptance energy of the analyzer for spectrometer tuning and spectrum collection.

The beam deflectors, elements 4 and 5 located in element 3, 10 and 11 in element 7, 20 and 21 in element 17, 30 and 31 in element 27, and 36 and 37 in element 35, are powered by 6 V lantern batteries. The circuit arrangement used for the deflector sets, shown in Figs. 5 and 6, allows the deflector potentials to be adjusted between -3 and +3 V of the lens elements in which they are located when the "ON/OFF" switch is in the "ON" position and sets the deflector potentials equal to that of their adjacent lens elements when the switch is in the "OFF" position. When the switch is "ON", a 50 KΩ or 100 KΩ resistance bridges the output terminals of the 6 V battery. Thus the deflectors should be "OFF" when not in use to prolong the battery life.

All variable resistances shown in Figs. 5 and 6 are provided by Bourns Inc. #3540-1 10-turn potentiometers, although any 10-turn, 1/2 W potentiometers of appropriate total resistance are acceptable for substitution or replacement.

All wiring for the control system is either enclosed in the grounded equipment rack or is fabricated of coaxial cable with BNC connectors, insuring that all conductors are surrounded by a grounded shield to prevent interference from external fields. To add further protection against interference from the low level 125 MHz field which permeates the laboratory and penetrates the braided shields of normal coaxial cables **(18)**, the bundle of cables leading to the spectrometer from the control panel is also wrapped in a second grounded shield of aluminum foil.

To insure that the potentials of the optical elements are stationary and free of noise, the current which flows through each resistive bridge of the control system must be large with respect to currents which may be induced by external fields in the conductors which lead from the control panel to the spectrometer, or with respect to currents which may result if a portion of the electron beam is collected by a lens element. It is this consideration which led to the sizing of the resistance magnitudes for each of the bridges. The largest current in the circuit (approximately 1 mA) is drawn by the cathode due to its emission of electrons to form the beam, and the resulting current load it places on the -RAIL necessitates the use of a power supply rather than a resistance bridge to fix the potential of the -RAIL with respect to ground with adequate stability. Most of the emitted current is collected by the anode, and this load necessitates the use of the "EMITTER" supply to fix the anode potential with respect to the cathode, independent of cathode emission current. Roughly 10 mA flows through the 2 KΩ resistance bridge with the "WORK FUNCTION" control which fixes the cathode and anode potentials with respect to the -RAIL, a value sufficiently large to insure stability of their potentials when compared to the current of approximately 10 μA which penetrates the anode aperture to form the EELS beam. The current which flows through the resistance bridges for all the other optical elements is on the order 1 mA, and this is sufficient to guarantee that the stability of the lens potentials is constrained by the stability of the power supplies used to operate the control panel.

Several operational and diagnostic advantages are realized if the hemisphere and Herzog potentials are adjusted carefully to make the vacuum potential defined by $(V'_{RAIL} - \varphi_{GR})$ the true zero of electron kinetic energy in the spectrometer, as was depicted in Fig. 1. When this condition is met, Eq. (4) for the beam becomes

$$H' = T' - \Phi + \varphi_{GR} \qquad (17)$$

where H' is the Hamiltonian, T' is the electron kinetic energy, Φ is the electrostatic potential applied to the electron optics, φ_{GR} is the work function of their graphite coating, and $(\Phi - \varphi_{GR})$ is therefore the surface potential of the optics which results from an applied potential Φ (all in eV energy units). Choosing $H' = \varphi_{GR}$ as the arbitrary reference potential, which is equivalent to adjusting the sphere and Herzog potentials to make $(V'_{RAIL} - \varphi_{GR})$ the zero of the electron beam kinetic energy, makes $T' = \Phi$, and the applied electrostatic potentials in the electron optical system are equal to the kinetic energies of the electron beam at the respective lens elements. This condition is accomplished by making the applied potential of the Herzog elements (and consequently the potential of the central, beam defining trajectory through the hemispheres) equal to the kinetic energy of the beam along that trajectory, i.e. the pass energy, through the use of the expressions derived in Section IV of this Appendix and listed in Table 1. The following adjustments of the Herzog and hemisphere potentials should be made:

1. Set the Herzog potential to the desired pass energy (all potentials measured with respect to the -RAIL, i.e. V of Fig. 1).
2. Set the inner and outer hemispheres to the potentials resulting from simultaneous solution of the "Pass Energy" and "Herzog Potential" equations of

Table 1 with V_{12} equal to E_0 for the monochromator and V_{32} equal to E_0 for the analyzer. The results for the monochromator hemisphere potentials are

$$V_{13} = 1.4612E_0, \quad V_{14} = 0.6843E_0 , \tag{18}$$

and those for the analyzer are

$$V_{33} = 1.2855E_0, \quad V_{34} = 0.7779E_0 . \tag{19}$$

Since the relationships derived above are all linear and free of additive constants, multiplication of the set of potentials $\{V_{12}, V_{13}, V_{14}\}$ for the monochromator or $\{V_{32}, V_{33}, V_{34}\}$ for the analyzer by a constant factor changes only the pass energy without affecting the potential which represents the zero of beam kinetic energy. This is exactly the effect produced by the "PASS ENERGY" controls shown in Fig. 5 for the monochromator and Fig. 6 for the analyzer, but only when the sphere and Herzog potentials are set according to the previously described prescription. Once these potentials are set for a chosen pass energy, the "PASS ENERGY" controls allow convenient and precise variation of these quantities while the spectrometer is being tuned for optimum resolution and throughput.

The "WORK FUNCTION" control shown in Fig. 5 allows variation of the cathode potential with respect to the -RAIL to insure that the maximum of the energy distribution of the thermally emitted electrons can be aligned with the kinetic energy origin of the electron beam, as defined by the monochromator sphere potentials and their pass energy. The use of the power supply labeled "EMITTER" to bias the anode with respect to the cathode and the resistive bridge to adjust the cathode potential with respect to the -RAIL guarantees that the emission properties of the cathode do not vary as the "WORK FUNCTION" control is adjusted. In this configuration, "ΔV" of Fig. 1, the difference between the cathode and -RAIL potentials when the "WORK FUNCTION" control is adjusted to maximize the beam current, is equal to $(\varphi_C + kT_c - \varphi_{GR})$ and is a convenient diagnostic monitor of the condition of the cathode. In normal operation with a healthy cathode, $\Delta V = -1.6$ to -1.8 V.

VIII. Start-Up, Tuning and Spectrum Collection

At this point, the principles which govern the operation of the various portions of the spectrometer should be well understood. This section will make use of these principles to describe a step-by-step procedure for turning on the spectrometer, obtaining an elastically scattered beam from the cathode to the multiplier, tuning the spectrometer to optimize its resolution and scattered intensity, and recording an energy loss spectrum.

The following sequence of actions should be followed to turn on the spectrometer and to obtain an elastically scattered beam from the cathode to the multiplier. Prior to attempting this, however, the sample should be cleaned and annealed to maximize its reflectivity. This will provide the best available scattered beam current for start-up detection by the analyzer.

1. Turn on the cathode heater power supply and adjust its output current at 0.75 to 0.85 A. Turn on the control panel power supplies, set the "EMITTER" supply output voltage at 20 to 30 V and trim the cathode heater current until the anode draws 0.5 to 1.0 mA of emission current, as measured with a suitable current meter. Set the -RAIL potentials to values near the desired beam energy, -5 to -10 V.
2. Set the monochromator and analyzer Herzog and sphere potentials to give pass energies of 0.8 to 1.0 eV via the method described in Section VIII of this Manual.
3. Adjust the potentials of elements 4, 5, 6 and 7 to maximize the beam current

collected at the outer hemisphere. This current can be monitored by breaking the BNC connection for 14 between the control panel and the chamber and connecting the input of a picoammeter or electrometer to element 14.

4. Monitor beam current at element 15, and adjust the "WORK FUNCTION" control and all preceding lens potentials to maximize the current obtained.

5. Continue by measuring current at the crystal and adjusting all lens potentials in the monochromator. Current on the order of 0.01 μA is expected.

6. Measure current collected at element 62 while varying the analyzer rotation angle and the crystal position.

7. Set elements 23, 24, 25, 26 and 27 to reasonable values (as listed in Table 3 and the lab notebooks) and look for beam current at element 34. This step is in general difficult, since passage of the beam through the apertures of element 62 does not follow easily after collection of beam current at 62, and by this point along the beam path currents are on the order of 0.1 nA. Optimize all lens potentials, the analyzer angle, and the crystal position.

8. Turn on the electron counting electronics and the high voltage power supply. Scan the analyzer acceptance energy via adjustment of "PS #3" or the "OFFSET" control of the function generator until the electron counts appear on the display dial of the Ratemeter. Adjust all lens potentials, positions, etc. to maximize the count rate of collected electrons, then perform a diagnostic test of the counting system to insure that all operating parameters are properly adjusted. Count rates under these conditions should exceed 300 K Hz.

Once these tasks have been accomplished, tuning to optimize the spectrometer's performance can commence. Again, a clean and ordered crystal will expedite this process. For tuning, the Function Generator should be set to provide a 15 to 30 mV scan width with a repeat rate of 3 to 4 Hz. Its output should not only drive the analzyer -RAIL, but also the "X" input of an X-Y oscilloscope. The Ratemeter should be set to an appropriate scale with a time constant of 0.03 s, and its output should drive the "Y" input of the oscilloscope. With the "OFFSET" control of the Function Generator adjusted appropriately, the oscilloscope should display continuously the elastically scattered beam intensity as a function of analyzer scan energy. Its width and peak intensity will be the important parameters monitored during subsequent tuning.

It should be remembered, as was described in Section IV of this Manual, the net width of the observed elastic peak is due to the convoluted widths of the hemispherical energy selectors in the monochromator (ΔE_1) and analyzer (ΔE_2) according to Eq. (15),

$$\Delta E(\text{net}) = \sqrt{(\Delta E_1)^2 + (\Delta E_2)^2}\ .$$

Evaluating the total derivative of ΔE with respect to both (ΔE_1) and (ΔE_2) yields:

$$d(\Delta E) = \frac{\Delta E_1}{\Delta E}\, d(\Delta E_1) + \frac{\Delta E_2}{\Delta E}\, d(\Delta E_2)\ . \tag{20}$$

If it is assumed that the resolution of one set of hemispheres is much greater than that of the other set, $\Delta E_2 \ll \Delta E_1$ for example, then Eq. (20) can be simplified [using the approximation $(\Delta E_2/\Delta E_1) << 1$] to read

$$d(\Delta E) = d(\Delta E_1) + \left(\frac{\Delta E_2}{\Delta E_1}\right) d(\Delta E_2)\ . \tag{21}$$

This relationship illustrates that the net resolution of the spectrometer, evidenced by the width of the elastic peak trace observed on the oscilloscope display during tuning, will be strongly sensitive only to ΔE_1 and rather insensitive to ΔE_2. For this reason, expeditious tuning of the spectrometer can be realized only by working simultaneously on both the monochromator and analyzer, being careful to keep the resolution of both comparable as the overall resolution is optimized.

Also discussed in Section IV of this Manual was the sensitivity of the resolving power of the hemispherical analyzers to E_0, their pass energies, to ΔS, their entrance and exit slit widths, and α, their entrance and exit beam angular divergences. Then, once a beam has been obtained through the spectrometer via the start-up procedure described, tuning proceeds via gradual reduction of the monochromator and analyzer pass energies in 50-100 mV increments, followed at each step by adjustment of the lens potentials, crystal position, analyzer angle, etc. to optimize the beam current and resolution. Adjustments are best made to optical elements in groups which affect selectively some portion of the beam path critical to resolution or transmission. For example, adjustments to elements 6 and 7, which control ΔS and α for the beam at its entrance to the monochromator spheres, should be made in conjunction with adjustments to elements 15 and 16, which control the same properties of the beam at the exit of the spheres. Similar considerations apply to elements 26, 27 and 35 for the analyzer. Also, elements 17, 22-25, the crystal position, and the analyzer angle should all be adjusted in unison, as these control the beam properties in the region between the monochromator exit and analyzer entrance. This process continues until further reduction of the pass energies leads only to loss in transmitted beam current with no apparent improvement in resolution, which typically occurs at pass energies below about 300 mV. For most experiments, an elastic peak width at half maximum intensity of 10 mV (80 cm^{-1}) or less with a maximum count rate in excess of 100 KHz is desired. When this condition is reached, useful experiments can be performed.

To collect an energy loss spectrum, the output of the Function Generator should be connected to the "X" input and the output of the Ratemeter to the "Y" input of the X-Y Recorder. The Function Generator should be adjusted to provide a scan of appropriate width to cover the spectral range to be investigated (0.4-0.5 V or 3200-4000 cm^{-1} is sufficient for nearly all vibrational measurements), and the X-Y Recorder should have its X and Y gains and offsets adjusted so that the recorded spectrum will fit properly on the chart paper. The "OFFSET" control of the Function Generator is used to adjust the acceptance energy of the analyzer to start the scan at the high energy tail of the elastic peak, and once an appropriate Ratemeter "RANGE" and "TIME CONSTANT" and Function Generator "PULSE WIDTH" are chosen, the scan can be started by depressing the "RUN" switch on the Function Generator. Since the scan will cover not only the elastic peak, with a maximum count rate on the order of 10^5 Hz, but also the loss region, where count rates less than 10^2 Hz are expected, the Ratemeter "RANGE" will have to be changed, perhaps several times, as the scan progresses. As will be discussed in the paragraphs to follow, this will also necessitate adjustment of the "TIME CONSTANT" setting and the scan rate to insure collection of high quality, noise free spectra.

The first important quantity which contributes to the quality of the collected spectrum is the time constant with which the Ratemeter output is damped to filter random noise from the spectra. The choice of the minimum acceptable time constant for each Ratemeter "RANGE" (or sensitivity) setting can be made on the basis of statistical arguments, which show that for a time average signal count rate of ρ Hz, the uncertainty in the measured count rate (one standard deviation) is given by

$$\sigma = \sqrt{\frac{\rho}{\tau}} \tag{22}$$

where τ is the time constant of the measurement circuit. As the Ratemeter sensitivity is changed, then, to maintain the output signal as a significant fraction of full scale of the Ratemeter output, τ should be adjusted to maintain a nearly constant *relative* uncertainty in ρ, i.e. σ/ρ should be kept nearly constant for all Ratemeter sensitivities. Experience has shown that for the EEL spectrometer

$$\frac{\sigma}{\rho} = \frac{1}{\sqrt{\rho\tau}} \leq 0.04 \tag{23}$$

is adequate to provide good counting statistics and clean, smooth spectra. Time constant selection corresponding to Ratemeter full scale sensitivity, as calculated by this formula, is listed in Table 4.

Once the Ratemeter sensitivity and time constant are selected appropriately to match the signal intensity in some portion of the energy loss spectrum, it remains then to adjust the analyzer scan rate, R = $d\omega/dt$ ($\mathrm{cm}^{-1}/\mathrm{s}$), to a value which allows rapid collection of data without "slewing" or distortion of the spectral features.

A practical limit for R in terms of τ and Δ, the minimum full width at half maximum of the spectral features (i.e. FWHM of the elastic peak) can be obtained through analysis of a simple analytical model which includes the effects of signal damping in a rigorous mathematical way.

First, let $I(\omega)$ be the true signal, assumed for this analysis to be free of noise, produced by the Ratemeter prior to the action of the time constant damping circuit, and $I'(\omega)$ the damped signal output by the Ratemeter to the X-Y Recorder. The rate of change of the damped signal with respect to time is proportional to the deviation of that signal from the true input signal, divided by the time constant of the damping circuit:

$$\frac{-dI'(\omega)}{dt} = \frac{I'(\omega) - I(\omega)}{\tau} . \tag{24}$$

Using the relationship between energy loss, ω, time, and the scan rate, R, this equation can be rearranged to read

$$\frac{I'(\omega)}{d\omega} + \frac{1}{R\tau} I'(\omega) = \frac{1}{R\tau} I(\omega) \tag{25}$$

For calculational simplicity, $I(\omega)$ is assumed to be sinusoidal with a maximum intensity of I_0 and a peak width of Δ (i.e. period = 2Δ), centered on loss energy ω_0 **(19)**:

$$I(\omega) = I_0 \cos\left[\frac{\pi}{\Delta}(\omega - \omega_0)\right] \tag{26}$$

Solving Eq. (25) for $I'(\omega)$ yields

$$I(\omega) = \frac{I_0}{1 + \left(\frac{R\tau\pi}{\Delta}\right)^2} \left\{\cos\left[\frac{\pi}{\Delta}(\omega - \omega_0)\right] + \frac{R\tau\pi}{\Delta} \sin\left[\frac{\pi}{\Delta}(\omega - \omega_0)\right]\right\} . \tag{27}$$

Since the position of spectral features is of paramount importance in spectroscopic measurements, the most useful measure of the distortion produced by damping is the change in the location of the peak maximum of $I'(\omega)$ as compared to $I(\omega)$. The location of the maximum of $I(\omega)$ is at $\omega = \omega_0$, and that of $I'(\omega)$ is given by the solution of

$$\tan\left[\frac{\pi}{\Delta}(\omega - \omega_0)\right] = \frac{R\tau\pi}{\Delta} \tag{28}$$

For peak position to be relatively unaffected by τ, the shift of $I'(\omega)$ from $I(\omega)$ should be small compared to the width of the peaks, Δ. A reasonable upper limit would be

$$(\omega - \omega_0) \leq 0.05\Delta \, . \tag{29}$$

This would give a peak position error of 4 cm^{-1} with an elastic peak width of 80 cm^{-1}, for example. For these conditions, the argument of the tan function is sufficiently small to allow use of only the first term in its series expansion, i.e. $\tan\alpha = \alpha$. Substituting this into Eq. (28) and simplifying gives the following final result:

$$\frac{R\tau}{\Delta} \leq 0.05 \ . \qquad (30)$$

Maximum scan rates for $\Delta = 80\ \mathrm{cm}^{-1}$ are listed along with the Ratemeter sensitivities and time constants in Table 4.

Acknowledgments

I gratefully acknowledge the assistance of Dr. Neil Avery in the repair and modification of the electron energy loss spectrometer and the work of Brian Toby in the design and fabrication of the electron optics control panel.

IX. References

1. See, for example, E. Harting and F. H. Read, *Electrostatic Lenses*, Elsevier, Amsterdam, 1976.
2. J. Hölzl and F. K. Schulte, *Solid Surface Physics*, Springer-Verlag, Berlin, 1979.
3. For graphite coating data and application technique, see *EELS Maintenance Log*, Rm. 111, Spalding Laboratory, California Institute of Technology.
4. M. H. Polley, W. D. Schaeffer and W. R. Smith, J. Phys. Chem. **57**, 469 (1953).
5. Approximate values for the parameters in these expressions are kT_c = 0.2 eV, φ_C = 1.5 eV (P. A. Redhead, J. P. Hobson and E. V. Kornelsen, *The Physical Basis of Ultrahigh Vacuum*, Chapman, London, 1968, p. 300), φ_{GR} = 4.5 eV (*Handbook of Chemistry and Physics*, R. C. Weast, ed., C.R.C., 1971), and φ_s = 5.4 eV for clean Ru(001) [F. J. Himpsel, K. Christmann, P. Heimann and D. E. Eastman, Phys. Rev. B **23**, 2546 (1981)].
6. R. H. Fowler, *Statistical Mechanics*, 2nd ed., University Press, Cambridge, 1955, pp. 346-358.
7. I. Langmuir, J. Am. Chem. Soc. **54**, 2798 (1932).
8. N. D. Lang, Phys. Rev. B **4**, 4234 (1971).
9. For example: D. Shafer and J. Turnbull, Appl. Surface Sci. **8**, 225 (1981); D. S. Chen, I. Lindau, M. H. Hecht, A. J. Viescas, J. Nogami and W. E. Spicer, Appl. Surface Sci. **13**, 321 (1982); R. Forman, Appl. Surface Sci. **17**, 429 (1984).
10. A. Shih and G. A. Haas, Appl. Surface Sci. **8**, 125 (1981); G. A. Haas and A. Shih, Appl. Surface Sci. **8**, 145 (1981); M. H. Hecht, I. Lindau and D. S. Chen, J. Appl. Phys. **53**, 9021 (1982).

11. J. K. Rice, PhD Thesis, California Institute of Technology, 1969, Ch. 4.

12. G. E. Thomas and W. H. Weinberg, Rev. Sci. Instrum. **50**, 497 (1979).

13. R. Herzog, Z. Physik **97**, 556 (1935); **41**, 18 (1940).

14. A. Chutjian, Rev. Sci. Instrum. **50**, 347 (1979).

15. H. Froitzheim, H. Hopster, H. Ibach and S. Lehwald, Appl. Phys. **13**, 147 (1977).

16. Technical aspects of multiplier design and operation are summarized in: D. S. Evans, Rev. Sci. Instrum. **36**, 375 (1965); E. A. Kurz, Am. Lab., March 1979.

17. The "dag" coating applied to the electron optics contains a colloid stabilizer of unknown chemical composition which at bakeout temperatures higher than about 250°C is present in the chamber in sufficient concentration to totally poison the electron multiplier's active surface.

18. R. Morrison, *Grounding and Shielding Techniques in Instrumentation*, Wiley, New York, 1967, Ch. 9.

19. The more accurate Gaussian model for $I(\omega)$, i.e. $I(\omega) = I_0 \exp\left[-\ln 16 \left(\frac{\omega - \omega_0}{\Delta}\right)^2\right]$ can also be used to solve Eq. (25), but introduces only computational complexity without affecting the physical significance or accuracy of the final result.

X. Tables

Table 1. Expressions for the pass energies and Herzog potentials in terms of the inner and outer hemisphere potentials for the electron monochromator and analyzer.

	Electron Monochromator	**Electron Analyzer**
Inner Hemisphere:		
Radius	0.8125 in.	1.3125 in.
Potential†	V_{13}	V_{33}
Outer Hemisphere:		
Radius	1.1875 in.	1.6875 in.
Potential†	V_{14}	V_{34}
Pass Energy	$E_0 = 1.287(V_{13}-V_{14})$	$E_0 = 1.970(V_{33}-V_{34})$
Herzog Potential†	$V_{12} = 0.4063V_{13} + 0.5937V_{14}$	$V_{32} = 0.4375V_{33} + 0.5625V_{34}$

†See Fig. 3

Table 2. Locations and diameters of apertures in the EEL spectra (as of 1/85).

Lens Element Number[†]	**Diameter of Aperture**
3	0.020 in.
7	2 x 0.020 in.
12	0.052 in.
15	0.020 in.
32	0.020 in.
35	0.052 in.
60	0.100 in.
62	0.030 in.

[†] See Fig. 3

Table 3. Typical lens voltages used for high-resolution electron energy loss spectroscopy.[†]

Beam Energy = 6 eV + $\varphi_{GR} - \varphi_S$.

Pass Energies = 0.400 eV, both monochromator and analyzer.

Monochromator		**Analyzer**	
Lens Element Number[‡]	Potential	Lens Element Number[‡]	Potential
0	-1.6 V	62	+6 V (GND)
3	+28 V	23	+4-10 V
6	+70-90 V	24	+15-30 V
7	+7-9 V	25	+5-15 V
12	+0.400 V	26	+30-50 V
13	+0.584 V	27	+3-5 V
14	+0.273	32	+0.400 V
15	+10-15 V	33	+0.514 V
16	+4-6 V	34	+0.311 V
17	+35-50 V	35	+3-5 V
22	+6-8 V	40	0 V
60	+6 V (GND)		

[†] All voltages measured with respect to the -RAIL potential of Fig. 1

[‡] Lens number system follows that is illustrated in Fig. 3.

Table 4. Scan rates and Ratemeter "TIME CONSTANT" settings as a function of Ratemeter "RANGE" setting for proper collection of EEL spectra.

Ratemeter		**Scan Rate**
Range	**Time Constant**	**($\Delta = 80$ cm^{-1})**
3×10^5 Hz	0.03 S[†]	130 cm^{-1}/s
10^5	0.03[†]	130
3×10^4	0.03	130
10^4	0.1	40
3×10^3	0.3	13
10^3	1.0	4.0
3×10^2	3	1.3
10^2	10	0.40
3×10	30	0.13
10	30[‡]	0.13

[†] Minimum time constant available for the Ortec 449 Ratemeter.

[‡] Maximum time constant available for the Ortec 449 Ratemeter.

XI. Figures

Figure Captions

Figure 1: Schematic diagram illustrating the relationship between externally applied voltages in the spectrometer and the kinetic and potential energies of electrons in the beam. All symbols are defined in the text.

Figure 2: Schematic diagram used to illustrate the energy dispersive and focal properties of the hemispherical electrostatic analyzer. All symbols are defined in the text.

Figure 3: Cross sectional view of the electron monochromator and analyzer showing the numbering scheme used to identify all the electron optical elements of the spectrometer.

Figure 4: Block diagram of the electron counting system, with operating settings for the various components listed below their representative blocks.

Figure 5: Schematic wiring diagram for the EELS monocromator control panel.

Figure 6: Schematic wiring diagram for the EELS analyzer control panel.

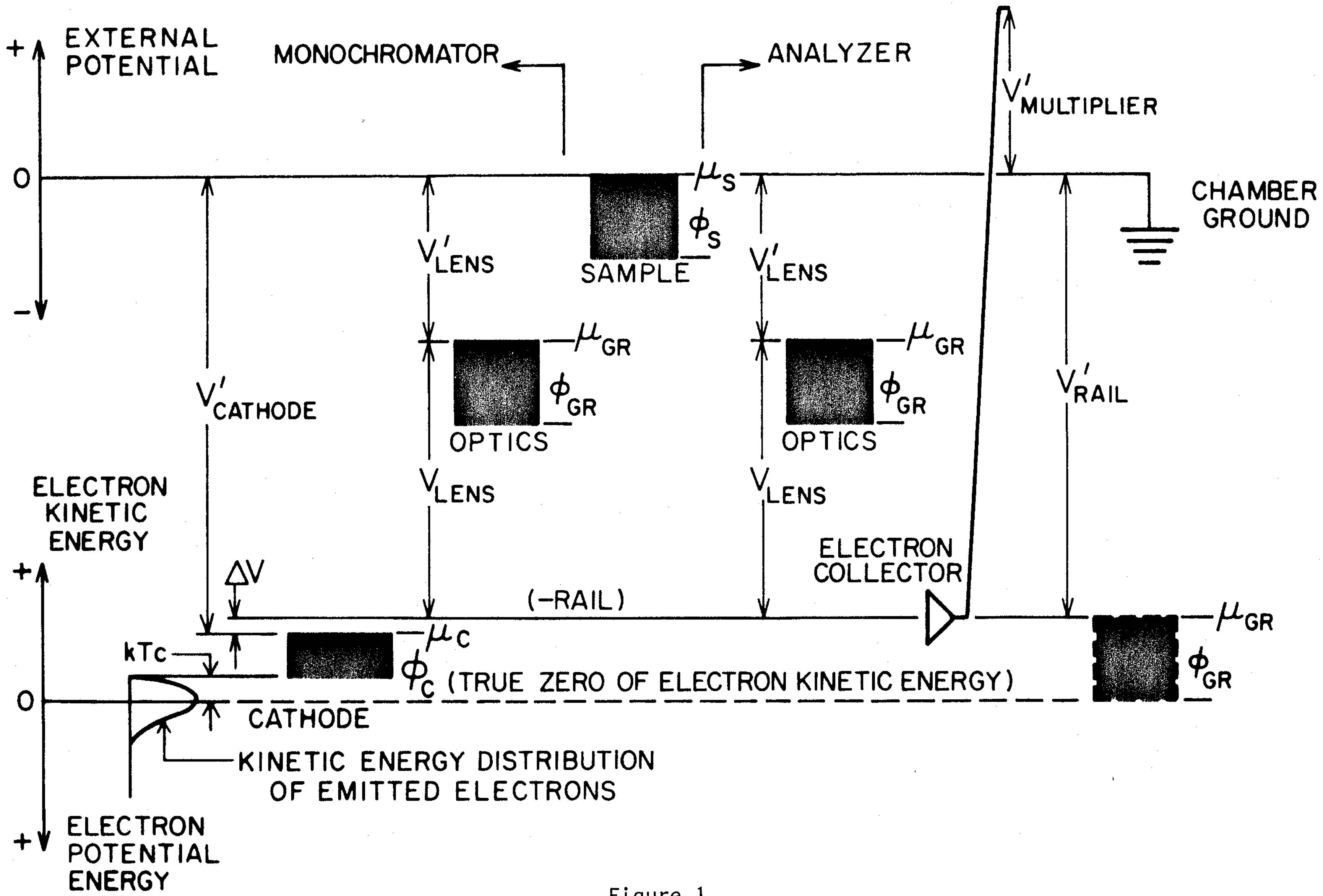
+
EXTERNAL POTENTIAL
0
−
MONOCHROMATOR
ANALYZER
$V'_{MULTIPLIER}$
μ_S
ϕ_S
SAMPLE
CHAMBER GROUND
V'_{LENS}
V'_{LENS}
μ_{GR}
ϕ_{GR}
OPTICS
μ_{GR}
ϕ_{GR}
OPTICS
$V'_{CATHODE}$
V'_{RAIL}
V_{LENS}
V_{LENS}
ELECTRON KINETIC ENERGY
+
ELECTRON COLLECTOR
ΔV
(−RAIL)
μ_{GR}
μ_C
kTc
ϕ_C (TRUE ZERO OF ELECTRON KINETIC ENERGY)
ϕ_{GR}
0
CATHODE
KINETIC ENERGY DISTRIBUTION OF EMITTED ELECTRONS
+
ELECTRON POTENTIAL ENERGY

Figure 1

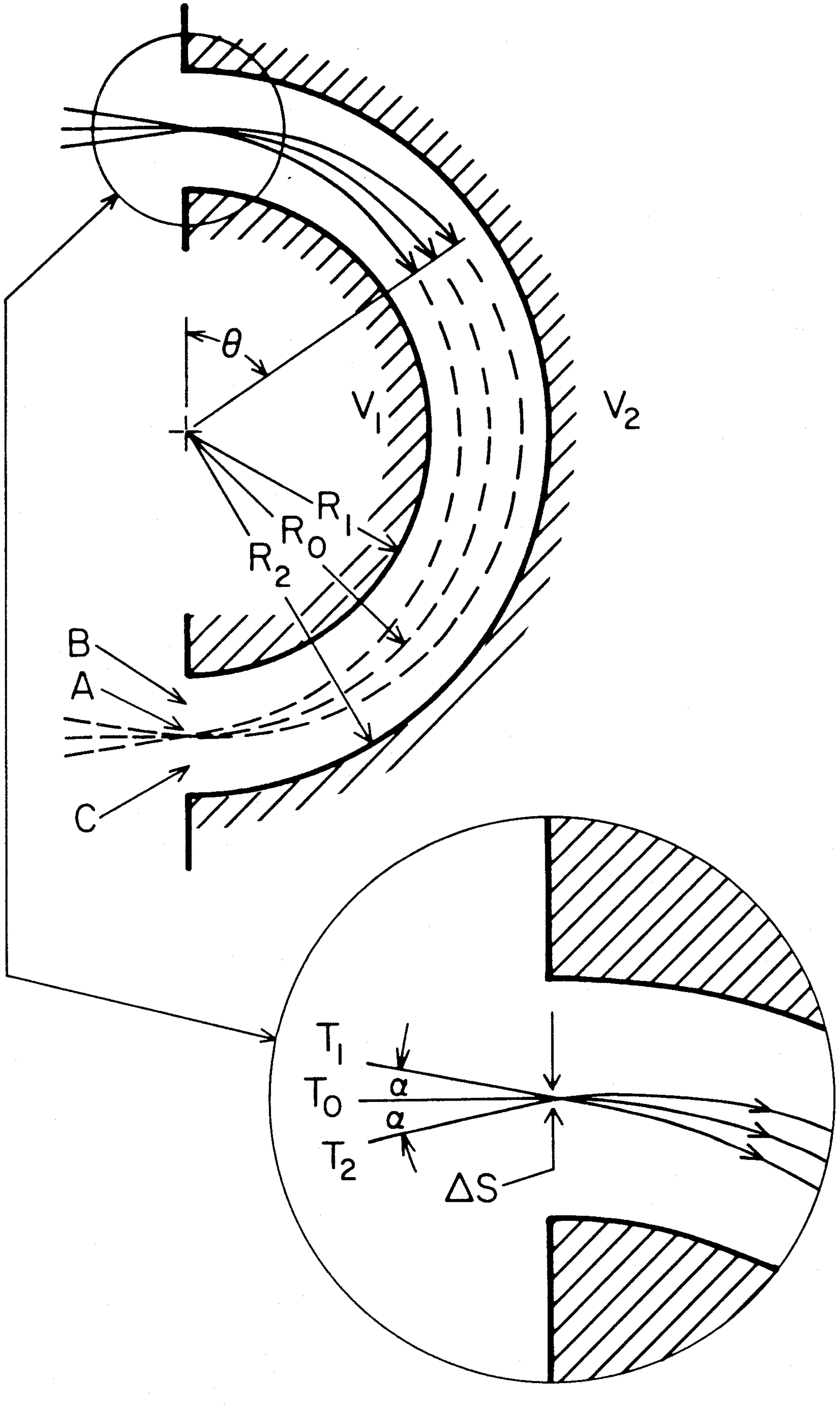

Figure 2

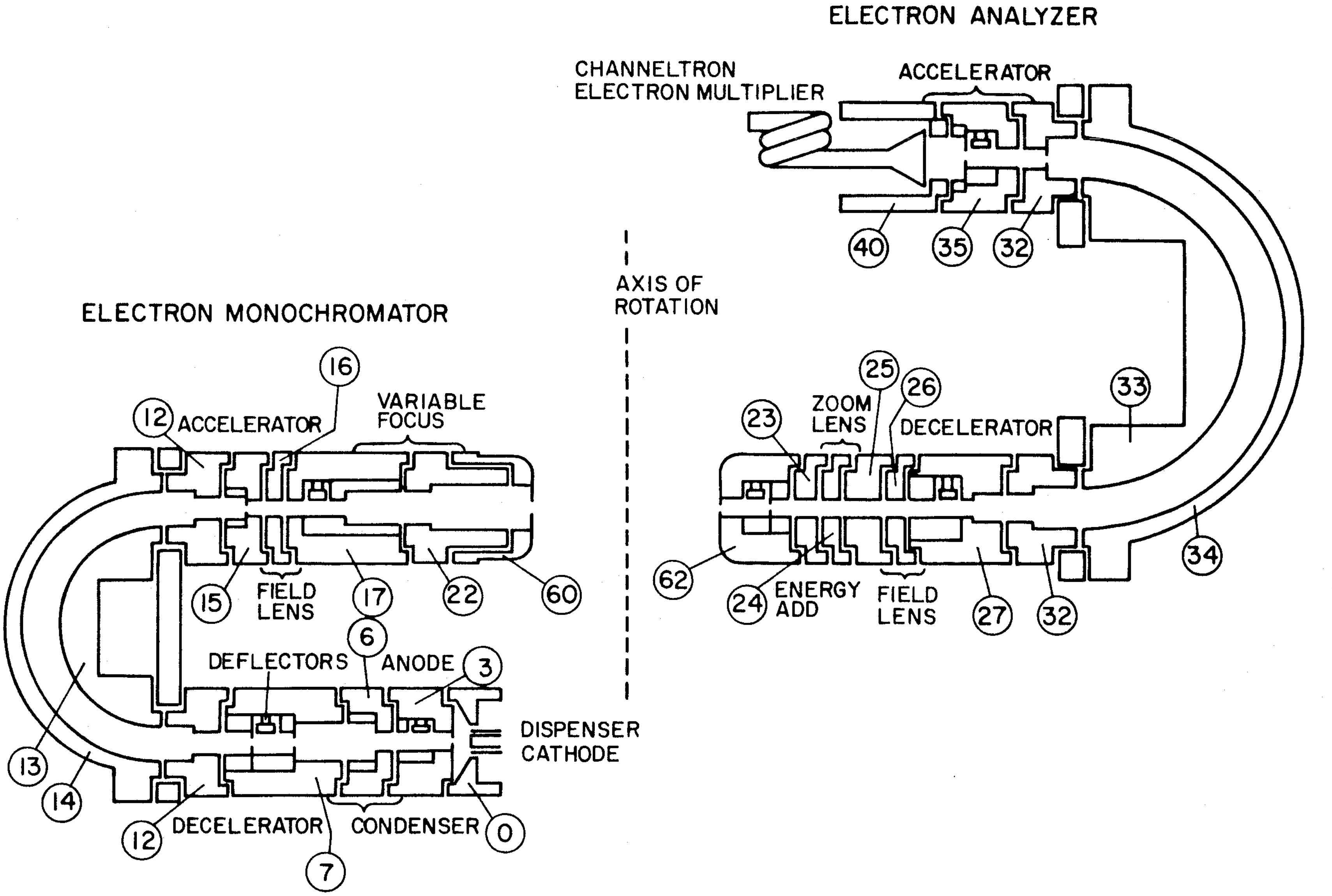
ELECTRON ANALYZER
CHANNELTRON
ELECTRON MULTIPLIER
ACCELERATOR
40
35
32
AXIS OF
ROTATION
ELECTRON MONOCHROMATOR
16
VARIABLE
FOCUS
12
ACCELERATOR
15
FIELD
LENS
17
22
60
6
DEFLECTORS
ANODE
3
DISPENSER
CATHODE
13
14
12
DECELERATOR
7
CONDENSER
0
25
26
23
ZOOM
LENS
DECELERATOR
33
62
24
ENERGY
ADD
FIELD
LENS
27
32
34

Figure 3

ELECTRON PULSE COUNTING ELECTRONICS

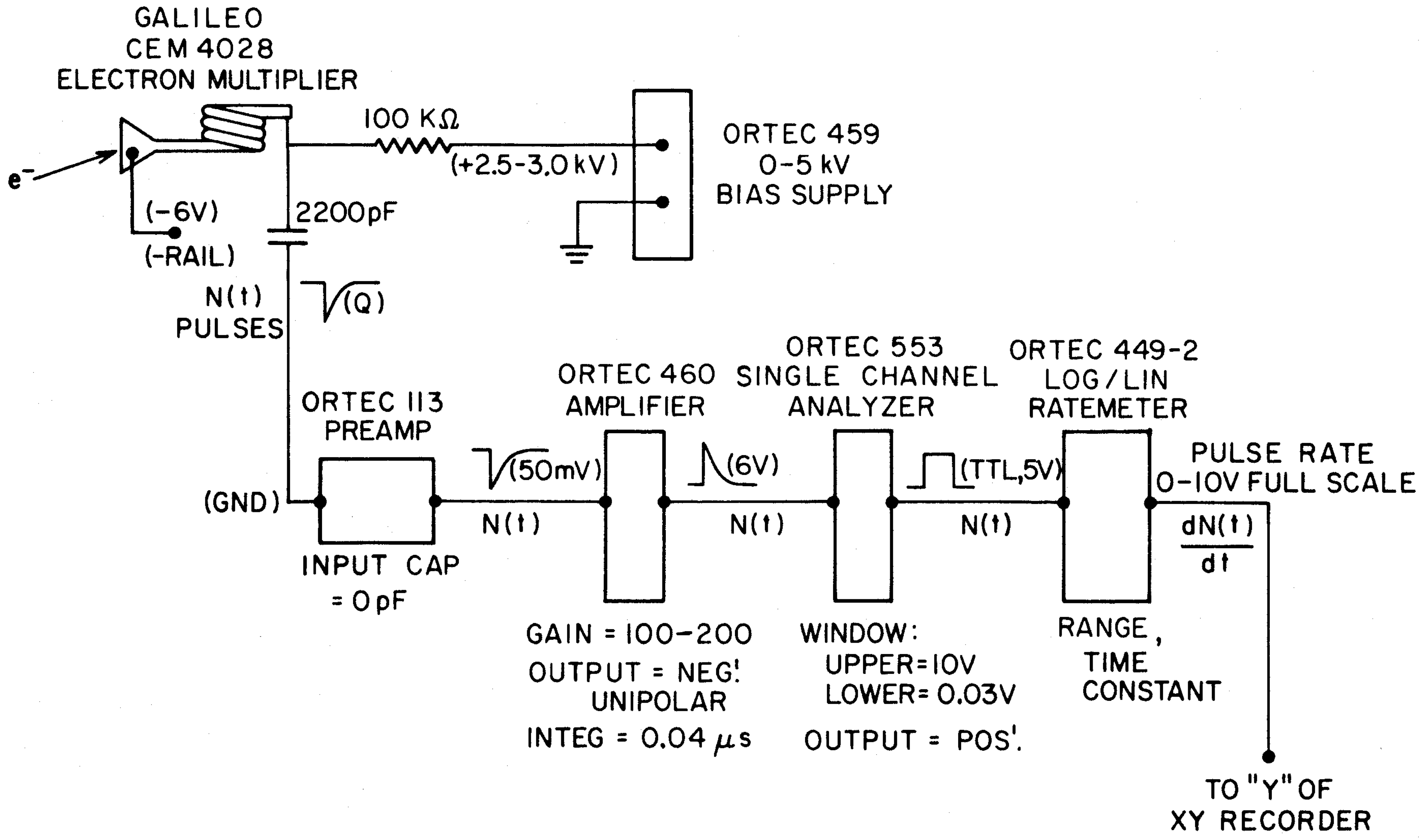

Figure 4

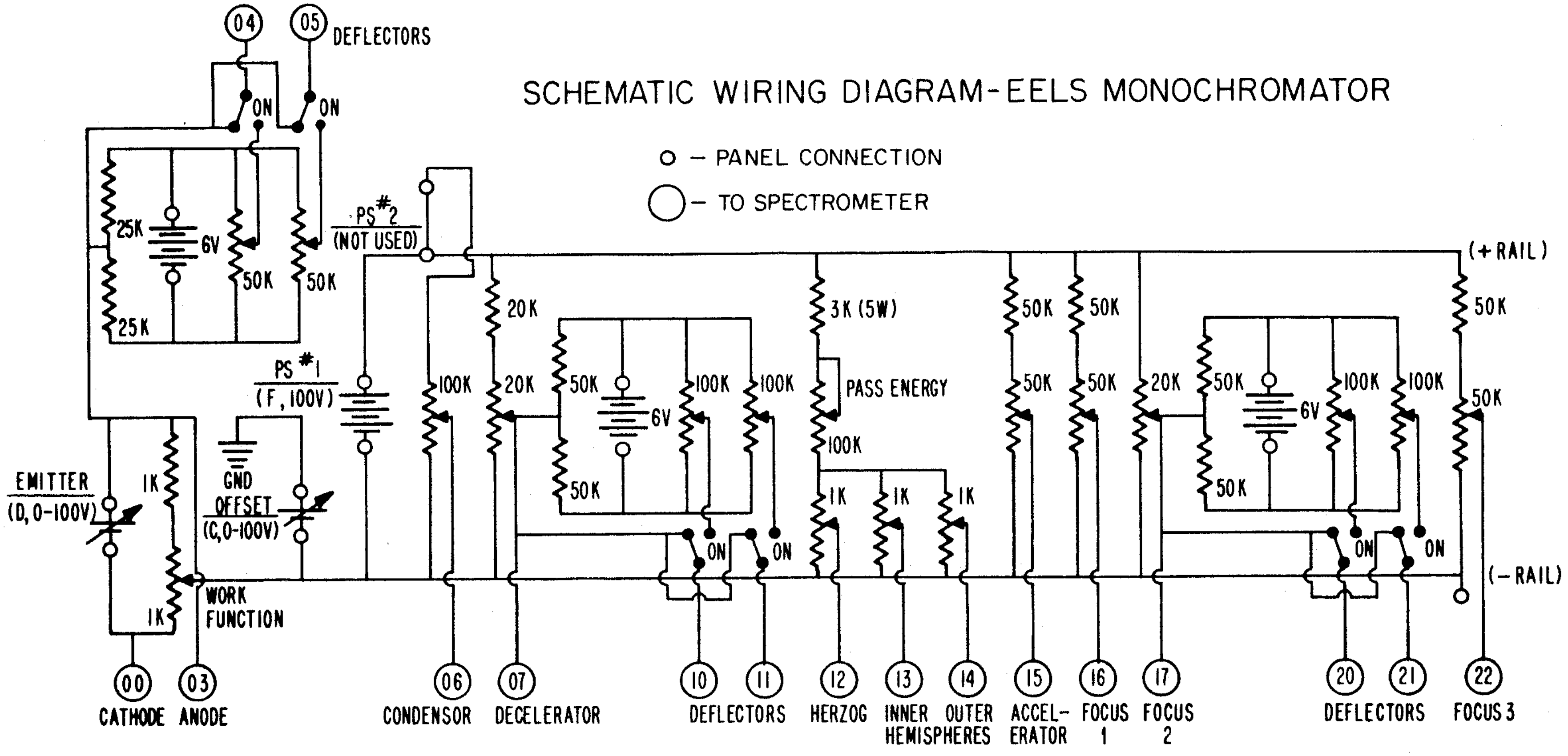

SCHEMATIC WIRING DIAGRAM-EELS MONOCHROMATOR

Figure 5

SCHEMATIC WIRING DIAGRAM - EELS ANALYZER

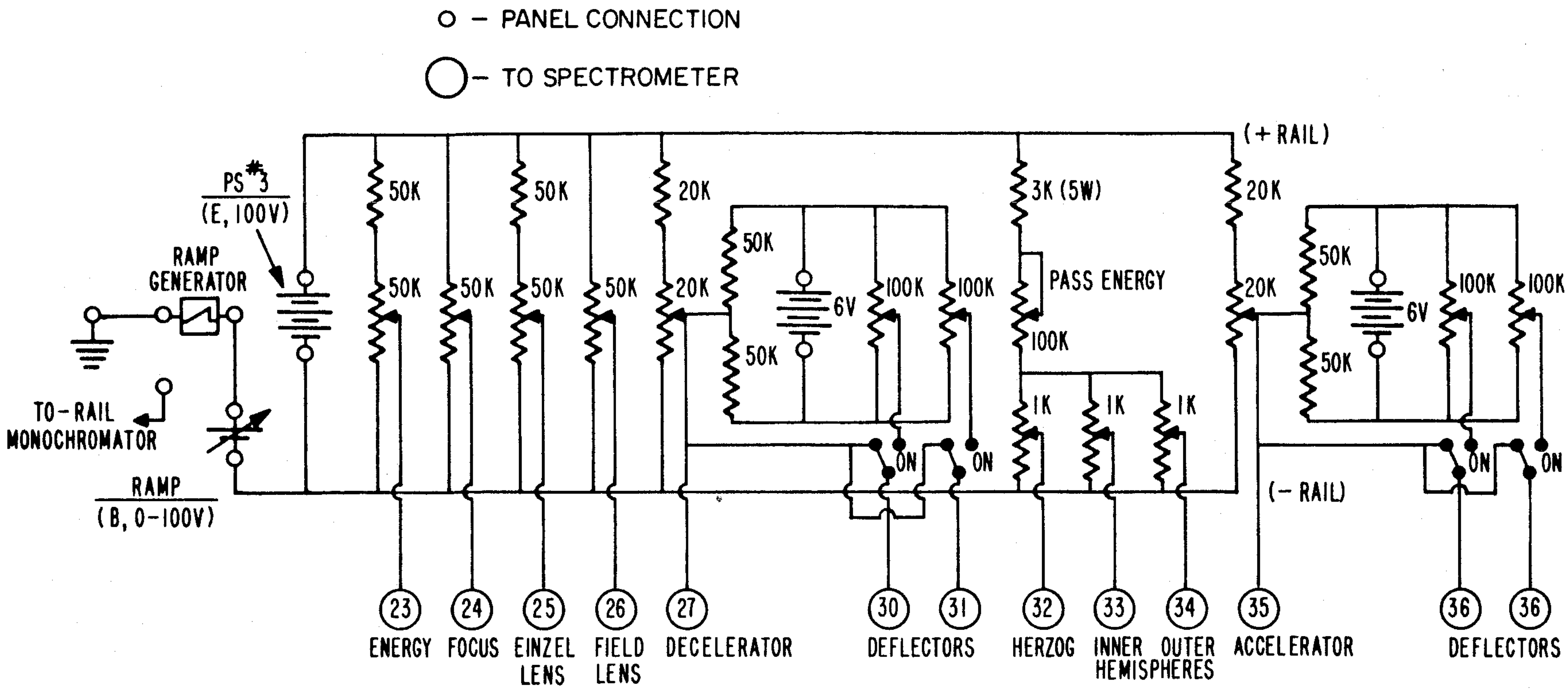

Figure 6